Investigating carbonation and other forms of chemical attack on GGBS based alkali activated materials

Cassandre F. Le Galliard

A thesis submitted in partial fulfilment of the requirements for the degree of

Doctor of Philosophy

Department of Materials Science and Engineering

Faculty of Engineering

The University of Sheffield

May 2023

Abstract

The growth in global population leads to an increase in the need for construction materials. Portland cement (PC) based materials are the most widely used due to their efficiency, price and durability. However, PC production is responsible for 5 to 8% of global carbon dioxide emissions. There is an urgent need to find (and use) alternative materials that have similar properties while having lower carbon footprint. One of the most encouraging alternatives is alkali activated materials (AAM).

An AAM is made by the reaction between an alkaline activator (such as sodium silicate or sodium hydroxide) and an aluminosilicate precursor (such as slag or fly ash). Unfortunately, there remains a gap in our knowledge concerning the durability of these materials. The durability of cementitious materials can be challenged by chemical and mechanical attack, either separately or in combination. Even though AAM microstructure and chemistry are slightly different from PC based materials, the main mechanisms of attack are believed to remain similar. In reinforced concretes based on PC, one of the main service life-limiting factors is carbonation.

Carbonation is the reaction between atmospheric CO_2 and cementitious materials. In PC based materials, carbonation causes a permeability change, by a redistribution of the pores structures, and a pH drop, potentially leading to the corrosion of the steel rebar in reinforced concrete. The corrosion products that form on steel rebar have a higher volume and can cause cracking of the concrete. Even if the carbonation process is slow, around a few millimetres per year, it is still one of the main durability challenges for concretes in service. Previous work has shown that the consequences of AAM carbonation are slightly different from those of PC carbonation.

Although the consequences of AAM carbonation depend on the mix design, past studies show that in these materials, it is possible that the pH drop is not low enough to lead to steel corrosion but the mechanical performance may decrease. To overcome the lack of service life data regarding AAM carbonation, there remains a need for an efficient and accurate standard test method to evaluate AAM carbonation, as the use of methods designed for measurement of PC carbonation may lead to inaccurate predictions.

The purpose of this PhD project is to understand the process of carbonation on GGBS based AAM, in order to advise on the design of structures containing these materials. To achieve this goal, it is necessary to understand the steps and outcomes of this reaction on AAMs, depending on the composition, to be able to predict service life under carbonation. In this work, the impact of carbonation alone, or coupled with efflorescence and/or soft water leaching on the GGBS based AAM microstructure will be observed with various test methods. This study presents the impact of the carbonation on both the reaction of the carbonatable species and the diffusion coefficient of AAM. This study also shows that when carbonation is coupled with efflorescence, the microstructure of both the non-carbonated and carbonated parts are affected, while it is not the case of when carbonation is alone or coupled with leaching. These findings should be considered while designing a structure containing GGBS based AAM. Finally, this study highlights that the change of colours in these materials is due to the oxidation of the sulphur species, and while these species are oxidised when the material is carbonated, it is not linked to the carbonation, and consequently the change of colours should not be associated to the carbonation front.

Acknowledgements

As Dr. Dan Geddes once said to me "this thesis will be a group project", and he was not that wrong. I would not have achieved this work, especially during a global pandemic, without the people acknowledged below. I will try to express my gratitude to everyone as it comes to my mind, in English and in French.

First, I would like to acknowledge my supervisors, official and non-official: Professor John L. Provis, Dr. Brant Walkley, Dr. Bruno Huet and Dr. Dan Geddes. John, thank you for offering me this wonderful opportunity and believing in me from the first day, thank you for the fruitful and the non-cement related conversation, thank you for your kindness and your leadership, and finally thank you for sharing your scientific knowledge and journey with me. Brant, thank you for still supervising me despite being my second supervisor on paper, thank you for your guidance and support in this journey, thank you for offering me a place in your research group and all the opportunities that went with it. Bruno, merci de m'avoir offert ce stage de master en 2018 sans lequel je n'aurais jamais continué dans le recherche (surtout dans le recherche sur les matériaux cimentaires), merci d'avoir accepté de collaborer pour un de mes chapitres expérimentaux de thèse et d'avoir fait le nécessaire pour rejoindre le réseau DuRSAAM, merci de m'avoir apporté exactement la quantité de supervision que j'avais besoin dans mon stage puis dans ma thèse durant mes déplacements à Lyon et durant nos réunions, et finalement, merci d'avoir partagé tant de connaissance et de savoir-faire durant ces 5 dernières années. Dan, thank you for the help and guidance from day one, despite your Donny accent (it was so hard at the beginning), you helped me so much in my experimental works and in this journey, thank you for sharing so many good (and bad) work and life experiences with me, thank you for your support in all of them, and finally thank you for introducing me to the Northern English culture while making sure I always had someone to rely on in this new country.

I would like to express my gratitude to all those who trained me or helped me in my experiments, during these last few years. I would like to acknowledge especially Dr. Oday Hussein, Dr. Martin Stennett and Dr. Sarah Kearney from the MSE department, Kieran Nash from the Civil department, Dr. Stuart Bartlett from the Diamond and Fabienne LeGrand from Holcim research center. Je voudrais aussi remercier aussi toute l'équipe de l'ex-durabilité groupe au Holcim research center, qui m'a accueillie et aidée durant mes déplacements à

Saint Quentin Fallavier. I also owe a huge thank you to my teams at the University of Sheffield: the ISL group, the cement@sheffield group and the SMASH group. In these groups, I would like to thank my co-workers that became my friends for their help and support: Tom, Ritesh, Tamara, Clem, Colleen, Antonia, Hannah, Dan, Sam, Amr, Steph, Matt, and Antonino. Ella, thank you for being the most amazing master student one could dream to have, and thank you after that for being such an amazing co-worker. Finally, this paragraph could not be complete without acknowledging my co-PhD that became lifelong friends by sharing this emotional journey, Marco, Laura, Gaone and Shaun, thank you for all!

Finally, I would like to acknowledge my friends and family for their support despite the obscure topic of my thesis. D'abord j'aimerais remercier ma famille pour leur support durant toutes mes études. Ensuite, j'aimerai remercier mes amis qui m'ont supporté dans les hauts et les bas. Laura, Fanny, Lucile, Coline, Juliane, Thibault, Elsa, Michele, Edo, Katie, Georgie, Matt, merci d'avoir été ma famille de cœur tout au long de ce chemin. Ensuite, j'aimerai aussi remercier Marie-Eve de m'avoir permis de garder un esprit clair dans toute cette tempête. Enfin j'aimerai remercier Mark pour m'avoir épaulé tout au long de ces deux dernières années.

I would like to dedicate this thesis to my grandfather René, who taught me how to make concrete at a young age, and inspired my love for the construction area.

Abbreviations

AAM	Alkali activated materials
AAS	Alkali activated blast furnace slag
ACC	Amorphous calcium carbonate
AFm	Aluminoferrite-mono
AFt	Aluminoferrite-tri
BSE	Back scattered electrons
C-A-S-H	Calcium aluminosilicate hydrate
CBC	CO_2 binding capacity
CO_2	Carbon dioxide
CSTM	Cross-linked Substituted Tobermorite Model
DoC	Degree of carbonation
EDS	Energy dispersive X-ray spectroscopy
EXAFS	Extended X-ray absorption fine structure
GGBS	Ground granulated blast furnace slag
GHG	Global greenhouse gas
IBR	Instantaneous CO_2 binding rate
MAS NMR	Magic angle spinning nuclear magnetic resonance spectroscopy
MBC	maximum binding capacity
MCL	Mean chain length

MIP	Mercury intrusion porosimetry
N-A-S-H	Alkali aluminosilicate hydrate
NDC	National determined contributions
PC	Portland cement
RH	Relative humidity
SCM	Supplementary cementing material
SE	Secondary electrons
SEM	Scanning electron microscopy
TAH	Third aluminate hydrate
TGA	Thermogravimetric analysis
TG-MS	Thermogravimetric analysis with mass spectroscopy
XANES	X-ray absorption near edge spectroscopy
XRD	X-ray diffraction
XRF	X-ray fluorescence

Contents

List of Figures

List of Tables

Chapter 1 : Introduction

Project scope

At the rate of 4 Gt per year, cement is one of the most consumed man-made materials in the world [1]. Unfortunately, this artificial binder is also responsible for 8% of the carbon dioxide (CO_2) emissions caused by human activities [2]. In the near future, these numbers are foreseen to increase as the population grows, and by then the demand in construction materials and its main component rises. Several solutions can, and must, be taken to mitigate the high environmental footprint due to the construction industry. In the short term, the content of cement in concrete can be lowered, or the content of concrete itself in structures can be reduced through a more efficient design, as the cement is responsible for 36% of the total CO_2 emissions released by the construction industry [3]. In the long term, the main solutions are proposed to be the capture and storage of the CO_2, and the use of alternative binders [4].

Some of the most promising alternative binders are alkali activated materials (AAM). These materials are formed by the alkali activation of an aluminosilicate precursor. The precursor is, in most cases, an industrial by-product or waste. The use of this waste avoids the need for additional landfilling [5]. Most European studies focus on slag based AAMs, a by-product from the steel industry, as it is the most available precursor in Europe. Even if AAMs have been known since 1895 thanks to Whiting, and popularised by Purdon in Western Europe in 1940 and by Glukhovsky in the former Soviet Union in 1959, the use of AAM at a large scale is limited [6–8]. This limitation is due to several factors including the design of an efficient regional mix, and the fact that many points related to durability remain unknown [5].

The carbonation reaction, between cementitious paste in concrete and the atmospheric CO_2, is one of the greatest threats to the durability of cementitious materials. It causes, in most cases, changes to the mechanical properties and a decrease of the pH, which increases the risk of depassivation of the steel rebar, and its potential corrosion. This process is driven by the diffusion of CO_2 into the cementitious matrix followed by its reaction with the cementitious phases [9–11]. Even though it is sometimes expected that the chemical reactions, CO_2 diffusivity as well as main controlling factors and products of the carbonation would be the same for AAM as for conventional cementitious materials, called Portland

cement based materials (PC), this is not the case. The main difference between the carbonation of PC based materials and of AAM is due to the differences in chemical composition, mainly the absence of portlandite in AAM, and the high alkali metal content in AAM pore solutions [12]. For AAMs, the CO_2 diffuses first through the capillary pores of the AAM. Then, the gas dissolves in the pore solution and reacts with the sodium rich phases, which leads to a drop of pH. Following this step, the calcium rich phases (if present) are decalcified and main hydrate products become carbonated. Consequently, depending on the choice of definition, two "carbonation depths" may exist: one corresponding to the pH changes, and the other corresponding to the reaction of hydrate products [13]. Unfortunately, few studies have been done on the analysis of the natural carbonation of in-service alkali activated binders, due to the small amount of old in-service structures available for analysis [14].

The aim of this study is therefore to understand the impact of carbonation in different environments on the microstructure and chemical composition of slag based AAM. Hence, the impact of different environments, and in particular of the relative humidity, on the material carbonation is compared.

Overview of results obtained

The carbonation of cementitious materials is highly linked to the relative humidity (RH) [15]. Even if several studies have observed the impact of a wide range of RH on these materials, none have quantified the impact of relative humidity on the amount of carbonatable products and the CO_2 diffusion of AAMs [16]. These parameters are essential to predict the carbonation depth. In order to predict the effect of the relative humidity on carbonation depth, the CO_2 binding capacity and CO_2 instantaneous binding rate are determined at several RH on one side, and the porosity and CO_2 effective diffusion coefficients at these same RH on the other side. The results are then used to predict the carbonation depth and is compared to the in situ carbonation rate. This study is conducted in collaboration with the Holcim research centre. Some of the test methods used are currently being developed in this research centre for PC, and this study proved that they could also be used with AAM.

AAMs are more likely to be subject to efflorescence than PC due to the high content of alkalis, which could be detrimental for their appearance and performance[17]. These materials are

also prone to the leaching of calcium and sodium, which could affect their microstructure severely [17,18]. Although several studies have already studied the combined effect of efflorescence and leaching, or efflorescence and carbonation, in the laboratory, no studies have addressed the problem of the combined effects of carbonation and other chemical attacks such as leaching due to rain water or leaching in outdoor conditions, on these materials [19]. In this study, the combined effect of these attacks on the microstructure under outdoor conditions have been compared to indoor natural carbonation. This has revealed the negative impact of efflorescence and carbonation on the material. Conversely, the samples exposed to the rain, and therefore exposed to leaching, are less impacted by carbonation.

Carbonation of slag based AAMs could result in harmful consequences on the mechanical properties. The oxidation of these materials seems to only alter its colour. These two processes are closely related as they are driven by diffusion processes, the first one from the CO_2 diffusion and the second one from the O_2 diffusion, and consequently could be linked. Very few studies have reported the relationship between the carbonation and the oxidation processes in slag based AAM [20]. In this study, samples have been exposed to both phenomena over a year. The reaction fronts have been observed, as well as the chemical compositions.

As part of the DuRSAAM network, two complementary studies have been conducted on high calcium content AAM as a co-investigator. These two studies led to articles published as co-author. These articles can be found in annexes attached to this thesis.

The first one, presented in annexe 1, explores the microstructural development for two alkali-activated slag mixes with different SiO_2/Na_2O ratios. The phase assemblages of these mixes were accurately predicted with a thermodynamic-kinetic model. The work performed by the author of the thesis was the SEM-EDS and NMR analysis, interpretation and drafting.

The second one, presented in annexe 2, examines how ferronickel slag, a by-product of the ferronickel alloy industry, can be used to make alkali-activated mortar. Researchers from the University of Patras, ETH Zürich and the University of Sheffield tested the mechanical properties of the mortar before and after exposure to high temperatures. The final mix design

produced 70% less CO_2 in comparison to traditional Portland cement. The work performed by the author of the thesis was the MIP and SEM-EDS analysis, interpretation and drafting.

Summary

The aim of this thesis is to have a better understanding of the carbonation mechanism depending on the environment for GGBS based AAM. In the first chapter, the RH affects the carbonation mechanism via the accurate assessment of its impact on the diffusion of the CO_2 and the reaction of the hydrated phases with the CO_2. In the second chapter, the combined effects of carbonation and other chemical attacks such as leaching due to rainwater or efflorescence in outdoor conditions, on these materials the chemical composition of these materials is evaluated. Finally, in the third chapter, the relationship between the carbonation and oxidation processes on GGBS based AAM is observed, as well as the impact of carbonation, soft water leaching and efflorescence on these processes. To conclude, the findings of this PhD project give new insight into carbonation under real conditions, while explaining in detail the carbonation process for slag based alkali activated materials. The results highlighted in this study will be important to consider while designing structures containing AAM. Indeed, if AAM is exposed to both carbonation and efflorescence, or carbonation and soft water leaching, their combined impact on AAM should be considered, on reinforced and unreinforced structures.

Chapter 2 : Literature review

2.1 Alkali activated materials

2.1.1 Concrete history and modern challenges

Concrete has been used as a construction material since before recorded history [21]. This material is a mix between a binder and aggregates [22]. The first hydraulic concrete comes from the Roman Empire. To achieve good strength, and durability that fits the climate of Italy, the Romans mixed water, aggregates, lime, and volcanic ashes called pozzolana. The term pozzolan comes from Pozzuoli, a small city of South Italy [21]. A large number of the structures made with this concrete are still standing to this day, like the arches of the Colosseum and the dome of the Pantheon in Rome, Italy [21]. Nowadays concrete is mostly made with a mix of aggregates, sand, water and Portland cement (PC). The term Portland cement comes from the patent of Joseph Aspdin in 1824, which patented a hydraulic cement made of clay and limestone heated at a temperature above 900°C [21,23]. It is interesting to highlight that: firstly Portland cement has nothing to do, apart from its colour, with Portland stone, it was just a marketing choice; secondly, Joseph Aspdin was not the only inventor of this method, he was just the first to patent it under this name [21,23]. After several improvements over the last centuries, PC as it is used now is completely different from Joseph Aspdin's original Portland cement [21]. Modern PC is a mixture of artificial calcium silicates made by heating at temperature above 1400°C a mixture of calcium carbonate based materials, such as limestone, and argillaceous materials, such as clay. The calcined mixture is then inter-ground with a small amount of calcium sulphate, usually gypsum, which is used as a setting retarder [23]. PC is now the most widespread construction material as it is cheap, predictable, workable and durable under a wide variety of environments [4,23].

Portland cement is one of the most consumed man made materials in the world, at the rate of 4 Gt per year [1]. Unfortunately, this artificial binder is also responsible for 8% of the carbon dioxide (CO_2) emissions caused by human activities, as Figure 2.1 shows [2]. This high number is because during the high-temperature decomposition of limestone, around 0.8 t of CO_2 per tonne of clinker is released from fuel and decarbonisation emissions [24]. And the total footprint of cement production should increase in the coming years as the population grows and the demand for construction materials, including cement, rises.

a The building stock

b One building

c One cubic metre concrete

d One cement bag

Legend for b (One building):
- Other
- Sanitary equipment
- Electrical equipment
- Finishing
- Insulation
- Windows
- Bricks
- Steel reinforcement
- Concrete

Legend for a (The building stock):
- Heating over lifetime
- Construction and maintenance

Legend for c (One cubic metre concrete):
- Concrete placement
  - On-site placement
  - Transport to construction site
- Concrete production
  - Concrete mixing
  - Transport raw material
- Material production
  - SCM processing
  - Cement production
  - Gravel production
  - Sand production
  - Admixture production

Legend for d (One cement bag):
- Cement final production
  - Cement grinding
  - SCM production
- Direct kiln emissions
  - Limestone decarbonation
  - Fuel burnt
- Material production
  - Fuel production and transport
  - Raw material transport and preparation

Figure 2.1: Contribution of each component to the total embodied CO_2 equivalent in a building [4].

According to the latest emissions gap report (2022) produced by the United Nations Environment Programme (UNEP) "to get on track to meet the Paris Agreement goal, the world needs to reduce greenhouse gases by unprecedented levels over the next eight years" [25]. The national determined contributions (NDC) are the contribution targets that each signatory country of the Paris agreement agreed on preparing, contributing and maintaining in the Article 4 of the Paris Agreement [25,26]. As the NDC are not strict enough, even if the unconditional NDC scenario is followed, the world temperature will rise by 2.6°C this century, which will still lead to extreme weather, depletion of drinkable water and food, as well as resources depletion, diseases and consequently large immigration flows. However, as Figure 2.2 shows, the policy now in place leads to a rise of 2.8°C, which is even worse [25]. To reach the goal of the Paris agreement, the global greenhouse gas (GHG) emissions must be reduced by 30% or 45% by 2030 to reach respectively a rise of "only" 2°C and 1.5°C [25]. The building sector needs to drastically reduce its emissions in the next eight years for these targets to be reached. To achieve this goal, the construction area needs to reduce its carbon footprint, and needs to produce sustainable infrastructure that is durable against extreme weather [25,27].
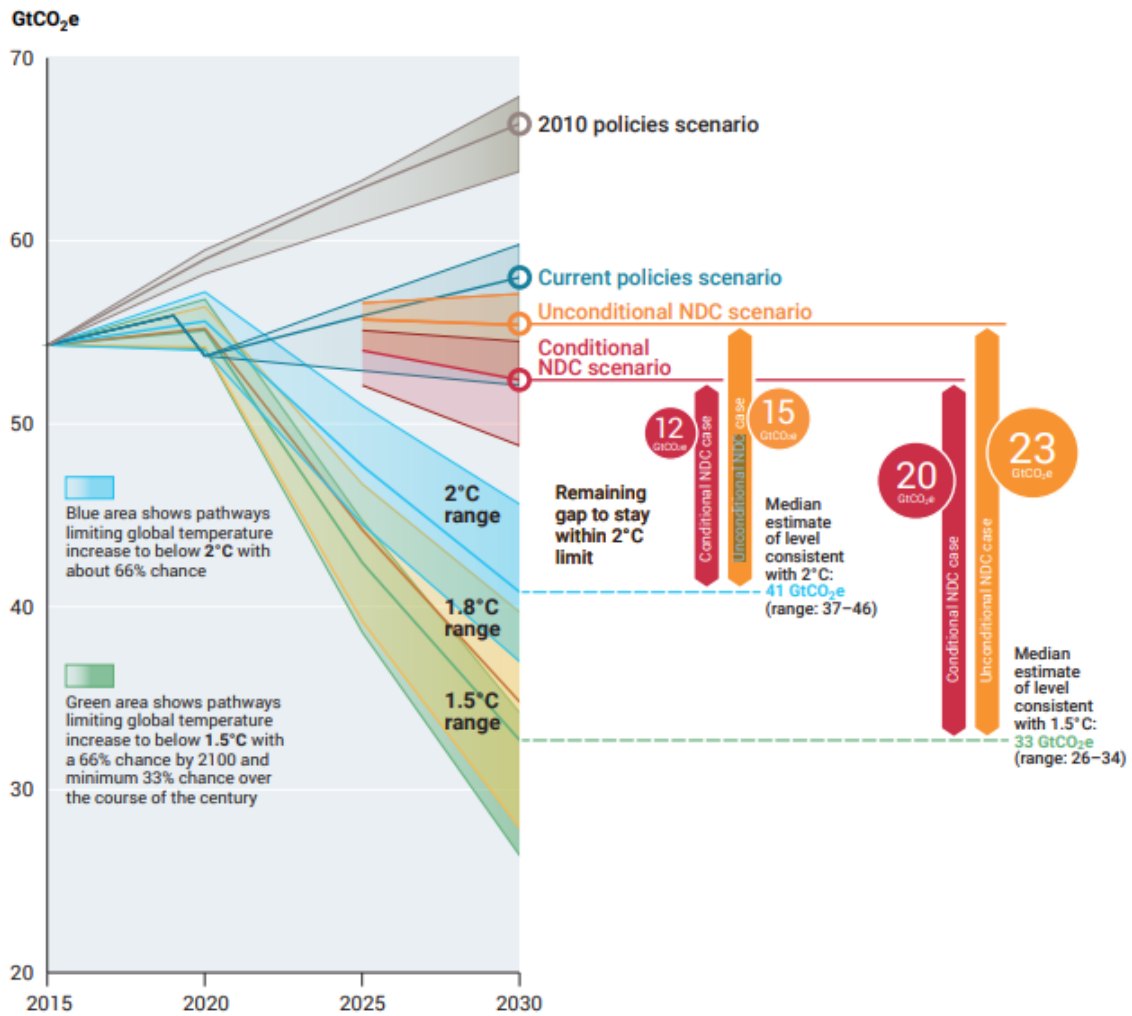
Figure 2.2: Gigatons of CO_2 equivalent ($GtCO_2$) emissions under different scenarios and the emission gap in 2030 (median and 10th to 90th percentile range). Adapted from the Emissions Gap Report 2022 produced by the UNEP [25].

Several solutions can, and must, be taken to mitigate the high environmental footprint due to the construction area. In the short term, as cement is responsible for 36% of the total CO_2 emissions released by the construction area, the content of cement in concretes can be reduced, and the content of concrete itself in the structure also reduced through a more efficient design [3]. In the long term, the main proposed solutions are the capture and storage of CO_2, and the use of alternative binders [4].

2.1.2 Alkali activated materials

In order to mitigate the high carbon footprint of PC, several substitutes have been developed. One of the most encouraging is alkali activated materials (AAM). Indeed, these materials allow

a saving of between 30% [28] to 80% [29] of CO_2 emissions compared to Portland cement. Moreover, AAMs can help to reduce landfilling by using industrial by-products and wastes as main precursors, and can give similar performance to PC [5]. These materials have been known since 1895 thanks to Whiting [6], and were initially popularised by Purdon in Western Europe in 1940 [8] and by Glukhovsky in the former Soviet Union in 1959 [7].

The reaction between an alkaline activator and an aluminosilicate precursor forms the binder called an alkali activated material [5]. As Figure 2.3 shows, two types of AAM exist depending on their main phases: high calcium content in blue in the figure, and low calcium content in green [5]. The calcium content from these materials varies depending on the precursors used, as explained in section 2.1.2.2. The activators can vary as well, which leads to a difference in several parameters such as strength development, workability and secondary products [5,14,30]. The activator categories, and their advantages and disadvantages, are presented in section 2.1.2.1.

The reduction of the environmental impact of AAM compared to PC systems is dependent on the precursors and activators used, as well as the emissions allocation used [31]. AAMs use by-product/waste materials, which leads to a controversy regarding the type of emission allocation that should be used, which is not the case to such an extent for PC materials [27,31–33]. The lowest GHG emissions reported for AAM are usually in studies done with no emissions allocations and little transport for the by-products/waste materials [33]. No allocation considers that the precursors used are a waste and not a by-product [31]. Conversely, a mass allocation of the GHG leads to a higher environmental impacts of these materials [31,33]. Economic allocation is more representative of the industries driving force compare to mass allocation, especially in the case of high economic product value. The main disadvantage of economic allocation is that it is unstable through time due to the price fluctuation of by-products [31]. Komkova *et al.* decided to use an economic allocation to evaluate the environmental impacts of AAM, and evaluated that ground granulated blast furnace slag (GGBS) based AAM could reduce by 57% the global warming potential in the case of the Belgium market [32]. One of the main issue of GGBS-based AAM is the dependency of these materials on the steel industry, which is a main carbon emitting industry [27,34,35]. Consequently, the production of steel should be reduced in Europe in the coming years [34]. Alternative precursors have been studied to fit a more responsible circular economy in Europe

[27,36]. One of the most promising material is municipal solid waste incineration ash, which could lead to 55% reduction of $CO_{2\,eq}$ in the case of the Switzerland market, according to Komkova *et al.* [37]. Consequently, in order to obtain the best AAM on environmental point of view, case-by-case precursors should be chosen depending on the countries and available resources, to limit the raw materials transport and environmental impact of AAM [35,36].
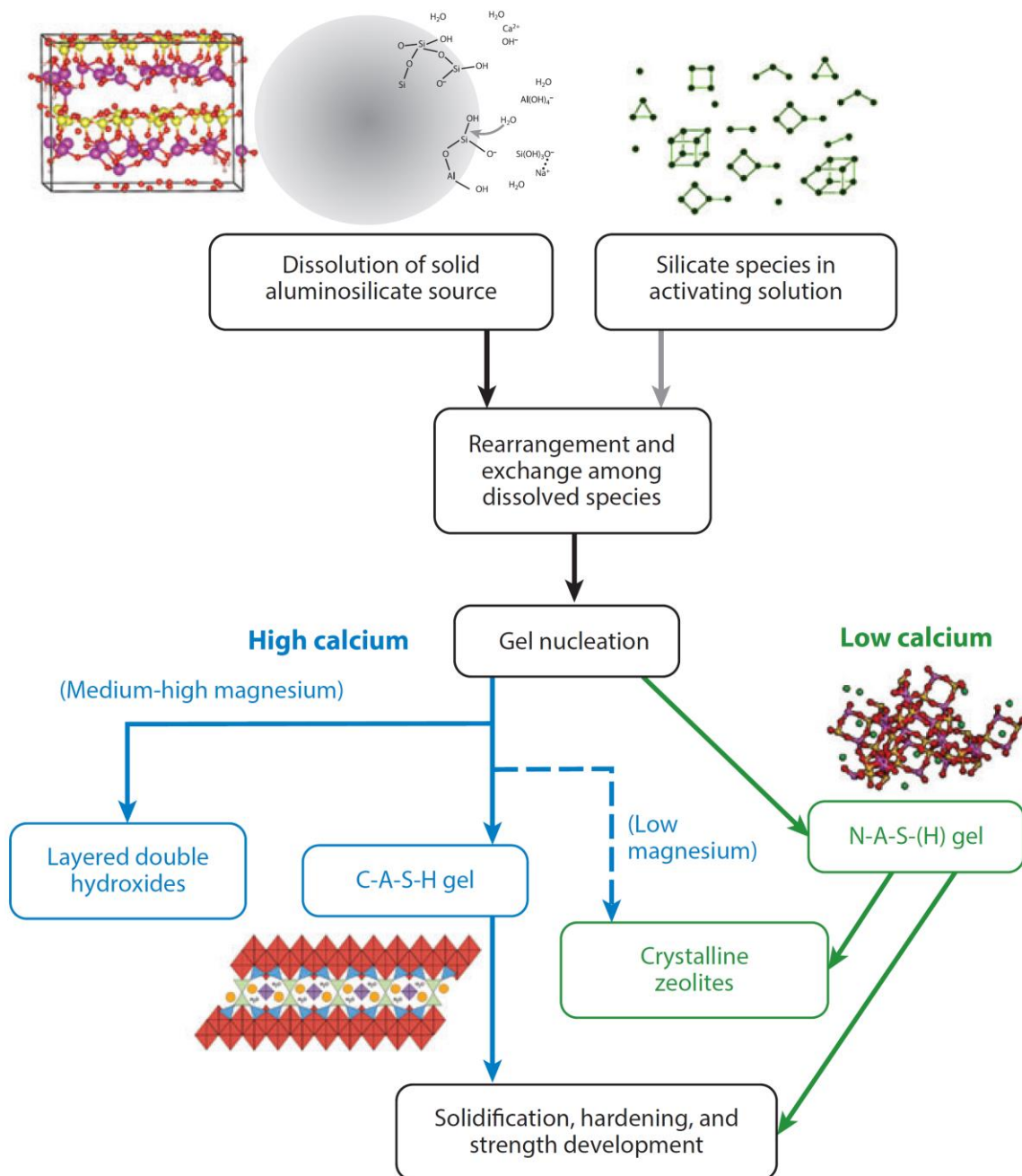
Figure 2.3: Figure from Provis & Bernal showing the "process and reaction products of alkaline activation of a solid aluminosilicate precursor. High-calcium systems react according to the left-hand

(blue) pathway, with the nature of secondary products determined by Mg content, whereas low-calcium systems react according to the right-hand (green) pathway." [5]

2.1.2.1 Alkali activators

The different activators used in AAMs are described below, from the most used to the least used.

Alkali silicates can be produced via two processes: melting carbonate salts with silicon dioxide to form a glass and dissolving this glass in water, or dissolving silicon dioxide into concentrated alkali salt solutions. Like the alkali hydroxide, silicates of sodium and potassium are the most commonly used. Lithium silicate is not soluble enough, and silicates of rubidium and caesium are too expensive to be products at an industrial level. Alkali silicate is usually produced by the calcination of silica and carbonate salts, followed by the dissolution of the products in water. Therefore, this process is highly energy-consuming and has a high carbon footprint [38].

Alkali hydroxide is the product of the electrolysis reaction of sodium chloride. Due to their high solubility in water and low cost, sodium hydroxide and potassium hydroxide are the most commonly used. Conversely, lithium hydroxide is less used due to its low solubility. As for rubidium hydroxide and caesium hydroxide, they are too expensive and scarce to be used at a commercial level. One of the main issues of alkali hydroxide activated binders is the efflorescence, which occurs mainly with sodium hydroxide and potassium hydroxide [38].

Alkali carbonate can be obtained either by the Solvay process or by the mining of carbonate salt deposits. Even if this activator is more environmentally-friendly and less hazardous, it is less commonly used than alkali silicates and hydroxides. Moreover, alkali activated binders activated with alkali carbonates generally have a much slower strength development than the ones activated with other activators. Alkali carbonates can be used only with high calcium precursors such as GGBS. With low-calcium precursors, the carbonates will leads to the formation of sodium carbonates, which are not binding phases, consequently, an additional source of calcium is necessary [14,39].

Alkali sulphates are less studied compared to other activators. They are either extracted from mining processes or by-product from the manufacturing of other chemical materials such as boric acid, silica pigments or ascorbic acid. Therefore, like alkali carbonates, these can be

potentially environmentally-friendly. However, in order to obtain a binder strength similar to the strength obtained with alkali hydroxide or silicate, it is necessary to use larger amounts of the activator, as the pH induced by these activators is lower than with alkali hydroxides and silicates. In the case of low carbon precursors, an additional source of calcium is necessary to achieve a higher strength [14].

2.1.2.2 Aluminosilicate precursors

Two main categories of AAM exist: high calcium systems (which have C-(A)-S-H gel type as main hydrate product) and low calcium systems (which have N-A-S-(H) gel type as main hydrate product) [5].

2.1.2.2.1 High calcium content AAM

Several precursors can be used to obtain high calcium content AAMs, such as different types of slag or bottom ashes. The most used and studied is GGBS. This popularity is due to its availability and composition. This by-product from the iron making industry is produced when the iron is extracted from its ores. It is mainly composed of a glass containing CaO, MgO, Al_2O_3 and SiO_2 with additional components depending on the raw materials composition [39,40]. Several types of steel slag can also be used as precursors; during the process of converting steel from iron, different types of slag are produced such as electrical arc furnace slag or basic oxygen furnace slag [41–43]. Furthermore, slags from non-ferrous metals production industries such as copper slag, nickel slag or titaniferous slag can be used as well [44–46].

The type and concentration of reaction products in AAM are highly dependent on the composition of the precursors, the activator type and concentration, and the curing conditions. The main reaction product of alkali activated blast furnace slag (AAS) is the C-(N)-A-S-H type gel, with a disordered tobermorite structure similar to the calcium hydrate phase C-S-H(I) [47,48]. The formation of AFm phases as secondary products is mainly observed in NaOH activated AAS, although strätlingite (a Si-containing AFm phase) is principally identified in sodium silicate activated binders. In AAS binders with high Al_2O_3 and low MgO content, the presence of zeolites (like gismondine and garronite) is observed, and, in contrast, AAS with a high MgO content, hydrotalcite is one of the main secondary products as Figure 2.4 shows [48–53].
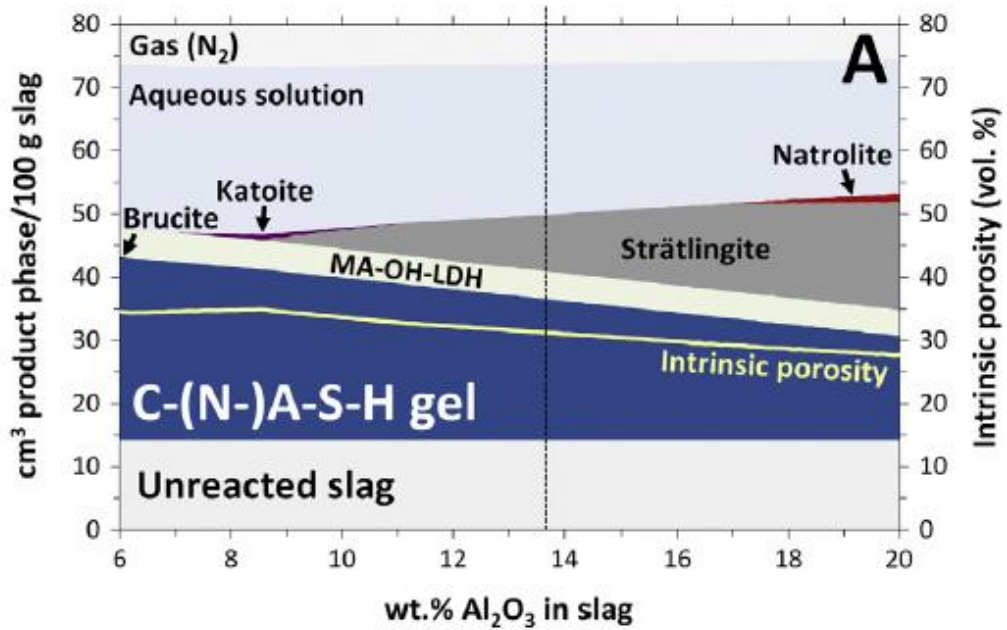
Figure 2.4: Simulated phase assemblage in Na_2SiO_3 activated slag cement, as a function of Al_2O_3 content in slag [48].

2.1.2.2.2 Low calcium content AAM

Several precursors can be used to obtain low calcium content AAMs, such as fly ash, metakaolin, feldspars, volcanic ashes, other types of clays, or even low calcium metallurgical slags. Even though the availability of fly ash from coal combustion is starting to become lower in western countries, this coal combustion waste remains the most used in low calcium content AAMs. The composition of fly ash is highly variable, but the main components are usually Al_2O_3, SiO_2 and Fe_2O_3 [5,39,40], mainly in glassy phases.

Metakaolin, the dehydroxylated product of the calcination of kaolinitic clay between 500 and 800◦C, is the other main precursor for this type of system. This type of clay has broadly similar chemical components to fly ash. Contrary to the other precursors cited above, metakaolin is not a by-product from another industry and, consequently, has a higher carbon footprint [54].

Alkali activated fly ash and metakaolin binders are the main low calcium AAM binders. The main reaction product is the N-A-S-H gel, an amorphous alkaline aluminosilicate hydrate. The secondary hydrate products are zeolites like zeolite P, Na-chabazite, hydroxysodalite and faujasite [55–58]. The composition and structure of the zeolites formed varies according to the type of activators and precursors used, and the curing conditions [59,60].

2.2 Durability

"The ability of a material to resist weathering action, chemical attack, abrasion, and other conditions of service" is called durability [61]. The durability of construction materials is a key component: it explains why some monuments like the Pantheon in Rome (Italy) can still stand almost 2000 years after their construction [21], while other can fall down over 50 years after their construction, like Morandi's Polcevera viaduct in Genoa (Italy) [62]. Many factors, either physical and/or chemical, can impact the durability of a structure. In the case of AAM structures, the long-term durability has a shorter track record than PC materials, which leads to a lack of confidence in these materials [27]. To compensate for this black spot, accelerated tests used for PC have been used for AAMs, which can lead to misleading results in some cases [63,64]. The main durability risks that can affect AAMs are listed below:

- Shrinkage causes cracking via tension, and deflection via axial deformation and warping in cementitious structures. Several types of shrinkage exist, such as plastic shrinkage, drying shrinkage, carbonation shrinkage, autogenous shrinkage and thermal shrinkage [65–68];
- Creep causes stress redistribution, loss of pre-stress, and strain and deflection in high rise structures such as bridges [69,70];
- Frost actions in cold climates may cause internal cracking via the freezing and thawing cycles, or surface scaling via the presence of de-icing salts which freeze [71,72];
- Fire can cause damage to the structure even though concrete is an incombustible material; a fire incident causes mechanical properties degradation and concrete spalling in the cementitious structure [73–75];
- Chemical attacks are caused by several aggressive aqueous solutions such as sulphate ions, acidic solutions, or soft water which causes leaching [63];
- Efflorescence causes the formation of visible surface salt deposits and may cause further degradation to the binder [19,76,77];
- Alkali aggregate reaction can cause cracking via component expansion resulting from the endogenous reaction of the internal components of the mixture [78];
- Chloride ingress causes the de-passivation and the corrosion of the steel rebar present in reinforced structures, which can lead to cracking in structures [63,79];
- Carbonation can facilitate the corrosion of the steel rebar and affect the permeability and mechanical strength of the binder [13,80,81].

Carbonation remains one of the main service life limitations due to the premature deterioration of concrete and safety of reinforced concrete structures that it causes. Consequently, the following section will focus on these mechanisms. Durability attacks that are closely related to carbonation will also be presented following the carbonation section.

2.2.1 Carbonation

2.2.1.1 Carbonation process

The reaction between cementitious paste in concrete and atmospheric CO_2, called carbonation, is one of the greatest threats to the durability of cementitious materials. The reaction process is driven by the diffusion of CO_2 in the cementitious matrix, dissolution into the pore solution, followed by its reaction with the hydrate phases containing carbonatable cations such as calcium and sodium, as Figure 2.5 shows. Figure 2.5 shows that the solid hydrate phases are decalcifies, which cause a change of porosity, in the case of Portland cementitious materials (PC), it leads to a pores refinement. It causes, in most cases, a decrease of the pH which increases the risk of depassivation of the steel rebar, and changes in mechanical properties that could have either a positive or negative impact depending on the material. The depassivation of the steel rebar is increasing the risk of corrosion of the steel rebar and is, for PC, the most harmful consequence of carbonation [9–11,82,83].
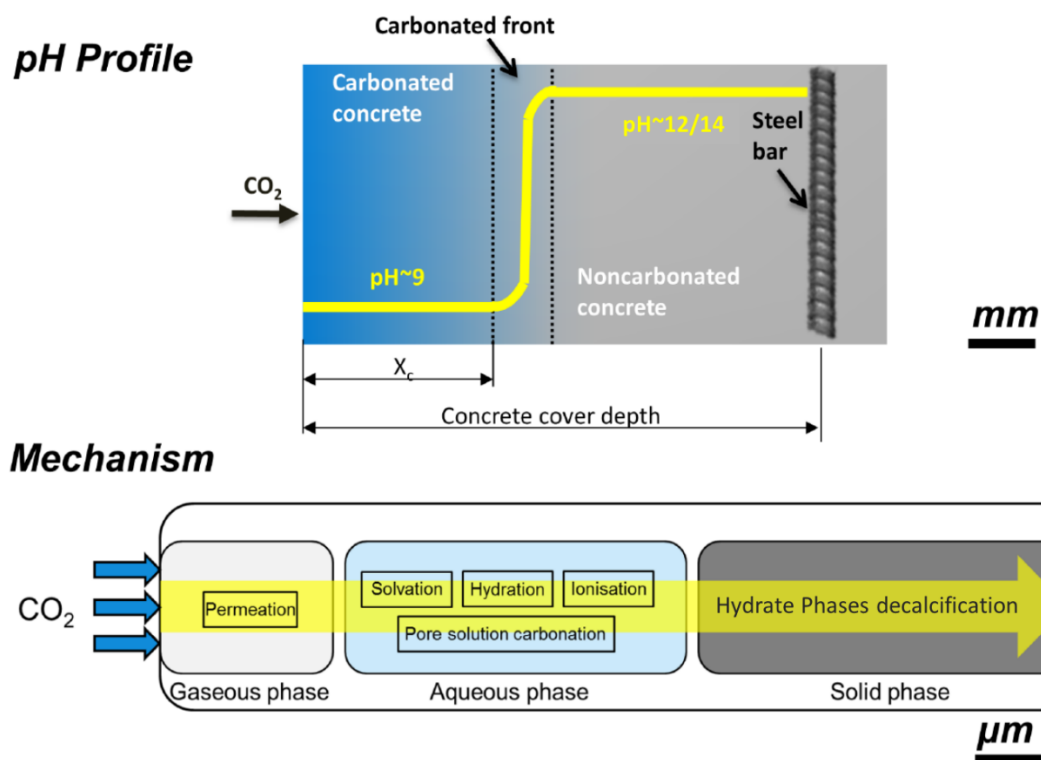
Figure 2.5: Schematic representation of the change of pH profile due to carbonation and the carbonation mechanism and driving forces in cementitious materials. Adapted from [84].

The CO_2 partial pressure, temperature, interconnectivity of the pores, relative humidity (RH), cementitious materials composition, and curing conditions, influence both the CO_2 diffusivity and reactivity, and thus also the carbonation. For example, carbonation is favoured by an intermediate (50-70%) relative humidity. If the relative humidity is too low, the pore solution saturation degree will be too low to allow the dissolution of the carbon dioxide gas. In contrast, if the relative humidity is too high, the carbon dioxide will not be able to diffuse [10,85,86].

2.2.1.2 Alkali activated materials carbonation mechanisms

Even though it is sometimes expected that the chemical reactions and the CO_2 diffusivity, main controlling factors and output of the carbonation would be the same for AAMs as for PC, it is not the case. The principal source of difference between AAMs and PC is the difference in chemical composition of AAMs and PC, and more precisely, the absence of portlandite in AAMs and the high alkali metal content in the AAM pore solution [12,87].

Unfortunately, few studies have been published on the analysis of the natural carbonation of in-service alkali activated binders, due largely to the small amount of old in-service structures available [14,88,89]. Shi et al. reported the carbonation rate of in-service AAM structures from Russia, Ukraine and Poland, and the results obtained are presented in Table 2.1 [14].

Table 2.1: Summary of in-service carbonation rates of AAM concretes according to [14].

Location	Application	Date	Compressive strength (MPa)	Average carbonation rate (mm/year)
Odessa, Ukraine	Drainage collector	1966	62 (34 years)	<0.1
Krakow, Poland	Precast floor slabs and wall panels	1974	43 (27 years)	0.4
Zaporozhye Oblast, Ukraine	Silage trenches	1982	39 (18 years)	0.2-0.4
Magnitogorsk, Russia	Heavy duty road	1984	86 (15 years)	1
Lipetsk, Russia	High-rise residential buildings	1986	35 (14 years)	0.4

| Tchudovo, Russia | Prestressed railway sleepers | 1988 | 82 (12 years) | 0.7-1 |

2.2.1.2.1 CO_2 diffusion

Firstly, the CO_2 diffuses through the capillary pores of AAM. PC and AAM CO_2 diffusion steps are similar. The CO_2 diffusion is affected by several parameters such as the relative humidity, the temperature, the pore structure, and the shrinkage [10,13,86]. A high relative humidity blocks the capillary pores and slows the CO_2 diffusion, whereas a low relative humidity lowers the pore solution content and consequently the scope for CO_2 dissolution [16]. However, a low relative humidity can also cause microcracking which leads to higher CO diffusion [90]. Furthermore, the cracking tendency due to shrinkage in dry conditions is higher in alkali activated slag, especially at early ages. The cracks caused by the shrinkage results in an increase in CO_2 diffusion [68,90–93].

The diffusivity is the rate of diffusion, which is express in $m^2.s^{-1}$ [94]. In a porous media, the effective diffusion coefficient is introduce, as the bulk diffusion coefficient overestimates the diffusion coefficient. The effective diffusion coefficient is "based on the average cross-sectional area open to diffusion and the distance traveled by molecules in the porous medium" [94]. To evaluate the effective diffusion coefficient, the most common approach is to use Fick's second law [95].

Boumaaza *et al.* developed a test method to evaluate the effective diffusion coefficient of various gas [96,97]. This method, which is non-destructive, can be performed at various relative humidities on a reasonable timescale depending on the materials permeability [96]. Boumaaza *et al.* highlighted that the carbonation increases the oxygen-effective diffusion coefficient of PC systems at all the RH with various water/binder ratio (w/b), with the notable exception of the PC with slag, as a supplementary cementing material (SCM), at 33% and 55% RH [98]. In this study, the oxygen gas diffusivity varies from one to two orders of magnitude upon the carbonation, due to the change in the water retention capacity and in the pore size distribution after carbonation [98]. This work highlights that the CO_2 diffusion coefficient, which can be calculated from the O_2 effective diffusion coefficient using the Graham law [99], is the main parameter that leads the carbonation rate [97,98].

2.2.1.2.2 Pore solution carbonation

After the diffusion of the carbon dioxide through the capillary pores of the cementitious matrix, the CO_2 dissolves in the pore water as bicarbonate (HCO_3^-) and carbonate ions (CO_3^{2-}) [100,101]. However, AAM contains more hydroxyl, and potassium or sodium, ions in the pore solution than PC, which leads to a higher alkalinity. The presence of the (bi)carbonate ions in pore solution drives the precipitation of alkali-rich carbonates [12,100,102]. The carbonation of the pore solution has as a consequence the decrease of the pH [100,103–105].

Bernal et al. studied the chemistry of the alkali activated slag pore solution under natural and accelerated carbonation [100]. Pastes of GGBS activated by sodium silicate were exposed to 1, 3 and 5% CO_2, and to natural carbonation. The samples were analysed by X-ray diffraction and the pore solutions of the samples were thermodynamically modelled. The authors observed the presence of nahcolite ($NaHCO_3$) and thermonatrite ($Na_2CO_3 \cdot H_2O$) in the samples exposed to high CO_2 atmospheres while in the paste exposed to natural carbonation, natron ($Na_2CO_3 \cdot 10H_2O$) was predominant. This difference is due to the variations in CO_2 concentration according to Figure 2.6. Moreover, the authors assert that due to the larger molar volume of the natron, this compound is more space filling than thermonatrite and nahcolite. Consequently, under natural carbonation the diffusion of the CO_2 will be lower than under accelerated carbonation due to the pore blockage by natron.
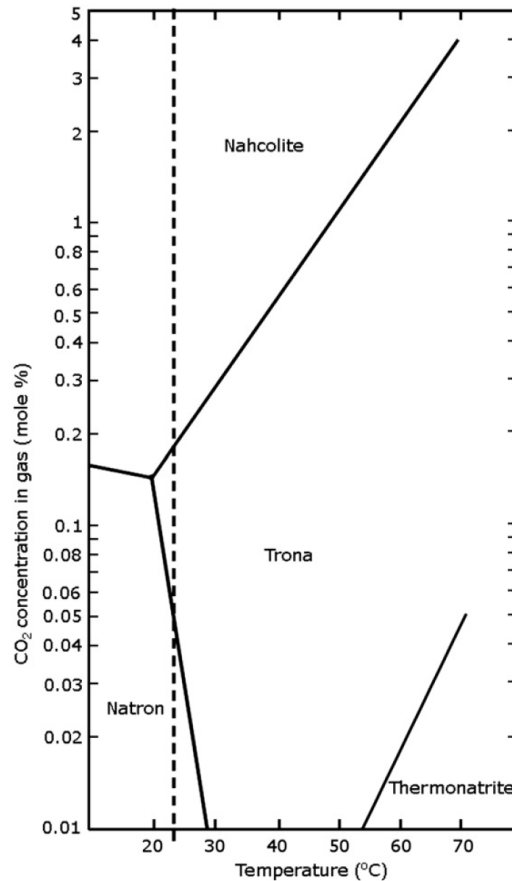
Figure 2.6: Phase diagram as a function of temperature and gas phase CO_2 concentration for the Na_2CO_3—$NaHCO_3$—CO_2—H_2O system in an air atmosphere at ambient pressure according to the article of Eugster [106]. The dashed line represents a temperature of 23°C, as used in the experimental work done by Bernal et al. reported in [100].

However, Nguyen *et al.* did not observe sodium carbonates in the carbonated sodium hydroxide and silicate activated GGBS AAM, which led them to undertake geochemical modelling of the stability of several sodium carbonates under their carbonation reaction conditions [107]. According to this study, sodium carbonates are intermediate carbonation products. Indeed, the hydroxide ion released during the reaction of the bi/carbonate ions will then react with the sodium carbonates and calcium ions present due to the decalcification of the C-A-S-H gel. This reaction leads to the formation of calcium carbonates, water and sodium hydroxide, which will then activated the unreacted slag to form more C-A-S-H, that will then undergo the same carbonation cycle again [107]. However, it is important to highlight that this study did not integrate trona into their model even though it is the form of sodium

carbonate that is calculated to be present at the CO_2 partial pressure used in this study, 1% CO_2, according to Figure 2.6.

In the study of Bernal *et al.* in the pore solution of samples exposed to natural carbonation, the bicarbonate ions were thermodynamically predicted to be present at only a very low concentration, as shown in Figure 2.7 [100]. The difference in the carbonate/bicarbonate ionic equilibrium can explain the compositional changes of the pore solutions. Bicarbonate ions are more acidic and correspond to a higher pH reduction than carbonate ions. Consequently, according to the thermodynamic model made by those authors, the pH of the pore solution exposed to natural carbonation is above 11 while the pH of the same solution exposed to 4% CO_2 is around 9 [100]. These results are also consistent with more recent studies [102]. Consequently, as the depassivation of steel rebar of the reinforced concrete is happening around a pH of 9, it may not corrode even though the binder around it is carbonated [100,103–105].
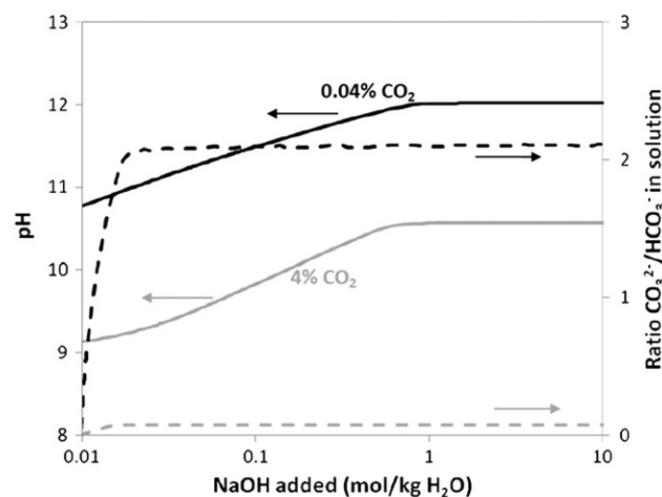
Figure 2.7: Results from thermodynamic study of Bernal et al. [100]: pH (solid lines) and carbonate/ bicarbonate ratio (dashed lines) as a function of NaOH addition and CO_2 concentration, for simulated alkali-activated binder pore solutions. Black lines are at 0.04% CO_2, and grey lines at 4% CO_2.

1.2.1.2.3 Carbonation of main phases

Following the dissolution step, the calcium rich phases (if present) are decalcified and the main hydrate products carbonate. Consequently, depending on the choice of definition, two "carbonation depths" may exists: one corresponding to the pH changes, and the other corresponding to the reaction of hydrate products [13,14,100,108].

The reaction of the bulk hydration products is different depending on the calcium content of the alkali activated materials. Indeed, the main hydrate product in the high calcium content alkali activated materials, C-A-S-H gel, appears to be less resistant to carbonation than N-A-S-H gel, which is the main product in the low calcium content alkali activated materials. The carbonation of the C-A-S-H gel happens in two steps. Firstly, the decalcification of the gel occurs: the calcium is removed from the interlayer to form calcium carbonate with the carbonate ions represented in yellow in Figure 2.8, causing a decrease of the Ca/Si ratio until the Ca/Si ratio reaches 0.67 which corresponds to an infinite silicate chain. Secondly, the gel starts to decompose to form amorphous silica gel composed of Q^4 and Q^3 silicate tetrahedral sites. The aluminium present in the gel precipitates and is integrated in the amorphous silica phase to form tetrahedral $Al(-OSi)_4$ sites [109,110]. Therefore, carbonation causes the decalcification of the C-A-S-H gel phases which results in a loss of mechanical strength and reduction of the gel pores [93,108,111,112]. The main hydrate phase of alkali activated fly ash binders, N-A-S-H gel, appears to be resistant to carbonation in chemical terms, even though it is possible that sodium can be removed from the gel to react with the (bi)carbonate ions [113,114].
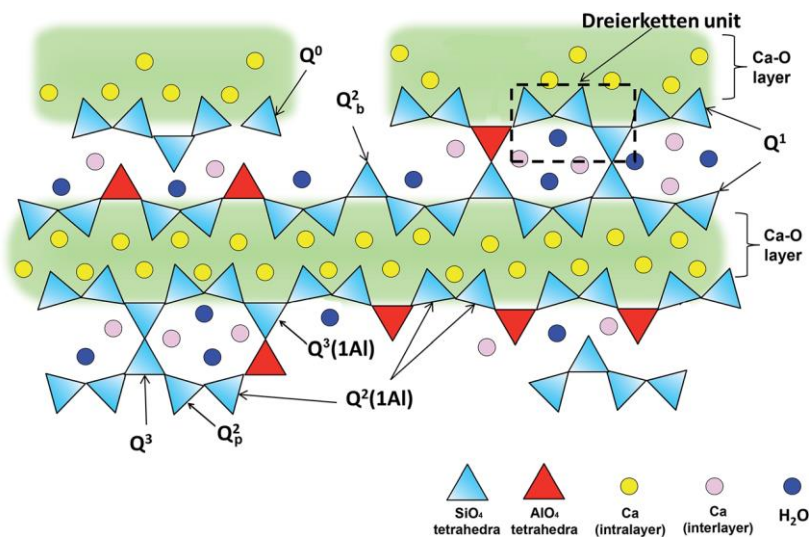
Figure 2.8: Schematic illustration of cross-linked and non-cross-linked C–(A–)S–H structures. Ca ions in the intralayer (marked as "Ca-O layer" in the graphic) are charge-balanced by oxygens of the Si(Al)O$_4$ tetrahedral chain that are adjacent to the intralayer Ca; the oxygens that point to the intralayer Ca; the oxygens that point to the interlayer Ca, protons, and partially by hydrogen bonds formed with water molecules. Adapted from [110].

The reaction between the calcium and the carbonate ions leads to the formation of calcium carbonates. For the high calcium content, the calcium comes from the C-A-S-H gel mainly [90,114,115]. As the polymorph which is the least stable and closer in energy to the original state will form according to the Ostwald Step Rule, the first polymorphs of calcium carbonate to form are aragonite (orthorhombic) and vaterite (hexagonal) [116]. Amorphous calcium carbonate (ACC) have also been observed as an intermediate carbonation product under accelerated carbonation [117]. Afterwards, calcite (rhombohedral) is formed [102,116]. Calcite is the main calcium carbonate polymorph formed under natural carbonation, whereas aragonite and vaterite are the main polymorphs formed under accelerated carbonation [100,112,114].

Several studies have shown that a high MgO content in slag based AAM reduces the carbonation depth significantly compared to alkali activated slag materials with a low MgO content. Indeed, these studies reveal that the C-A-S-H gel is less decalcified which means it is less subject to carbonation. It has been concluded that the layered double hydroxides with a hydrotalcite type structure chemically bind with the CO_2, and avoid the carbonation of the C-A-S-H gel [118–123]. The high content of magnesium could leads thermodynamically to the formation of dolomite, even though kinetically the formation of dolomite is too slow to be observed as carbonation products [124]. Ke *et al.* show that the addition of calcined layered double hydroxides with a hydrotalcite type structure can chemically bind the CO_2, and avoid the loss of mechanical strength on account of the reduction of the decalcification of the C-A-S-H type gel [118]. Moreover, according to Wang *et al.*, a high magnesium content induces lower structural changes in the pores during carbonation, and indeed, less loss of volume of gel pores and consequently less capillary pores and more tortuosity after carbonation [120]. Consequently, a high magnesium content increases the service life of the alkali activated slag binders by reducing the negative outcomes of the carbonation.

2.2.1.3 Carbonation standard test methods

Currently, the standard test methods to assess the carbonation of AAM are the same standard test methods used to assess PC carbonation. These standards are divided into two steps, the exposure and the measurements [125–130]. The main standards used in Europe are presented in Table 2.2. As the natural carbonation process is usually very slow (a few mm per

year), the exposure of the samples is conducted under an atmosphere with a high CO_2 partial pressure in order to accelerate the process. The atmospheric CO_2 partial pressure is around 0.041% while the accelerated tests are performed with a CO_2 partial pressure between 1% to 100% [125–129,131]. The only exception is the European standard EN 12390-10 "Determination of the carbonation resistance of concrete at atmospheric levels of carbon dioxide" published in 2018. The carbonation process is done under atmospheric CO_2 partial pressure [130]. This standard might be more reliable for AAM as several studies suggest that accelerated carbonation tests could be representative of the natural reaction only below 1.5% CO_2. Indeed, the saturation of the pore solution with CO_2 at higher partial pressures leads to different chemical reactions than atmospheric carbonation, as it affects the carbonate/bicarbonate equilibrium [100,104,112,123,132].

After exposure, the samples are cut in half and phenolphthalein is sprayed on the newly exposed surface; this chemical indicator is pink when the pH is above 9.5, and colourless below. The line between the two colours is taken to represent the carbonation front. The table below summarises some of the main test methods used to evaluate the carbonation resistance of cementitious binders [125–130]. However, the phenolphthalein presents several disadvantages. Firstly, it is now considered carcinogenic and is suspected to cause genetic defects according to the regulation (EC) N°1272/2008. Chinchón-Payá *et al.* proposed to replace phenolphthalein by curcumin in ethanol solution. This solution is harmless but has pH indicator properties similar to phenolphthalein. Figure 2.9 shows a mortar made with CEM III/A and siliceous aggregate sprayed with ethanol solution containing curcumin on the left side, and phenolphthalein on the right side [133].

In the case of alkali activated binders, some of them can be carbonated and still have a pH above 9.5 [100,101,104]. Hence, the phenolphthalein may remain pink while the binder is carbonated. Several studies have been conducted to develop more relevant pH indicators for alternative materials such as AAM, but none of them have been implemented in standards [134,135]. Finally, the phenolphthalein needs to be dissolved in a solvent to be sprayed on the concrete. The effect of the solvent, especially if it is water, is unknown. Indeed, the water might reveal an alkaline surface by redissolving the dried pore solution [39]. Despite its known disadvantages, the phenolphthalein-based test method is widely accepted and used

[136,137]. Therefore, the carbonation depth of alkali activated binders, obtained with these test methods, reported in the literature should be considered carefully.
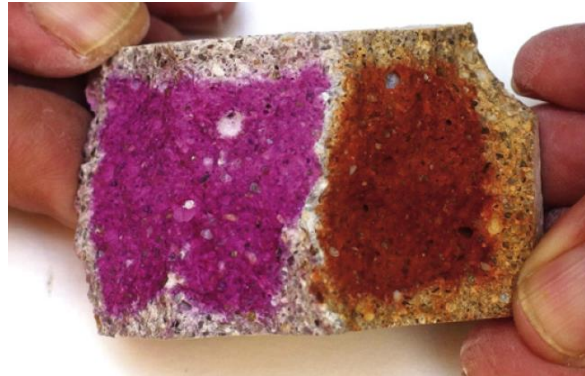
Figure 2.9: Mortar made with CEM III/A and siliceous aggregate sprayed with ethanol solution containing 0.5% curcumin on the left side, and 1% phenolphthalein on the right side. Image from [133]

Table 2.2: Some of the main test methods used to evaluate the carbonation resistance of cementitious binders. Adapted from chapter 12 of [80]

Name	Curing time	% CO_2	Conditions	Indicators
EN 13295:2004 [125]	25 days at 60% RH 21°C Stored during 56 days preconditioning	1%	60±10% RH 21±2°C	1 g of phenolphthalein in a solution of 70 mL ethanol and 30 mL demineralised water
French test method AFPC AFREM [126]	28 days in water Stored at 50% RH / 20°C	50%	65% RH 20°C	0.1% alcoholic solution of phenolphthalein
Portuguese standard LNEC E391 [127]	14 days in water 20°C Stored during 28 days at 50% RH / 20°C	5±0.1%	55-65% RH 23±3°C	0.1% alcoholic solution of phenolphthalein
NORDTEST METHOD: NT Build 357 [128]	14 days in water 20±2°C Stored during 28 days at 50±5% RH / 20±2°C	3%	55-65 % RH	1 g of phenolphthalein in a solution of 500mL of ethanol and 500 mL

			Tempera-ture not specified	distilled water/ion exchanged water
EN 12390-12:2020 [129]	28 days at ≥ 95% RH 20±2°C Stored during 14 days preconditioning	3±0.5%	57±3% RH 20±2°C	solution of 0.8 g of phenolphthalein dissolved in a solution of 70 mL ethanol and 30 ml of deionised water or a suitable alternative indicator giving a colour change in the range pH 8 to 11 e.g. thymolphthalein
BS EN 12390-10:2018 (Climate controlled chamber)[130]	Set the specimen in the mould sealed for at least 16 h, but not longer than 3 days, at a temperature of (20 ± 5) °C (or (25 ± 5) °C in hot climates), protected against shock, vibration and dehydration. Cured for 27 days at ≥ 95% RH 20±2°C Exposed the sample to laboratory air, T = (20 ± 2) °C, RH = (65 ± 5) % for (16 ± 2) h	(0.040 ± 0.001) % with no variation outside (0.040 ± 0.005) %	20 ± 2°C 65 ± 2 % RH	1 g of phenolphthalein powder dissolved in a solution of 70 mL ethanol and 30 mL of deionized water.
BS EN 12390-10:2018 (Natural exposure site)[130]	Set the specimen in the mould (24 ± 2) h. Demould and seal it, and store it in an environment at 20 ± 2) °C until they have reached 50 % of the reference strength. In case of the strength development unknown, tested at different ages to check that the 50 % of the reference strength has been achieved. At least 2	CO_2 concentration recorded with a precision of ± 0.001 % by volume. If it is not possible, local meteorological data	Natural exposure protected from direct precipitation. RH (precision ± 1.0%) and temperature (precision ± 0.5°C) should be measured	1 g of phenolphthalein powder dissolved in a solution of 70 mL ethanol and 30 mL of deionized water.

specimens should be tested at 28 days to confirm the reference strength.	can be used.	at least 4 times per day.
		If it is not possible, local meteorological data can be used.

It is important to notice that all these tests are destructive, hence, the key structure in service cannot be analysed and the same specimen cannot be tested several times to observe the carbonation depth evolution over time. Some tests, e.g. EN 13295, attempt to avoid this problem by taking progressive slices of a large test specimen for analysis, but this introduces its own difficulties in the specimen fabrication and handling [138].

2.2.1.4 Carbonation prediction

Prediction models can help to improve the understanding of cementitious materials carbonation. Three main types of prediction models exist: carbonation front predictions, reactive transport models, and thermodynamic models. The first type predicts the rate of ingress of the carbonation front, which is where the pH changes. The second one connects transport and reaction in a simulated microstructure. The third type is able to predict the chemical phases obtained through a more rigorous approach, and consequently may be argued to be more chemically precise, but does not give direct information about carbonation rates.

2.2.1.4.1 Carbonation depth prediction

The carbonation depth is an important piece of data that is used to calculate the service life of concretes as a function of the cementitious materials used in them. The most widely used and simplest prediction model is a semi-analytical model derived from Fick's first law of diffusion [94,139]. In this model, the average carbonation depth is a function of the carbonation rate multiplied by the square root of time. Nowadays, several standard carbonation test methods such as EN 13295:2004 are based on this model, which can be

empirically fitted to measured carbonation depths by defining a carbonation rate coefficient [125].

The second most used model is the Papadakis model. Papadakis *et al.* developed an empirical model based on accelerated carbonation tests conducted on Portland cement based concrete and mortars. This model assumed that the carbonation is divided into two steps: the CO_2 diffusion in the capillary pores, and the chemical reaction of the major cementitious components (portlandite, C-S-H gel, alite and belite), called the carbonatable mass, with the carbonate ions [11].

$$X = \sqrt{\frac{2D_{e,CO2}^{c}[CO_2]^0}{[Ca(OH)_2]^0 + 3[CSH]^0 + 3[C_3S]^0 + 2[C_2S]^0}t}$$

<div align="right">Equation 2.1</div>

Here, $D^c_{e,CO2}$ is the CO_2 diffusion coefficient, t is the time, X is the carbonation depth, $[CO_2]^0$ is the initial concentration of CO_2, and ($[Ca(OH)_2]^0$ + $3[CSH]^0$ + $3[C_3S]^0$ + $2[C_2S]^0$) is the carbonatable mass.

This model is obviously designed for application to Portland cement, and does not consider non-Portland cements such as AAMs. It also does not take into account all the external factors such as the relative humidity or the temperature. Consequently, several more extended models have been developed during the last fifteen years to predict the carbonation depth while including more parameters [139–141]. For example, Van-Loc Ta *et al.* developed a meta-model to calculate the carbonation depth [139]. The input data of this model are the concrete mix design (type of cement, additions type and quantities, water to cement ratio, aggregate to cement ratio, maximum aggregate size), the environmental conditions (relative humidity, temperature, environmental CO_2 partial pressure) and the quality of the execution (initial curing period). The predictions of this model are similar to the carbonation depth data of several experimental campaigns collected in the literature. For example, the calculated carbonation depth evolution of a concrete bridge structure in Seoul (South Korea) is compared with the data obtained with the model by Papadakis [11] and that of Yang [141], in Figure 2.10 [142].
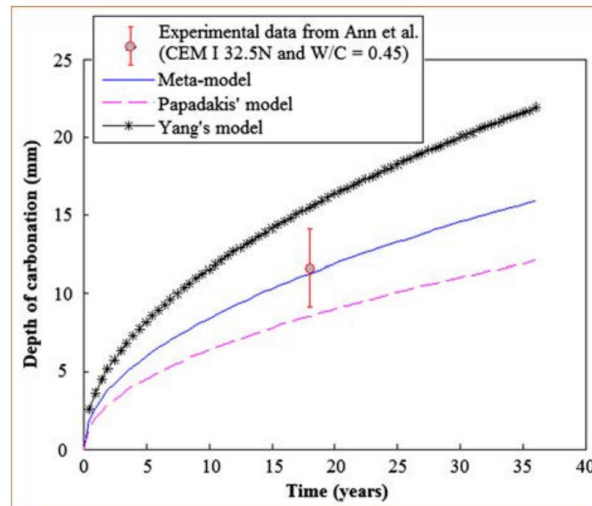
Figure 2.10: Comparison between calculated and experimental carbonation depth results [139].

2.2.1.4.2 Coupled reactive transport models

Several researchers have addressed the development of coupled reactive transport models for the carbonation of cementitious materials. These types of models predict the carbonation front more accurately. Isgor and Razaqpur have developed a nonlinear finite element model that couples heat transfer, moisture transport and carbonation processes for concrete structures [143]. This model has been developed on CONDUR, a Windows based finite element program. It determined the CO_2 partial pressure, the moisture and the heat transport in the concrete structure while taking into account the cracking in the structure. Moreover, the authors included a description of the effects of microstructure changes due to the carbonation on the CO_2 diffusion coefficient. The carbonation front obtained in two dimensions has been compared to the results obtained experimentally by Jones *et al. for* PC based concretes [144]. Even though the experimental results were in one dimension, the modelling carbonation depth was similar to the one obtained experimentally [143].

Seigneur *et al.* developed a coupled two-phase reactive transport model [145]. This model is based on a sequential iterative approach; the diffusion triggers the reaction which will impact the diffusion in return. The simulation considered the following processes to be closer to reality: aqueous and gas transport, two-phase compressible flow, gas-liquid-solid chemical equilibrium, including water consumption/production through porosity changes and chemical reactions. The results of these simulations have been compared to experimental studies on

two systems: a hydrated C_3S paste, and a low-pH paste composed of C-S-H with a Ca/Si ratio of 1.4 and small traces of portlandite. The modelling results were similar to the C_3S paste observations, but uncertainties remain for the low pH paste. These differences were attributed to the tendency of this material to develop cracks [145].

Even if these models could be extended or adapted to predict the carbonation depth for alkali activated materials by adapting the chemistry, they are only characterising the changes of pH and not the mechanical properties changes. Therefore, obtaining information about the evolution of the binder chemistry and microstructure changes to predict the pH and mechanical properties changes is necessary to more accurately predict carbonation effects in alkali activated materials.

2.2.1.4.3 Thermodynamic modelling

Thermodynamic modelling enables calculation of the phases present within a given system at equilibrium. The most widely used thermodynamic modelling approach in cement chemistry is the Gibbs free energy minimisation technique, which gives the phase equilibrium of a system at a chosen temperature and pressure. The Gibbs free energy of a system is minimised when a system is at equilibrium. Thus, by calculating this minimum, it is possible to find the phase equilibrium of a system [146]. This approach cannot directly predict transport rates, but can potentially be coupled with transport simulations, or may be used as a "titration" simulation that is calculated on the basis of quantities of material reacted but not necessarily with a link to spatial resolution[147] .

A popular program used in geosciences and other areas to find the equilibrium phase assemblages in chemical systems is the GEM-Selektor software [148]. In cement chemistry, the thermodynamic database used with this software is CEMDATA, developed by Lothenbach *et al.* [48,149]. This database has been produced specifically to predict phase assemblages and chemical compositions for Portland cement based binders, alkali activated materials, calcium aluminate and calcium sulfoaluminate cements.

Ke *et al.* compared the carbonation of GGBS-based AAM depending on the activators used and the MgO content, by thermodynamic modelling [147]. The GEM-Selektor V.3 software with CEMDATA18 was used. The phase assemblage and the pH evolution of the sodium activated and sodium silicate activated cements are presented respectively in Figure 2.11 and Figure 2.12. In both cases, the unreacted slag amount is set at 70% and the Na_2O percentage

is 4%. These results are predicted for a step-wise accelerated carbonation at 1% CO_2. In the case of the sodium silicate, the Na_2O/SiO_2 molar ratio is 1. To model the aqueous activity coefficients, the extended Debye–Hückel model is used [147]. This study predicted that the main carbonation products are calcite and an aluminosilicate gel. It also shows that a small amount of M-S-H and huntite should be present due to the carbonation of the hydrotalcite type phases. The AFm and ettringite phases, which are the sulphate-bearing phases in these systems, carbonated into gypsum. The main difference between the sodium hydroxide and sodium silicate activated sample is the composition of the aluminosilicate gel. Stilbite, analcime and Na-Ca_NAT (an ideal solid composed of scolecite and natrolite) are all zeolites with different Si/Al ratios that represent the aluminosilicate gel formed after carbonation. [147].
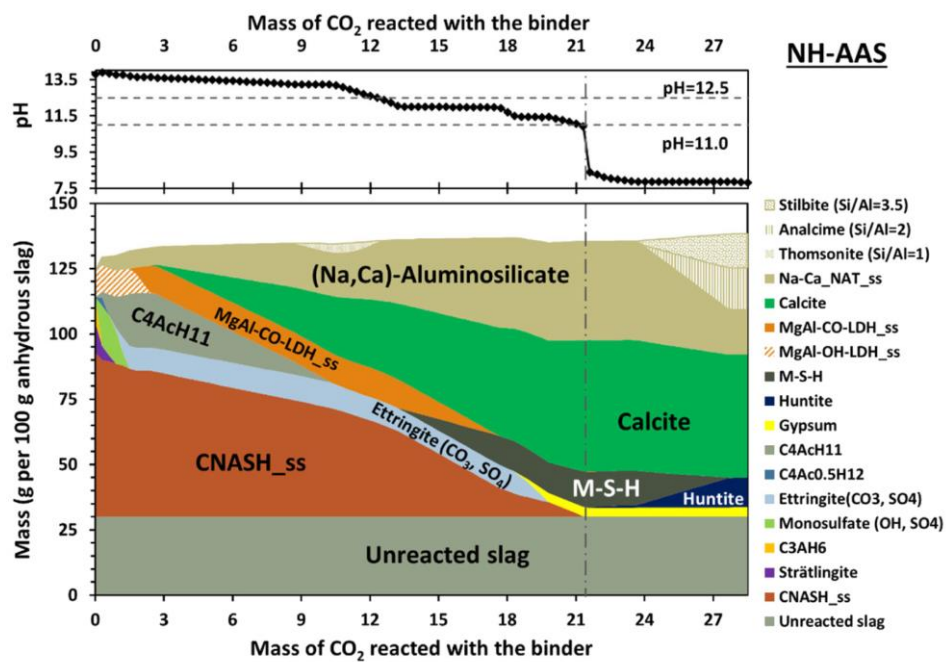
Figure 2.11: Phase assemblage of sodium hydroxide activated slag paste predicted under step-wise 1% CO_2 carbonation, and the corresponding pH in the aqueous phase (pore solution). The horizontal dashed lines represent pH values of 12.5 and 11 respectively, and the vertical dash-dot line indicates the predicted phase assemblage and the pH at the exhaustion of all the C-(N)-A-S-H. Results from the study of Ke et al. [147].
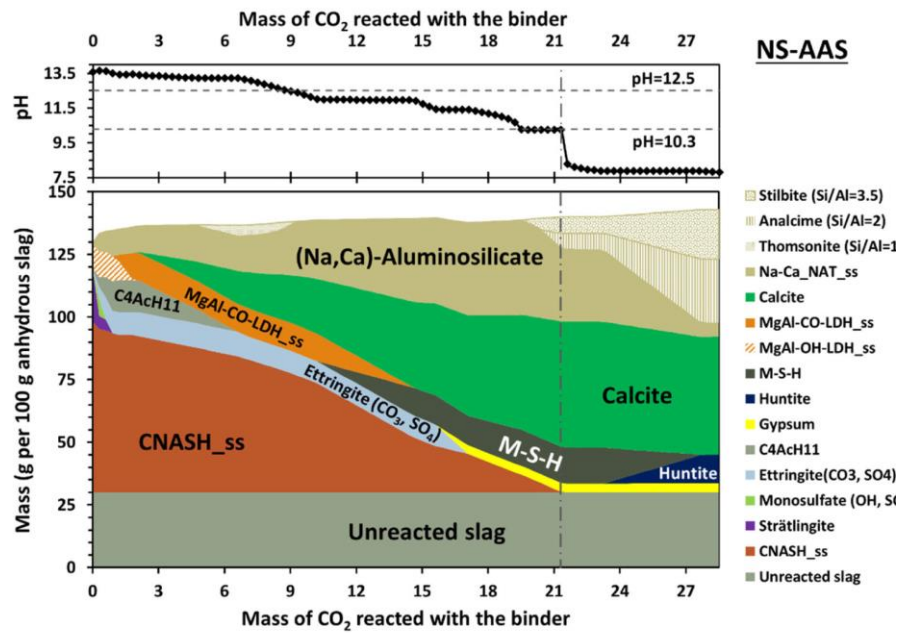
Figure 2.12: Phase assemblage of sodium silicate activated slag paste predicted under step-wise 1% CO_2 carbonation, and the corresponding pH in the aqueous phase (pore solution). The horizontal dashed lines represent pH values of 12.5 and 10.3 respectively, and the vertical dash-dot line indicates the predicted phase assemblage and the pH at the exhaustion of all the C-(N)-A-S-H. Results from the study of Ke et al. [147].

Park *et al.* did a similar thermodynamic modelling study in [150] compared to Ke *et al.* in [147]. Park *et al.* used the same software and database as Ke *et al.* [147,150]. Park *et al.* also included an experimental study of the carbonation of the same systems that are modelled, and the experimental and thermodynamic methods led to similar results [150]. The thermodynamic results from this study are less detailed than the study of Ke *et al.* [147,150]. Both studies present similar thermodynamic results.

For AAMs, Bernal *et al*. modelled the carbonation of alkali activated binder pore solution as a function of the sodium hydroxide concentration as shown in Figure 2.13. The HSC Chemistry 4.1 software package was used with the default database of the software. This software has a Gibbs free energy minimisation routine, similar to GEM-Selektor. The activity coefficients of the species were calculated using the Pitzer model. This model is potentially more accurate than the Debye–Hückel model for solution with an ionic strength greater than 0.1 mol/L (which is the case for the pore solution of AAM) [100].
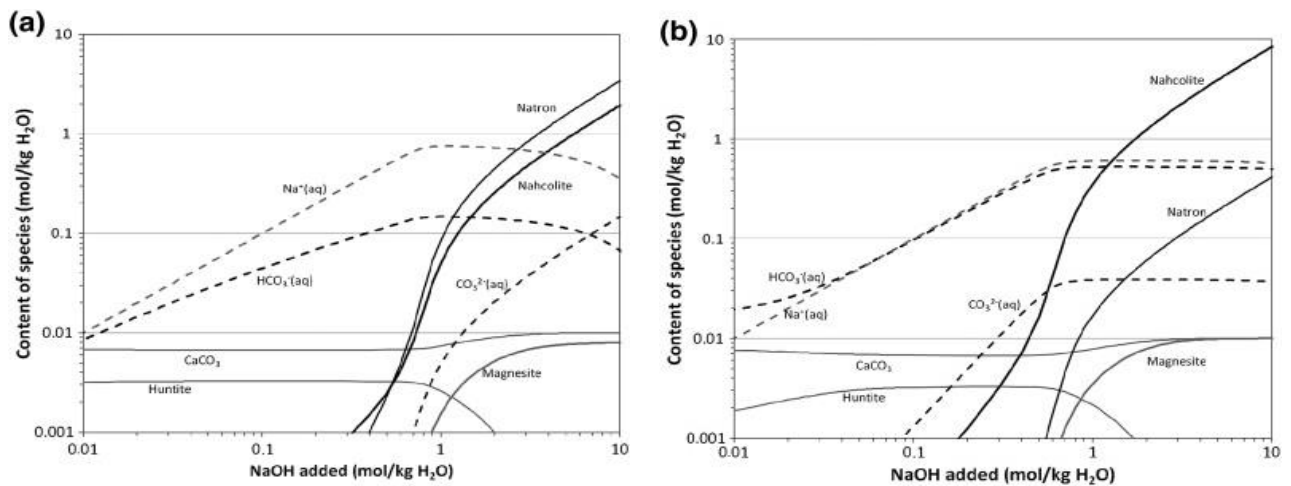
Figure 2.13: Calculated concentrations of key species present in, or precipitated from, simulated alkali-activated slag pore solutions (10 mmol/kg Ca, 10 mmol/kg Mg) as a function of NaOH concentration, under (a) natural (0.04% CO_2) and (b) accelerated carbonation (4% CO_2) conditions. Dashed lines are dissolved species, solid grey lines are alkaline earth carbonates, and solid black lines are alkali metal carbonates. Results from the modelling work done by Bernal et al. [100].

This type of modelling is interesting as it gives an indication of the systems that should form in an ideal situation if the reaction was not time-dependent. These models can be used to help looking for the right phases that would be formed during the experimental carbonation. It can also help the user to optimise a mix design in order to mitigate carbonation. However, it is important to highlight that Gibbs free energy minimization modelling does not take into account the diffusion of the CO_2 in the cementitious matrix. This would require either coupling with a reactive transport code, or empirical (or manual) insertion of transport kinetics into the thermodynamic modelling framework.

2.2.2 Efflorescence

2.2.2.1 Efflorescence definition

Efflorescence refers to the migration of water with salt across the material to the surface, followed by the evaporation of the water, leaving the salt to crystallise at the surface, making a small cover white on top of the materials [39]. In cementitious materials, efflorescence is responsible for the formation of a usually white deposit on the surface of these materials. For PC it is often consider only as an aesthetic problems, as it does not affect the integrity of the materials, even though it is not harmless for AAM [151,152].

2.2.2.2 Efflorescence mechanism

The formation of efflorescence is due to the formation of a layer of water around the cementitious materials. This layer of water can be due to several external factors such as rain, fog or dew. The thin film of water form does not need to be thick to allow efflorescence to occurs, in most cases it is even below a millimetre [151].

The process of efflorescence is described schematically in the Figure 2.14, from the work of Dow and Glasser [151]. In the first and second steps the CO_2 present in the atmosphere dissolve in the water to form bicarbonate ions if the pH of the water is below 10.3, which is the case for rain water [153,154]. In the third and fourth steps, the alkalis, which are potassium and sodium components, get released into the water, as well as the calcium. These species will dissolve in the aqueous solutions in the fifth step. In the last step, calcium precipitates with bi/carbonate ions to form calcium carbonate. For alkali activated materials, the sodium and potassium also precipitate to form sodium carbonates and potassium carbonates [77,151]. The chemical reactions are similar to the carbonation reaction. The main difference between the two processes are the migration and precipitation at the surface of the species, which may or may not affect the integrity of the cementitious material [39]. Consequently, efflorescence is affected by the same parameters as carbonation (porosity, mix design, relative humidity), but also by the cyclic wetting and drying and/or capillary moisture movement, which allows the movement of ions toward the surface [39,77].

SCHEMATIC PROCESS DIAGRAM

PROCESSES

① CO_2(g) dissolving in H_2O
② Conversion of CO_2 to aqueous species
③ Release of alkali
④ Dissolution of calcium
⑤ Diffusion of reactants through solution
⑥ Precipitation of calcium carbonate
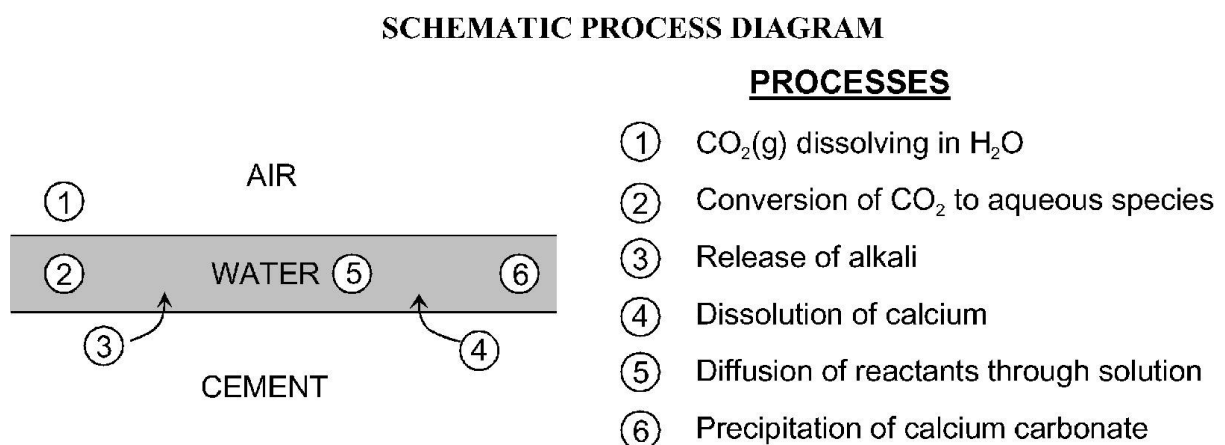
Figure 2.14: Process diagram for the formation of efflorescence according to Dow and Glasser [151].

2.2.2.3 Efflorescence for AAM

The presence of alkali in pore solution of these materials is essential to the initial setting of these materials [5]. This high content of alkali makes the AAMs more likely to be subject to

efflorescence than PC, which could be detrimental for their structures [17,155,156]. Zhang *et al.* highlighted that the addition of slag to a low calcium content AAM mix helps to reduce the efflorescence. It is most probably due to the reduction of porosity linked to the addition of slag [157]. Saludung *et al.* showed that the slag based AAMs are also affected by efflorescence, and that reducing the Na/Si atomic ratio helps against efflorescence [158]. This reduction is linked to the reduction of remaining alkali ions in the pore solution after the activation and curing of the AAM. Consequently, less free alkalis are available in the pore solution to crystallise [77,158]. Alkalis are less leachable if they are incorporated in the gel [77].

Škvára *et al.* showed that in the case of the fly ash based AAM the compressive strength is not affected by leaching [18]. However, many studies show that efflorescence has a detrimental effect on the mechanical properties [17,152,159]. According to Srinivasamurthy *et al.*, the formation of the crystal deposit inside the sample leads to an internal pressure and consequently reduce the splitting tensile strength of AAM [19]. This process is called subflorescence [152].

2.2.3 Soft water attacks

2.2.3.1 Soft water attack

The water coming from the rain can impact the cementitious materials that is in contact with it. This water causes leaching [160]. Rain water has a pH that varies depending on the atmospheric composition and the surrounding industries, it is usually between 5.5 and 6 [154,160]. The UK has put in place a program to significantly reduce "acid" rain, which is caused by the released of sulphur dioxide and nitrogen oxides in the atmosphere by heavy industries and vehicles using fossil fuel [161]. Consequently, in the following section, the focus will be on soft water leaching. The CO_2 in the atmosphere will dissolve in the soft water, to form carbonate ions. The process is then similar to the carbonation process describe above, where the presence of these ions leads to the decalcification of the hydrate products [162]. The calcium ions and hydroxide ions are then leached out from the PC cementitious materials by the flowing water [163,164].

2.2.3.2 Soft water in alkali activated materials

Although AAM have been proven to be more resistant to acidic water attack than PC systems [165,166], few studies have been published on the resistance of soft water attacks of AAM [40]. However, several studies indicate that the leaching of the alkalis present in the pore solutions would be detrimental to the durability of the materials. The leaching of these alkalis would lead to a decrease of the pH and consequently, the de-passivation of the steel rebars [156]. However, Škvára *et al.* shown that in fly ash based AAM, even if almost all of the sodium and potassium are leached out of the materials, the compressive strength is not affected [18]. Conversely, Longhi *et al.* shown that an excessive removal of the alkali could affect the stability of the gel, and thus the flexural and tensile strength of a metakaolin based AAM [159].

2.3 Summary

It is urgent to act to reduce as much as possible the anthropogenic CO_2 emissions to avoid the most extreme consequences of climate change [25]. However, the rise of global temperature due to climate change is inevitable given the direction taken by governments and society in the past years [25,26]. It means that extreme weather will happen, and is already happening [167]. Consequently, the construction industry needs to significantly reduce its carbon footprint, while producing durable infrastructure [4,25,27]. Alternative binders such as AAM are an excellent "tool in the toolbox of solutions" that should be used to tackle these issues [4].

The mechanisms of AAM carbonation have been investigated in several studies in the last decade [84,87,168]. However, the current standards and tests used to predict the carbonation are mostly based on accelerated carbonation, which takes long time to perform, as section 2.2.1.3 explained. Consequently, new tests, faster, easy to perform and reliable must be developed to predict the carbonation for AAM. Chapter 4 will focus on this problem, by using test methods that are currently developed for the PC systems for slag based AAM, to predict the carbonation front.

These materials are also prone to the leaching of calcium and sodium, which could affect their microstructure severely [17,18]. They are also more prone to efflorescence than PC, which

can lead to detrimental effects on their structure [19,77,157,159]. Although several studies have already studied the combined effect of efflorescence and leaching, or efflorescence and carbonation, in the laboratory, no studies have addressed the problem of the combined effects of carbonation and other chemical attacks such as leaching by rain water or in outdoor conditions, on these materials [19,155,169,170]. Consequently, Chapter 5 will reveal the impact of combined reaction on the phase compositions of slag based AAM, under outside exposure to be as close as possible as on-site durability. Chapter 6 will then highlight the impact of these combined attacks on the microstructure of slag based AAM.

Chapter 3 Materials and Methods

3.1 Materials

3.1.1 Ground Granulated blast furnace slag

A ground granulated blast furnace slag supplied by Ecocem (France) was used in this study. The composition of the slag analysed by XRF is described in the table below. The XRF results have been performed on the same slag used in this study, by Stefanini in her PhD study, are presented in Table 3.1 [171].

Table 3.1: Chemical composition of the slag of the main elements, used in this study (mass %), as determined by X-ray fluorescence, according to Stefanini [171].

Components	CaO	SiO_2	Al_2O_3	MgO	SO_3	Fe_2O_3	K_2O	Na_2O
GGBS	43.37	34.41	10.54	7.01	1.35	0.51	0.35	0.16

3.1.2 Activators (Preparation)

First, to prepare the alkali activator, NaOH pellets (Sigma-Aldrich) are dissolved into water along with a commercial sodium silicate solution (PQ Silicates). The composition of the PQ silicate solution is 55.9 wt% H_2O, 14.7wt% Na_2O and 29.4wt% SiO_2, with wt% being the weight percentage. The ratio of activators used is 4 g NaOH/100 g GGBS and 3.86 g Na_2SiO_3/100 g GGBS. To achieve a water/binder ratio of 0.42, the water is added to the activator solution. The mix design was chosen in order to be close to the mix design used S3a used in the Rilem Technical Committee 247-DTA on AAM mix design [40]. The solution is then stirred at room temperature (20± 2⁰C) until the mix is homogenous before being allowed to equilibrate for at least 24 hours.

3.2 Sample preparation

3.2.1 Cement paste preparation

Half of the slag and the activator solution is mixed at the slowest speed (60 rpm) of the mixer. Once the mix is homogenous (usually after 30 seconds), the other half of the slag is added.

The solution of slag and activators is then mixed on the slowest setting for 5 min, followed by the highest speed (280 rpm) setting for 10 min. After being mixed on a Kenwood benchtop mixer, the paste is poured in the appropriate mould to set. This mould is sealed for 24 hours at 100% RH and 20 ± 2°C. After being demoulded, it is stored sealed at 20°C and 100% RH for 7 days or 3 months, depending on the experiment that would be performed on the sample.

3.2.2 Mortars preparation

In order to reduce drying shrinkage, mortars are used for the diffusion test and the carbonation front measurements. Two mortars are studied, one with a sand/binder ratio of 1:1 and the other with a ratio of 3:1. The sand used was EN 196-1 standard sand. For the diffusion test, the mortars are cylinders of 100 mm diameter and 200 mm length. These mortars were cured for 3 months. For the carbonation front measurements, the samples have been cast in a rectangular mould with a length of 100 mm and a side of 50 mm. These mortars were cured for 3 months.

Conversely, as the drying shrinkage is not an issue for the CO_2 binding rate experiment as the material is ground, cement pastes are used. The cement pastes were cured for 3 months before being tested.

3.2.3 Solvent exchange

To perform some tests such as SEM-EDS or MIP, the hydration should be stopped. According to Zhang *et al.* [172], the most effective technique to preserve the microstructure while removing the free water is to exchange it by isopropanol. Consequently, the samples are immersed into isopropanol for one week after being crushed into 10 mm pieces. The isopropanol solution is changed regularly during this week. Thereafter, the samples were dried in an ambient environment and then stored under vacuum at ambient temperature before performing the tests.

3.3 Test methods

3.3.1 Carbonation front: Phenolphthalein test

The carbonation depth measurement is performed via the measurement of the change of pH level in the pore solution on the inner surface of a freshly cut alkali activated material. 1% diluted phenolphthalein in a solvent consisting of 30% water and 70% isopropanol was used

to reveal the pH of the pore solution. The phenolphthalein turns colourless below a pH of 9, however in the case the materials studied, the phenolphthalein almost never turns colourless. So, it is assumed that when the solution turns lighter pink, the sample is carbonated. Indeed, according to Bernal *et al*., under natural carbonation conditions for alkali activated slag materials, the pH is only reduced from 13 to 9.5, which makes the solution only turn lighter pink [100]. The carbonation depth is then calculated manually by taking three measurements on each side of the cube samples according to EN 12390-10 [130].

3.3.2 Thermogravimetry analysis TG-MS

The thermogravimetry analysis (TGA) monitors the sample weight during a progressive heating ramp chosen by the user. The decomposition of the phases occurs at characteristic temperature, depending on their crystal structure, which leads the user to determine the phase assemblage of the sample [173]. To help in this identification, the TGA is usually coupled with mass spectroscopy (MS). Thermogravimetric analysis with mass spectroscopy (TG-MS) helps in quantifying the quantities of calcium carbonate products present, as well as identifying the evolution of the hydration products through the carbonation process [113,173].

In this study, TG-MS is performed using a Perkin Elmer TGA 4000 coupled with a Hiden Analytical mass spectrometer. 40 ± 2 mg of 63 μm powder sample was tested under an inert nitrogen atmosphere from $20^{o}C$ to $800^{o}C$ at a heating ramp of $10^{o}C.min^{-1}$. The nitrogen was used as protective gas at a flow rate of 20 mL/min. The mass spectrometer identified ions assigned as carbon dioxide and water.

3.3.3 X-ray diffraction (XRD)

X-ray diffraction (XRD) helps identifying crystalline phases, and can give information about poorly crystalline phases such as C-(N)-A-S-H gels [113,173]. When X-rays interacts with a crystalline material, it produces XRD pattern that presents peaks of different intensities depending on the diffraction angles. These diffraction angles are dependent on the size of the atoms and the symmetry of their position in the material, according to Bragg's law. With the database available, it is possible to identify the composition of the crystalline phases via the pattern obtained.

In this study, XRD is performed with a Bruker D8 Advance instrument with Cu Kα radiation, in order to analyse the crystalline structure of the phases present in the materials. The step size is 0.026° and the 2θ range is from 5° to 70°. A divergence slit size of 0.5° is added. The samples are crushed into 63 μm powder before stopping the hydration. The data is analysed with the ICCD database. Table 3.2 presents the phases identified in this thesis.

Table 3.2: Phases identified in the XRD patterns in this thesis.

SYMBOLS	COMPOUND NAME	MINERAL NAME	PDF #
H	Magnesium-aluminium carbonate layered double hydroxide	Hydrotalcite	04-015-4253
C	C-A-S-H gel	9 Å tobermorite	04-012-1761
Q	Silica	Quartz	00-046-1045
K	Calcium carbonate	Calcite	01-072-4582
V	Calcium carbonate	Vaterite	00-033-0268
A	Calcium carbonate	Aragonite	01-076-0606
P	Calcium hydroxide	Portlandite	00-044-1481
G	Hydrated sodium-calcium carbonate	Gaylussite	Crystal structure from [174]
T	Sodium sesquicarbonate dihydrate	Trona	Crystal structure from [175]

3.3.4 Scanning electron microscopy

In scanning electron microscopy (SEM), a beam of electrons is bombarded at a sample. Once the beam reaches the material, the electron undergoes a series of collisions in a specific zone in the material, which is called interaction volume as Figure 3.1 shows. Following these collisions, several signals are generated: the back scattered electrons (BSE), the secondary electrons (SE) and the characteristics energy dispersive X-rays (EDS) [176,177].
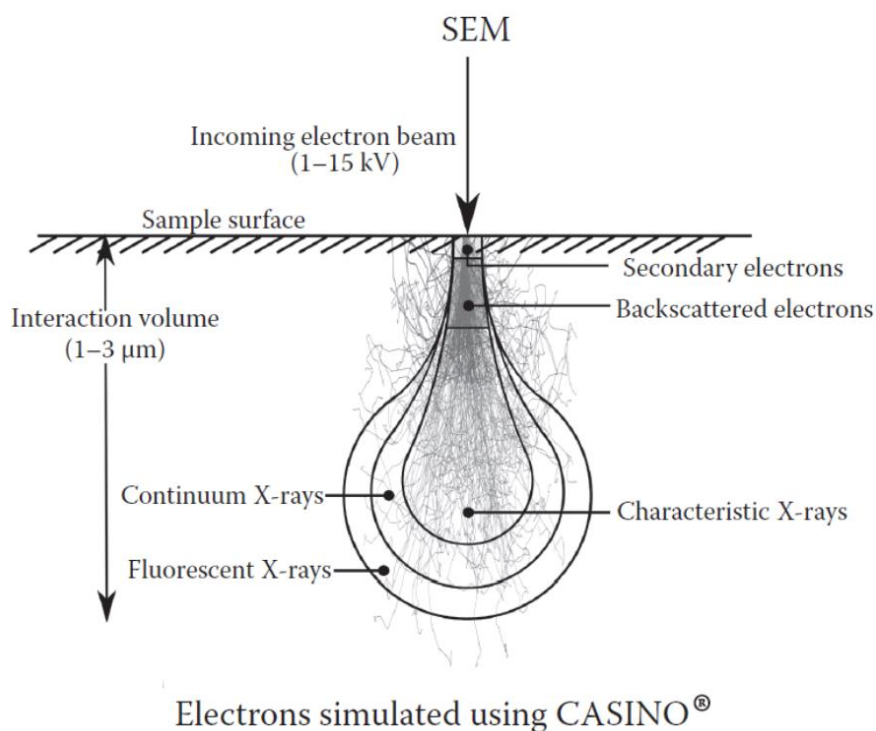
Figure 3.1: Schematic representation of the interaction of electron with matter and the signal generated in a SEM. Adapted from [177].

3.3.4.1 Sample preparation

The sample hydration is stopped with the solvent exchange methods explained in section 3.2.3. The samples are mounted into epoxy and left to harden for 24 hours at ambient temperature. Then, the samples were ground and polished on an Automet polisher, using isopropanol as a solvent to avoid unwanted reaction with the samples. Each sample is carbon coated using an Agar Scientific coater when the sample was tested on the Hitachi ESEM TM3030 and on the Inspect F50, as described below.

3.3.4.2 ESEM TM3030

Environmental scanning electron microscopy and energy dispersive X-ray spectroscopy (SEM-EDS) is performed to obtain elemental maps and scanning electron micrographs in order to observe the structural and chemical element changes. A Hitachi benchtop ESEM TM3030 coupled with a Bruker Quantax 70 X-ray microanalysis detector is used to perform this test. One millimetre of working distance and 15 kV of acceleration voltage is applied.

3.3.4.3 Inspect F 50

Secondary electron imaging (SE), backscattering imaging (BSE) and energy dispersive X-ray spectroscopy (EDS) is performed to obtain elemental maps and scanning electron micrographs using an Inspect F50 FE-SEM instrument. The accelerating voltage used was 10 kV for the SE images and 20 kV for the BSE images and EDS maps. The spot size varies between 3.5 and 4 depending on the dead time for the elemental maps. The working distance is 10.5 ± 0.5 mm.

3.3.5 ^{27}Al and ^{29}Si MAS NMR

Magic angle spinning (MAS) nuclear magnetic resonance (NMR) spectroscopy gives information on the local structure of the phases and especially the poorly crystalline and amorphous phases of the alkali activated slag paste, and therefore can complete the information obtained by the XRD. NMR is investigating the local environment of specific nuclei that have an odd number of protons and/or neutrons, such as ^{27}Al or ^{29}Si. These nuclei are exposed to a strong magnetic field that will polarise them. A pulse of radiofrequency is then applied, which will cause the sample to transition to higher states of energy. As the nuclei relax, they produce an electromagnetic signal, which is processed to a spectrum with a Fourier transformation. The spectrum produced is expressed as a function of chemical shift (δ).

3.3.5.1 Al NMR

Solid state ^{27}Al MAS NMR is used to determine the tetrahedral and octahedral coordinated Al sites presents in the CASH phases and other secondary products. Complementary to this, ^{29}Si MAS NMR is used to determine the different coordinated Si sites in the C-A-S-H gel and the different characteristic parameters of the gel structure, according to the CSTM model developed by Myers *et al.* [178]. The samples studied are crushed into 63 μm powder before stopping the hydration according to the methods described in section 3.2.3.

In this study, solid state MAS NMR is performed on a Bruker Avance III HD 500 (11.7 T) spectrometer, with a 4.0 mm dual resonance CP/MAS probe, operating at Larmor frequencies of 99.35 MHz and 130.32 MHz for Si and Al respectively. For ^{27}Al MAS NMR, the spinning speed is 12.5 kHz with a relaxation delays of 5 s, a pulse duration of 1.70 μs and 512 repetitions. ^{27}Al shift is referenced to an external 1.0 M aqueous solutions of Al(NO$_3$)$_3$.

3.3.5.2 Si NMR

^{29}Si MAS NMR is acquired with a spinning speed of 12.5 kHz with a relaxation delays of 50 s, a pulse duration of 5.50 µs and 256 repetitions. The ^{29}Si shift is referenced to an external sample of tetramethylsilane (TMS).

3.3.6 Mercury intrusion porosimetry (MIP)

To evaluate the size of the pores within a porous material, a nonwetting fluid, mercury, is intruded in the material under an increasing pressure. Mercury being non-favourable to the liquid intrusion, an external pressure is necessary to achieve infiltration. The pressure is called pore pressure (P) and is related to the pore radius according to Washburn equation, presented in the Equation 3.1. In this equation, the contact angle is Ө, the surface tension of the mercury is γ and the pore entry also called meniscus curvature is r [173].

$$P = \frac{2\gamma \cos(\theta)}{r}$$

Equation 3.1

The sample porosity was characterized by MIP on a Micromeritics Autopore V. Each sample has undergone solvent exchange before being tested. Each sample weighed 1.8 ± 0.2 g. The contact angle used during these tests was 130° [179] and a surface tension of 0.485 Nm^{-1} was used in calculations.

3.3.7 Test methods for gas transport and CO_2 binding capacity

3.3.7.1 CO_2 binding rate capacity

The CO_2 binding capacity (CBC) is a key parameter to understand the kinetics of the carbonation reaction of the cementitious phases. The CBC is determined with the help of the method developed by Boumaaza *et al.* [180,181].

Figure 3.2: Pictures of the setup used to determine the instantaneous CO2 binding rate.

To obtain the CBC at a chosen relative humidity, several instantaneous CO_2 binding rate (IBR) measurements at different carbonation states must be determined. Both IBR and CBC are expressed in $g_{CO2} \cdot g_{binder}^{-1} \cdot s^{-1}$. These rates are determined by measuring the amount of CO_2 that can react a with sample that has been previously ground into a 63 µm powder to avoid diffusional effects. The setup to measure the instantaneous rate is presented in Figure 3.2. The samples are stabilised for three days, carbonated for 28 days, and tested during this time at chosen relative humidity. The experiments can be stopped before 28 days if the CO_2 uptake is below the known value of the leakage of the cell. The leakage value for each cell is determined for the minimum volume as it is the most likely to affect the data. To perform the leakage test, the empty cell is filled with nitrogen gas for 24 hours, during this time period the CO_2 concentration is measured to determine the leak value. After measuring at what rate the CO_2 increases in the cell, the leak rate is converted to an effective IBR, which corresponds here to 10^{-9} $g_{CO2} \cdot g_{binder}^{-1} \cdot s^{-1}$.

As Figure 3.2 shows, the sealed set-up is composed of three pieces. The upper one is used to measure the CO_2 as it holds the CO_2 sensor, the middle one is used to hold the powder sample as it is removable, and finally the last one has an adjustable height so the initial volume of the air (and CO_2) can be controlled.
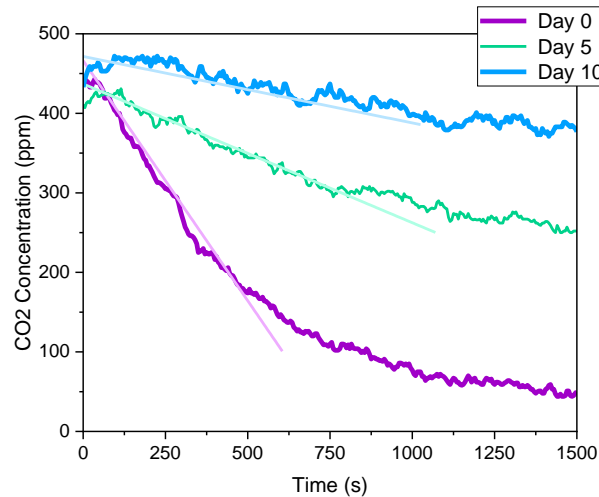
Figure 3.3: Evolution of the CO_2 concentration in the sealed upper chamber of the cell at 60% RH for different time points.

To determine the IBR, Equation 3.2 is used, with S the CO_2 uptake initial slope in ppm.s^{-1}, T the temperature in Kelvin, P the pressure in pascal, R the ideal gas constant (8.314 m^3.Pa.K^{-1}.mol^{-1}), M_{CO2} the molar mass of carbon dioxide in g.mol^{-1}, V the inner volume of the cell in cubic metres, m_0 the mass of the dried sample materials in grams (without CO_2 or H_2O). The initial slope, drawn in pastel colours, is determined as shown in Figure 3.3. This mass is calculated using the thermogravimetric results as the Equation 3.3 shows, knowing that m_{900^oC} (g) corresponds to the mass of the uncarbonated sample heated to 900°C, and $m_{initial}$ (g) is the initial mass of the sample tested in the TG.

$$IBR = \frac{S \times P \times M_{CO2} \times V}{R \times T \times m_0}$$

Equation 3.2

$$m_0 = \frac{m_{900^oC}}{m_{initial}} \, m_0$$

Equation 3.3

The CO_2 binding capacity (CBC) corresponds to the integral of *IBR* over the total test timeframe of the experiment, so it is equal B_{CO2}, presented in the Equation 3.4, at the end of the carbonation experiment. The maximum binding capacity (MBC) corresponds to the sum of all the elements that could react with the CO_2: in AAM it is CaO, MgO, Na_2O and K_2O, and the amount of SO_3 is subtracted from this sum as it is assumed to react with the CaO to form $CaSO_4$. In the following equations, M_x is the molar mass of the element *X*, expressed in g.mol^{-1}. To calculate the degree of carbonation (DoC) from the instantaneous CO_2 binding rate, Equation 3.5 is used:

$$B_{CO2}(t) = \int_{t=0}^{t} IBR\, d$$

Equation 3.4

$$DoC = \frac{CBC}{MBC}$$

Equation 3.5

$$MBC = \%CaO \times \frac{M_{CO2}}{M_{CaO}} + \%MgO \times \frac{M_{CO_2}}{M_{MgO}} + \%K_2O \times \frac{M_{CO_2}}{M_{K_2O}} + \%Na_2O \times \frac{M_{CO_2}}{M_{Na_2O}} - \%SO_3$$
$$\times \frac{M_{CO_2}}{M_{SO_3}}$$

Equation 3.6

3.3.7.2 O_2 binding capacity

To determine the O_2 diffusion coefficient, and from this the CO_2 diffusion coefficient, before and after carbonation, the method developed by Boumaaza et al. [96,97] has been used.

In the cell presented in the schema in the Figure 3.4, the experiment happens in 3 steps:

-   The upper part of the setup is purged with nitrogen;
-   The setup is placed in a climate chamber at a controlled relative humidity;
-   The oxygen passes through the concrete or mortar sample until it reaches the atmospheric concentration.

To obtain the effective diffusion coefficient of the sample, Fick's 2nd law must be solved to describe the measured data. Firstly, the oxygen concentration as a function of time is fitted to the solution of Fick's 2nd law via the least-squares method. Then, from this, the oxygen effective diffusion coefficient can be determined. Fick's 2nd law in the case of one dimensional diffusion for a gas g, in the case where the absorption process is neglected, is presented in Equation 3.7, where $D_{e,g}$ is the gas effective diffusion coefficient and C is the gas concentration in the cell (mol.m^{-3}) [95,97].

$$\frac{\partial C}{\partial t} = \frac{\partial}{\partial x} \left(D_{e,g} \frac{\partial C}{\partial x} \right)$$

Equation 3.7
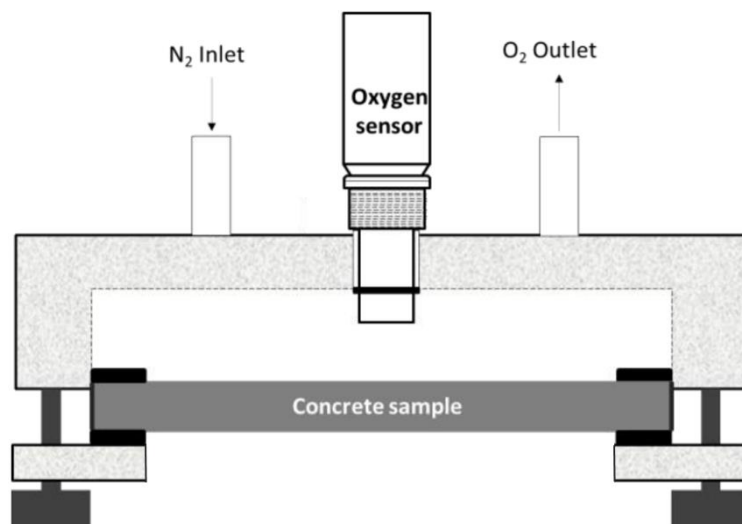
Figure 3.4: Schematic diagram of the setup used to determine the effective oxygen diffusion coefficient, adapted from the PhD thesis of Boumaaza [97].

3.3.8 Synchrotron experiments

The following tests are perfomed in the Diamond light source in Oxfordshire. The diamond is a synchrotron, which is a circular particle accelerator as Figure 3.5 shows. In the Diamond, the electrons, produced in the injection system (1 in the schema), are accelerated in the injection system and then in the booster system (2 in the schema). Once it reaches a precise energy,

the electrons beam is stored and curved in the storage ring (3 in the schema). The light is then extracted from the storage ring and transfer to the beamline (4 in the schema) by the front end (5 in the schema). The beamlines are then divided between the optics hutch, where the beam is filtered and focused (6 in the schema), to be targeted at a sample where several detectors allow a wide variety of analyses in the experimental hutch (7 in the schema). The results are then interpreted by the user that is situated in the control cabin (8 in the schema). Radiofrequency cavity help maintaining a fixed orbit around the storage ring (9 in the schema). The diamond staffs is working on the diamond house, which contains meeting room, offices and conference rooms (10 in the schema)
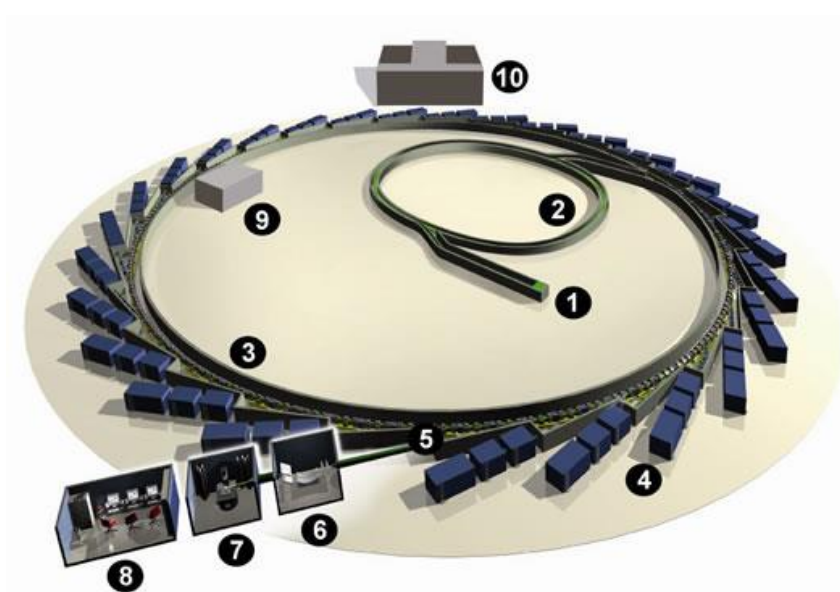
Figure 3.5: Schematic illustration of the Diamond Light Source synchrotron [182]

3.3.8.1 µ-XRF mapping

µ-X-ray fluorescence (µ-XRF) resolves around an X-ray beam, tightly focused, that is targeted at a material which results in the emission of X-ray fluorescence. By moving the beam and evaluating the generated fluorescence signal, it is possible to map the materials [183].

Each sample tested by XRF mapping has been solvent exchange first to avoid supplementary carbonation while waiting to be tested. Between the solvent exchange and the XRF mapping test preparation, the samples were stored under vacuum at ambient temperature. The samples used for the µ-XRF surface mapping and XANES are mounted into epoxy and left to harden for 24 hours at ambient temperature. Then, the samples were carefully ground and polished to ensure a flat sample surface to obtain fluorescence measurements. The µ-XRF

mapping experiments were performed on beamline I18 at the Diamond Synchrotron in Oxfordshire (UK). μ-XRF surface mapping was conducted using a 2600 eV incident beam.

3.3.8.2 Sulphur X-ray absorption near edge spectroscopy (XANES)

When an X-ray is targeted to a material, it results into a scattering and absorption of the ray. By comparing the intensity of the incident beam and the transmitted beam, the absorption coefficient of the material is determined. During the X-ray absorption test, the sample is scanned across a chosen continuous range of energies that are situated below and above the absorption edge. The XAS spectrum obtained is defined in four regions: the pre-edge features, the absorption edge, the X-ray absorption near edge structure (XANES) and the extended X-ray absorption fine structure (EXAFS). The XANES features are sensible to the coordination environments and oxidation state of the absorbing atoms. The absorption energy is specific to a specific atom and specific shell, like sulphur K in the case studied here [184].

A suite of selected sulphur-containing mineral standards are also measured using bulk K-edge XANES for comparison against the collected μ-XANES spectra (e.g. using linear combination fitting techniques), including: gypsum (S^{6+}), anhydrite (S^{6+}), ettringite (S^{6+}), lapis lazuli (S^{6+}, S^{4+}, S^{2-}), elemental sulphur (S^0), pyrite (S^-), zinc sulphide (S^{2-}), iron sulphide (S^{2-}). The sulphur K-edge XANES measurements were performed on beamline I18 at the Diamond Synchrotron in Oxfordshire (UK); both single-point spectra and XANES maps were collected.

Chapter 4 : Impact of the CO$_2$ diffusion coefficient and of the CO$_2$ binding capacity on the carbonation depth of alkali activated slag.

4.1 Introduction

As discussed in section 2.2.1, carbonation of slag based AAMs could result in a deterioration of the mechanical properties and/or in corrosion of steel reinforcement [9–12,14]. To mitigate this reaction and its consequent detrimental effects, a better understanding of the reaction mechanisms is required. As explained in the literature review chapter, the carbonation mechanism is driven by the diffusion of the CO$_2$ and the reaction of the hydrated phases with the CO$_2$ [11,185]. These parameters are impacted by the relative humidity of the environment [10,85,86]. Consequently, in this study, the O$_2$ diffusion coefficient before and after carbonation, the CO$_2$ binding capacity (CBC) and the instantaneous binding rate (IBR), are determined at four different relative humidities (RH). O$_2$ diffusion coefficients are observed to vary by up to two orders of magnitude upon carbonation and depending on RH. These parameters enable the prediction of the depth of carbonation, as well as an improved understanding of their impact on the material durability in terms of the length scale over which theCO$_2$ diffusion and carbonation reaction compete.

4.2 Experimental protocol

The carbonation reaction is driven first by the diffusion of CO$_2$ in the cementitious matrix, followed by its reaction with the cementitious phases [9,11].In order to mitigate this reaction and its consequent, potentially detrimental, effects, a better understanding of the reaction mechanisms and their dependence on the relative humidity is sought in this study.

4.2.1 Sample and shape

Mortars are used for the diffusion test and the carbonation depth measurements. Indeed, if cracks appear where the CO$_2$ can diffuses, the measurement of the rate of diffusion will not be relevant anymore. Two mortars are studied, one with a sand/binder ratio of 1:1 and the

other with a ratio of 3:1. For the diffusion test, the mortars are cylinders of 100 mm diameter with a length of 8.5 ± 0.5 mm, as the diffusion coefficient test cells used are designed to fit samples of this geometry. These mortars were cured for 3 months sealed, to avoid any hydration effects during testing.

For the carbonation depth measurements, mortars are used again to avoid drying shrinkage. Samples have been cast in a rectangular mould, 50×50×100 mm. This shape will allow cutting of the same sample at different time points. These mortars were also cured sealed for 3 months.

Conversely, as the drying shrinkage is not an issue for the CO_2 binding rate experiment as the material is ground, cement pastes are used. The cement pastes were also cured for 3 months sealed before being tested. Before being carbonated, the samples have been ground into a 63 μm powder to have only the carbonation reaction effect, decoupled from diffusion. The powder samples were equilibrated at their corresponding relative humidity (RH) in an atmosphere without CO_2: samples were put into a sealed desiccator with the corresponding salt solution to generate and control the desired relative humidity, and lime to avoid the presence of carbon dioxide. Once the weight of the sample became stable, the powders were tested. Each powder has been tested by TG-MS after being stabilised, and after being tested under the CO_2 binding test where there were aged under natural carbonation. The TG-MS parameters are presented in section 3.3.2 Thermogravimetry analysis TG-MS.

4.2.2 Carbonation conditions

The mortars for the diffusion test were divided into 2 groups, one carbonated at 65 % RH and 1% CO_2 for 3 months, and the other one, non-carbonated stored in an atmosphere without CO_2 and at 60% RH.

The mortars for the carbonation depth measurements were divided in three batches. The first batch was carbonated at 65% RH and 1% CO_2 (accelerated carbonation); the second batch was carbonated at 65% RH and at 400 ppm CO_2 (natural carbonation); the third batch, in an atmosphere without CO_2 and at 60% RH. All the samples were stored at 20°C. To measure the

carbonation depth, it has been assumed that the change between the lighter pink and the dark pink correspond to the carbonation depth as shown in Figure 4.1.
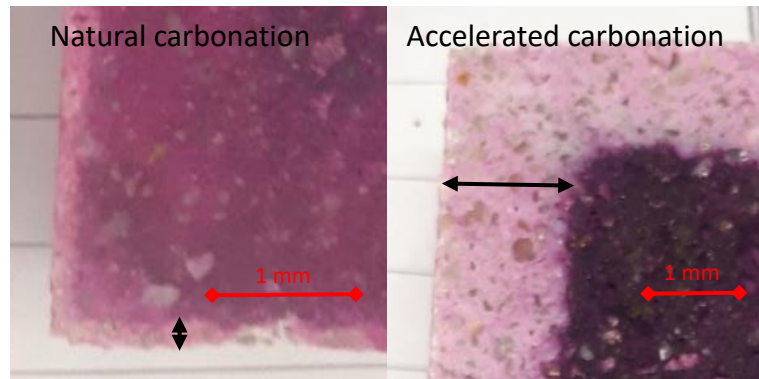
Figure 4.1: carbonation depth measurement for natural and accelerated carbonation.

The samples used for the CO_2 binding test have been carbonated under an atmosphere at 20°C and 400 ppm CO_2. Four RH values have been chosen strategically to gain a broad representation of the impact of the relative humidity: 33%, 60%, 86% and 93%.

4.2.3 Relative humidity

In order to stabilise relative humidity, the samples have been stabilised in containers with a saturated salt solution. The saturated salt solutions for each humidity were the following [186]:

- Magnesium chloride for 33% RH;
- Sodium bromide for 60% RH;
- Potassium chloride 86% RH;
- Potassium nitrate 93% RH.

To carbonate the powder sample at 400 ppm while maintaining the desired RH, the setup presented in Figure 4.2 has been used. The RH, temperature and CO_2 was evaluated during the all experiments to insure that the conditions where stable.
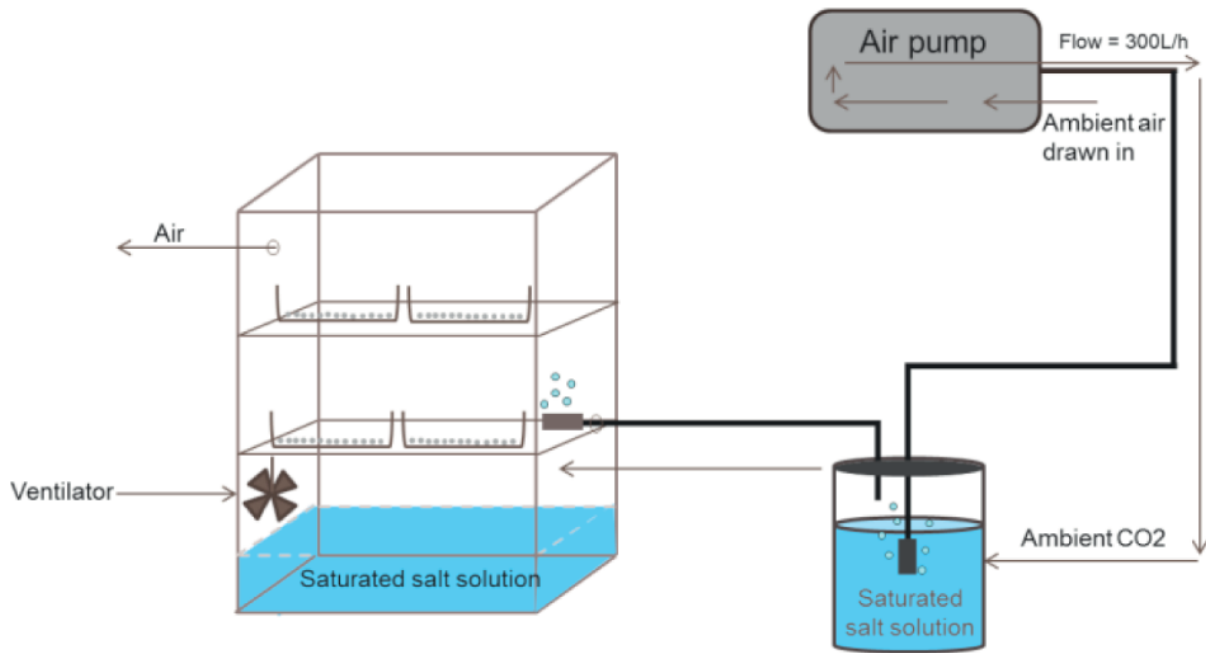
Figure 4.2: Setup used to maintain the RH at 400 ppm; figure reproduced from [181].

4.3 Results

4.3.1 Thermogravimetry analysis

Thermogravimetry analysis coupled with mass spectroscopy has been done on the samples before and after the CO_2 binding capacity experiment, for each relative humidity, as shown in Figure 4.3. The mass spectroscopy is performed for CO_2 (mass/charge = 44) and H_2O (mass/charge = 18). It is important to note that the free water has not been removed from the samples with any solvent exchange methods. The samples have been stabilised in an atmosphere without CO_2 at the chosen relative humidity before the CO_2 binding capacity experiment. Before performing this experiment and after stabilising the samples, a small portion of each sample has been saved to perform the TG-MS experiment on it. The TG-MS experiment helps to measure the carbonation before the experiment and make sure that the sample has not carbonated during the curing and stabilisation periods.
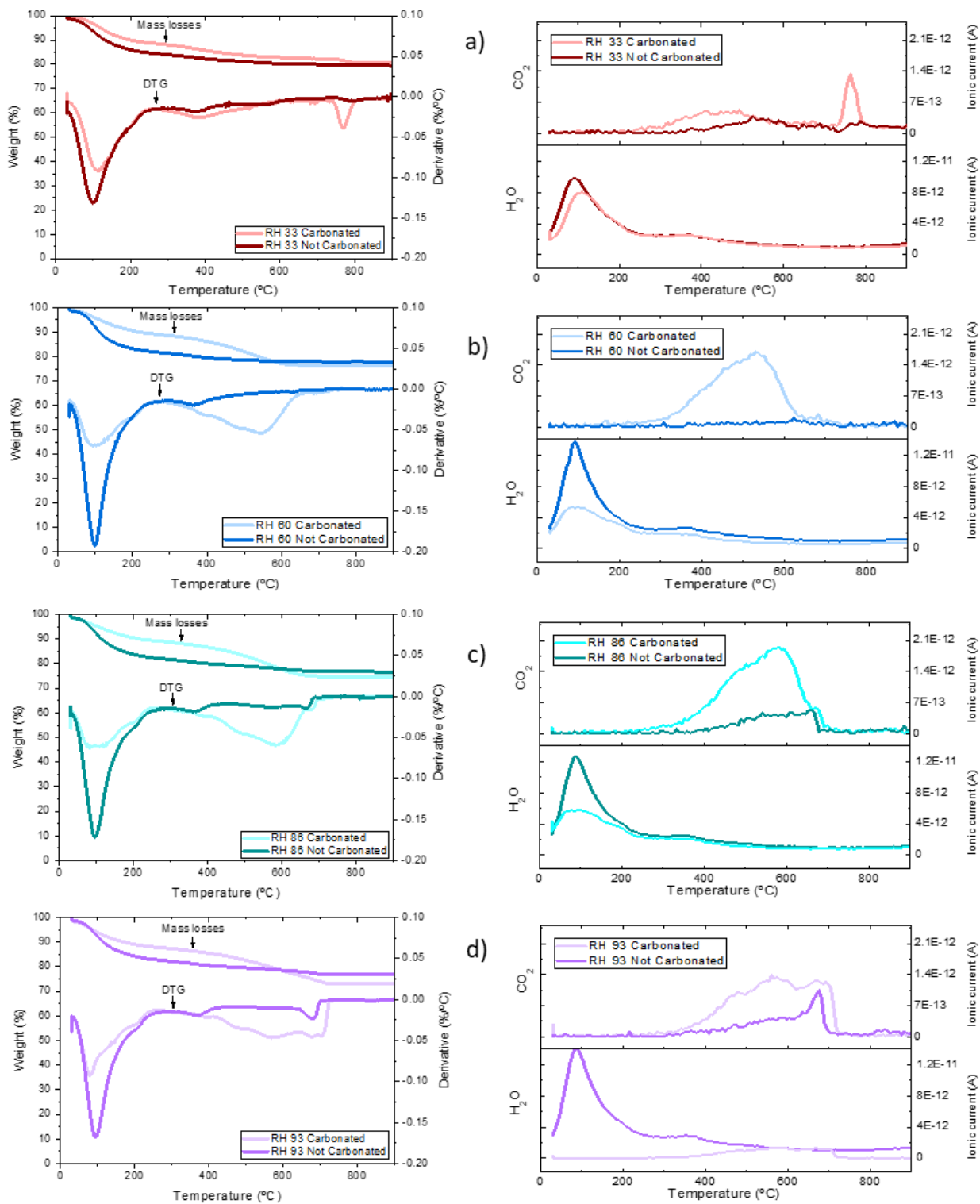
Figure 4.3: Thermogravimetry curves (left) and mass spectra (right) of CO_2 (m/z=44) and H_2O (m/z = 18) for the sample exposed before and after carbonation at a relative humidity of 33% (a), of 60% (b), of 86% (c) and of 93% (d).

All the samples in Figure 4.3 show the same mass loss before and after carbonation, with some slight variation that will be discussed in the following paragraphs.

The main peak from $45^{\circ}C$ to $200^{\circ}C$ is attributed mainly to the evaporation of water. The two main causes of this peak are:

- The loss of free water between $20^{\circ}C$ to $105^{\circ}C$, as the hydration has not been stopped in these samples [187].
- The loss of bound water within the C-A-S-H gel phases between $50^{\circ}C$ to $215^{\circ}C$ [188,189].

Hydrotalcite presents two main losses of water, one around $270^{\circ}C$, which corresponds to some water from the interlayer structure of this LDH phase, and another one around $400^{\circ}C$, which corresponds to the molecules of water being released from the main layer [173]. Additionally, a peak around $373^{\circ}C$ and $400^{\circ}C$ can be attributed to the release of CO_2 from the hydrotalcite that has been carbonated during the experiment [190].

The mass loss between $400^{\circ}C$ and $800^{\circ}C$ is attributed to the loss of CO_2 within the calcium carbonates phases. The mass loss from $400^{\circ}C$ to $500^{\circ}C$ could be attributed to the amorphous calcium carbonates. The mass loss from $500^{\circ}C$ to $700^{\circ}C$ is mainly attributed to the CO_2 emissions from crystalline $CaCO_3$ such as the less thermally stable calcium carbonate polymorphs vaterite or aragonite. The mass loss from $700^{\circ}C$ to $800^{\circ}C$ is mainly attributed to the CO_2 emissions from highly crystalline carbonates or the most thermally stable calcium carbonate polymorph such as calcite [93,101,102,191,192].

The free water loss is higher for humidities above 60% than at 30% RH. Less free water remains within the sample at a lower relative humidity once it is stabilised with its environment.

The peak that is attributed to the C-A-S-H gel is lower for all the samples once it is carbonated. However, it can be noted that the reduction of these peaks is significantly lower for 60% and 80% RH compared to 33% RH. For 93% RH, the peak is lower as well, but due to the free water peak, it is harder to evaluate the reduction of the C-A-S-H gel peak. The mass spectroscopy data show that the peak corresponding to the water loss from hydrotalcite around $400^{\circ}C$ is unchanged by the carbonation. This shows that the structure of hydrotalcite has not been affected by the carbonation. It is important to note that the water mass spectroscopy for the

76

carbonated sample at 93% RH shows no peaks, even for below 100°C when it is supposed to show the loss of free water. It can be concluded that a technical error happened during this measurement, as it is not representative of the known behaviour of the sample.

The carbon dioxide peaks due to the CO_2 present in the hydrotalcite around 370°C are slightly visible for the samples exposed to 30% and 60% RH. However, these peaks do not seem to appear for 86% and 93% RH. This peak overlaps within the peak attributed to the carbon dioxide loss from the least thermally stable calcium carbonate. This peak between 400°C and 600°C is higher for the 60% and 86% RH samples compared to the other relative humidities after carbonation. For the lower relative humidity, even if a peak can be observed after carbonation, it is quite low. However, at 33% a peak, which could be attributed to the calcite formation after carbonation, is observed. For the 93% RH sample, a peak before carbonation at 700°C is observed; this mass loss could be attributed to a small amount of stable forms of carbonates, formed during the sample preparation, where the sample have been slightly carbonated despite sealing the sample as much as possible. It appears that this peak is blended in a peak starting at 600°C and finishing around 750°C, which could be attributed to more thermally stable calcium carbonate. A similar small peak at 700°C before carbonation is also observed in the sample at 86% RH. This type of mass loss around 700°C could be due to the carbonation of the sample during the sample preparation.

The amount of bound CO_2 B_{CO_2} (g$_{CO2}$.g^{-1}$_{binder}$) for the initial and final stage can be calculated from the thermogravimetric data, with m$_{CO2}$ (g) and m$_{900°C}$ (g) respectively the mass of CO_2 present in the sample and the mass of the sample at 900°C, which corresponds to the mass of the sample with the water and CO_2 bound. The mass of CO_2 is calculated in this study as the mass loss between 370°C and 800°C. Some residual water loss can still be observed until 400°C, and the mass loss of the CO_2 for the hydrotalcite starts at 350°C, so both peak overlap. Consequently, to isolate the overlapping peaks, the temperature of 370°C was chosen. The amount of CO_2 bound, B$_{CO2}$, is then defined as:

$$B_{CO_2} = \frac{m_{CO_2}}{m_{900°C}}$$

Equation 4.1

The amount of CO_2 bound during the carbonation, CBC, corresponds to the B$_{CO2}$ before carbonation subtracted from the B$_{CO2}$ after carbonation. Equation 3.5 shows how to obtain

the degree of carbonation, DoC. Table 4.1 shows the DoC for each relative humidity, calculated from the thermogravimetry mass loss.

Table 4.1 CBC and DoC calculated from the thermogravimetry analysis:

Relative humidity	33%	60%	86%	93%
CBC ($g_{CO2} \cdot g^{-1}_{binder}$)	0.0253	0.0882	0.0895	0.0894
DoC (%)	8.8	30.5	30.9	30.9

The degree of carbonation is significantly lower for the lowest relative humidity; the CO_2 dissolves less in the pore solution as there is less pore solution available [86]. At the three other RH values, the degree of carbonation is around 30%, with less than 0.5% difference between each DoC. This low difference shows that the extent of carbonation achieve above 60% RH is the same under all these relative humidities. As the test has been performed on powder sample, the diffusion of the CO_2 in the capillary pores is not a main parameter. Consequently, it can be observed that contrary to the carbonation in bulk samples, the most carbonated sample is not the one around 60% RH, but all samples with a relative humidity above 60% reach the same degree of carbonation.

Moreover, Galan *et al.* suggested that PC based materials were almost not carbonated at 33%, as the amount of portlandite stayed the same. However, in this study, the TG-MS and CO_2 binding experiments both show that the AAS is carbonated at 33%, and the TG-MS results show that the amount of the main hydration phases, C-A-S-H gel, is affected by the carbonation even at low RH [15].

4.3.2 CO_2 binding experiments

The instantaneous binding rates (IBR), as a function of time, measured using the cell apparatus described in section 3.3.2 are presented below. All the IBRs at t = 0 are around 10^{-6} $g_{CO2} \cdot g_{cement}^{-1} \cdot s^{-1}$, and the highest starting IBR corresponds to 93% RH. All the IBR data in Figure 4.4 are noisy due to the calculation procedure used to obtain the initial rate. Indeed, numerical differentiation is inherently prone to scatter. However, the trend obtained via this method is consistent and clear. The IBR for 33% RH decreases rapidly, by almost two orders

of magnitude in the first day. At 60% RH the IBR decreases more than at higher RH at first, but the IBR seems more stable after 3 days and reaches an IBR that is similar to the higher RH. The IBR for 86% and 93% RH are similar and seem to follow each other, except at the beginning, where the IBR is higher for 93% RH than 86% RH. These results show that the carbonation of the hydrated phases needs sufficient water to proceed, as the free water, which increases with RH, present in the sample enable the CO_2 to dissolve and then react with the main phases. Consequently, at low RH, only a small part of the carbonatable mass is carbonated [15,86].
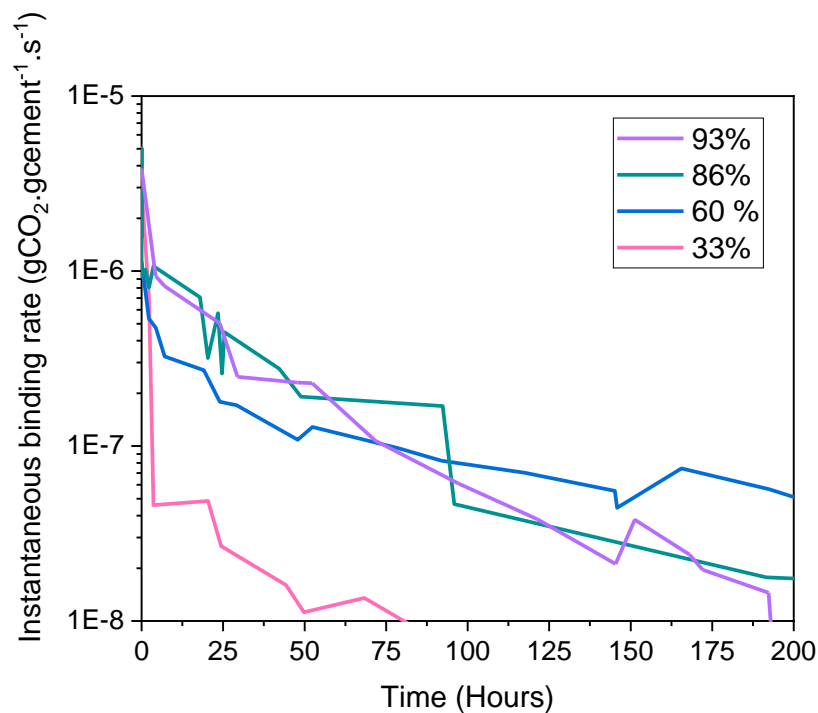
Figure 4.4: Evolution of the IBR as a function of time at the four relative humidities tested.

The instantaneous binding rates can also be presented with respect to the degree of carbonation, as presented in Figure 4.5. The IBR at 33% is quite high at the beginning but drops drastically after 5% of the carbonatable mass is carbonated. At 60% RH the IBR decreases almost linearly with the DoC until it reaches 25%, and then drops at 30%. The IBR trends at 86% and 93% are similar after 15% DoC even though the IBR is higher for 93% at low DoC than for 86%. To summarise, these results show once again that if the diffusion parameters are removed from consideration, one of the controlling factor for carbonation of these materials is the relative humidity. Consequently, for low relative humidity, increasing the relative humidity from 30% to 60%, and by then the free water available, seems leads to

a faster carbonation of the hydrated phases. According to the previous results, at higher relative humidity, the amount of products carbonated is not dependant on the relative humidity. Boumaaza showed in her PhD thesis, that for Portland cement pastes, even containing slag as a supplementary cementitious material, the maximum degree of carbonation is obtained at 55% and not 93% RH [97], which is not the case for the alkali activated slag paste in this study. In reference [97], the DoC for the sample containing 50% slag in a blend with PC reached 15% at 33% RH, and 46% at 93% RH. In this study, the DoC is lower at 33% RH, but higher from 60% RH. The slag based AAM seems more sensitive to the RH than PC blend with slag.

According to Figure 4.5, the DoC reaches a maximum depending on the each relative humidities. Close to this DoC, the IBR decreases drastically. For example, at 30% RH, when the DoC reaches 8%, the IBR drops drastically. According to these results, a DoC limit seems to exist for each relative humidity. A proposed hypothesis is that the rate of reaction, called IBR in this case, is controlled by the distance from the equilibrium state. Once the equilibrium is close or reached, the rate becomes low. However, no definitive conclusions can be drawn on this short time period and with this equipment.
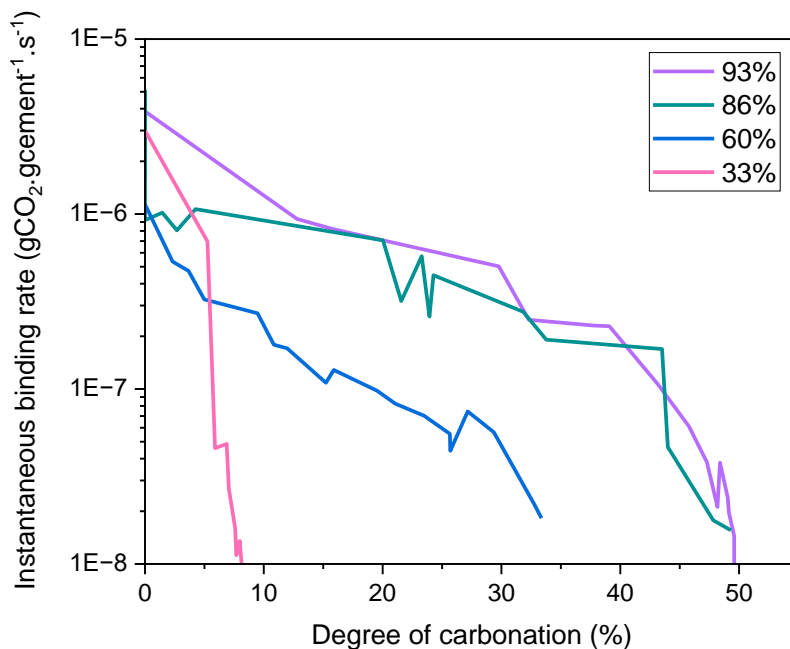
Figure 4.5: Evolution of the IBR as a function of the degree of carbonation, at the four relative humidities tested.

Table 4.2: CBC and DoC calculated from the CO_2 binding capacity methods.

Relative Humidity	33%	60%	86%	93%
CBC ($g_{CO2} \cdot g^{-1}_{binder}$)	0.02410	0.09516	0.14255	0.14474
DoC (%)	8.3	32.9	49.3	50.1

The DoC at 33% RH is only 8%, which is low, but expected as the free water in the sample is low [86]. The DoC at 60% suggested that 30% of the sample is carbonated, which is less that the DoC at 86% and 93% which reach almost 50%.

None of the samples reached, or even approached, a degree of carbonation of 100%. This could be due to several factors, the first one is that the calcium carbonate will precipitate around the hydration products and block their carbonation [97]. In section 6.3.3 of Chapter 6, the SEM analysis shows that, in the case of the carbonation alone, the outer C-A-S-H is carbonated first, and then calcium carbonate forms around the inner C-A-S-H. Consequently, the calcium in the inner C-A-S-H is not carbonated. The second one is that not all the slag has been hydrated, consequently, the CaO and MgO available in the unreacted slag does not carbonate. In section 5.3.3.2 of Chapter 5, the NMR deconvolution results show that, in average, 45% of the silicon sites are unreacted in the carbonated parts of the sample, so 45% of the slag is not hydrated on average. Nguyen *et al.* suggested that the slag will keep reacting over time, and that the newly formed C-A-S-H gel will keep carbonating over time [107]. This study does not allow to either confirm or deny this theory, as it will necessitate a study over several years to challenge this. Finally, it is also possible that once the equilibrium is reached, depending on the relative humidity, the thermodynamic driving force might not be strong enough to carbonate the calcium in the C-A-S-H.

4.3.3 Porosity

Table 4.3 shows that the carbonation process is affecting the porosity of the material. The porosity, evaluated by MIP, is decreasing with the binder content. This result was expected,

as the binder is a porous materials to the contrary of the sand, so the total porosity decreases when the content of binder decreases [193]. In these results, the porosity also decreases once the carbonation occurs. In PC based materials, including blends with GGBS, the precipitation of calcium carbonate phases under accelerated carbonation leads to a decrease of the porosity [98,194,195]. However, several studies observed that the porosity of sodium hydroxide activated slag based AAM decreases with carbonation, while the porosity of sodium silicate activated slag based AAM increases with carbonation [112,196]. In this PhD work, the sodium silicate dose is lower than the sodium hydroxide dose, which could explain the decrease of porosity after carbonation.

Table 4.3: Total porosity (%) before and after carbonation for the mortars depending on their sand/binder ratio, based on mercury intrusion porosimetry tests.

Sand/binder ratio	Not Carbonated	Carbonated
1:1	21.7 ± 1.5 %	11.0 ± 1.5 %
3:1	13.6 ± 1.5 %	7.9 ± 1.5 %

Figure 4.6 and Figure 4.7 show respectively the pore size distributions of the samples with binder to sand ratios of 1:1 and 3:1, before and after carbonation. The pore size distribution of the samples are presented depending on the cumulative volume in percentages of the gel pores (< 10 nm), small pores (10-50 nm), medium capillary pores (50-500 nm) and large capillary pores (> 500 nm), using the classification according to Mindess and Young [197].

For both mixes, the carbonation decreases the content of the gel pores. This decrease is caused by the carbonation of the main hydrate phases, particularly the C-A-S-H gel in these alkali-activated slag binders [198]. It should be noted that the smallest gel pores might not be observed as the mercury cannot enter the fine pores [199]. So to quantify the change in the smaller gel pores, the sample should be analysed by nitrogen absorption [173], which was not

done in this study due to instrument failure and for reasons related to instrument availability under Covid19 disruption.

In both samples, the amount of small capillary pores only decreases by 1% with carbonation, which is not significant enough to draw conclusions out of this result, as the uncertainty linked to these measures is higher than 1%. Indeed, duplicate measurements on these samples showed a difference of 1.5% in total porosity and 1.2% in the average pore diameter in the pore size distribution, which is higher than 1%. The amount of large capillary pores increases by almost a factor of two after carbonation. Some studies suggest that the decalcification of the C-A-S-H gel might lead to the shrinkage of the materials [200]. According to Ye and Radlińska [66], the carbonation of alkali activated slag leads to volumetric expansion that can result in micro-cracking within the materials, which would lead to a higher level of large capillary pores.

To conclude, the overall porosity decreases in these mortar samples after carbonation. However, a redistribution of the pore structure can be observed after carbonation, with a decrease of the gel pores and small capillary pores combined with an increase of the large capillary pores. This result is concerning as the pores above 50 nm are harmful to the materials and can promote the diffusion of CO_2 [98,201,202].
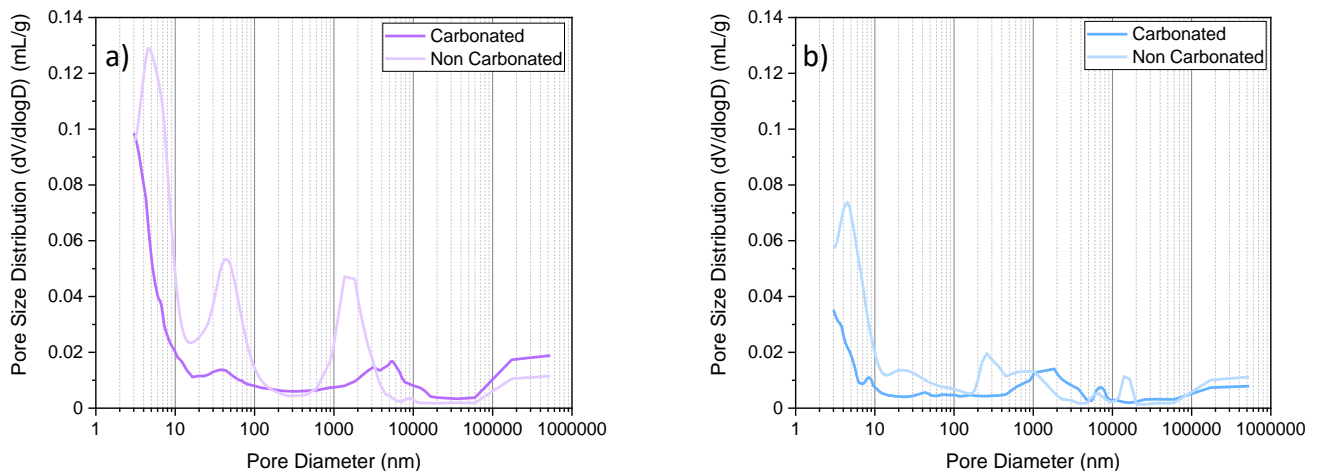
Figure 4.6: Pore size distributions of the mortars with a sand/binder ratio of 1:1 (a) and 3:1 (b).
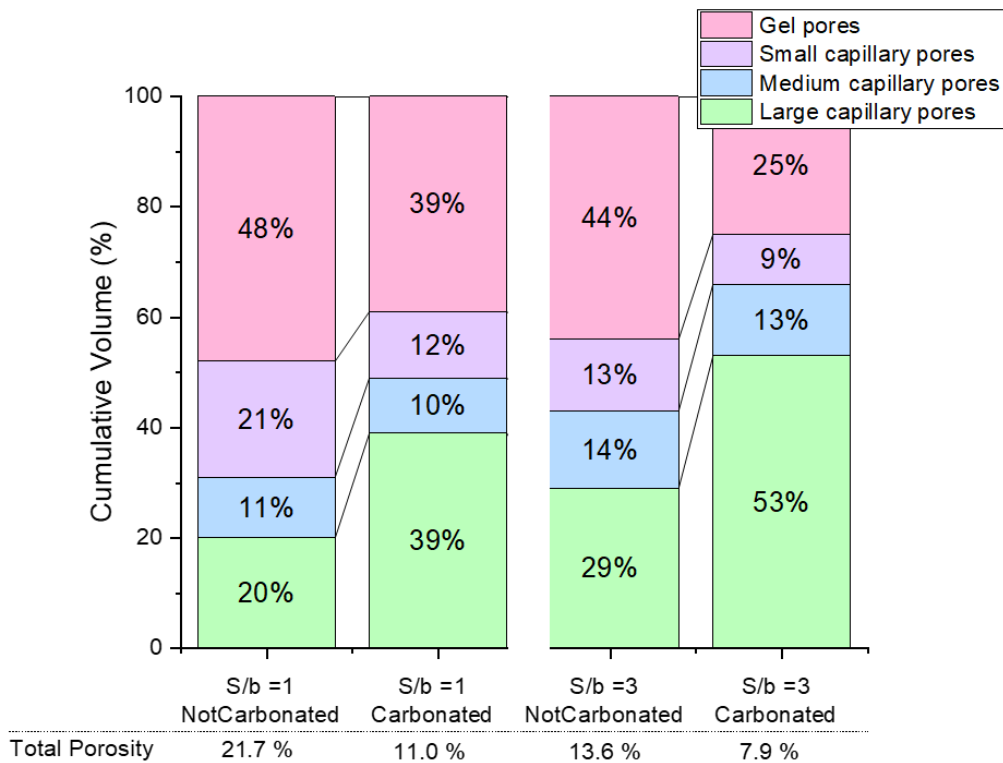
Figure 4.7: Pore distributions (%) depending on the samples, and total porosity (%) of each samples.

4.3.4 Effective diffusion coefficients

The O_2 diffusion coefficient is determined via the methods described in section 3.3.7.2 of Chapter 3. The O_2 diffusion coefficients determined at each RH are presented below. For each point, three replicates samples of the same batch have been measured in order to ensure the reproducibility of the method and results. The uncertainty bars on Figure 4.8 correspond to the standard deviation between the three samples, and the data presented correspond to the average of the three data points.
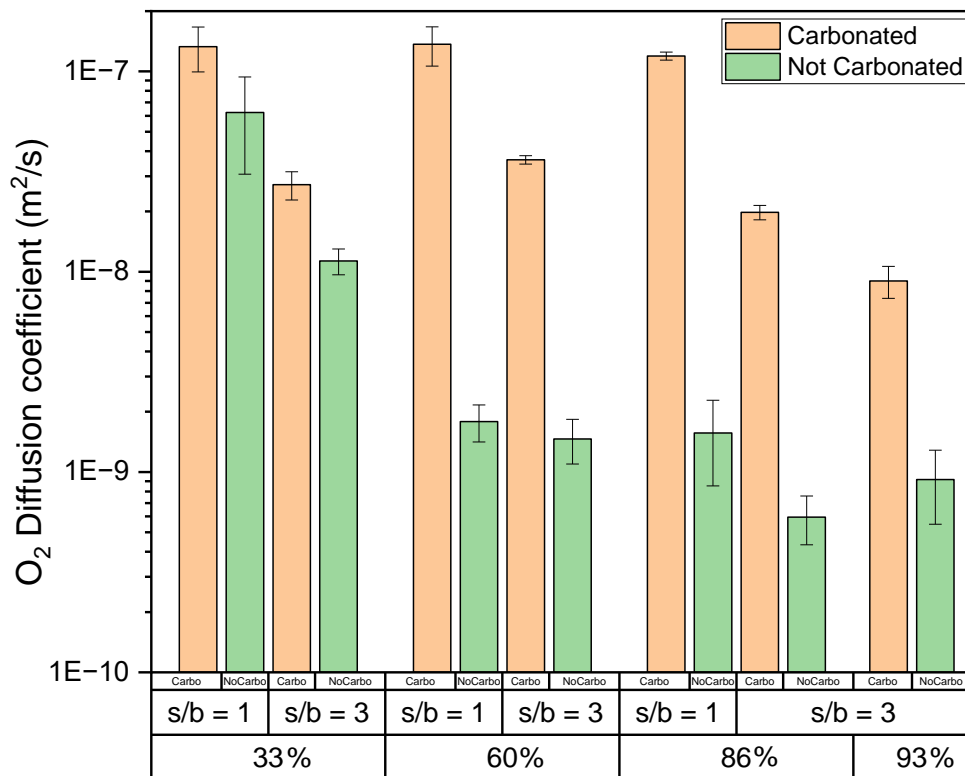
Figure 4.8: O_2 effective diffusion coefficients of the sample depending on the RH, for carbonated and non-carbonated samples.

The sample with a higher sand to binder ratio presents a lower diffusion coefficient. These results are linked to the discussion in the previous section on the porosity of the materials; the porosity is lower when the sand content is higher. Consequently, the diffusion coefficient is also lower [193,203].

The diffusion coefficient of the non-carbonated samples above 60% RH are all around 10^{-9} m^2s^{-1}, which is lower than all the published results for PC systems tested with the same method [98]. The O_2 diffusion coefficients vary up to two orders of magnitude upon carbonation. These results are quite surprising, as this coefficient has previously been observed to vary from only half to one order of magnitude upon carbonation for the Portland based cementitious materials with the same test method [97]. The $D_{e,O2}$ values of the carbonated samples are the same order of magnitude than the PC samples at the same RH [97]. It could be noted that the samples tested in the study of Boumaaza are concretes and

not mortars, however this should not impact the diffusivity coefficient according to Wong *et al.* [203].

For the relative humidity above 60% RH, a higher relative humidity leads to a lower diffusion coefficient, for the carbonated sample. The free water in the pore is blocking the diffusion of the gas at these relative humidities [204]. Conversely, the diffusion coefficient at 33% RH is similar to the one at 60% RH. It is unexpected as the diffusion coefficient should be higher as there is less free water in the capillary pores, and thus more available volume of pores for transport in the gas phase. The samples were already well stabilised at this relative humidity as the weight has been measured consistently until the stabilisation. Wong *et al.* showed that the transport properties of blast furnace slag grouts decrease with the relative humidity only for RH values higher than 55% [204]. In Wong's study, it is argued that below 55% RH, the capillary pores where the gas diffuses are emptied [204,205]. According to Ye *et al.,* when the relative humidity is lower than 50% only the interlayer and small gel pores are saturated and at 70% RH, only the pores below 5 nm are saturated for alkali activated slag based materials [65].

The coefficients at 33% RH for carbonated and non-carbonated samples are similar. This result is odd as it is not the case for the other RH values. The 33% RH were the last samples tested, and so due to technical reasons and limitations of instrument availability, these samples have been equilibrated at 33% during almost five months. Consequently, the sample non-carbonated at 33% was oxidised, which was not the case of the same sample at higher relative humidities. The sample at 60%, 86% and 93% RH were still partially blue/green, which was not the case of the non-carbonated sample at 33% RH. According to Chapter 6, the sulphur oxidation is responsible for the change of colours of the sample. Indeed, the sulphur species are initially sulphide and become sulphate once completely oxidised. Consequently, for a sample with a sand:binder ratio of 1, with a weight of 130 g and a degree of hydration of 55%, given that the sulphur represents 0.4% of the total elemental composition according to the XRF presented in section 3.1.1, 639 cm^3 of air would be necessary to oxidise the sulphides if all the sulphur species in the binder are sulphides. The upper volume of the cell is less than 900 cm^3, so it is possible that the oxidation of the sulphur species affected the measurements of the oxygen effective diffusion coefficient for the non-carbonated samples at 60%, 86% and 93%.

The CO_2 diffusion coefficient D_{e,CO_2} can be calculated from the O_2 diffusion coefficient D_{e,O_2} according to Equation 4.2, assuming Graham law of the diffusion of gases for these materials [97,99]. M_{CO2} and M_{O2} are respectively the carbon dioxide and oxygen molar masses.

$$D_{e,CO_2} = \sqrt{(M_{O2}/M_{CO2})} \times D_{e,O_2}$$

Equation 4.2
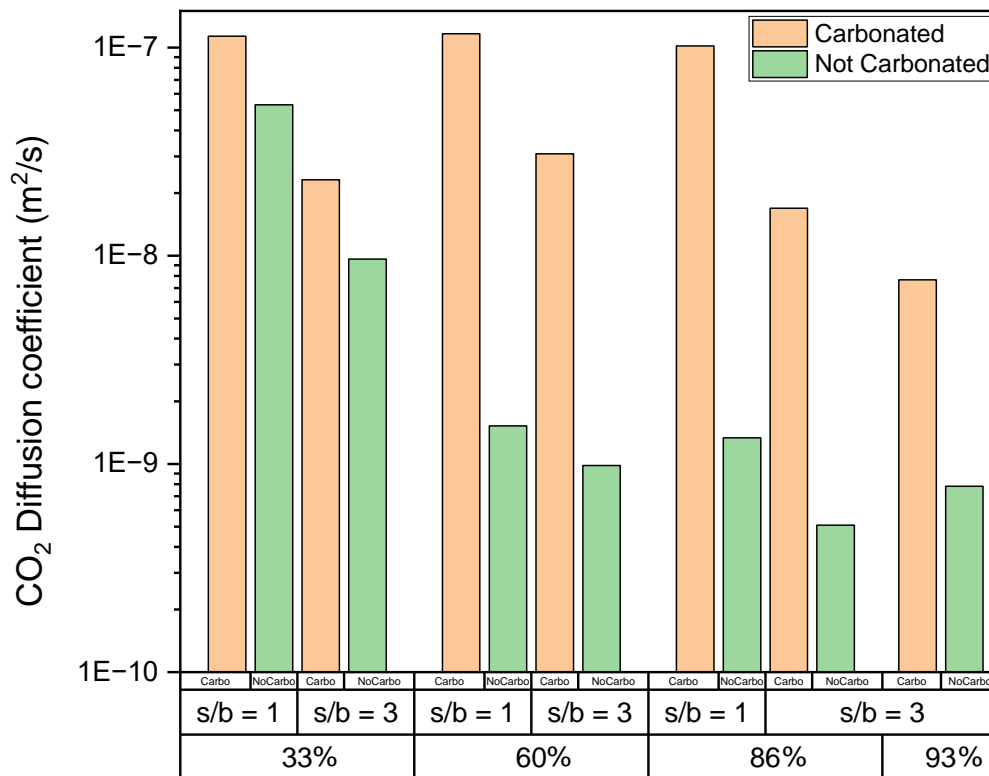
Figure 4.9: Diffusion coefficients before and after carbonation at several RH values, for mortars at different sand/binder ratios.

The D_{e,CO_2} presented in Figure 4.9, shows the same properties and trends between samples as the D_{e,O_2} as it is calculated from the oxygen diffusion coefficient via a multiplication factors, so the same conclusions as above can be drawn. Testing the materials with oxygen and not carbon dioxide enabled to obtain the diffusion coefficient before and after the carbonation without changing the microstructure of the samples, by carbonating the materials during the test.

4.3.5 Carbonation depth

Figure 4.10 presents the evolution of carbonation depth under accelerated carbonation at 1% CO_2, with a RH of 65% and a temperature of 20°C. The carbonation depths have been determined with the phenolphthalein method, so in this case, the carbonation depth is represented by the change of pH front. The carbonation depth increases faster when the sand to binder ratio is lower. This is due to the higher porosity and also to the diffusion coefficient, as shown in the previous sections, within the sample with a sand to binder ratio of 1.
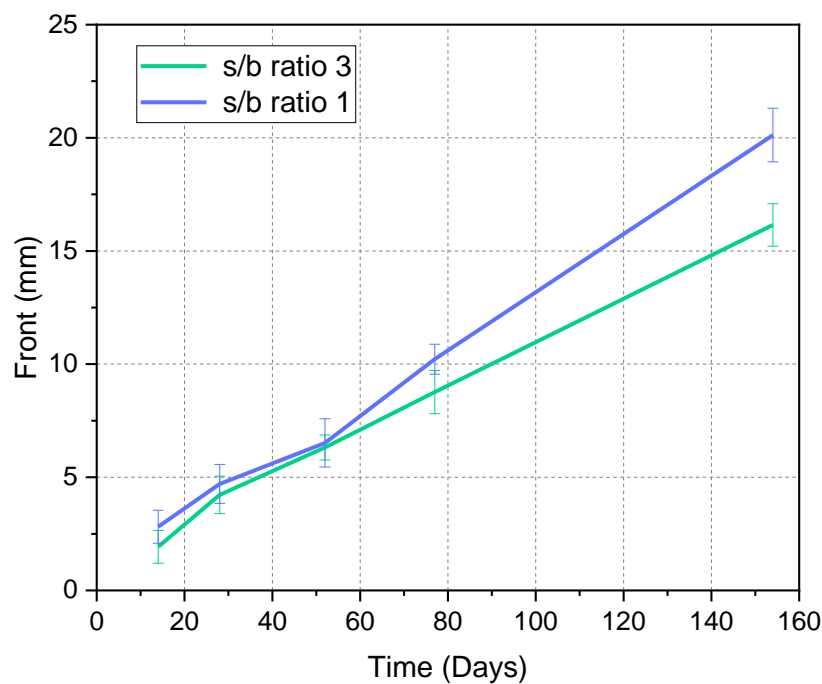
Figure 4.10: Accelerated carbonation depth of the mortars with sand to binder ratios of 1 and 3, at 65% RH and 1% CO_2.

Figure 4.11 presents the evolution of carbonation depth under natural carbonation at 60% RH and 23°C ± 3°C. It is important to highlight that no carbonation was measured before 77 days, as the carbonation depths were too low to be measured, as shown in Figure 4.12. In this picture there is an evident change between a very dark pink to a lighter pink; this change of colour is due to the oxidation front rather than carbonation as explained in Chapter 6, as the sample is dark blue when the sulphur is not oxidised, as can be observed in Figure 4.12 (a).

When the phenolphthalein is sprayed onto the surface of the mortar, where the oxidised material is white in colour, due to the high pH it turns dark pink, whereas the part that is not yet oxidised is already dark blue, and so it leads to a darker shade of pink. In comparison, the shade of pink due to the carbonation is significantly lighter, as it can be observed in Figure 4.12.
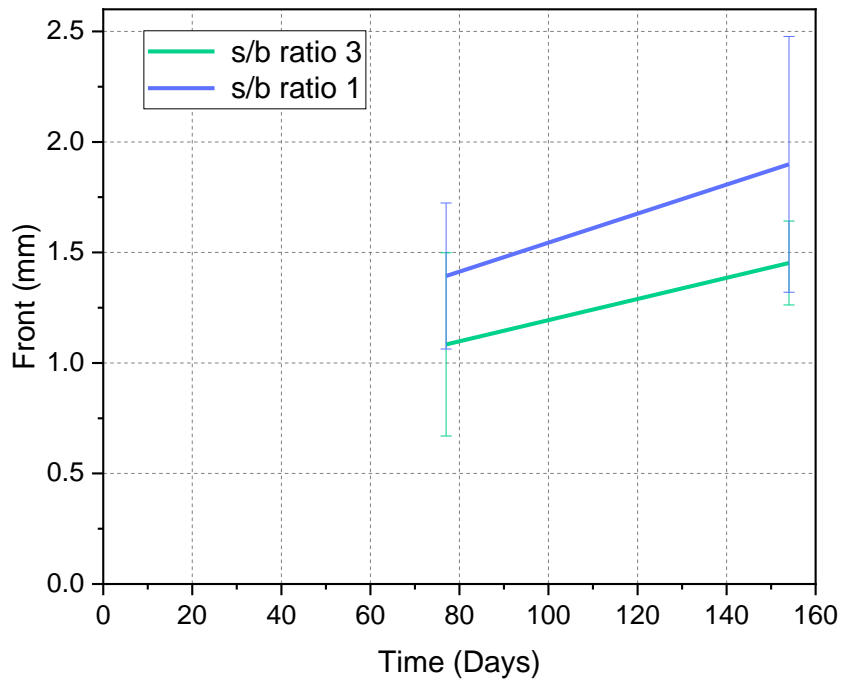
Figure 4.11: Natural carbonation depths of the mortars with a sand to binder ratio of 1 and 3, at 65% RH at 400 ppm CO_2.
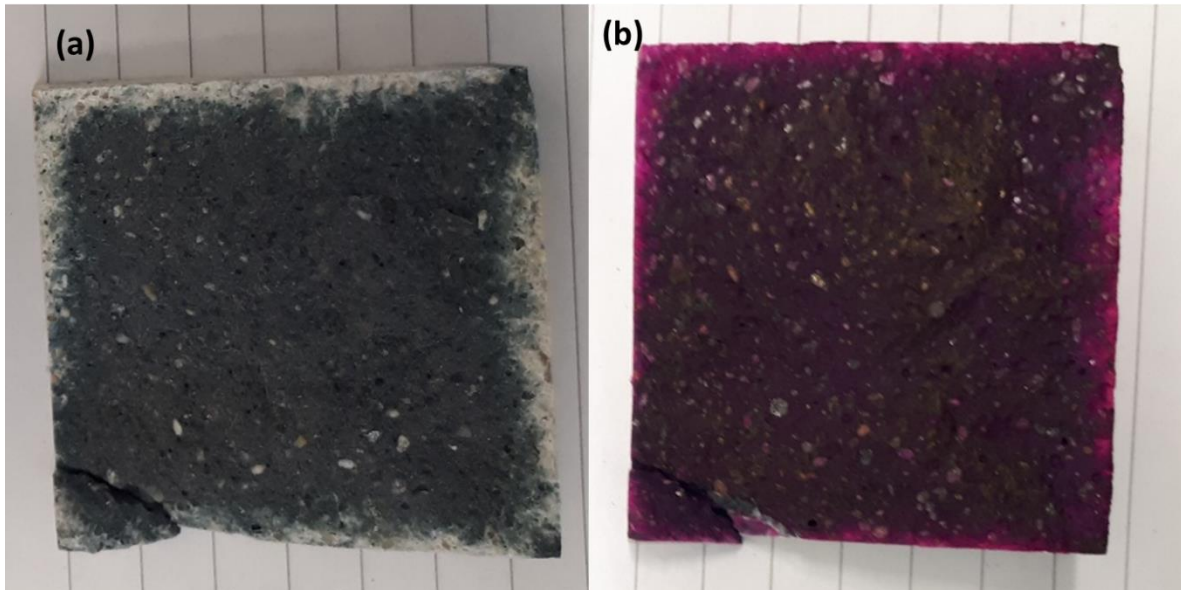
Figure 4.12: Photographs of the sample containing a sand to binder ratio of 1, exposed to natural carbonation for 28 days, with (a) and without (b) spraying with phenolphthalein. The sample dimensions are 50×50 mm.

The carbonation depth of the mortar which contains less sand is higher, similar to the results for accelerated carbonation. The main difference between the accelerated carbonation and natural conditions is that the depth is significantly lower. Indeed, the carbonation depth at 156 days at natural carbonation is almost 10 times lower than under accelerated carbonation, due to the higher content of CO_2 in the air; this concentration dependence will be discussed in more detail below. According to Bernal *et al*. [16], as the sample have not been condition at 65% RH before the exposure to carbonation, the carbonation of the sample will be low at the beginning of the carbonation, even under accelerated carbonation, and then the carbonation will follow the drying front.

In order to compare the values obtained to previous studies, the carbonation coefficient k_c is calculated. This coefficient is controversial for alkali activated materials, as it is based on Fick's first law, which uses a diffusion-control assumption to find that the carbonation depth of the material is the product of the carbonation coefficient and the square root of time. This product is consider to not be representative of long-term natural carbonation as it is based mostly on diffusion in this case, and considers that this reaction is not chemically controlled

[100,168]. However, to compare the results obtained in this study to previous studies, k_c is calculated with *Equation 4.3*:

$$d_c = k_c \times \sqrt{t}$$

The carbonation rate k_c is expressed in mm/√day and the depth of carbonation d_c is express in mm. In this study, k_c is estimated by fitting a linear function to the points obtained. The results obtained are presented in Table 4.4:

Table 4.4: Carbonation rate for the different samples tested.

Sand/binder ratio	1	1	3	3
Carbonation conditions	Natural	Accelerated	Natural	Accelerated
k_c (mm/√d)	0.14	1.99	0.10	1.62

Gluth *et al.* showed that the ratio of the mass of water per mass of $CaO+MgO_{eq}+Na_2O_{eq}+K_2O_{eq}$ ($w/(CaO+MgO_{eq}+Na_2O_{eq}+K_2O_{eq})$) is related to the carbonation rate for slag based alkali activated mortars and concretes. Each alkaline element is expressed in equivalent mass to CaO, by multiplying their mass by the ratio of the CaO molar mass to their molar mass. Gluth *et al.* study highlights that there is a correlation between the ratio $w/(CaO+MgO_{eq}+Na_2O_{eq}+K_2O_{eq})$ and the carbonation rate [81]. In this thesis, $w/(CaO+MgO_{eq}+Na_2O_{eq}+K_2O_{eq})$ equals 0.82. The results obtained in this work are very similar to the results obtained in the literature data analysis from Gluth *et al*. [81]. This ratio gives a good indication of the resistance against the carbonation of slag based alkali activated materials, from its mix design. However, many other parameters play a role in the carbonation, and consequently this parameter cannot be the sole carbonation indicator [81].

According to Kondo *et al.* [206,207]*,* which based the analysis on Papadakis *et al.* model [11], argue that, according to this same square root law, the ratio of k_c under accelerated carbonation to k_c for natural carbonation should follow the law below:

Equation 4.4

In Equation 4.4, C_{CO2} is the gaseous concentration of CO_2 in percentage. In the case of this study, this ratio equals 5, as $C_{CO2, accelerated}$ is 1% and $C_{CO2, natural}$ 0.04%. For the sample that has a s/b of 1, the ratio of the two carbonation rates is 14, and for s/b of 3 this ratio is equal to 16. So this equation is not representative of the dependence of carbonation rate on CO_2 concentration in this case. This is probably because the carbonation rate of alkali-activated slag under natural conditions is overestimated by the accelerated carbonation test conditions, as has been discussed in the literature [81,100,168].

4.4 Discussion

4.4.1 Degree of carbonation

Figure 4.13 compares the DoC obtained via TG-MS against the DoC obtained via the IBR method, as a function of the relative humidity. At 33% and 60% RH, the degrees of carbonation are close, with a difference of 5% and 7% respectively. Conversely, at the two other RH values, 86% and 93%, there is respectively 37% and 39% difference between the two methods. The difference between the two methods could be due to the fact that the H_2O and CO_2 peaks of the hydrotalcite overlapped. In the DoC calculation for the TG-MS methods, it has been decided that the mass losses above 370C were attributed to the CO_2 losses, even though CO_2 losses for the hydrotalcite start at lower temperature. This assumption could lead to a misrepresentation of the amount of CO_2 in the sample. However, the results for 33% and 60% have less than 10% difference, which is encouraging as the two methods are radically different as one is based on the CO_2 uptakes of the sample, and the other one is based on the loss of CO_2 during the destruction of the sample once the experiment is done.
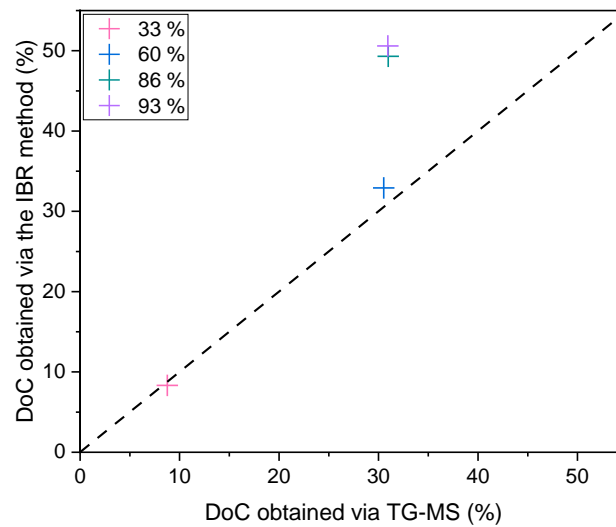
Figure 4.13: DoC obtained via TG-MS vs DoC obtained via the IBR method, at different RH.

The calculation of the degree of carbonation is based on the maximum binding capacity (MBC). In this study, it has been assumed that all the CaO, MgO, Na_2O and K_2O could react with the CO_2. However, it could be argued that not all of them could, and would, react with the CO_2. Firstly, the elements that are present in the unreacted slag will not carbonate, as it should be activated first [107]. As mention in section 4.3.2, only 45% of the slag is hydrated in the sample. It should be noted that not all the MgO will react with the carbon dioxide, as the hydrotalcite, which contains the MgO, will decompose into M-S-H at a high degree of carbonation, and only at a pH below 8 the M-S-H will form huntite under carbonation [147]. However, it seems that the pH is still higher than 9 under natural carbonation as the phenolphthalein remains light pink in the carbonation depth experiment done in this study. Finally, the formation of the calcium carbonate around the C-A-S-H gel, as the reaction happens at the surface, might slow down the carbonation reaction and even block it [181].

In the maximum binding equation, it is also assumed that all the SO_3 present will react with calcium oxide. However, the sulphate reacts with the sodium also. The sulphate evolution during carbonation will be studied in more detail in Chapter 6.

4.4.2 Diffusion and porosity

It has been shown previously that the diffusion coefficient is directly linked to the pore structure [194,208,209]. For example, Houst and Wittmann [86], have shown that an exponential relationship exists between the porosity that is not filled by water and the effective diffusion coefficient. It is observed in this study that the samples containing a sand to binder ratio of 3 exhibit a lower porosity than the samples with a ratio of 1. The diffusion coefficients of these samples exhibit the same trend, it is lower for the one with a ratio of 3. These results clearly show a link between the porosity and the diffusion coefficient. However, it is important to highlight that the porosity cannot solely explain the difference between the diffusion coefficients, as the porosity of the carbonated sample with a s/b of 3 is almost the same as the non-carbonated sample with a s/b of 1 (respectively 13.6% and 11.0%), while the diffusion coefficient of the first one is lower by one and half orders of magnitude. Figure 4.14 and Figure 4.15 show that in these samples, no direct link can be observed between the oxygen effective diffusion coefficient and the pore distribution or the content of pores in the samples.
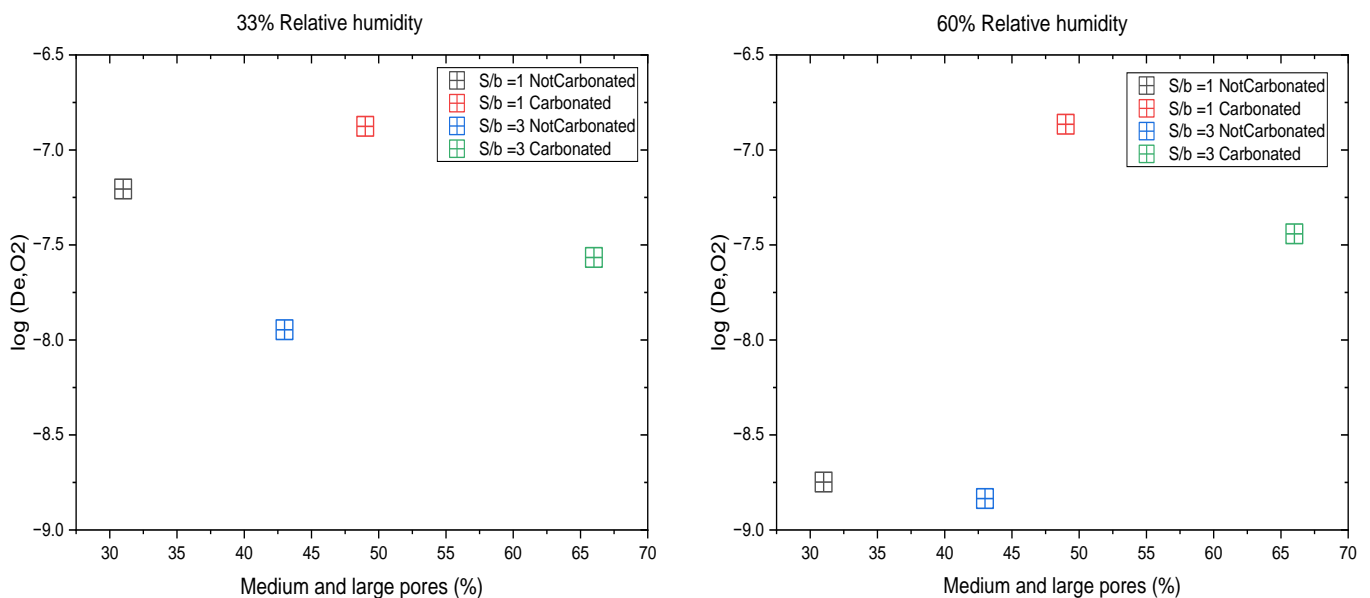
Figure 4.14: Logarithm of the effective diffusion coefficients as a function of the percentage of medium and large pores in the total pores of the sample carbonated at 33% and 60% RH.

94
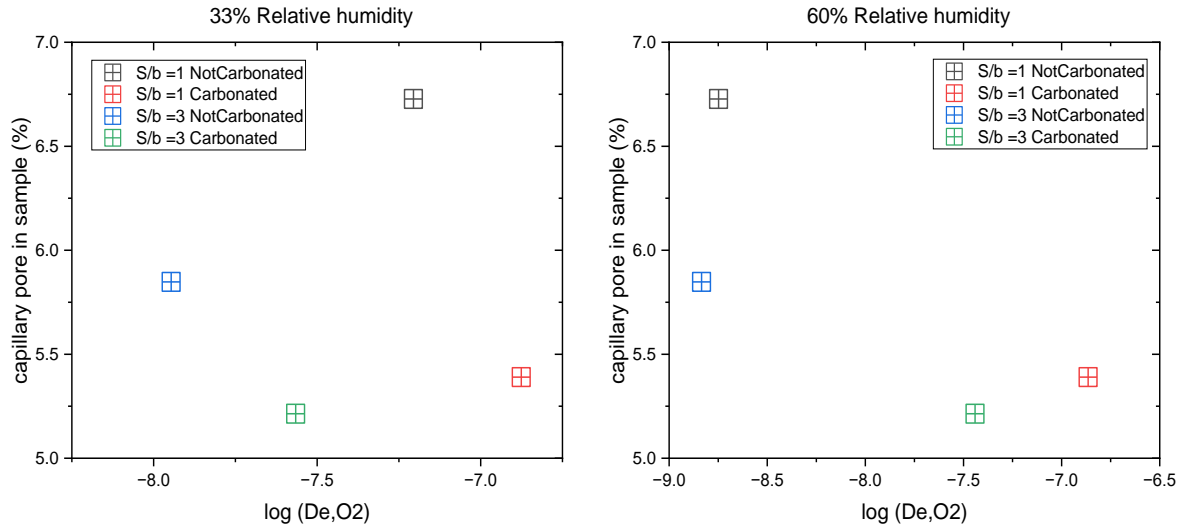
Figure 4.15: Percentage of capillary pores in the samples as a function of the logarithm of the effective diffusion coefficients for the samples carbonated at 33% and 60% RH.

It is also observed that the diffusion coefficients of the non-carbonated alkali activated slag in this are lower than those of PC systems in similar studies [97]. This result could be explained by two main reasons, the pore size distribution and the tortuosity. Indeed, Provis et al. showed that the tortuosity of alkali activated materials is higher than for PC even at the same porosity [210], while Collins and Sanjayan have demonstrated that alkali activated slags have a more refined pore structure than PC [211].

The $D_{e, O2}$ varies by two orders of magnitude with carbonation. Several parameters could play a role in this significant difference. Firstly, as observed, the pore size distribution shows that the amounts of medium and large pores significantly increase after carbonation, which could facilitate the diffusion. However, this is not enough to fully explain the difference in diffusion coefficient. Another parameter that has not been studied in this study, due to the high uncertainty of its measurement, is the pore network tortuosity, which might decrease after carbonation and thus leads to a higher diffusion [212]. Finally, it could be argued that the sulphur present in the sample can react with the oxygen and thus be decreasing the "real" diffusion coefficient before carbonation, as explained in section 4.3.4. The discussion of sulphur oxidation will be developed in Chapter 6.

4.4.3 Prediction carbonation

The alkali-activated slag sample shown here exhibits a slightly different trend regarding the effects of carbonation, compared to Portland based cementitious materials. To predict the carbonation depth d_c, the Equation 4.5 inspired by the work of Papadakis *et al.* is used: [213]

$$d_c = \sqrt{\frac{2D_{e,CO_2}[CO_2]_0}{carbonatable\ compounds}t}$$

The concentration $[CO_2]_0$ is the concentration of carbon dioxide during the experiment converted to mol.m^{-3} using the ideal gas law. The effective CO_2 diffusion coefficient $D_{e,CO2}$, expressed in m^2.s^{-1}, is determined via the diffusion coefficient experiment described in the paragraphs above. The time t is expressed in seconds. The carbonatable compounds (mol.m^3) represent the amount of materials that will be carbonated, on a molar basis, and is calculated using the Equation 4.6:

$$carbonatable\ compounds = CBC\frac{binder\ dosage}{M_{CO_2}}$$

The binder dosage, expressed in g.m^{-3}, corresponds to the amount of cementitious components, such as activators and precursors, per cubic metre of concrete or mortar. The molar mass of the carbon dioxide M_{CO2} is expressed in g.mol^{-1}.

In Equation 4.5 the diffusion coefficient can be determined via the experiment presented in the paragraph above. Two diffusion parameters can be used, the one corresponding to the carbonated mortars or the one corresponding to the non-carbonated mortars. Equally, the CBC calculated for the TG-MS results can be used, or the one calculated from the IBR method. Figure 4.16 to Figure 4.19 show the measured depths compared to the predicted depths, depending on whether the calculations use the $D_{e,CO2}$ carbonated or not carbonated, and the CBC obtained via the TG-MS or IBR methods.
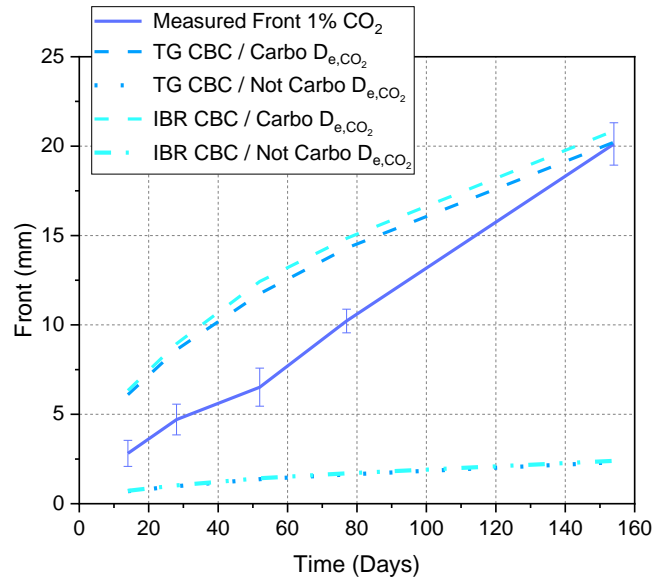
Figure 4.16: Carbonation depth measured compared to the depths predicted with the $D_{e,co2}$ for carbonated and not carbonated samples, and with the DoC calculated via the TG and the IBR methods, for the mortars with a sand/binder ratio of 1 at 60% RH and 1% CO_2.
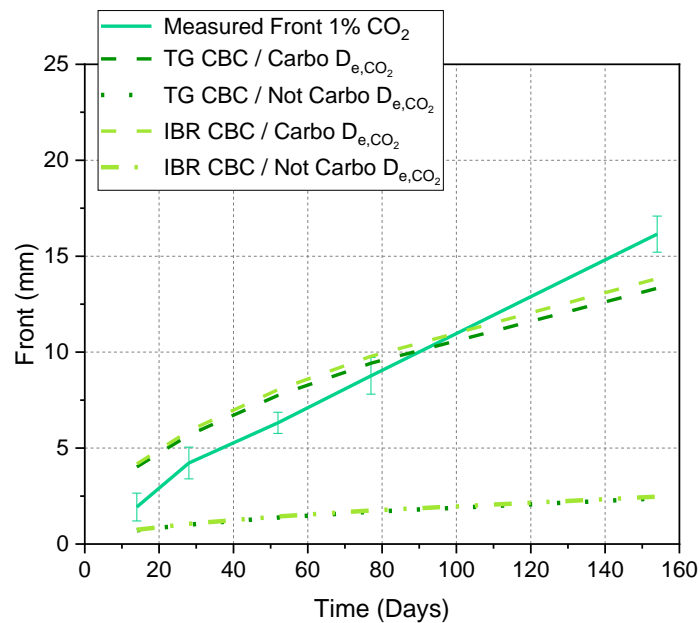
Figure 4.17: Carbonation depth measured compared to the depths predicted with the $D_{e,co2}$ for carbonated and not carbonated samples, and with the DoC calculated via the TG and the IBR methods for the mortars with a sand/binder ratio of 3 at 60% RH and 1% CO_2.
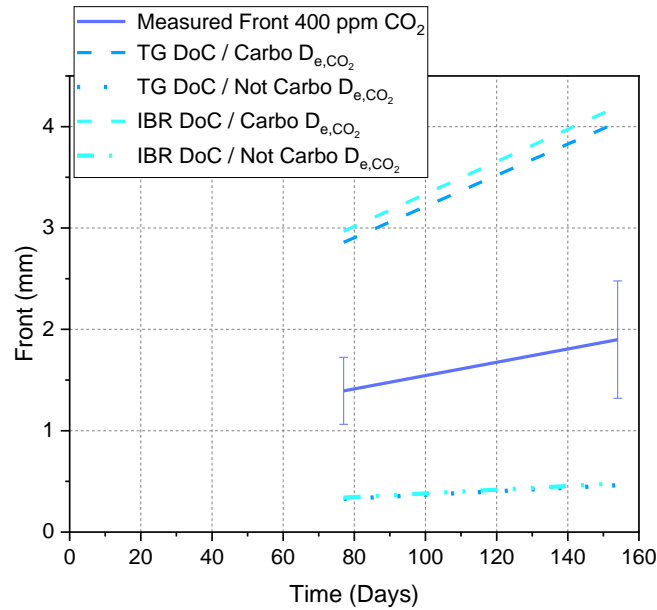
Figure 4.18: Carbonation depth measured compared to the depths predicted with the $D_{e,co2}$ for carbonated and not carbonated samples, and with the DoC calculated via the TG and the IBR methods for the mortars with a sand/binder ratio of 1 at 60% RH and 400 ppm CO_2.
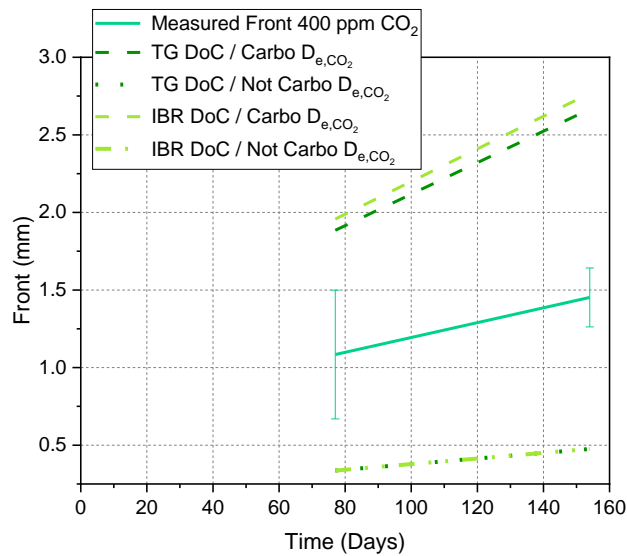
Figure 4.19: Carbonation depth measured compared to the depths predicted with the $D_{e,co2}$ for carbonated and not carbonated samples, and with the DoC calculated via the TG and the IBR methods for the mortars with a sand/binder ratio of 3 at 60% RH and 400 ppm CO_2.

Figure 4.16 and Figure 4.17 for accelerated carbonation show that the use of the diffusion coefficient of the mortars that were not carbonated strongly underestimated the carbonation depth. This result was expected as the carbon dioxide diffuse through the carbonated

materials to reach the carbonation front, where it dissolves and reacts. Consequently, the diffusion coefficient that corresponds to the carbonated regions of the sample are the most representative of the carbonation process [11,97]. Conversely, under natural carbonation it seems like neither of the measured values correspond to the correct diffusion coefficient. It could be due to the fact that the diffusion coefficient was determined with a sample that was carbonated at 1% CO_2. Consequently, the natural carbonation is damaging less the structure of the carbonated part than the carbonation at 1%. The diffusion coefficient for the sample exposed to carbonation at 400 ppm seems to be between the non-carbonated diffusion coefficient and the carbonated at 1%. Maybe it could be interesting for a future work to do it with a sample that has been carbonated under natural carbonation. However, due to the time limit of this study, only the diffusion coefficient under accelerated carbonation could be determined.

As mentioned in the paragraph above, the CBC and the degree of carbonation determined by TG-MS or by the IBR method are very similar at 60% RH. However, as it is not similar at 86% and 93% RH and the carbonation depths have only been measured at 60%, it has been decided to use the CBC determined via the IBR method, as it is more realistic as explained in the section above.
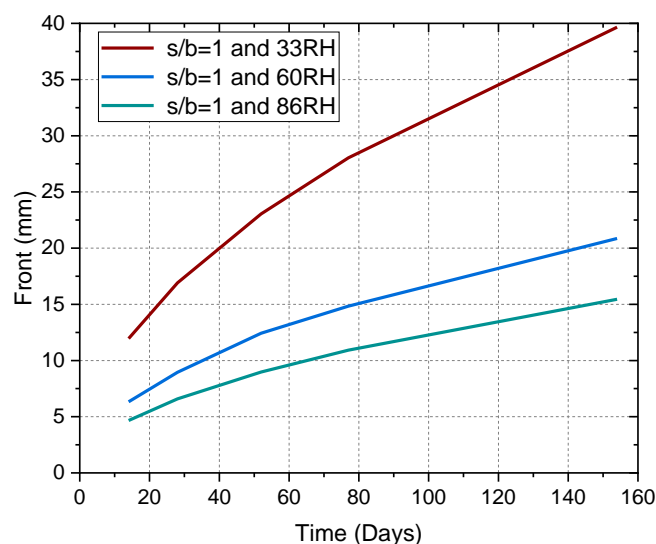
Figure 4.20: Carbonation depths predicted with the $D_{e,co2}$ carbonated and with the DoC calculated via IBR method for the mortars with a sand/binder ratio of 1, at different RH values and at 1% CO_2.
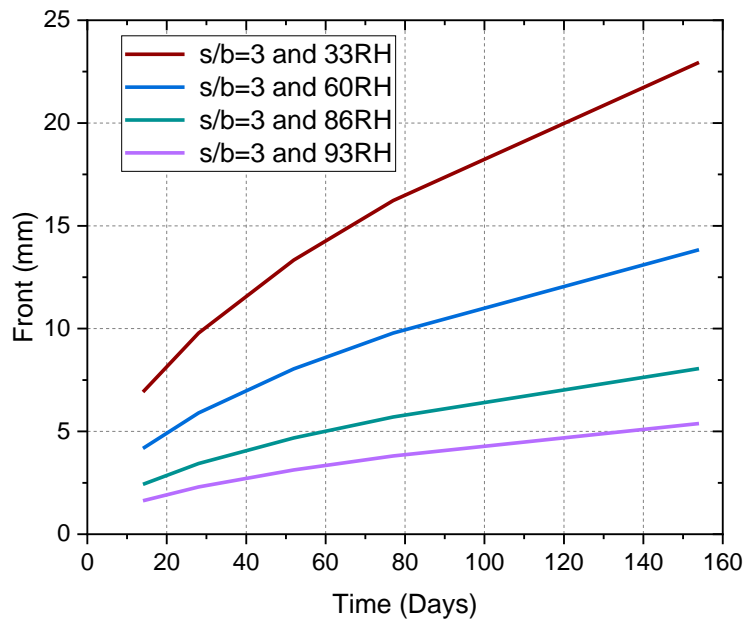
Figure 4.21: Carbonation depths predicted with the $D_{e,co2}$ carbonated and with the DoC calculated via IBR method for the mortars with a sand/binder ratio of 3, at different RH values and at 1% CO_2.

The predicted depths show that the carbonation front for 33% penetrates faster than the other ones. At 33% RH for both mortars, the diffusion coefficient is similar to the one at 60% RH, which means that the high difference is due to the large difference between the degrees of carbonation. However, the use of the accelerated carbonated diffusion coefficient and natural CO_2 binding capacity is not leading to results reflecting the carbonated depth under natural carbonation. As only 8% of the carbonatable mass is carbonated at 33% RH, the structure might not change drastically between carbonated and not carbonated, which would leads to a lower diffusion coefficient. Moreover, at 33% RH, if only 8% of the carbonatable mass is carbonated, it might not be enough to change the pH. According to the model of Ke *et al.*, 18 g of CO_2 per 100 g of binder must have reacted with the hydrated Na and Ca ions before the pH drops below 10 [147]. Further experimental work should be done to explore this point.

The predicted depth for 86% is higher than at 93% for both mortars. The DoC is similar at these two RH, but the DoC is higher for both mortars at 86%. It shows that the relative

humidities and the amount of available pores available for CO_2 diffusion play a key role in the carbonation.

4.5 Conclusion

In this chapter, the diffusion coefficient and the porosity evolution of slag based alkali activated mortars during carbonation is observed. As it has been observed in the literature previously for cementitious materials, a higher sand/binder ratio helped to reduce the carbonation depth by reducing the porosity and the diffusion coefficient [193]. The carbonation prompted a redistribution of the pore structure by reducing the amount of gel pores and increasing the amount of larger capillary pores, as previous studies have already highlighted in similar systems [66,198]. The carbonation of alkali activated slag significantly increased the diffusion coefficient, by almost two orders of magnitude. This high difference might be due to the oxygen uptake of the sulphur species for the non-carbonated samples. The carbonated samples were already oxidised during the carbonation, so the sulphur species could not interfere in the measurement of the oxygen effective diffusion coefficient. To estimate the CO_2 effective diffusion coefficient of non-carbonated cementitious materials containing a high content of GGBS, the use of another inert gas, like nitrogen, would be more effective. However, the diffusion coefficient of the sample that had not been carbonated is low compared to the diffusion coefficient of the PC based materials as previously published. So, the diffusion coefficient of the sample carbonated is similar to the one from carbonated PC based materials [97].

In this chapter, the evolution of CO_2 binding capacity for slag alkali activated materials as a function of relative humidity was observed. The highest degree of carbonation observed in this study is 50%, for the higher RH. So only 50% of the compounds that could be carbonated are carbonated under natural conditions. A higher RH encourages the carbonation of the carbonatable compounds. However, a high RH reduces the diffusivity of the CO_2 in the samples.

The parameters obtained in this study have been integrated in the Papadakis model to predict the carbonation depths, and compare to on-site carbonation depths. The test methods used here seem reliable to predict approximately the carbonation depth under accelerated

conditions; further testing should be performed to verify that these test methods could also predict the carbonation depth under natural carbonation by assessing gas diffusion in naturally carbonated samples.

This chapter has looked at the impact of the relative humidity on the diffusion of alkali materials under accelerated carbonation at 1% and at the CO_2 binding capacity under natural carbonation, for alkali activated slag based materials. This chapter also demonstrated that these parameters can be used in the Papadakis model for alkali activated materials, even though this model was developed to predict the carbonation depth for PC based materials. This chapter identifies the further work regarding the sulphur species evolution during the oxidation and carbonation. Chapter 5 will address the precise evolution of the chemical composition during the carbonation process. Chapter 6 will address this by studying the evolution of the oxidation state of the sulphur along the oxidation and carbonation front, by using the sulphur K-edge XANES experiments combined with μ-XRF mapping.

Chapter 5 : Combined effect of carbonation and other chemical attacks on alkali activated materials.

5.1 Introduction

As presented in section 2.2.1, carbonation of slag-based AAMs could result in corrosion of steel reinforcement and/or poorer mechanical properties, by affecting the materials microstructure and pore solution pH [9–11]. AAM are more susceptible to efflorescence than PC due to the high alkali content, which could be detrimental for the integrity of the structures [17,155]. These materials are also prone to leaching of calcium and sodium, which could affect their microstructure severely [17,18]. Although several studies have already studied the combined effect of 1) efflorescence and leaching or 2) efflorescence and carbonation in the laboratory, no studies have addressed the problem of the combined effects on these materials of carbonation and other chemical attacks such as leaching due to rain water or efflorescence in outdoor conditions [19,155,169,170]. In this study, the combined effect of these attacks on the microstructure of AAMs experiencing outdoor natural carbonation in the UK under sheltered and unsheltered conditions have been compared to indoor natural carbonation under both ambient and controlled conditions during two different time periods: three months during winter, and 12 months.

5.2 Experimental protocol

5.2.1 Samples

In order to study the carbonation reaction, which happens in the pastes between the aggregates and sand particles, cement pastes are used in this chapter. The samples were cast in 50 mm cubic moulds. Three cubic samples were produced for each of the four carbonation conditions, to provide a sufficient number of samples such that carbonation can be assessed after both 3 months and 12 months, with an additional sample available if necessary. The samples were cured for 7 days at 100% RH but without being put in water to avoid leaching.

5.2.2 Carbonation conditions

In order to provide conditions closest to real on-site carbonation, the samples have been exposed to carbonation environments that were the closest to these types of on-site exposure from the 27th October 2020 to the 27th October 2021. The humidity records for this period in Sheffield are presented in Figure 5.2. The minimum and maximum temperatures are presented in Figure 5.3. The precipitation records are presented in the Figure 5.4. The samples have been carbonated in four different carbonation environments:

- Outside in Sheffield exposed to the rain, these samples were thus exposed to soft water leaching;

- Outside in Sheffield protected from the rain by a shelf, these samples were exposed to conditions causing efflorescence as Figure 5.1 shows;

- Inside in the laboratory, where the temperature and the relative humidity (RH) were partially, but not precisely, controlled (respectively $20 \pm 5\,^{o}C$ and $35 \pm 15\%$);

- Inside a climate chamber, where the temperature and the relative humidity were controlled (respectively $20 \pm 0.5\,^{o}C$ and $30 \pm 2\%$).

Figure 5.1: Photograph of the sample exposed to the weather and protected from the rain during a year
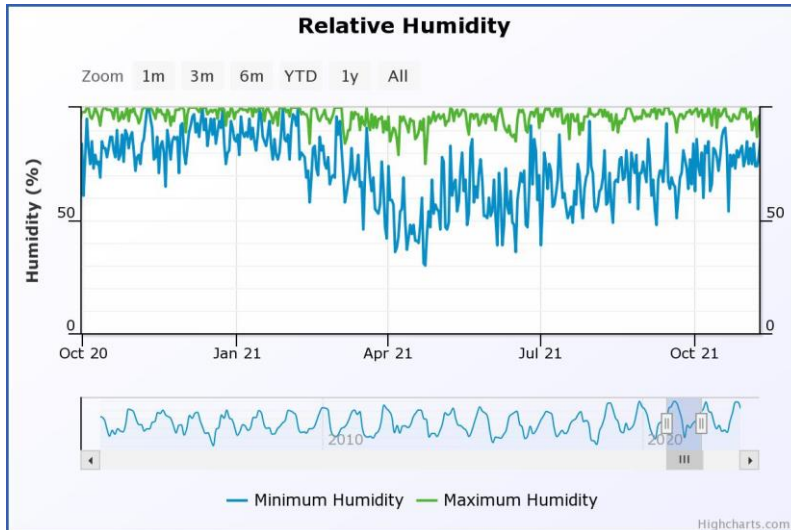
Figure 5.2: Maximum and minimum relative humidity records in Sheffield during the exposure period, adapted from [214].
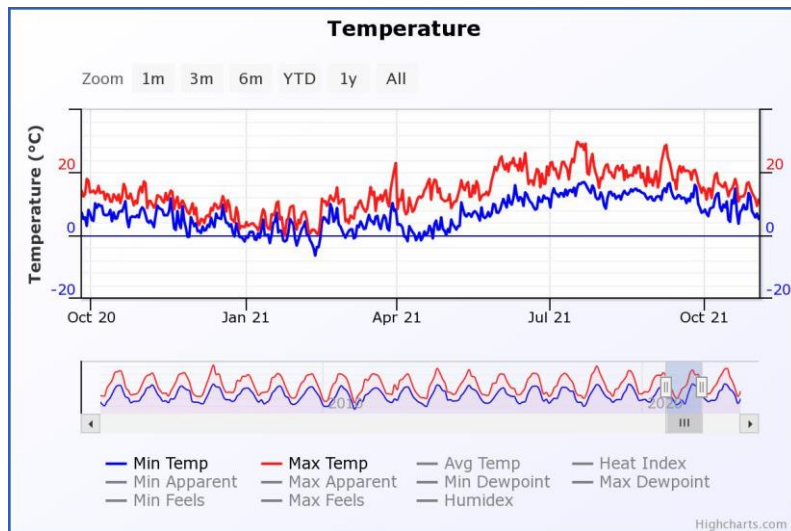
Figure 5.3: Maximum and minimum temperature records in Sheffield during the exposure period, adapted from [214].
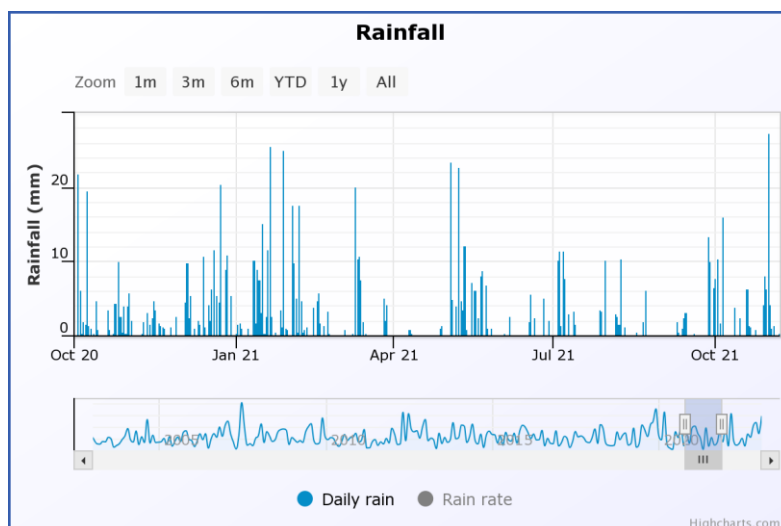
Figure 5.4: Daily rainfall records in Sheffield during the exposure period, adapted from [214].

5.2.3 Methods

Once the samples were removed from their exposure conditions, they were cut in two. On one surface, a solution of phenolphthalein was sprayed to reveal the carbonation depth. The results of this test are presented in the next chapter. Once the carbonation depth was revealed, the non-sprayed half of the original sample was itself cut in two to have on one side the carbonated parts and on the other the non-carbonated. Each part of this sample was analysed using the analytical methods described below.

Analytical methods used to analyse the samples include X-ray diffraction (XRD), thermogravimetry with mass spectroscopy (TG-MS), and magic angle spinning (MAS) nuclear magnetic resonance (NMR) spectroscopy probing aluminium (^{27}Al) and silicon (^{29}Si) nuclei. For the samples used to perform XRD analysis, ^{27}Al MAS NMR and ^{29}Si MAS NMR spectroscopy, the AAM reaction was stopped. According to Zhang *et al.*, the most effective technique to preserve AAM microstructure while removing the free water is to exchange it by isopropanol [172]. Consequently, the samples were immersed into isopropanol for one week after being crushed into 10 mm pieces. The isopropanol solution is changed regularly during this week. Thereafter, the samples were dried in an ambient environment and then stored under vacuum at ambient temperature before performing the tests. The samples were crushed and sieved to produce a 63 µm powder before being tested. To perform TG-MS, the samples were directly crushed and sieved to produce a 63 µm powder immediately before being tested. TG-

MS has been performed on the samples after 3 months and 12 months. Unfortunately, the TG-MS malfunctioned and was not usable during the experiments for the sample exposed to a year of carbonation, so the results are not reliable and could not be done again in the time available for this work. The phases identified in the XRD analyses in section 5.3.1 are presented in the Table 3.2 of Chapter 3.

5.3 Results

5.3.1 X-ray diffraction (XRD)

5.3.1.1 Efflorescence

The sample exposed to the weather and protected from the rain, during three months and a year, presented a white deposit on their surface. This white deposit shown on Figure 5.1 has been analysed by XRD. The XRD data show strong reflections due to the presence of trona, a hydrated form of sodium carbonate. Reflections due to gaylussite are also present in the XRD data, as well as those due to vaterite, a polymorph of calcium carbonate. Due to the high density of overlapping peaks, other forms of calcium carbonate might be present but hard to identify. Sodium and calcium carbonates are formed during the efflorescence reaction of alkali activated materials [39,151,158]. Several studies have also observed the presence of the carbonate double salt gaylussite in surface deposits resulting from efflorescence [215,216]. Gaylussite is also sometimes observed after the carbonation of alkali activated slag systems [101,113]. In this case, both the sodium and calcium ions are reacting with the CO_2 dissolved in water, to form gaylussite.
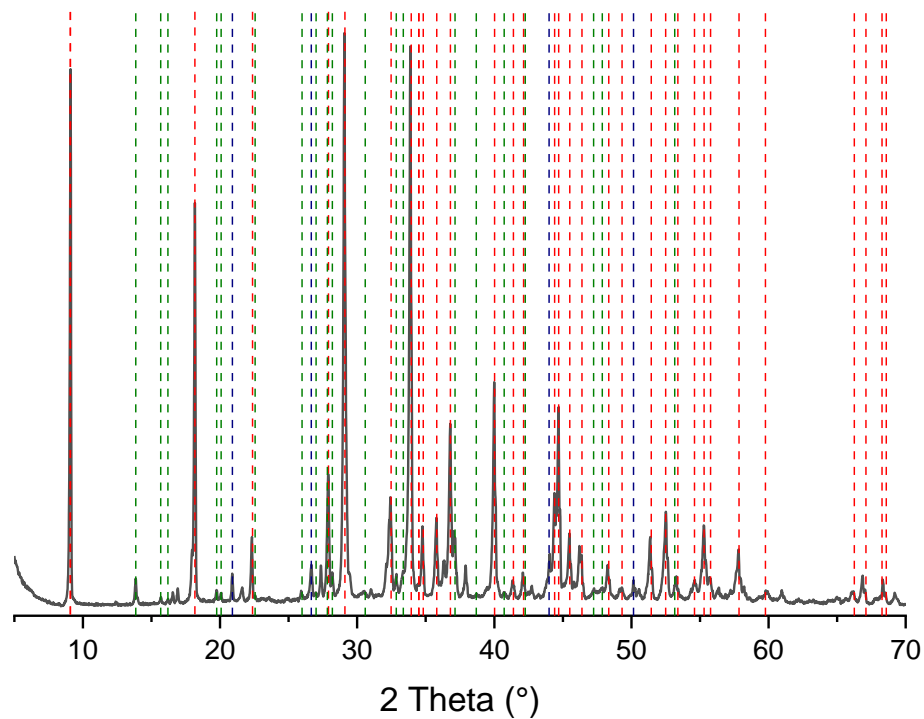
Figure 5.5: XRD pattern of the white deposit formed on the sample exposed outside protected from the rain after 12 months

5.3.1.2 Sample analysis

The XRD patterns of the carbonated and non-carbonated parts of the sample exposed to carbonation outside and inside, after 3 months and a year of exposure are presented below. The phases identified in the XRD analyses in section 5.3.1 are presented in the Table 3.2 of Chapter 3. The XRD pattern of the non-carbonated parts of the samples after three months and a year are presented in Figure 5.6 and Figure 5.7, respectively. The main phases present in these samples are the hydration products hydrotalcite and C-A-S-H gel. The large broad feature around 30° arises due to diffuse scattering as a result of the disordered nature of the main binding phase of high calcium content AAM, C-A-S-H gel [87,100]. The reflections due to the C-A-S-H gel indicate that it exhibits strong structural similarity to 9 Å tobermorite, however, there are also similarities with reflections due to 11 Å and 14 Å tobermorites, or a mix of these structures [217]. Indeed, the main difference between the XRD patterns of 9 Å, 11 Å and 14 Å tobermorite are the peaks present below 10° 2θ, however the XRD patterns have only been collected between 10° and 60° in this study, due to the noise before 10°.

In all the samples, hydrotalcite-group phases can be identified. Hydrotalcite is a common hydration product for high calcium alkali activated materials containing a significant amount of magnesium [5]. A small amount of quartz can be observed in the parts of the samples that are not carbonated outside protected from the rain after 3 months and 12 months, as well as in the sample chamber after 3 months. The presence of quartz is due to the unreacted slag in the sample [52,218].

A small amount of portlandite ($Ca(OH)_2$) can be identified in some of the non-carbonated and carbonated regions of some samples, especially in the sample exposed to rain outside. The presence of portlandite in the non-carbonated region of the sample is surprising as portlandite is not a hydration product of alkali activated slag materials for the non-carbonated samples [5]. It is also surprising to observe it in the carbonated parts of the samples, as the portlandite is the first product to carbonate in Portland cement-based materials, so it is expected that it would have carbonated here as well [213]. The portlandite might have precipitated due to the moderate pH, the high water content in the sample and the presence of isopropanol, which limits the carbonation of the calcium ions. To confirm whether the presence of portlandite is associated with the solvent exchange process, the 12 months carbonated sample exposed to the rain outside has also been analysed prior to solvent exchange. Figure 5.10 shows the spectrum of the sample before and after solvent exchange. Portlandite does not appear before the solvent exchange process, which confirms that its presence is linked to the solvent exchange process; this is an important finding when considering the methods used to stop hydration of different cements.
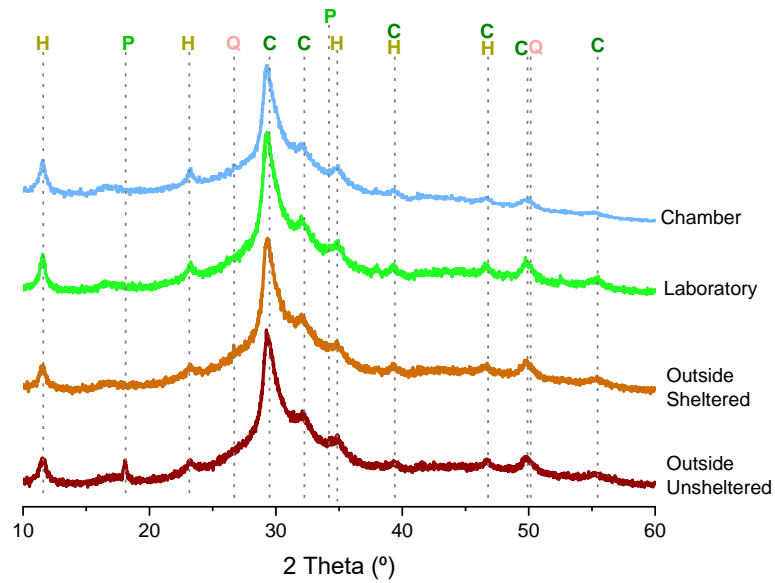
Figure 5.6: XRD pattern of the non-carbonated regions of the samples exposed to carbonation for 3 months in different conditions. The blue pattern was exposed to carbonation in a climate chamber. The green pattern was exposed to carbonation in the laboratory. The light brown was exposed to carbonation in outside sheltered from the rain. The dark brown was exposed to carbonation outside unsheltered from the rain.
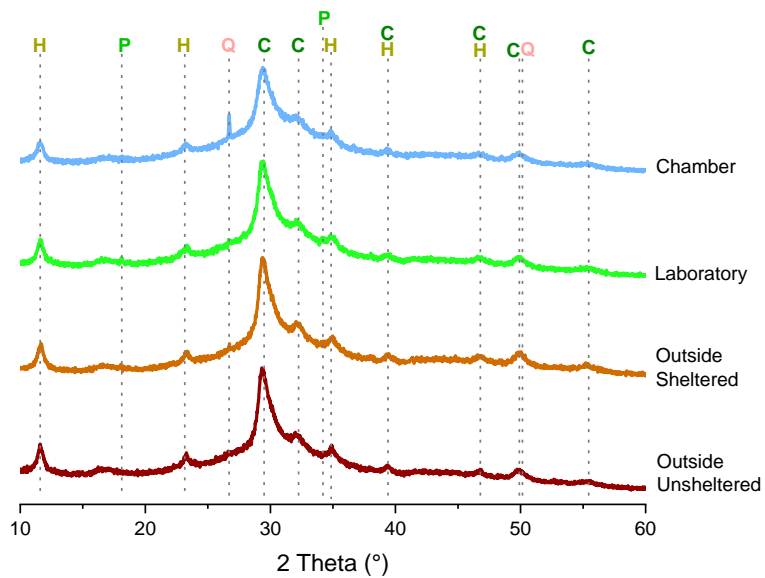
Figure 5.7: XRD pattern of the non-carbonated regions of the samples exposed for 12 months in different conditions. The blue pattern was exposed to carbonation in a climate chamber. The green pattern was exposed to carbonation in the laboratory. The light brown was exposed to carbonation in outside sheltered from the rain. The dark brown was exposed to carbonation outside unsheltered from the rain.

In Figure 5.8 and Figure 5.9, each of the three polymorphs of calcium carbonate (calcite, vaterite and aragonite) are identified in the samples, with the polymorph identified depending on the sample. After 3 months of carbonation, the carbonated parts of the samples inside present almost no trace of calcium carbonate. Some small peaks that could corresponds to calcium carbonate can be distinguished in the XRD data for the sample exposed to carbonation in the laboratory, however, these peaks are not much bigger than the noise. Conversely, calcite and vaterite, products of carbonation of the C-A-S-H gel, are present in large amounts in the samples that have been exposed to natural carbonation outside in ambient conditions. The XRD data for the sample that showed traces of efflorescence reaction show more intense reflections due to calcite compared to the ones exposed to soft water leaching and carbonation. These two samples have less intense C-A-S-H peaks in the XRD data than the sample in the laboratory and in the chamber. These results show that carbonation reduces the amount of C-A-S-H gel while forming calcium carbonate [87,93,100,101].

The XRD data for the samples carbonated inside for 12 months presents clear calcium carbonate peaks. The main difference between the XRD patterns for the two samples carbonated inside (one in a controlled environment chamber, one in ambient conditions) is that the sample in the chamber shows the presence of the three calcium carbonate polymorphs whereas the sample in the laboratory does not exhibit the aragonite peaks. Conversely, the samples exposed outside after 12 months present almost the same patterns as those for the samples exposed outside after 3 months: the XRD data for the sample protected from the rain show more intense peaks for calcite than vaterite, whereas the XRD data for the sample not protected from the rain show similar intensity for calcite and vaterite.

The main difference between the XRD data for the sample exposed from the rain at 3 months and 12 months is the presence of aragonite; indeed, the XRD data for the sample after 12 months show some small peaks corresponding to aragonite. Vaterite is the less stable calcium carbonate polymorph, and it is usually a transition phase toward calcite, whereas aragonite can be stable in some specific situations such as high pressure [219]. In most cases, aragonite is formed from vaterite and turns into calcite, except at higher temperature where aragonite will be favoured over vaterite [116,219–221]. A study from López-Arce *et al.* shows that vaterite, calcite and aragonite are formed during portlandite carbonation at higher relative

111

humidities, while at lower relative humidities, only vaterite is formed [222]. So the presence of aragonite in the samples after 12 months in the chamber and outside exposed to the weather might be due to several factors. One possible explanation could be that the vaterite transformed into aragonite at higher temperatures, as the chamber is held at a constant temperature of 20°C, whereas the temperature in the laboratory varies more, which may not be ideal for the formation, and stabilisation, of aragonite [219]. Moreover, the sample exposed to the rain was also exposed to the sun, which could have warmed the sample at high relative humidities, which leads to the formation of aragonite [219].

The hydrotalcite peak positions are not affected by the carbonation alone or with efflorescence according to these results. However, the intensity of the peaks is smaller after carbonation for all the samples. Some studies show also that the carbonation of the hydrotalcite results in the reduction of the peak intensities associated with this phase [114,122]. This reduction is due to a higher degree of local disorder in this phase due to the incorporation of carbonate ions [190]. The hydrotalcite peaks of the sample being exposed to leaching and carbonation are slightly less intense after being exposed for 3 months and a year. These results imply that the hydrotalcite carbonation is favoured by the soft water leaching.
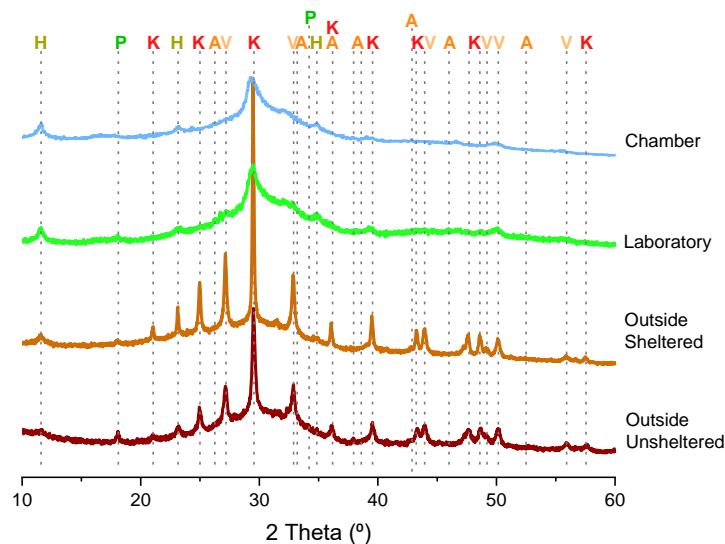
Figure 5.8: XRD patterns of the carbonated regions of the samples exposed for 3 months in different conditions. The blue pattern was exposed to carbonation in a climate chamber. The green pattern was exposed to carbonation in the laboratory. The light brown was exposed to carbonation in outside sheltered from the rain. The dark brown was exposed to carbonation outside unsheltered from the rain.

112
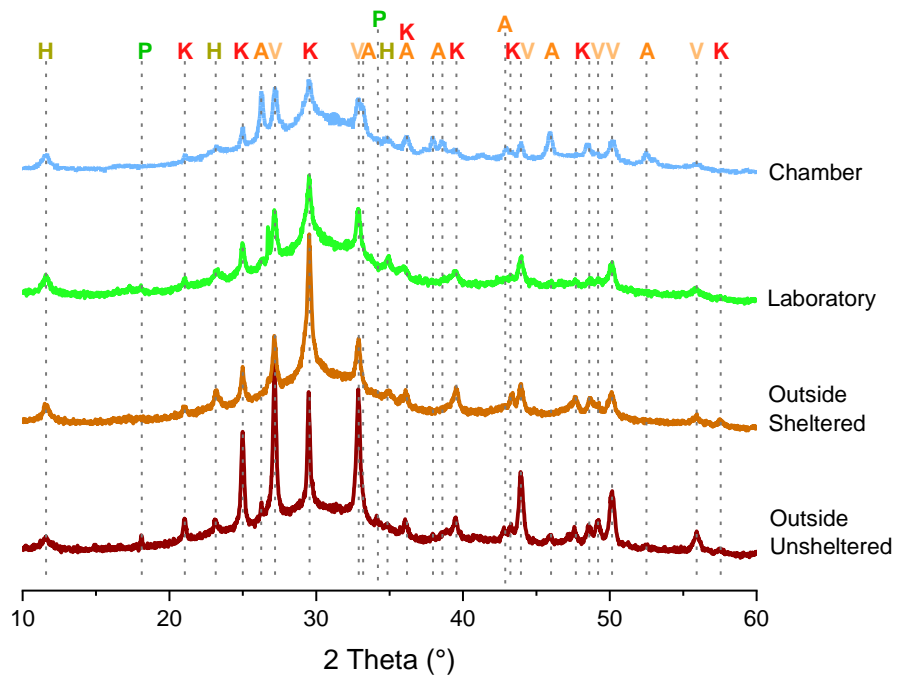
Figure 5.9: XRD patterns of the carbonated regions of the samples exposed during 12 months in different conditions. The blue pattern was exposed to carbonation in a climate chamber. The green pattern was exposed to carbonation in the laboratory. The light brown was exposed to carbonation in outside sheltered from the rain. The dark brown was exposed to carbonation outside unsheltered from the rain.
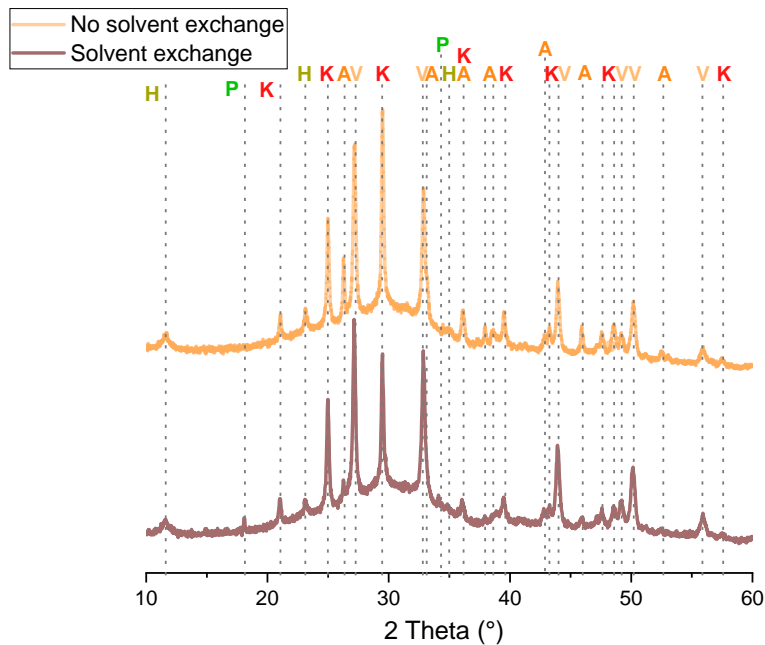
Figure 5.10: XRD patterns of the carbonated regions of the samples exposed outside unsheltered from the rain for 12 months with and without solvent exchange.

5.3.2 Thermogravimetric analysis coupled with mass spectroscopy (TG-MS)

TG-MS has been performed on the samples after three months. No solvent exchange procedure was applied to the samples used for TG-MS analysis. Figure 5.11 and Figure 5.12 are respectively the data for the non-carbonated and the carbonated parts of the sample exposed under different conditions for a duration of 3 months. Both plots show the weight loss of the sample on the upper curves and, on the lower curves, the derivative thermogravimetry (DTG) trace which is obtained by computing the first derivative of the TG curve. Figure 5.13 is the corresponding mass spectroscopy plot for these samples, for both the non-carbonated and carbonated parts, for H_2O (mass/charge = 18) and CO_2 (mass/charge = 44).

The TG-MS results are analysed with the same interpretation used in Chapter 4. The main peak from 45°C to 200°C is attributed mainly to the evaporation of water. The two main causes of this peak are the loss of free water between 20 and 105°C and the C-A-S-H gel phases between 50°C to 215°C [187–189]. Hydrotalcite presents two main water loss events. The first one around 270°C for interlayer water, and another one around 400°C, which correspond to the molecule of water in the main layer [173]. The second one around 373-400°C can be attributed to the release of CO_2 in the hydrotalcite. [190] The mass loss between 400°C and 800°C is attributed to the loss of CO_2 within the carbonate phases: from 400 to 500°C indicates amorphous calcium carbonates; 500 to 700°C is mainly attributed to vaterite or aragonite; 700 to 800°C is identified as gaylussite or calcite [93,101,102,191].

The non-carbonated parts of all the samples exhibit similar weight loss events when analysed by TG-MS. All samples exhibit a large mass loss event at 100°C due to water loss, according to the MS results of the sample exposed outside sheltered and unsheltered. This water mass loss event is attributed to the free water and the water present in the C-A-S-H gel [187–189]. The water MS results of both of the samples carbonated inside (one in a controlled environment chamber, one in ambient conditions in the laboratory) are not coherent and cannot be trusted. Indeed, the MS identify a constant water loss through the entire temperature range, even though no similar loss is observed on the TG measurements. In Figure 5.11, the weight loss event of the water at 100°C has a smaller magnitude for the samples carbonated outside, sheltered and unsheltered, than those carbonated inside in the laboratory and in the chamber.

Two weight loss events associated with hydrotalcite can be also be identified. The first one from 150 to 230°C is due to the water in the interlayer. The second one from 270 to 400°C is due to the chemically bound water, and potentially carbonate hydrotalcite [223]. Small weight loss events can be observed between 700 and 900°C, which are confirmed by MS as loss of CO_2, due to stable carbonate phases present in the unreacted slag like calcite or gaylussite [52,187].
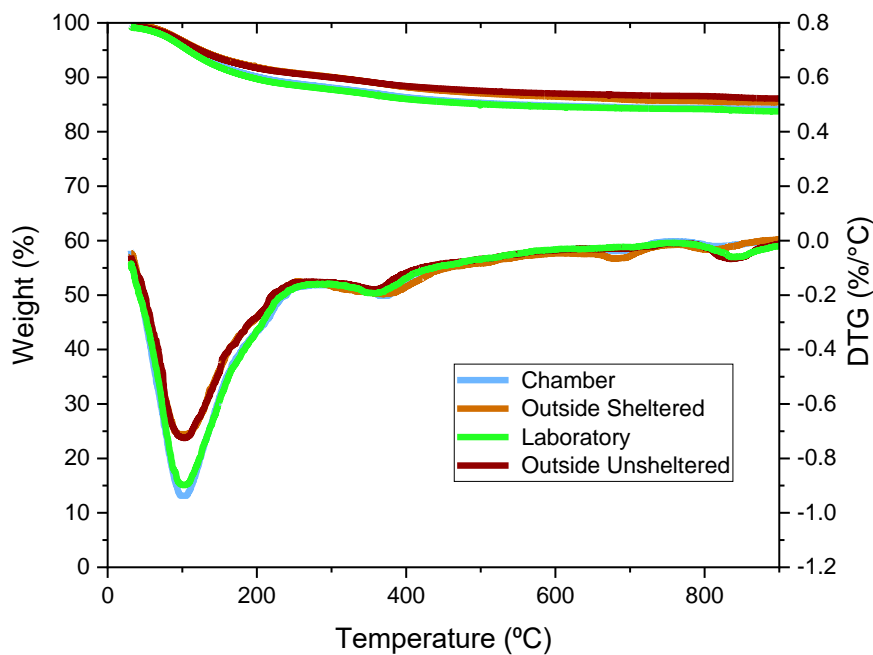
Figure 5.11: Thermogravimetry curves of the non-carbonated parts of the sample exposed to 3 months carbonation.

The TG analysis of the carbonated sample outside protected from the rain shows a small weight loss event around 500°C and a larger weight loss event around 800°C. According to the MS, these two mass loss events are due to CO_2 loss. The first mass loss event is attributed to the least stable form of calcium carbonate, vaterite, as the XRD results show the presence of this phase. The second mass loss event is attributed to the most stable calcium carbonate polymorph, calcite, which is present in a large quantity according the XRD diffractograms presented in Figure 6.8.The water loss at 100°C, caused by the water loss from the C-A-S-H gel, is less prominent than the non-carbonated part of this sample. This result shows that the amount of C-A-S-H gel is lower in the carbonated part of the sample; this indicates that the

C-A-S-H gel has reacted with the CO_2 to form the calcium carbonate phases, and has thus lost some of its structural water.

The TG analysis of the carbonated sample outside exposed to the rain present two medium size weight loss around 500°C and around 800°C. According to the mass spectroscopy, these are due to the loss carbon dioxide. As the XRD diffractogram of this sample shows, vaterite is responsible for the first mass loss and calcite is responsible for the second one. Both techniques confirm that the amounts of these two phases are similar. This sample presents also a strong, sharp weight loss at 100°C that can be associated to the C-A-S-H gel and/or to the free water in the sample. The sample has been analysed just after being exposed outside to a rainy day. Consequently, the sharp peak is most likely due to the free water in the sample. However, the mass loss occurs over a narrower temperature range than the sample inside and occurs at a similar range as the mass loss for the sample outside protected, which means that the same conclusion can be drawn for this sample than for the sample that was outside but protected from the rain. Despite the large amount of free water due to the rain, it remains clear that the C-A-S-H gel carbonated to form calcium carbonates.

The TG curves of the carbonated parts of the two samples inside are similar. The water mass loss attributed to C-A-S-H is slightly smaller than for the respective non-carbonated cases: the non-carbonated sample DTG curves show that these mass losses have a maximum rate of - 0.9 %/°C whereas the carbonated ones are at -0.7 %/°C. These results indicate that the amount of C-A-S-H is lower in the carbonated part, so this phase has already started to carbonate.

A wide mass loss can be observed from 300 to 550°C, which is due to the loss of water and CO_2 from the hydrotalcite and another phase, as the hydrotalcite H_2O and CO_2 mass losses are only from around 300°C to 400°C [223]. Consequently, these mass losses are likely due to several phases. The MS results confirm that the mass loss from 300 to 550°C is due to a loss of H_2O first and then CO_2. Morandeau and White [224] have shown that, in the case of accelerated carbonation, the C-A-S-H decalcification leads to the formation of amorphous calcium carbonate (ACC) which later turns into calcite or vaterite, for the case of low magnesium content alkali activated slag (< 7 wt. % MgO in the slag). No clear peaks associated with crystallised calcium carbonates have been observed in the XRD patterns, so the presence of ACC would explain this mass loss [224] These curves confirmed that the sample has started

to carbonate, and to form ACC, as well as hydrotalcite with CO_2 in its interlayer, despite the lack of crystalline calcium carbonates.
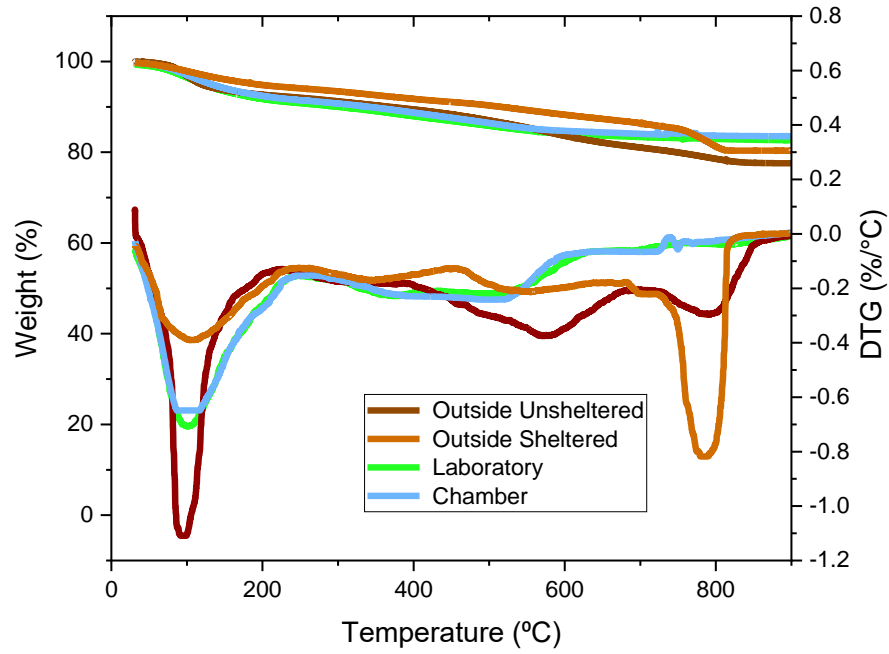
Figure 5.12: Thermogravimetry curves of the carbonated parts of the samples exposed to 3 months of carbonation.
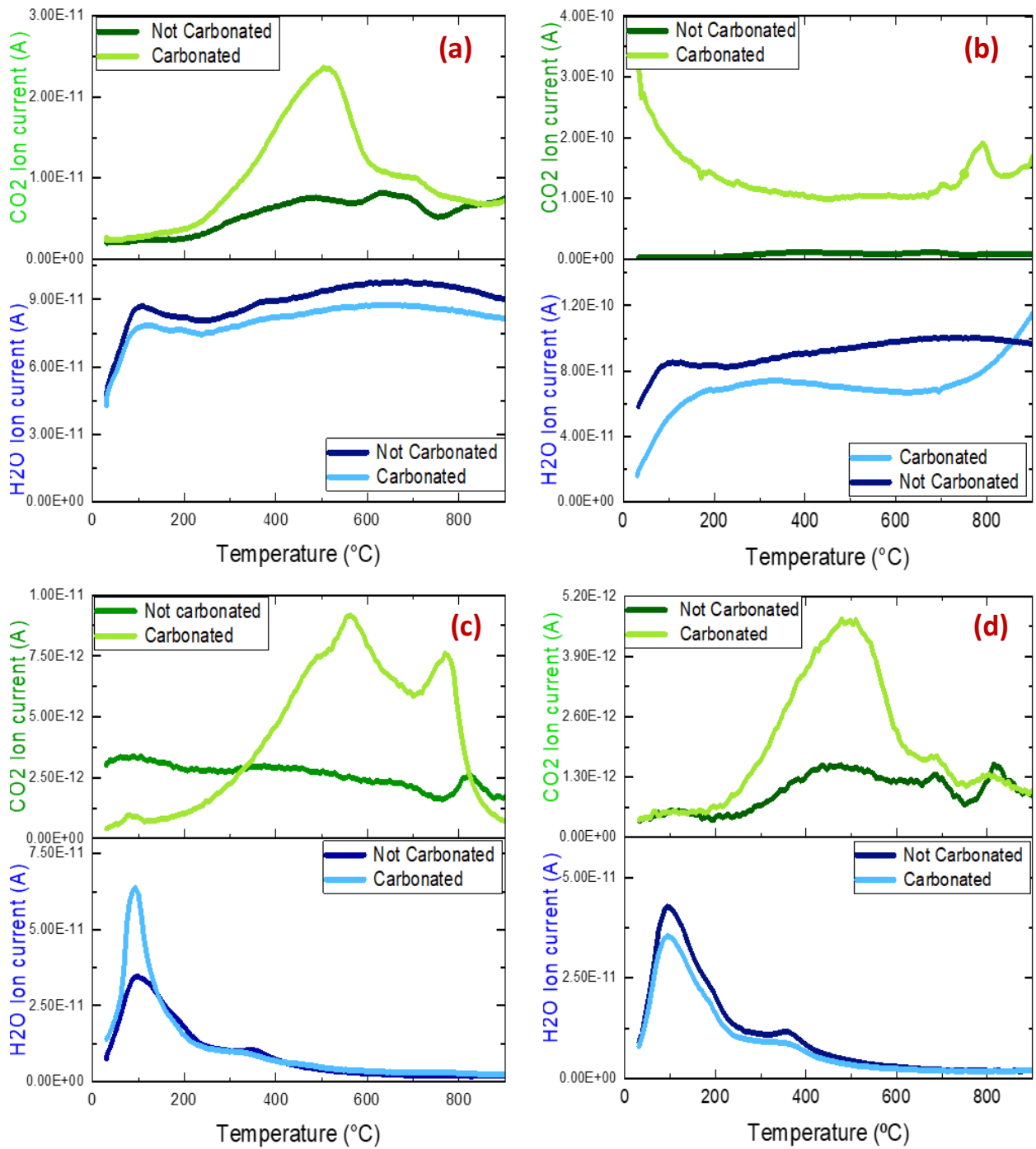
Figure 5.13: Mass spectra of CO_2 (m/z=44) and H_2O (m/z=18) for the samples exposed for 3 months, in the chamber (a), in the laboratory (b), outside sheltered from the rain (c), outside unsheltered from the rain (d)

5.3.3 ^{27}Al and ^{29}Si MAS NMR spectroscopy analysis

5.3.3.1 ^{27}Al MAS NMR

The ^{27}Al MAS NMR spectra of the non-carbonated parts of the samples, after 3 months and 12 months of exposure, as well as the unreacted slag, are presented in *Figure 5.15* and *Figure 5.16*, respectively.

All the spectra exhibit a high intensity peak with an observed chemical shift, δ_{obs}, of $\delta_{obs} = 11.5$ ppm. This peak corresponds to Al^{VI} sites in AlO$_6$ environments in hydrotalcite [225]. This peak could also be characteristic of aluminate ferrite monosulfate (AFm) phases [226,227]. However, the XRD data of these samples show the presence of hydrotalcite phases and not AFm phases. Consequently, this peak should be related to the Al^{VI} sites in hydrotalcite. According to Bernard *et al.* [223], the hydrotalcite peak can be decomposed into two peaks: one symmetric at $\delta_{obs} = 9.1$ ppm (called in the figures HT(II)) and one asymmetric at $\delta_{obs} = 11$ ppm (called in the figures HT(I)). However, it can be observed that there is an overlapping contributions from both HT(I) and HT(II) in the carbonated and non-carbonated samples. The third aluminate hydrate (TAH) peak occurs at $\delta_{obs} = 6$ ppm, and overlap slightly with the hydrotalcite peaks. The position of this peak is rather surprising as the peak attributed to octahedral aluminium of hydrotalcite in alkali activated slag is usually situated around $\delta_{obs} = $ 9-10 ppm [113,121]. This shift difference might be due to the difference of magnetic fields, which is 14.1 T in the studies cited and 11.7 T in in this study [113,121]. However, several studies done only on aluminium double layer hydroxides shows this peak between 11-11.8 ppm, that were performed at 8.45 T [225] and 11.7 T [228].

A small peak is observed at $\delta_{obs} = 38$ ppm for all the non-carbonated samples. This peak is due to the presence of pentacoordinated aluminium sites in Al^{V} environments [109,226]. This pentacoordinated aluminium is a charge-balancing aluminium cation situated in the interlayer of the C-A-S-H gel [173,229]. As the intensity of this peak is small, the errors associated with this estimate of relative change in intensity are sufficient to make this exercise uninformative for the determination of a change of intensity between all the non-carbonated samples. The pentacoordinated aluminium can be presented as the schema below according to Walkley *et al.*[229].

The peak observed at δ_{obs} = 6 ppm is due to an octahedrally coordinated aluminium site called "Third Aluminate Hydrate" (TAH), this phase is a poorly crystalline aluminate hydrate according to Anderson *et al.* [226], but detailed information about TAH is scarce as this phase can only be identified by ^{27}Al NMR. Renaudin *et al* suggested that TAH is situated in the interlayer of C-A-S-H, and thus is linked to the concentration of calcium and sodium cation in the interlayer [230]. Kunhi Mohamed *et al.* identified the TAH not as a specific phases but as a silicate bridging site with a structure corresponding at $[AlO_2(OH)_4]^{5-}$, this site is stable due to the prescence of calcium cations and hydroxyl ligands [231].

A large asymmetrical peak is present between δ_{obs} = 80 and 55 ppm. This peak is composed of three overlapping peaks associated respectively with the tetrahedral aluminium AlO_4 sites in the C-A-S-H gel, called $q^2(I)$ and $q^2(II)$ and q^3 (Figure 5.14). This peak is also composed of a large peak at 64 ppm, which corresponds to Al^{IV} site in the unreacted slag presents in the sample. Figure 5.15 and Figure 5.16 presents the ^{27}Al MAS NMR spectrum of the unreacted slag. The $q^2(I)$ peaks has been located at 75 ppm, the $q^2(II)$ peaks at 68 ppm and the q^3 at 62 ppm. The schematic presented in the Figure 5.14, done by Walkley *et al.* [232] explained the close atomic environment of each site. The main peak, for the non-carbonated regions, is the $q^2(I)$, which is a bridging tetrahedral site balanced by Ca^{2+}, which leads to a higher resonance, as Figure 5.14 shows [232]. The peak associated to $q^2(II)$, which is a bridging tetrahedral site balanced by Na^+ or H^+ as Figure 5.14 shows, has smaller intensity than $q^2(I)$ [232]. The q^3 sites peaks might be present but its identification is challenging due to the overlap of the q^2 sites and the Al^{IV} slag peak. Figure 5.16 shows that the non-carbonated regions of the sample exposed in the chamber during 12 months, presents a higher intensity for the Al^{IV} slag peak compares to the other samples. These results will be discussed more in detail with the ^{29}Si NMR data, which are needed to provide a fuller understanding here.
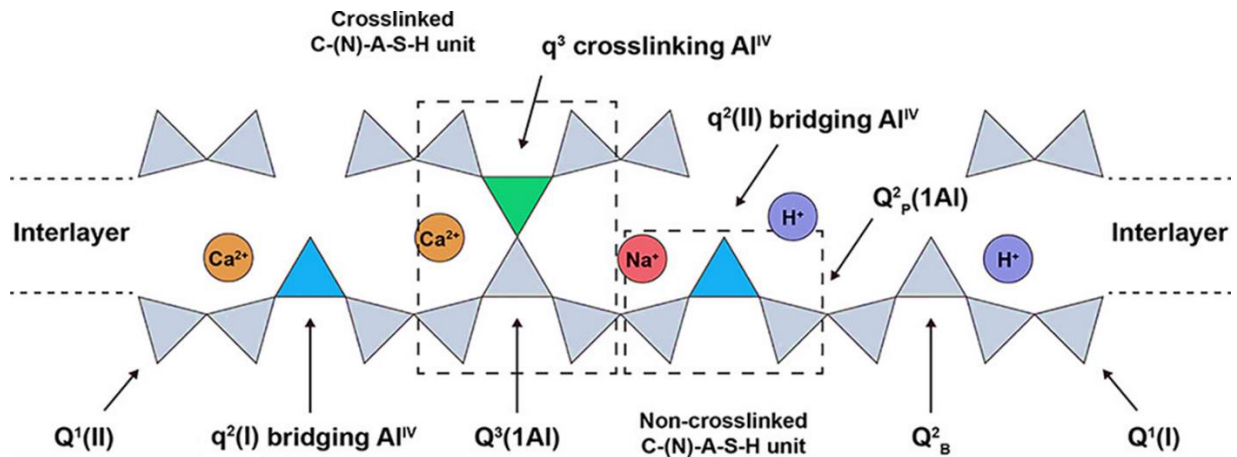
Figure 5.14: Schematic of the aluminium sites in the C-A-S-H gels. Cross-linking q^3 Al tetrahedra are green triangle and non cross-linking q^2 Al tetrahedra are blue triangle. Si tetrahedra are shown by the grey triangles, and charge-balancing alkali cations and protons are orange for Ca+, red for Na+ and violet for protons, adapted from [232].
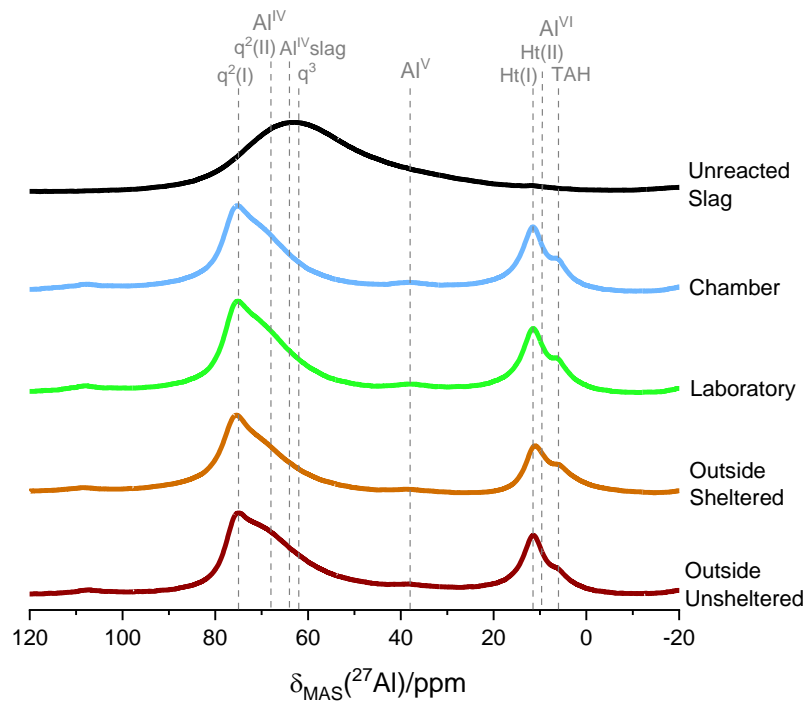
Figure 5.15: ^{27}Al MAS NMR spectra (11.7 T) of the non-carbonated regions of the samples exposed to 3 months of carbonation and of the unreacted slag.
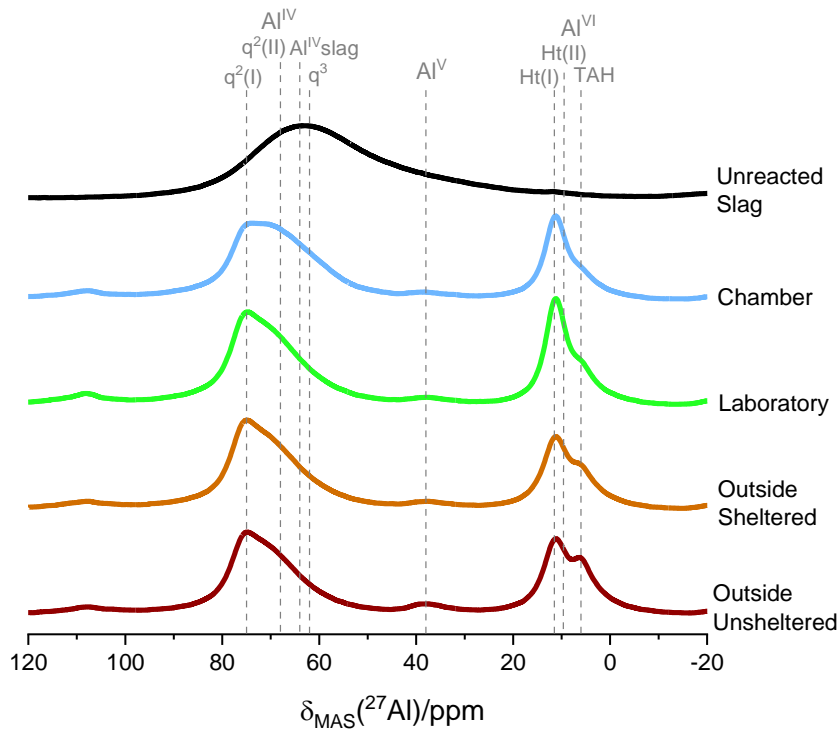
Figure 5.16: ^{27}Al MAS NMR Spectra (11.7 T) of the non-carbonated regions of the sample exposed to 12 months of carbonation and of the unreacted slag.

The ^{27}Al MAS NMR spectra of the carbonated parts of the samples, after 3 month and a year of exposure are presented in Figure 5.17 and Figure 5.18, respectively.

Hydrotalcite has the capacity to adsorb CO_2 in its interlayer [121,223]. After carbonation, the peak attributed to Al^{VI} is wider and has less intensity compared to the same peak in the data for the sample before carbonation. Bernal *et al.* [121] argue that this is due to the expulsion of aluminium and their replacement by carbonate. The presence of this broader peak might also be due to a higher disorder in the interlayer caused by the replacement of the OH- sites by the carbonates [225]. The sequestration of CO_2 in the hydrotalcite phases can result in the limitation of negative consequences of carbonation [118,121].

After carbonation, the peak attributed to TAH disappears. Similar observations have been made in the studies of Bernal *et al.* and Sevelsted *et al.*[109,121]. If the TAH peak is a bridging sites in the interlayer of the C-A-S-H gel and is balanced by the calcium cations, then the TAH should disappear after carbonation as the bi/carbonate ions react with the calcium cations, and the interlayer disappears once the aluminolicate gel is formed [113,231]. The aluminium in the TAH is most likely integrated in the tetrahedra q^3 or q^4 sites. The TAH peak has smaller

intensity in the non-carbonated part of the sample exposed to the rain outside, after 3 months, compared to the other conditions; this could be due to the significant reduction that leaching can cause in the ion concentrations. However, after a year of exposure the TAH peak is still present, even more intense than after 3 months. This result is inconsistent with the discussion presented above, and might be due to a rehydration of the slag, but it is very difficult to reconcile this finding with the results from other analysis, so it is unclear why this peak appears more prominent for this specific sample. Finally, it is also interesting to highlight that the non-carbonated part of the sample exposed inside for a year presents a peak with a low intensity for the TAH.

The Al^{IV} peak disappears after carbonation for all the samples. Instead, pentacoordinated aluminium sites are being incorporated into the aluminosilicate gel that is formed after the decalcification of the C-A-S-H gel [109,113].

Among the carbonated samples, only the samples exposed to carbonation inside in the laboratory and in the chamber for 3 months contains a visible peak for the $q^2(I)$ sites, even though this peak is significantly smaller than for the non-carbonated samples. The decrease of $q^2(I)$ sites is associated with a decrease of the calcium cations. The peak associated with $q^2(II)$ reduces significantly with the carbonation as well. This peak is higher for the both samples carbonated only 3 months inside in the laboratory and in the chamber. This result shows that, even if the XRD patterns show that crystalline calcium carbonate cannot be observed in these samples, the C-A-S-H has already started to carbonate, as the reduction of these sites means that the amount of ions in the interlayer has already started to be decreases, so the gel starts to be decalcify which leads to a more cross-linked gel. Therefore, the C-A-S-H gel is being decalcified before the formation of crystalline calcium carbonates, consistent with the discussion of ACC above. The large reduction of $q^2(I)$ and $q^2(II)$ for the other samples is linked with the decalcification of the C-A-S-H gel which leads to the formation a more crosslinked siliceous gel and the reduction of C-A-S-H gel within the samples [109,113,121,232].

For all the carbonated samples, the main [27]Al peak observed is an overlap of the Al^{IV} slag peak and the q4 peak, apart from the 3 months inside sample that shows a smaller q^4 peak compared to the q^3 peak. The Al^{IV} slag peak is caused by the aluminium sites still presents in the unreacted slag. The gel formed after carbonation has a structure close to the

aluminosilicate gel (N,K)-A-S-H formed by alkali-activation with low calcium precursors. According to Walkley et al. [233], this gel could be described as a highly cross-linked gel that contains "AlO_4^- and SiO_4 tetrahedra linked via bridging oxygen atoms, with a small number of terminal hydroxyl groups forming Q^3 sites"[233]. Similar observations have been made in previous studies on C-A-S-H carbonation [109,113,121]. It is important to highlight that the spectrum of the sample exposed to carbonation and efflorescence is similar to the ones exposed only to carbonation after a year. Conversely, the sample exposed to leaching and carbonation for a year has a higher q^4 peak than the other spectra at the same time, whereas at 3 months the intensity of this peak is smaller than the sample exposed to accelerated carbonation or to efflorescence. These results show that the gel formed is more cross-linked in the long term, if the carbonation is combined with soft water leaching.
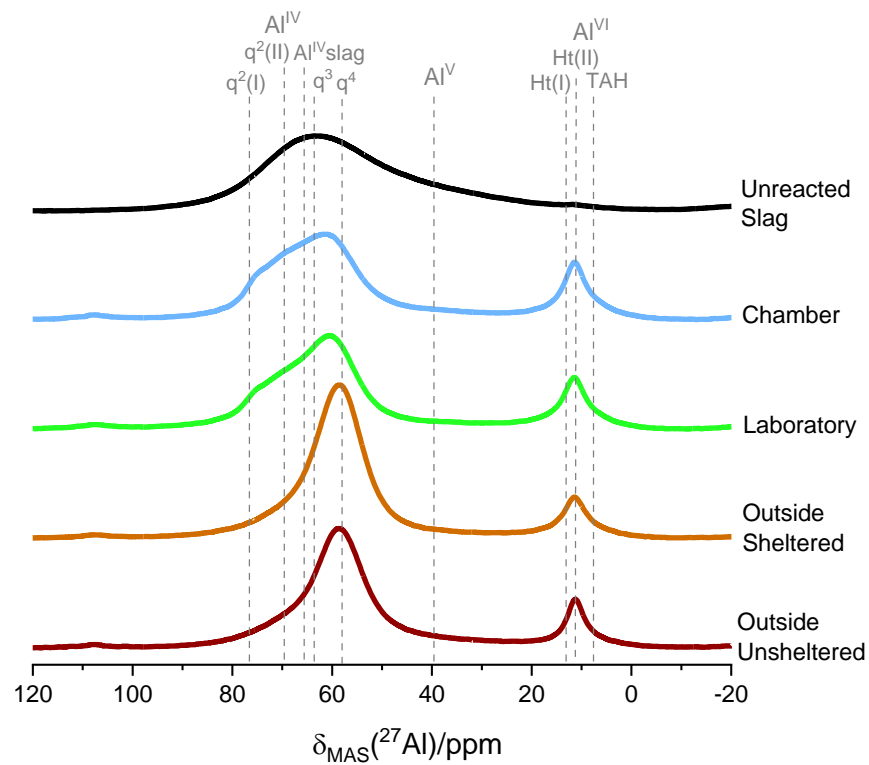
Figure 5.17: ^{27}Al MAS NMR spectra (11.7 T) of the carbonated parts of the samples exposed to 3 months of carbonation.
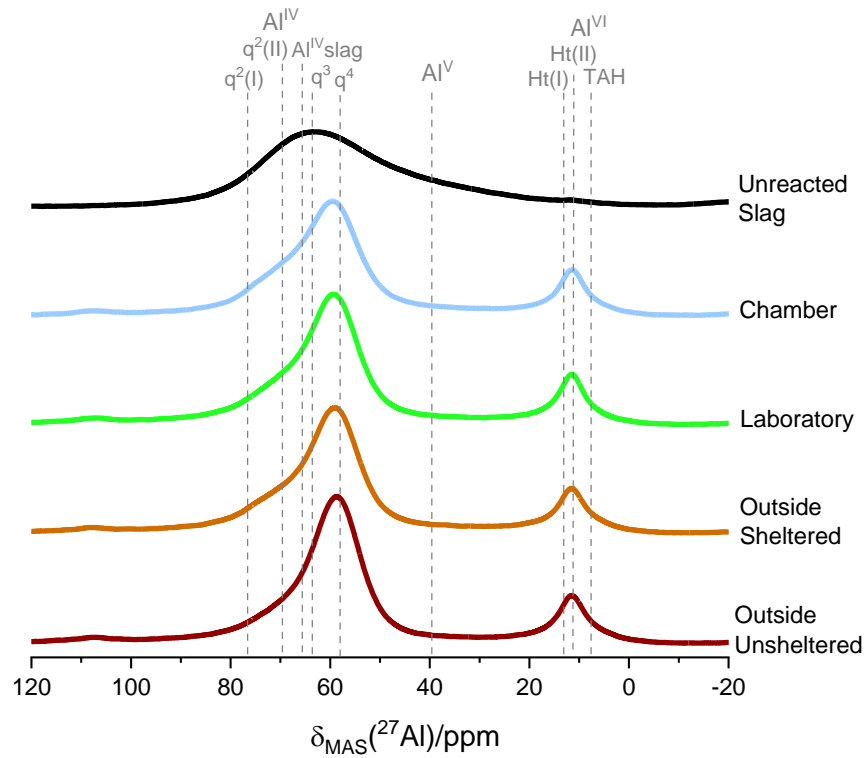
Figure 5.18: ^{27}Al MAS NMR spectra (11.7 T) of the carbonated parts of the samples exposed to 12 months of carbonation.

5.3.3.2 ^{29}Si MAS NMR

The ^{29}Si MAS NMR spectroscopy analysis has been performed on most of the samples at 3 months and 12 months, with some exceptions. The non-carbonated parts of the sample outside under the shelf and inside for 3 months have not been analysed, as the preliminary test done indicated that their structures were similar to the non-carbonated parts of the sample outside under the shelf and inside for 1 year. The non-carbonated part of the sample in the chamber exposed for a year has not been analysed as the preliminary test done indicated that the structure was similar to the non-carbonated part of the sample in the laboratory exposed for a year. To identify the unreacted slag in the deconvolution of the sample spectrum, the ^{29}Si MAS NMR data for blast furnace slag has been also analysed and deconvoluted. The slag has been deconvoluted using three Gaussian sub-peaks, the parameters for which are described in Table 5.1.

The first step to deconvolute the spectrum is to identify the potential Q sites present in the samples. To have a clear understanding of what each Q sites represent, a schematic of the Q

sites in the C-A-S-H gel as shown by Ortaboy *et al.*[110] is presented below. Each tetrahedral silicon atom, called a Q site, is denoted $Q^n(mAl)$, with n being the number of tetrahedral atoms this Si is bound to (in this work the sites can be Si or Al) and m the number of aluminium sites among these n sites. Consequently, n is between 0 and 4, while m is between 0 and n. When m is equal to 0, the Q sites will simply be denoted Q^n [229,234].
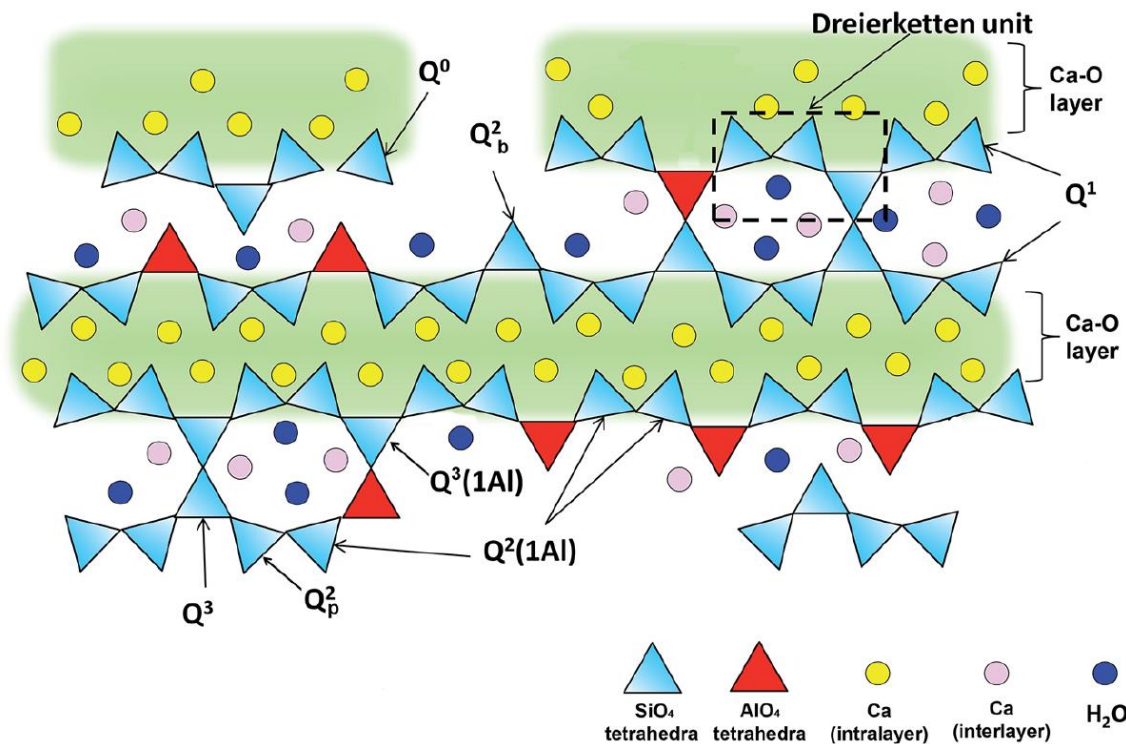
Figure 5.19: Schematic illustration of cross-linked and non-cross-linked C–(A–)S–H structures. Ca ions in the interlayer are charge-balanced by oxygens of the Si(Al)O₄ tetrahedral chains that are adjacent to the interlayer Ca, the oxygens that point to the interlayer Ca, protons, and partially by hydrogen bonds formed with water molecules, adapted from [110].
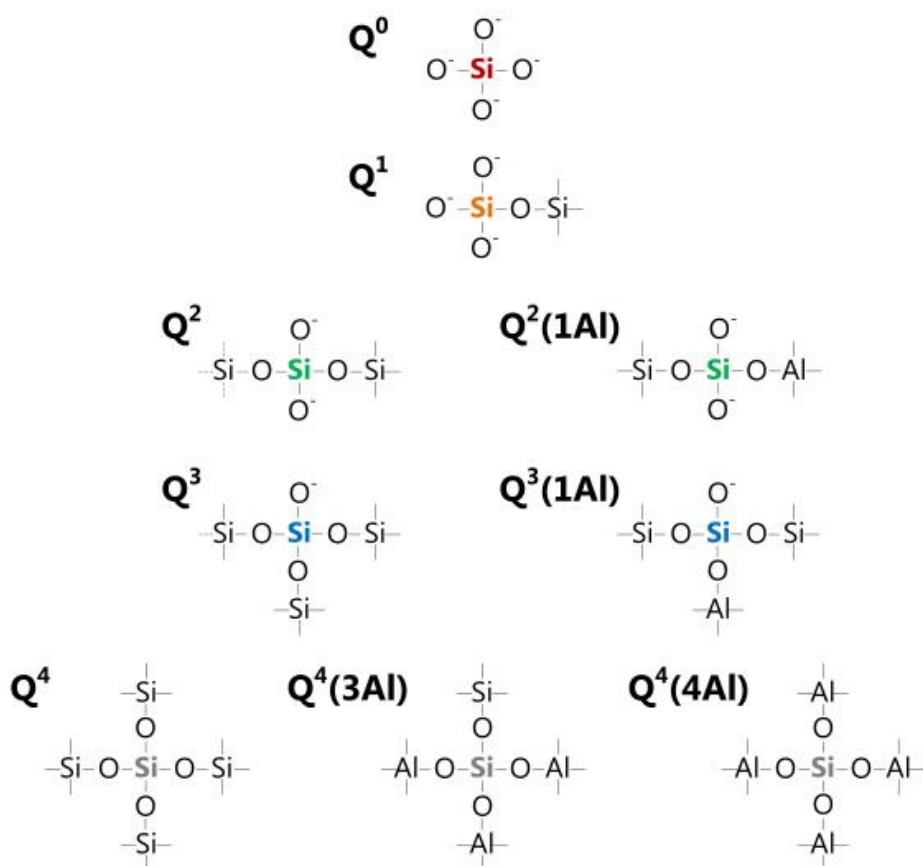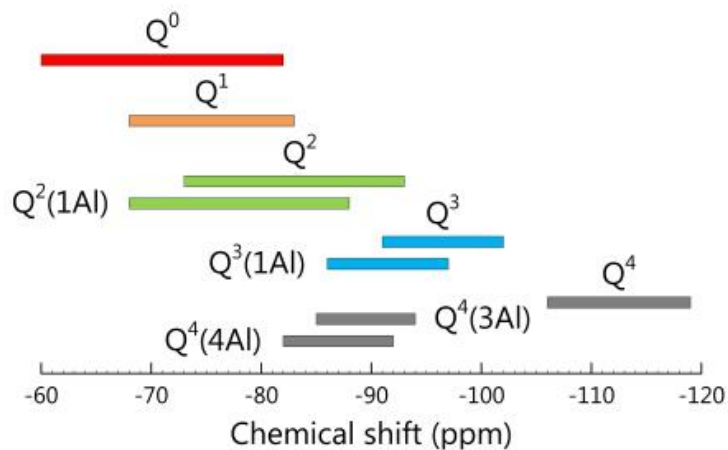
Figure 5.20: Q^n(mAl) notation and ^{29}Si NMR chemical shift range for the Q^n(mAl) sites presented in this study [234].

The second step is to deconvolute each spectrum using Gaussian curve fitting. In this study, this Gaussian curve fitting is conducted using an Excel spreadsheet. *Table 5.1* presents the full width at half-maximum (FWHM), isotropic chemical shift (δ_{iso}), and sites attributed for each Gaussian sub-peak used. Each peak has been identified using data from previous studies on similar systems [107,109,121,178,229,233,235,236]. The δ_{iso} of these peaks has then been

shifted no more than ± 5 ppm compared to that published in the literature, depending on the data obtained. The same peak δ_{iso} and FWHM values have been used for the same sites in all the spectra studied here, to be consistent and compare them, once the peaks have been clearly identified. The deconvulation does not include the $Q^2(2Al)$ and the $Q^3(2Al)$, as the peaks are consistent with the structural model used for C-A-S-H, the cross-linked substituted tobermorite model (CSTM) from Myers *et al.* [178,234]. The CSTM highlights that the presence of the $Q^1(1Al)$, $Q^2(2Al)$ and the $Q^3(2Al)$ sites occurs only when Al are presents in paired sites, which is not the case as the section 5.3.3.1 showed [178,234]. The peak at δ_{iso} = -87 ppm will contain contributions from both $Q^3(1Al)$ sites in the C-A-S-H gel and $Q^4(4Al)$ sites an alkali aluminosilicate hydrate (N-A-S-H) gel, consistent with previous studies [178,237]. In this study, this peak will be called $Q^3(1Al)$ + $Q^4(4Al)$ but it is important to highlight that this peak before carbonation will be mainly attributed to $Q^3(1Al)$, and after carbonation mainly to $Q^4(4Al)$. The amount of the other Q^4 peaks will give a good indication of the composition of this peak. Figure 5.21 presents for the non-carbonated part of the sample, exposed during a year in the laboratory, the ^{29}Si NMR spectrum as well as the fit of this spectra, with the addition of the Gaussian curves drawn on the same graph. Figure 5.22 shows the same data for the carbonated part of this sample.

Table 5.1: Position and FWHM of the slag and Q sites Gaussian sub-peaks used in all deconvolutions in this study

Name	Isotropic chemical shift (δ_{iso})	FWHM (ppm)
Slag 1	-60.6	11.9
Q^0	-74.2	3.5
Slag 2	-74.5	12.3
Q^1	-78.5	4.3
$Q^2(1Al)$	-81.5	4.3
Slag 3	-84.6	11.8
Q^2	-85	3.5
$Q^3(1Al) + q^4(4Al)$	-87.1	8.5
$Q^4(3Al)$	-93.5	8.5
Q^3	-97	8.5
$Q^4(2Al)$	-102	6
$Q^4(1Al)$	-107	5.5
Q^4	-113	12
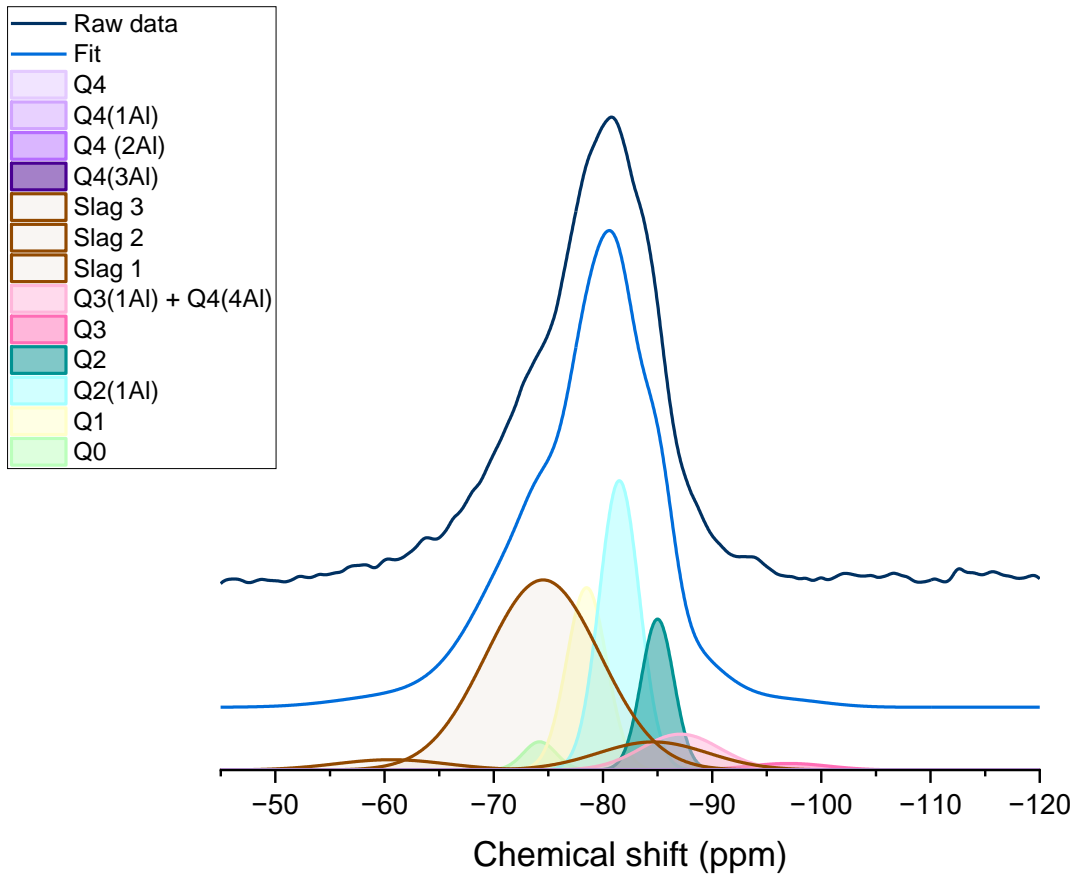
Figure 5.21: ^{29}Si MAS NMR spectrum (11.7 T) of the non-carbonated part of the sample in the laboratory for 12 months, with Gaussian deconvolution into sub-peaks as marked.
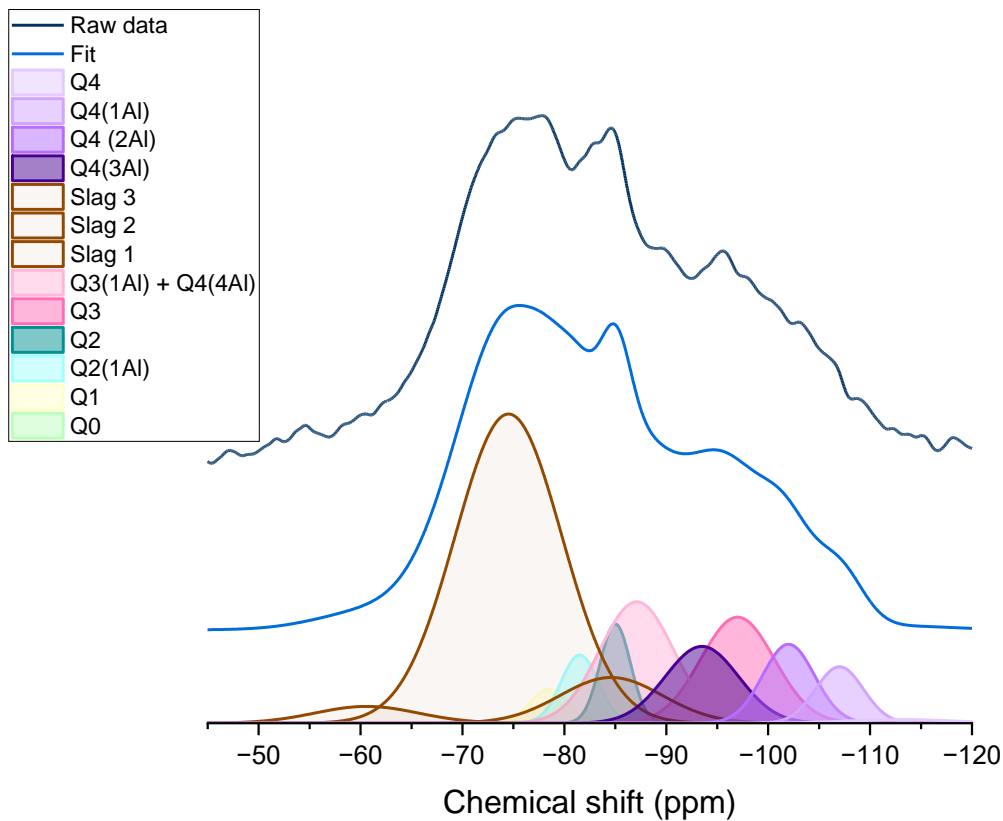
Figure 5.22: ^{29}Si MAS NMR spectrum (11.7 T) of the carbonated part of the sample kept in the laboratory for 12 months, with Gaussian deconvolution into sub-peaks as marked.

Table 5.2 shows the percentage of unreacted slag in each samples according to the deconvolution. Most of the samples contain 50% ± 10% silicon sites in the unreacted slag. The sample exposed to carbonated unsheltered during 12 months and the one sheltered carbonated contains a lower percentage of silicon sites in the unreacted slag, with respectively 29.5% and 35.9%.

Table 5.2: Amount of unreacted slag in each sample according to the ^{29}Si MAS NMR deconvolution

Exposure time	Samples	Unreacted slag content (%)
12 months	Chamber Carbonated	48.3
12 months	Laboratory Carbonated	52.0
12 months	Outside Sheltered Carbonated	50.0
12 months	Outside Unsheltered Carbonated	29.5
12 months	Laboratory Not Carbonated	48.9
12 months	Outside Sheltered Not Carbonated	39.5
12 months	Outside Unsheltered Not Carbonated	62.6
3 months	Chamber Carbonated	39.8
3 months	Laboratory Carbonated	56.4
3 months	Outside Sheltered Carbonated	35.9
3 months	Outside Unsheltered Carbonated	59.8

The distributions of the Q sites, normalised to the total of all silicate sites in the C-A-S-H gel, are presented in Figure 5.23 for the sample exposed for 3 months, and in Figure 5.24 for the sample exposed for a year.
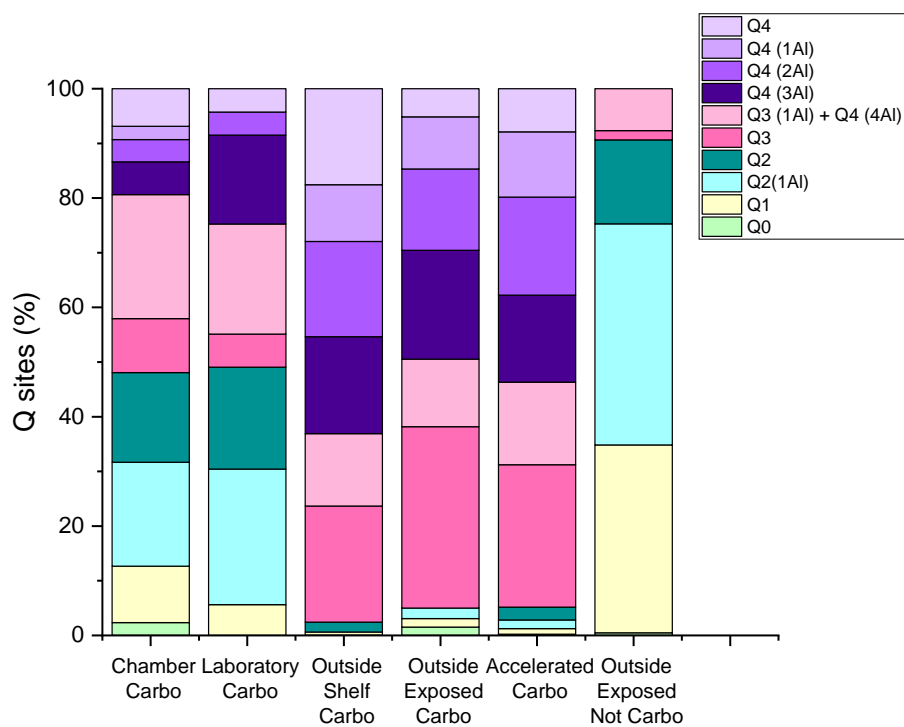
Figure 5.23: Q site distributions determined from deconvolution of ^{29}Si MAS NMR spectra for the samples analysed after three months. The uncertainty in the absolute site percentages is ± 2%.
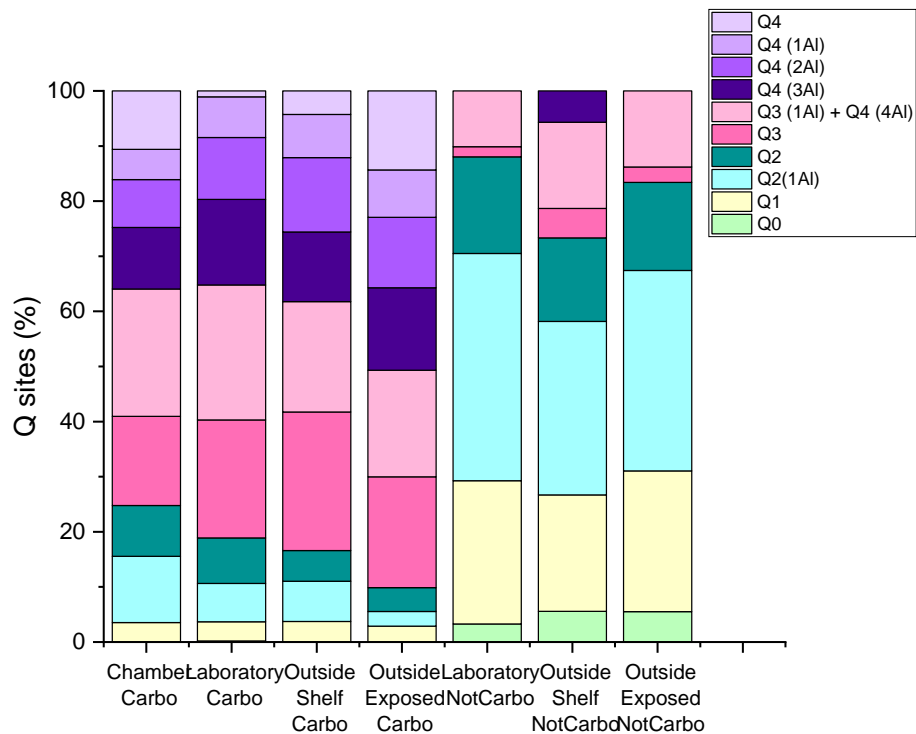
Figure 5.24: Q site distributions determined from deconvolution of ^{29}Si MAS NMR spectra for the samples analysed after 12 months. The uncertainty in the absolute site percentages is ± 2%.

Q^0 sites are identified in all the non-carbonated samples and in the carbonated samples exposed in the chamber and outside under the rain, exposed to carbonation for a year. This site is usually attributed to unreacted slag [107,238]. However, the unreacted slag has already been fitted and integrated in the deconvolution of the data, so this peak appears to be a reaction product. Even though the presence of this isolated hydrated silicate monomer has been observed in recent studies, its precise structure is unclear [121,178,227,229]. This Q site is present in a larger quantity in the non-carbonated sample. According to Gao et *et al.* [236] a high content of Q^4 sites is linked to a low content of Q^0. After carbonation, the amount of Q^4 sites significantly increases, probably leading to the decrease of the Q^0 sites and their integration into the carbonated siliceous gel in higher connectivity states.

The non-carbonated samples presented the Q sites that are usually observed in the cross-linked C-A-S-H gel usually: Q^1, Q^2, $Q^2(1Al)$, Q^3 and $Q^3(1Al)$. For all these samples the main peak is due to $Q^2(1Al)$, which represents between 31% to 41% of the total Q sites content. The non-carbonated samples present a small amount of Q^3 sites, less than 3 % except for the sample outside under the shelf for a year, which contains 5.4 % Q^3 sites. For the non-carbonated samples the "$Q^3(1Al) + Q^4(4Al)$" peak is proposed to be composed only of $Q^3(1Al)$ sites, as these spectra do not show the presence of Q^4 sites. The only exception is the sample sheltered, that contains 5% $Q^4(3Al)$ sites, which indicates that the $Q^3(1Al) + Q^4(4Al)$ peak probably contains contributions from both site types in this instance. The presence of $Q^4(3Al)$ and $Q^4(4Al)$ sites may indicate that the efflorescence is affecting the C-A-S-H that is not carbonated. These Q^4 sites are most likely situated in the aluminosilicate gel that forms after the decalcification of the C-A-S-H gel [113,178].

The sample that have not been carbonated or subjected to efflorescence-causing conditions have a content of $Q^3(1Al)$ between 8% to 17%. This ratio is just slightly less than half of the amount of $Q^2(1Al)$. To simplify the discussion, it is assumed that despite respecting exactly the limitation for the cross linked model of C-A-S-H in the "cross-linked substituted tobermorite model" (CSTM) developed by Myers et al., the C-A-S-H in this study could still be modelled according the non-cross-linked tobermorite model in the CSTM [234].

The Al/Si ratio, the Ca/Si, the Ca/(Al+Si) ratio, the main chain length (MCL), the parameter α and the parameter δ, as defined in the CSTM for the cross-link C-A-S-H developed by Myers *et al.* are presented in Table 5.3 [178].

Table 5.3: Al/Si ratio, the Ca/Si, the Ca/(Al+Si) ratio, the main chain length (MCL), parameter α, parameter δ, as defined in the CSTM for the cross-linked C-A-S-H developed by Myers et al. [178]

Exposure Time	Samples	MCL	Al/Si	α	δ	ω	Ca/Si	Ca/(Al+Si)
12 months	Chamber Carbonated	98.5	0.36	1.66	0.06	0.25	0.98	0.72
12 months	Laboratory Carbonated	102.7	0.38	1.72	0.06	0.25	1.00	0.72
12 months	Outside Sheltered Carbonated	87.8	0.32	1.54	0.07	0.25	0.96	0.72
12 months	Outside Unsheltered Carbonated	113.4	0.40	1.76	0.05	0.25	1.01	0.72
12 months	Laboratory Not Carbonated	16.4	0.10	0.75	0.33	0.25	0.88	0.79
12 months	Outside Sheltered Not Carbonated	19.8	0.18	1.13	0.28	0.25	0.92	0.78
12 months	Outside Unsheltered Not Carbonated	17.0	0.14	1.00	0.31	0.25	0.91	0.79
3 months	Chamber Carbonated	39.1	0.29	1.50	0.15	0.25	0.96	0.74
3 months	Laboratory Carbonated	67.8	0.27	1.35	0.09	0.25	0.92	0.73
3 months	Outside Sheltered Carbonated	344	0.36	1.60	0.02	0.25	0.97	0.71
3 months	Outside Unsheltered Carbonated	157	0.25	1.24	0.04	0.25	0.90	0.72

The results obtain in Table 5.3 for the non-carbonated samples are coherent with the literature [147,178,227]. However, the results are not coherent for the carbonated regions of the samples. Indeed, the MCL values are longer than the MCL in the literature results, and the

Al/Si ratios are too high [147,178,227]. These results are due to the presence of aluminosilicate gels following the carbonation. As the C-A-S-H gel is decalcified, the aluminosilicate is formed. The CSTM can describe only C-A-S-H gel and not aluminosilicate gel. Consequently, this model is inappropriate to describe the gel composition after carbonation, but the fact that the non-carbonated samples give coherent values can bring further confidence in the validity of the deconvolutions presented here.

The carbonated samples showed the conventional C-A-S-H Q site types in smaller quantities compared to the non-carbonated samples. The amount of Q^1, $Q^2(1Al)$, Q^2 and Q^3 sites was between 55%, for the less carbonated samples, to 30%, for the most carbonated samples, of the total Q sites. Conversely, for the non-carbonated samples these represent between 70 and 90% of the total Q sites. The proportion of Q^3 sites is considerably increased. These Q^3 sites could be part of the C-A-S-H gel, or of the silicate gel formed by the decalcification of the C-A-S-H gel. The proportion of Q^4 sites increases significantly, as does the proportion of the $Q^3(1Al)$ + $Q^4(4Al)$ peak. The composition of this peak cannot be determined exactly for the non-carbonated material, however, the presence of Q^4, $Q^4(1Al)$, $Q^4(2Al)$ and $Q^4(3Al)$ sites together indicates that this peak is very likely to also contain some $Q^4(4Al)$ sites. The presence of q^3 and q^4 sites identified by ^{27}Al MAS NMR is coherent with the increase of the Q^4 and Q^3 sites found via ^{29}Si MAS NMR [229]. The increase of these aluminosilicate gel sites shows that the gel is more cross-linked after carbonation,[237] with the formation of a highly cross-linked silicate gel composed of Q^3 and Q^4 sites and with extensive Al substitution [109,113].

The samples exposed to carbonation inside present a similar structure. The evolution of the effect of the carbonation after 3 months and then a year is clear. After 3 months, the samples contain between 20-25% $Q^4(mAl)$ sites (with m equal to 0,1,2 or 3), while the amount of these sites after a year is about 45%. Similarly, the amount of Q^1, $Q^2(1Al)$ and Q^2 significantly decreased: it is between 48-50% after three months, but after a year is between 20-25%. These results show that the C-A-S-H is more cross linked due to the decalcification of the gel, and the presence of Q^4 sites shows that the silicate gel already started to form after 3 months. The XRD patterns of these samples show almost no trace of crystallised calcium carbonate, and the TG-MS shows a mass loss that could be most likely attributed to amorphous calcium carbonate. Even though the hydrotalcite seems to have absorbed some CO_2, according to the ^{27}Al MAS NMR and XRD, in the light of this experiment, it is now evident that the CO_2 reacted

also with the C-A-S-H gel and leads to the formation of amorphous calcium carbonate that will later transform into crystalline calcium carbonate as the 12 months sample results show. The study of McCaslin and White [123] highlighted a similar process at 100% CO_2, but it has not been observed in this way under natural conditions before.

The spectrum of the carbonated sample outside under a shelf after 3 months shows almost no trace of C-A-S-H gel, with almost no Q^1 and Q^2 sites. However, after a year, the spectrum presents some Q site types associated to the C-A-S-H gel. The difference is probably due to the uncertainty in spectral deconvolution, as it is about 2%, so it falls into the uncertainty detection limits. The same conclusion can be drawn from the difference between the samples exposed to the weather after a year and three months. It is also important to highlight that the carbonated part of the sample exposed to efflorescence and carbonation presents similar results to the samples inside after a year. Consequently, it appears from these results that efflorescence does not change the effect of carbonation on the C-A-S-H gel.

The spectrum of the carbonated part of the sample from outside exposed to the rain show similar results to the carbonated sample inside after a year, with a slight difference: the amount of $Q^4(mAl)$ sites (with m equal to 0,1,2 or 3) is higher. It shows that the C-A-S-H gel has been more decalcified when the sample has also been exposed to soft water leaching, leading to the formation of a higher amount of silicate gel. The removal of the ions (calcium and sodium in this study) from the interlayer by the soft water leaching might be responsible for the acceleration of the carbonation process. Studies on metakaolin-based AAM have shown that leaching is removing weakly bonded ions, so the mechanism may be similar for slag based AAM [159].

5.4 Conclusion and Discussion

The carbonation of alkali-activated slag binders has a considerable impact on the binder structure, even though the process is slow. The results of the carbonation after a year provided some points of information that reinforce the results of past studies:

- The C-A-S-H is decalcified by the CO_2 to form calcium carbonate, which then increases cross-linking in the residual C-A-S-H gel and leads to formation of a highly cross-linked silicate gel;

- Calcite and vaterite are the two main calcium carbonate polymorphs formed;

- Hydrotalcite, the secondary hydration product, absorbed some of the calcium carbonate;

- The third aluminate hydrate disappears after carbonation;

- The charge balancing aluminium cations situated in the C-A-S-H gel interlayer, called Al^V, are incorporated in the silicate gel formed during the carbonation.

The results also bring some new elements towards the understanding of the carbonation process:

- The formation of aragonite seems to be dependent on the conditions of carbonation, probably facilitated by a relatively higher temperature;

- The decalcification of the C-A-S-H is followed by the formation of a transient product that is identified in this study as amorphous calcium carbonate. The process has been observed under accelerated carbonation by McCaslin and White [123], but never under natural conditions. This product is only present after 3 months of carbonation and then disappears while crystalline calcium carbonate appears. A deeper analysis with ^{13}C MAS NMR or Raman analysis could help to confirm this result.

- The TAH disappears following the carbonation because its concentration is linked to the sodium and calcium cations, which reacts with the bi/carbonate ions during the carbonation process.

This study reveals that the efflorescence under real service conditions leads to the formation of deposits composed of hydrated forms of calcium carbonate and sodium carbonate as well as gaylussite. The effects of efflorescence combined with carbonation are similar to the effect of carbonation alone on the carbonated part of the sample, with the formation of calcium carbonate with calcite as the main polymorph. The main finding of this study is that efflorescence causes the partial decalcification of the C-A-S-H gel and the formation of a small amount of aluminosilicate gel, in the part of the sample that is not carbonated.

Finally, when the carbonation is combined with soft water leaching, the carbonation process is slightly different from when carbonation is the only mode of attack. The non-carbonated parts of the sample remain unaffected by the carbonation. Conversely, the C-A-S-H gel is more

cross-linked than solely under carbonation. The main calcium carbonate polymorph formed after a year is not calcite, as it is in the other environments, but vaterite.

Chapter 6 : Evolution of the oxidation and carbonation fronts.

6.1 Introduction

Carbonation of slag based AAMs has been reported to result in harmful consequences on the mechanical properties [93,108,111–113]. Conversely, the oxidation of the sulphur in these materials seems to only alter its colour. These two processes are closely related as they are driven by the diffusion process of gases entering from outside the material, and consequently could be linked. Very few studies have explored the sulphur oxidation process in alkali activated slag materials [20,239,240], and to date no studies have reported the relationship between the carbonation and the oxidation processes on slag based AAM. In this study, samples have been exposed to both phenomena for a year of indoor exposure. Another pair of samples has also been exposed for three months and a year to the combined attacks of soft water leaching and carbonation; and to the combined attacks of efflorescence and carbonation. These samples, which were exposed outside, were oxidised as well. The reaction fronts and the chemical compositions have been observed.

6.2 Experimental protocol

6.2.1 Samples

The samples used in this chapter are the same samples used in Chapter 5. To understand accurately the carbonation and oxidation fronts, cement paste is used, as the carbonation and oxidation reactions mainly happen in cement paste between the aggregates and the sand grains. Each sample was cast as 50 mm cubes according to the mixing parameters described in Chapter 3. After casting, the samples were cured sealed for seven days in an atmosphere at 100% RH, but not in water to avoid leaching the alkali ions out. Once cured, three cubes were placed in each carbonation condition.

6.2.2 Carbonation conditions

To observe the effects of the combined attacks on the oxidation and carbonation fronts, the samples were exposed to several carbonation environments for three months and a year. These environments were chosen to be as close as possible to on-site conditions. The first set of samples was inside in the laboratory, so exposed to carbonation and oxidation. The second set of samples was inside in a climate chamber at 20 ± 0.5^{o}C, so exposed to carbonation and oxidation as well. The third set of samples was outside exposed to the rain on a plastic support, so exposed to carbonation, oxidation and soft water leaching. The fourth set of samples was outside protected from the rain by a shelf and dispose on a wood support, so exposed to carbonation, oxidation and efflorescence. The evolution of the ambient relative humidity, temperature and rainfall for the third and fourth conditions are described in section 5.2.2.

6.2.3 Methods

After the end of the exposure period, the samples were removed from their environments and were split in half. The change of colours of their inner surfaces revealed the oxidation front, so these surfaces were photographed. These surfaces were then sprayed with a phenolphthalein solution to reveal the carbonation front. The results obtained in this chapter on the carbonation and oxidation fronts for one year and three months are similar, except for the two first sections. To avoid repetitions, only the sections associated with the phenolphthalein tests and the photography of the cubes opened present the three months samples, in this chapter. In the XRD, SEM-EDS and synchrotron experiments, only the year-old samples are presented.

After being split the samples were carefully broken into smaller pieces that still contain the carbonation or/and the oxidation fronts. The free water in the samples was then removed via the isopropanol solvent exchange method. To confirm that the change of colours was not due to a change of composition, XRD analysis was performed on the blue and white parts that were not carbonated. The microstructure evolution of the reaction fronts was then observed by SEM-EDS and μ-XRF mapping. The evolution of sulphur oxidation states of the samples tested by μ-XRF mapping was observed by performing sulphur K-edge XANES measurements on several points, taken at 0.5 mm difference from each other along a straight line, which

went from the carbonated part to the non-oxidised part, as *Figure 6.1* shows. Each of the methods used in this chapter is described in detail in the Chapter 3.
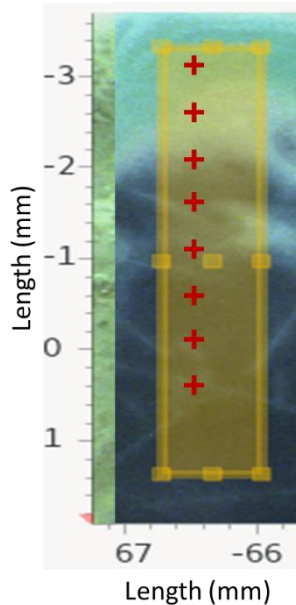
Figure 6.1: Representation of the XANES scans and µ-XRF mapping conducted on the oxidation and carbonation fronts of the sample exposed to rain outside for a year. The µ-XRF map taken is represented by the yellow rectangle, while the XANES scans are represented by the red cross.

6.3 Results and Discussion

6.3.1 Carbonation depth measurements

6.3.1.1 Oxidation fronts

One sample exposed to each of the conditions has been split in two after 3 months, and then another one after a year. Once the cubes opened, several colours appear inside the samples. Figure 6.2 shows the inside surfaces of these samples, and it can be noticed that the samples exposed inside present a large amount of visible cracks. These cracks are most likely due to drying shrinkage as these samples were in low humidity environments, as explained in the section. This reaction is due to the water loss caused by the exchange with the exterior [138]. Therefore, it is linked to the pore structure of the samples at early age, because they are exposed as early as 7 days. Drying shrinkage could be limited by using sand and aggregates to produce mortar or concrete, rather than the pastes used in this chapter. Other factors can help reducing the drying shrinkage such as decreasing the water:binder ratio, decreasing the

amount of activators or curing under sealed conditions for a longer time [67,91,241–243]. The presence of these cracks may lead to a misrepresentation of the carbonation or oxidation rate measurements, so the measurements of these depths will not be presented for paste samples. In this chapter, using paste samples enable to study of the evolution of the microstructure, without the noise due to the quartz in the aggregates.
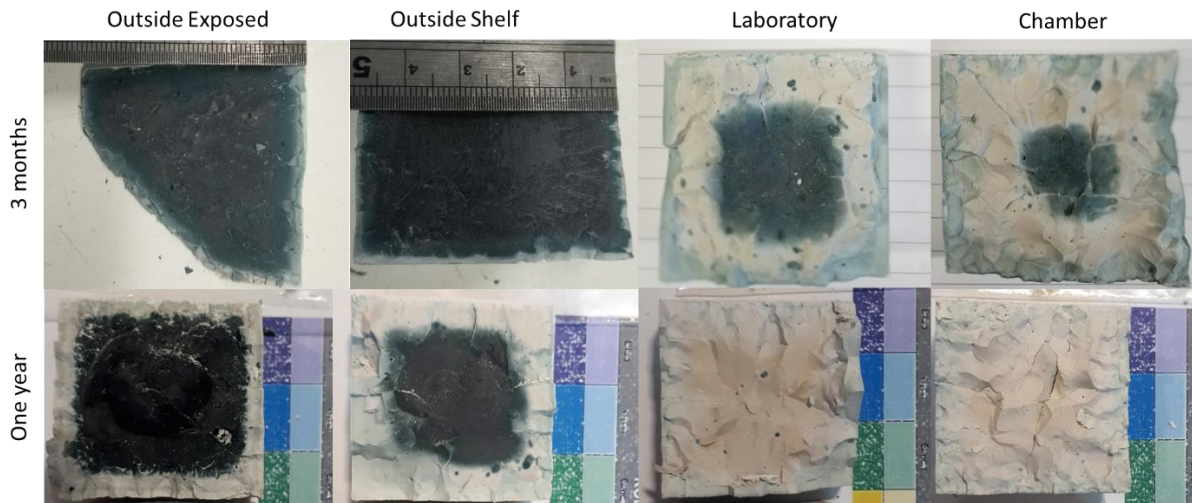
Figure 6.2: Pictures of the samples cut after 3 months and 12 months in the different conditions. The 12 months samples present a colour scale to correlate the lighting conditions between images.

Table 6.1: Name attributed to each colour, as well as oxidation and carbonation states associated, as determined in this chapter.

Picture	Colour	Carbonated	Oxidised
	Grey-White	Yes	Yes
	Yellow-White	No	Yes
	Light-Blue	No	Front
	Blue	No	No
	Dark-Blue	No	No

143

The Table 6.1 is the colour definition tables, with the abbreviations associated to each colours, as well as their carbonation and oxidation fronts, as proven in this chapter. The exterior of all of the samples present a grey-white layer. Then, a yellow-white colour is present in the middle layer of the samples inside after 3 months and the samples outside after a year. The same colour is present as an interior layer for the sample inside after a year. Finally, the interior layers of all the samples, except the one kept inside for a year, are blue. It is also interesting to notice that the exterior of this part is lighter, while the interior tends toward a dark-blue colour. Several blue spots can be observed in all these layers, even if they are less noticeable in the darker layers. According to Chaouche *et al.* the darker parts correspond to the non-oxidised parts and the white parts to the oxidised parts, as the sulphur present from the slag changes colours when it reacts with the oxygen [20]. The darker blue spots might be due to the presence of iron [240,244,245]. These theories will be investigated in the following sections of this chapter with the help of sulphur K edge XANES analysis. In the next paragraph, it will be assumed that the colours are due to the oxidation of the sulphur, which will be proven in the last sections of this chapter.

The 12 months old samples kept inside have no dark coloration, which leads to the conclusion that these samples are entirely oxidised. The oxidation might have been facilitated by the presence of cracks in the samples. The sample kept in the chamber presents a higher level of cracks compared to the one in the laboratory, which is most likely due to the lower relative humidity in the chamber, which is 30 ± 2%, compared to the one in the laboratory, which is 35 ± 15%. Consequently, the sample inside in the chamber after 3 months has a larger grey-white layer than the one in the laboratory. The samples kept outside for a year have almost no white parts, which means that the oxygen has not entered and reacted with the interior of these samples. The high relative humidity might have led to a lower amount of capillary pores being available for the oxygen to enter the sample. After a year, the sample kept outside under the rain has a smaller grey-white layer compared to the one protected from the rain. Conversely, after a year, both samples outside present a grey-white layer situated on their exterior.

6.3.1.2 Carbonation front

The samples opened have been sprayed with a phenolphthalein solution, and the results of this experiment are presented in the figures below. The first observation is that, contrary to what is observed for PC systems, the phenolphthalein solution is never colourless. Different shades of pink can be observed: light pink close to the sample surface and darker pink in the middle of the samples. The carbonation process leads to a pH reduction [100,213]. The phenolphthalein is colourless at a pH of 9 and bright pink at 12, and between this, the more the pH decreases, the less pink the phenolphthalein is [246–248]. Consequently, it is assumed that, in this study, the lighter pink areas correspond to the carbonated parts, while the darker parts correspond to the non-carbonated parts. These results show that the pH does not drop as drastically as it does in Portland cementitious materials, as Bernal *et al.* predicted [100].

The lighter pink areas after phenolphthalein spraying correspond to the grey-white layers observed in the section above. The yellow-white areas become dark pink, as do the darker areas. As the darker areas are already dark in colour, the phenolphthalein seems darker in these areas than in the yellow-white one, which is a just an inherent difficulty of using colour changing indicators to describe changes in materials that are already dark coloured. Consequently, it is seen that the change of pH does not correspond to the oxidation front, which indicates that the carbonation front differs from the oxidation front if it is assumed that the change of pH corresponds to the carbonation front. XRD and SEM analysis will be performed in the following sections to confirm that these two fronts are not the same.

In Figure 6.3, the sample exposed outside to the rain for 12 months is colourless after the phenolphthalein test. This may be due to the soft water leaching which leached out the alkalis from the pore solution as the SEM-EDS results in section 6.3.3.2 confirmed. It leads to a lower pH than in the carbonated parts of the other samples, where the reduction of pH is only due to the carbonation of the pore solution.

The carbonation depth is deeper for the sample inside than the sample outside. The carbonation depth is deeper for the sample in the chamber than the sample in the laboratory, due to the larger amount of cracks that lead to a higher diffusion of CO_2.
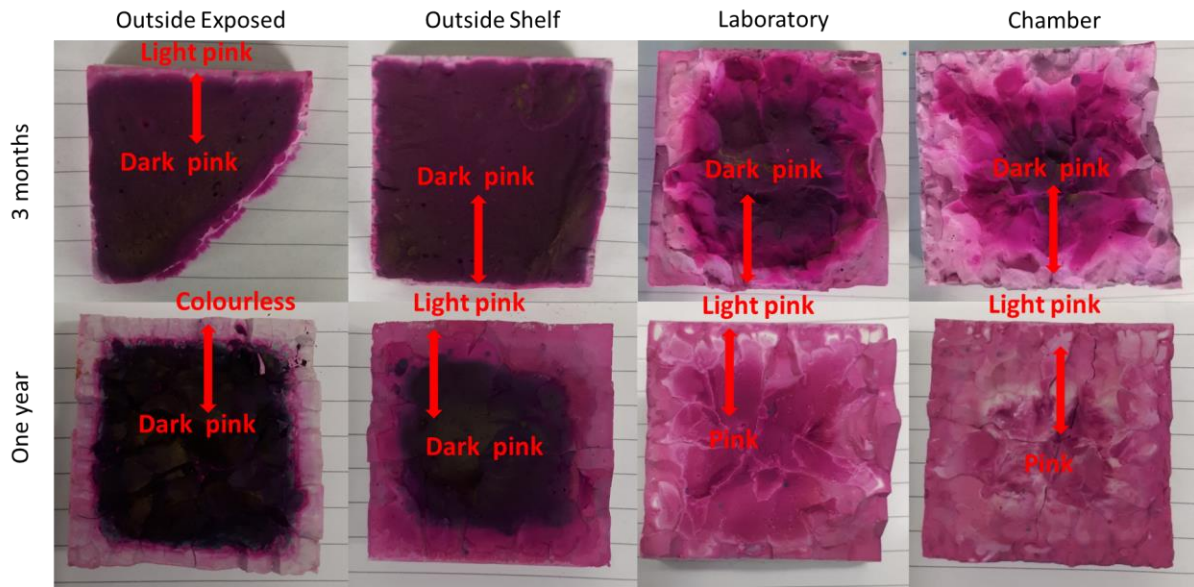
Figure 6.3: Surfaces of the 3 months and 12 months old cubes, exposed to different conditions, sprayed with 1% phenolphthalein solution.

6.3.2 X-ray diffraction analysis

To confirm the differences between the two non-carbonated areas, the yellow-white and the blue-dark ones in each sample, XRD analysis has been performed on the 3 months samples that displayed both of these regions. The XRD patterns of the blue-dark parts of the outside and inside samples are presented in Figure 6.4, as well as the XRD patterns of the yellow-white parts of the inside samples. The PDF numbers of the phases identified is presented in Table 3.2 in the Chapter 3. These patterns clearly show the presence of the two hydration products of slag based AAM, hydrotalcite and C-A-S-H gel [53,237]. Portlandite can be observed in the yellow-white samples in the laboratory and in the blue-dark samples outside exposed to the rain. The presence of portlandite is most likely due to the solvent exchange method conducted on the sample before the test, as explained in the previous chapter. The patterns of the yellow-white samples and the one of the blue-dark samples are similar. The oxidation of the sulphur only changes the oxidation state of the sulphur so it is not detectable by XRD. To observe the change in the sulphur oxidation state, a more powerful technique such as S-K edge XANES is necessary. These similarities confirm that the change of colours is most likely related to the sulphur oxidation, as observed in previous studies on similar systems [20,239,240]. Moreover, no trace of calcium carbonates or sodium carbonates can be

observed in the XRD patterns. Hence, despite being oxidised, the yellow-white regions of the samples are not carbonated.
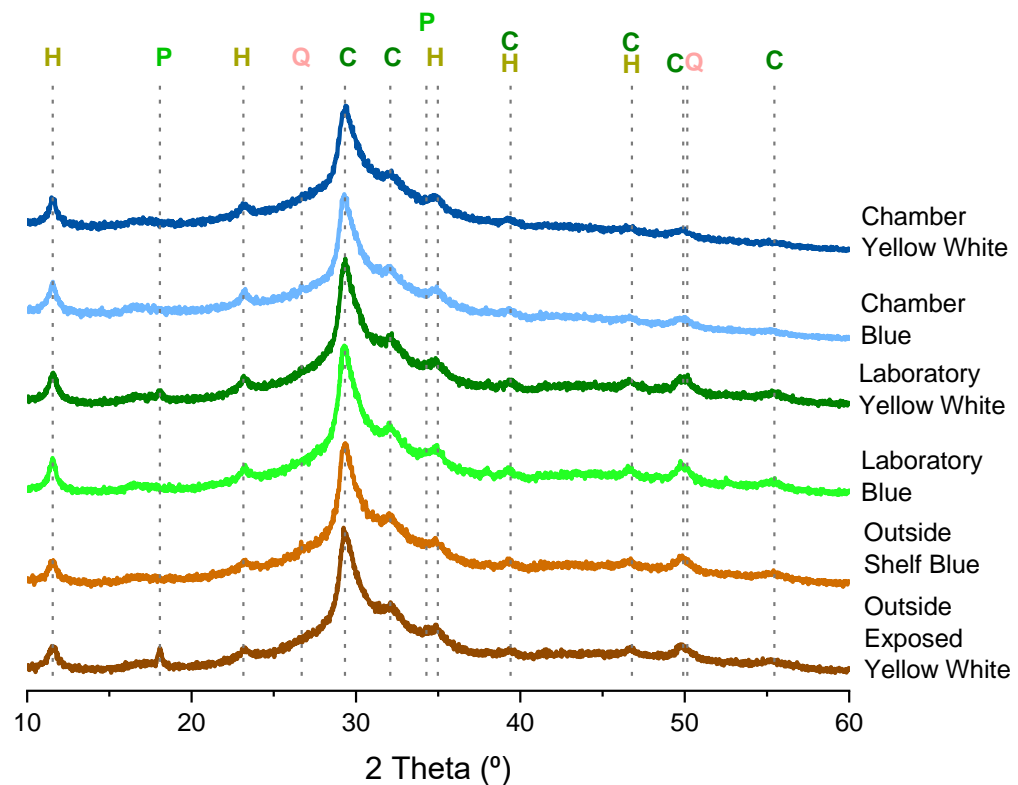
Figure 6.4: X-ray diffractograms of the blue and yellow-white non-carbonated regions of samples.

6.3.3 Scanning electron microscopy analysis

6.3.3.1 Images of uncarbonated samples

Backscattered electron (BSE) images, secondary electron (SE) images and elemental maps obtained by Energy Dispersive X-ray Spectrometry (EDS) of the non-carbonated parts of the samples were taken. The BSE and SE images are presented in Figure 6.6 . The EDS maps of the samples exposed outside, and protected from the rain, are respectively presented in Figure 6.7 and Figure 6.8. The non-carbonated parts of the samples exposed inside were both similar, so only the EDS maps of the sample held in the chamber is presented in Figure 6.9.
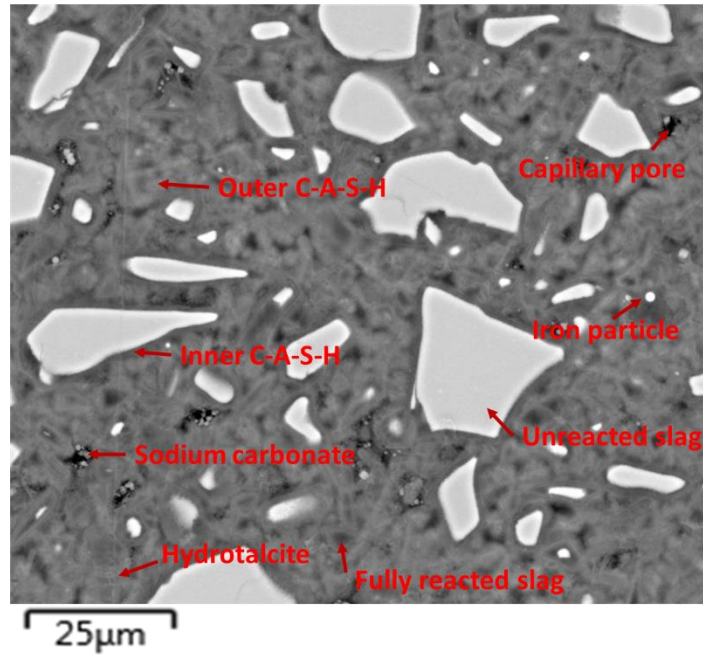
Figure 6.5: Backscattered electron image of the non-carbonated part of the sample exposed to the rain outside, with key phases and features identified.
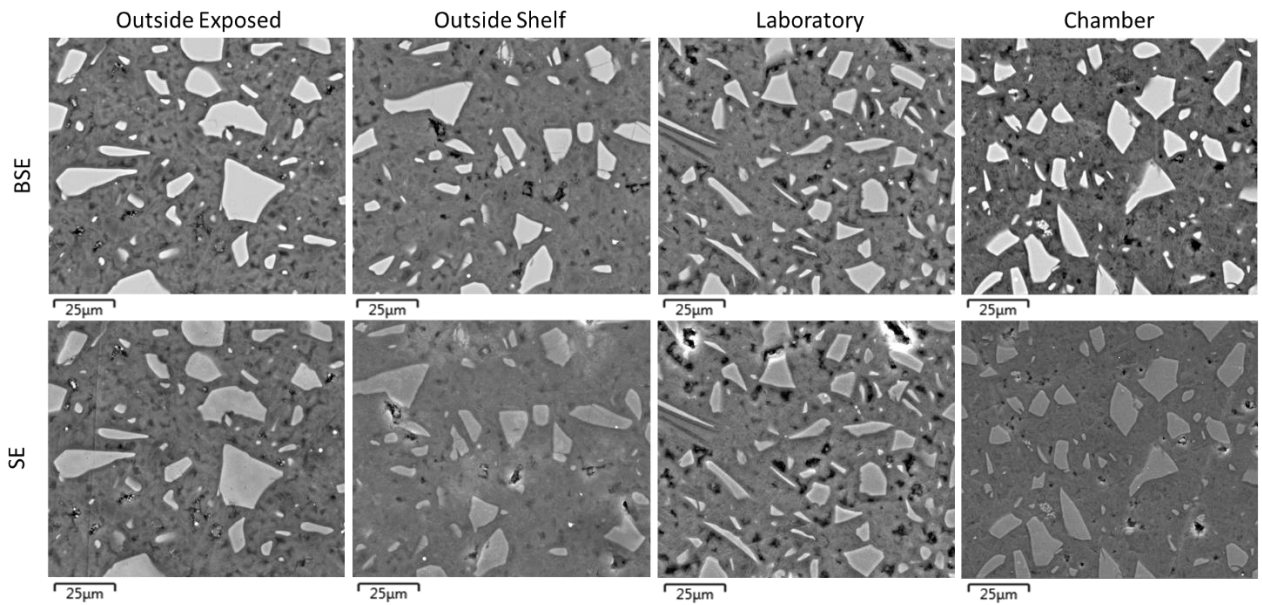
Figure 6.6: Backscattered electron images and secondary electron images of the non-carbonated samples which are in the blue parts, exposed to different environments for a year.

Figure 6.7: Elemental maps and backscattered electron image of the non-carbonated parts of the sample outside exposed to the rain for 12 months.

Figure 6.8: Elemental maps and backscattered electron image of the non-carbonated parts of the sample outside protected from the rain for 12 months.

Figure 6.9: Elemental maps and backscattered electron image of the non-carbonated parts of the sample kept inside in the laboratory for 12 months.

Angular lighter grey particles can be observed in all the micrographs. As Figure 6.5 shows, these particles correspond to unreacted slag particles [249]. According to the EDS maps, these particles are composed mainly of calcium, silicon, magnesium and aluminium. The composition of the unreacted slag has been evaluate by EDS as well, and is similar to the XRF composition. Fully hydrated particles (called reacted particles in Figure 6.5 Figure 6.5) are present as well, these are a darker shade of grey with an angular form [249,250]. These particles have a high content of magnesium according to the Mg elemental maps. Small crystalline pellets that are lighter grey can be observed in between the unreacted slag particles; these platelets are hydrotalcite [53]. Some small circular particles that are bright white are observed as well. According to the Fe elemental maps, these particles are iron particles from the slag [245]. In between the unreacted slag particles, a less dense light grey phase, lacking distinct morphology, is observed. This phase is the outer C-A-S-H gel. A layer of darker grey product, that contains a higher amount of magnesium, is observed around each of the unreacted slag particles, which is inner C-A-S-H gel according to previous studies [50,53,250]. These particles are slighter richer in sodium than the outer C-A-S-H, as the Na elemental maps shows [53,251]. However, it is hard to distinguish it, as the sodium carbonate

150

present in the capillary pores is highly concentrated in sodium, and dominates the ability to view any change of sodium concentrations in the rest of the sample. The sodium carbonate particles are mainly formed in the capillary pores, which appear black in these images. This phase is crystalline, and comes from the efflorescence of the sodium in the pore solution, between the sample preparation and the SEM analysis, as there are no traces of sodium carbonate in all the other analysis (XRD and TG-MS). To avoid the formation of this phase, the sample should be analysed just after being polished. However, in this case it was not possible to do this due to time and instrument availability constraints [159].

The sodium distribution in the samples carbonated inside, and outside sheltered, present high amounts of sodium within the pores due to the formation of sodium carbonate during sample preparation and storage. The sample outside sheltered present a slightly different sodium distribution: larger amount of sodium are present around some unreacted slag particles. The differences between the sodium distributions in the samples might be due to the larger-scale efflorescence which has already removed the sodium form the pore solution in the sheltered sample.

The samples exposed inside present a larger amount of capillary pores. In these same samples, a larger amount of unreacted slag can be observed, which leads to the conclusion that the inside samples, according to these micrographs, have a lower degree of hydration than the outside samples. This lower amount of hydration is most likely due to moisture removed from the indoor samples. The amount of porosity decreases when the degree of hydration increases, so these samples might present more capillary pores due to their higher amount of unreacted slag [53,249,250]. It is important to highlight that one micrograph of one sample is not enough to affirm that the degree of reaction is definitely lower for the samples inside, as it should be done a minimum of 20 images, and ideally 50-100 images to evaluate the degree of hydration [177], but it is representative of the areas observed in these precise samples.

In the secondary images of some samples, a white "phase" can be observed around some of the capillary pores, this "phase" is just the electron charging on the pores. To avoid this, a lower voltage could have been used, but this would have come at the cost of the ability to see some of the differences between the phases as clearly with a lower voltage, hence this choice of voltage [177].

6.3.3.2 Oxidation front images

The micrographs of one colour front are presented on Figure 6.10. To locate the colour front, several dots of ink have been placed on the sample. One of these dots can be observed on the Figure 6.10.b, in the darker region at the top of the sample. These images clearly show the same phases as the non-carbonated one: hydrotalcite, unreacted slag, and inner and outer C-A-S-H gels. Figure 6.11 presents the elemental maps of the Figure 6.10.c. These micrographs show no systematic difference in the composition of the sample with the change of colours. This observation is expected as Chaouche *et al.* discussed that the colour change is due to the sulphur oxidation state and not to a change of chemical composition [20]. The oxygen has a low energy X-ray emission, and consequently this small change of oxygen content cannot be observed or quantified accurately via EDS [177].
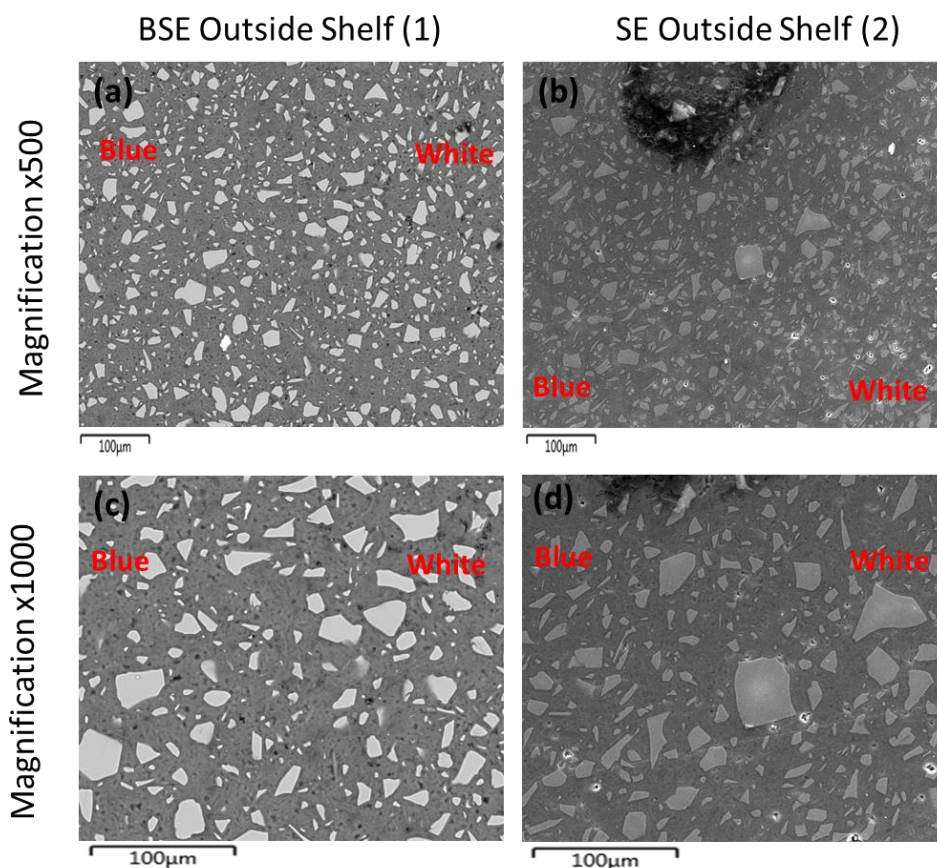
Figure 6.10: Backscattered electron images and secondary electron images across the colour front of the sample exposed outside protected from the rain during a year. The blue coloured part is at the left part of the samples as shown in each image, and the white part is at the right part of the image.
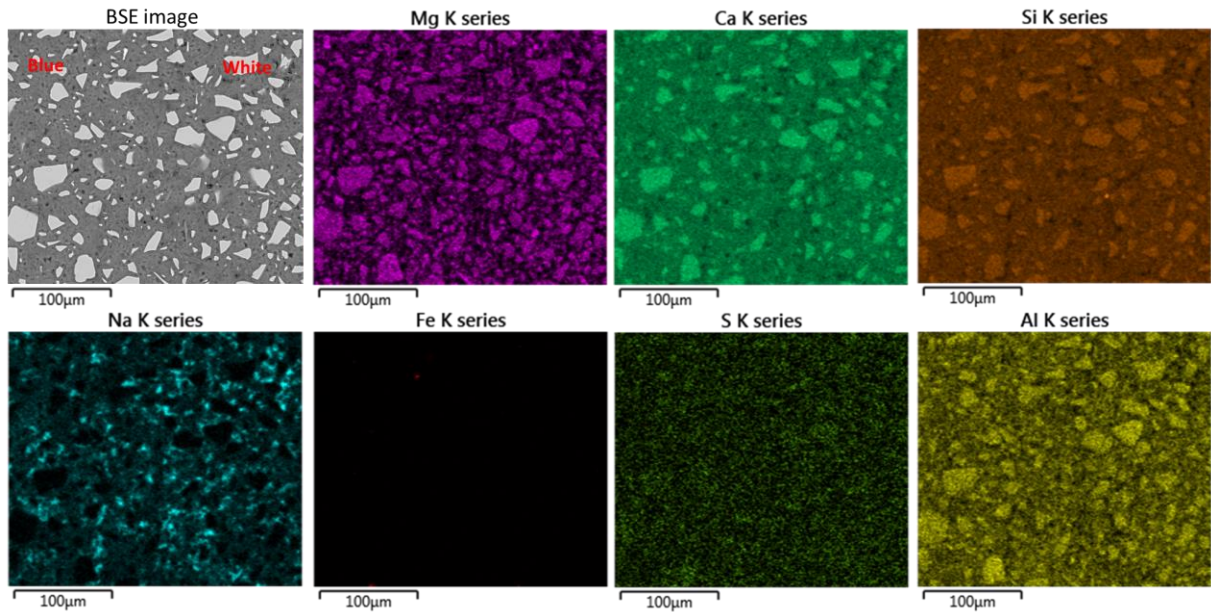
Figure 6.11: Elemental maps and backscattered electron image of the colour front of the sample outside protected from the rain for 12 months.

6.3.3.3 Images of carbonation fronts

Backscattered electron (BSE) images and elemental maps obtained by Energy Dispersive X-ray Spectrometry (EDS) of the carbonation fronts of the samples were also taken. The BSE at two different magnifications, one high and one low, are presented in Figure 6.12. The EDS maps of the samples outside exposed and protected to the rain are respectively presented in Figure 6.13 and Figure 6.14. The carbonation fronts of the samples kept inside in the laboratory and in the chamber are presented respectively in Figure 6.15 and Figure 6.16.

Figure 6.12: Backscattered electron images at two different magnifications, of the carbonation fronts of the samples exposed to different environments for a year. The carbonation side is the left of each sample as imaged, and the non-carbonated side is the right.
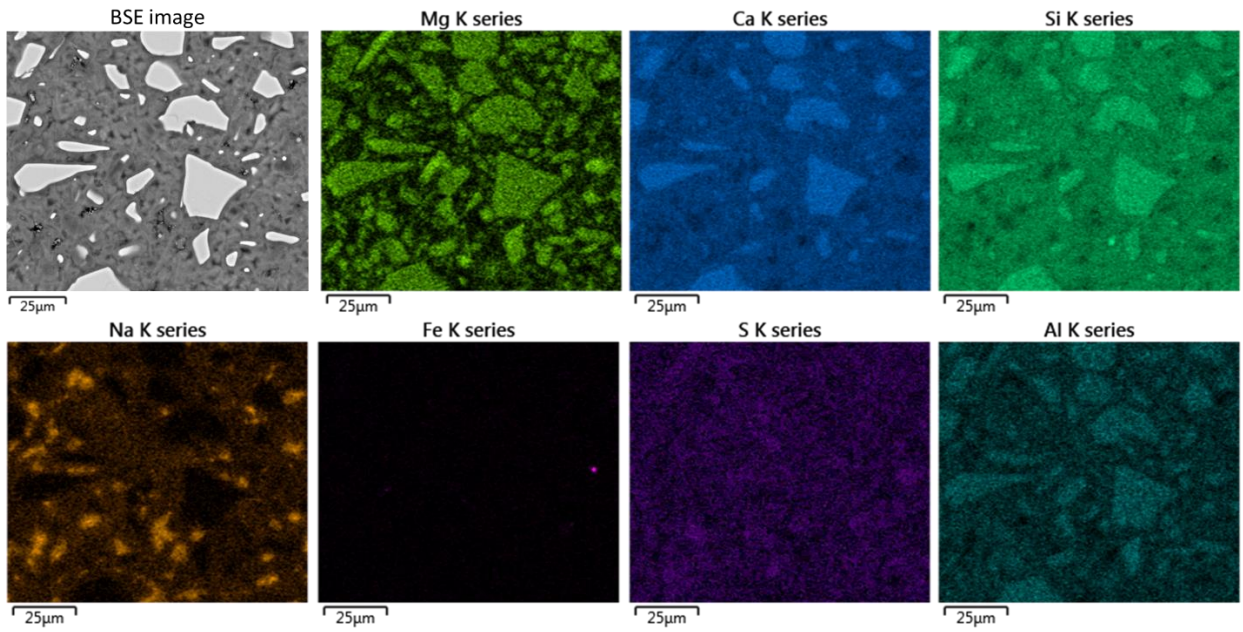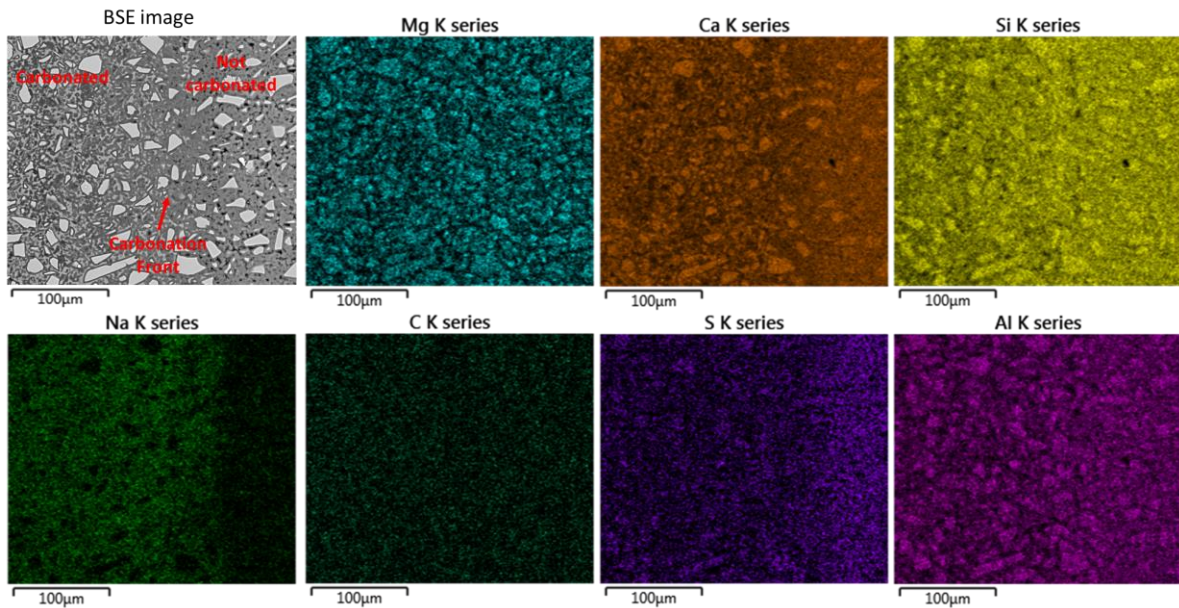

Figure 6.13 : Elemental maps and backscattered electron image of the carbonation front of the sample outside exposed to the rain for 12 months.
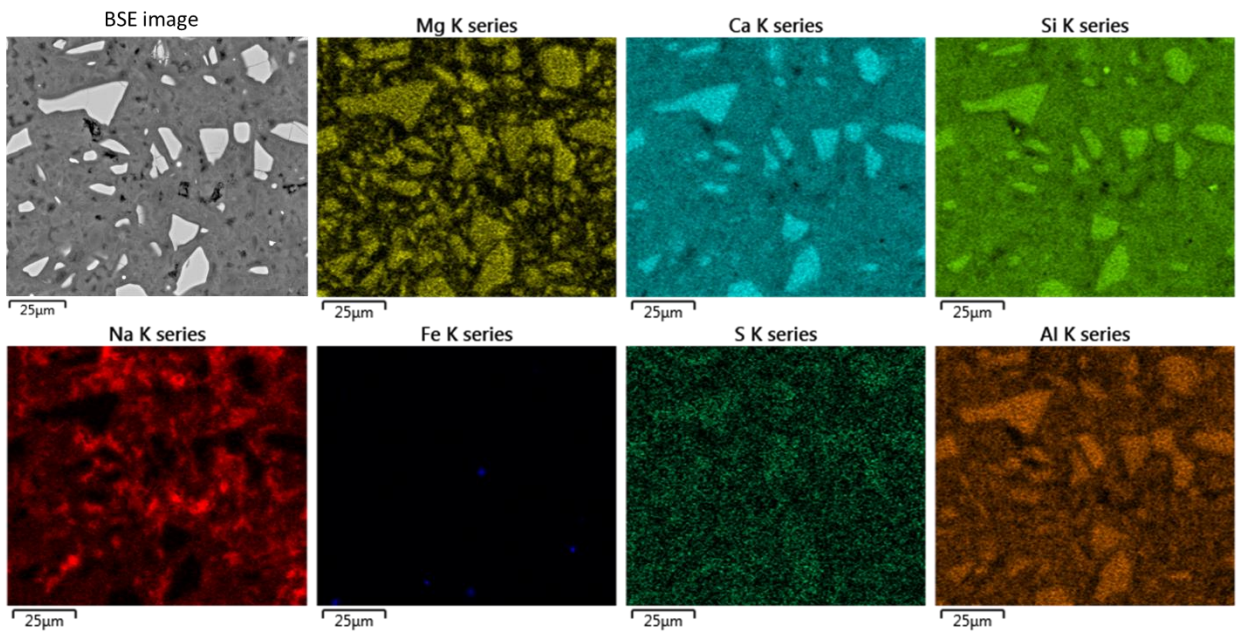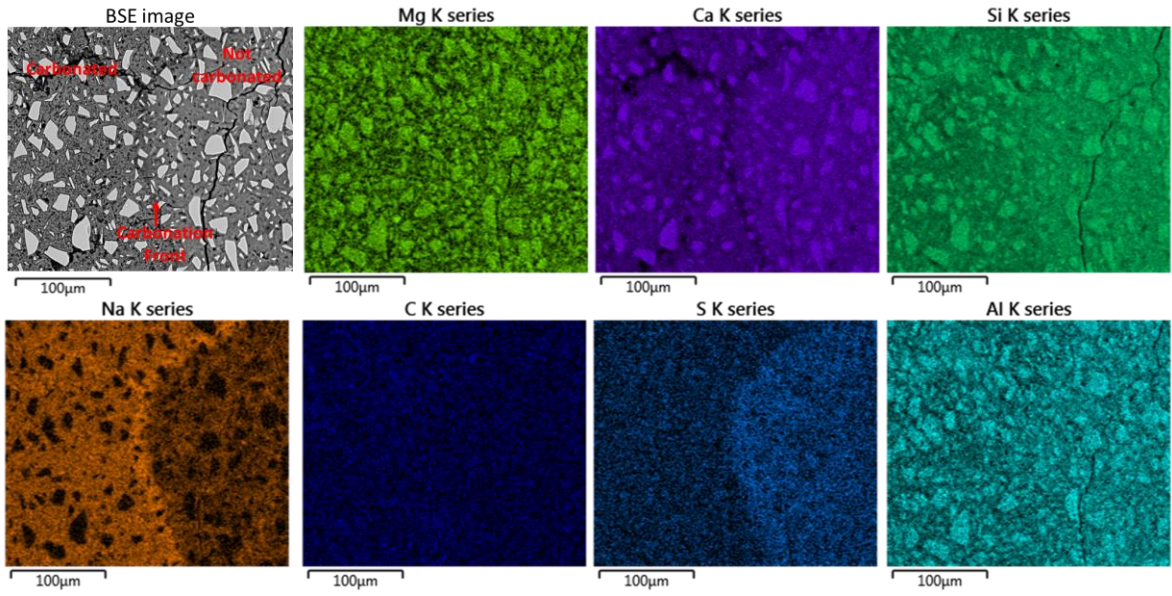
Figure 6.14: Elemental maps and backscattered electron image of the carbonation front of the sample outside protected from the rain for 12 months.
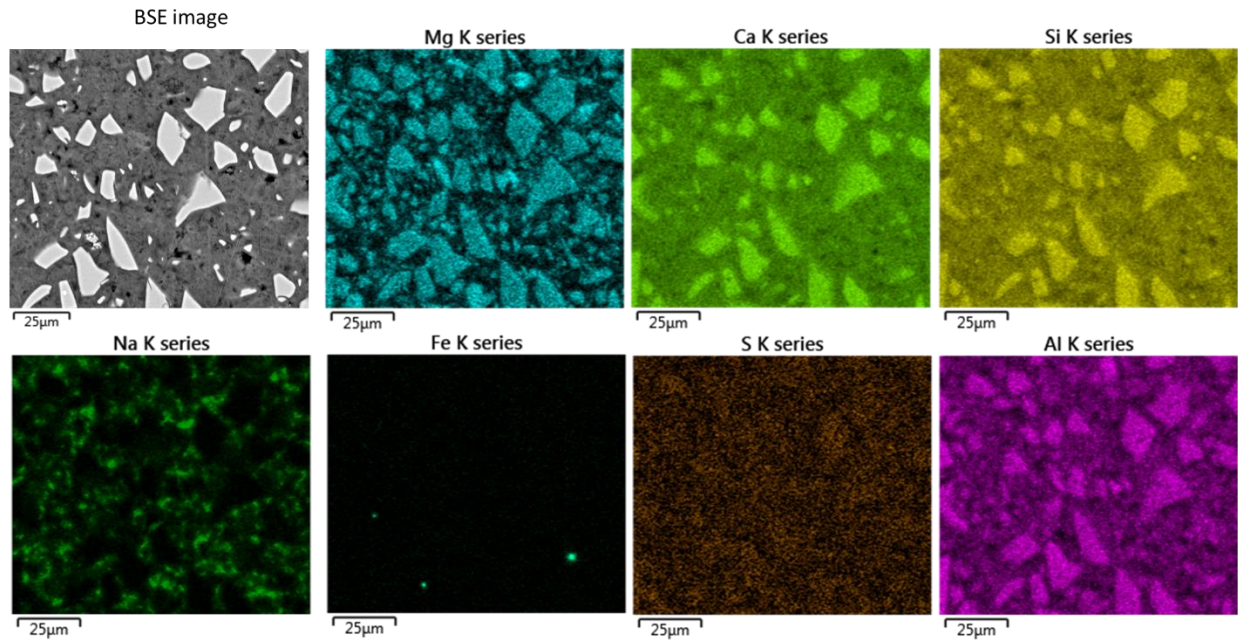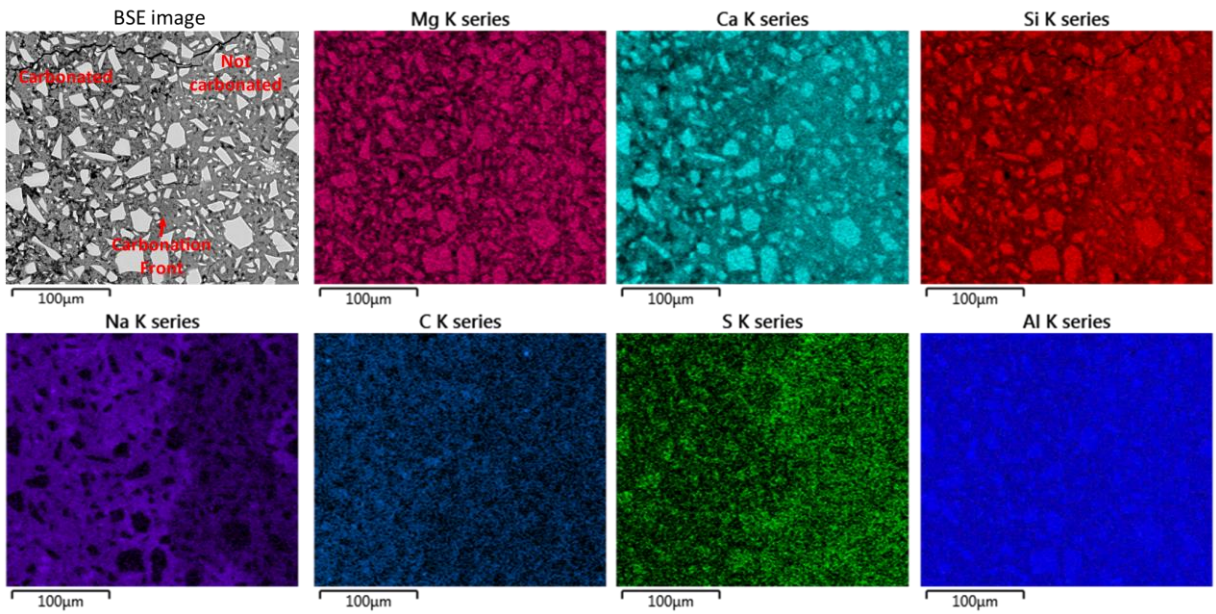

Figure 6.15: Elemental maps and backscattered electron image of the carbonation front of the sample kept inside in the laboratory for 12 months.
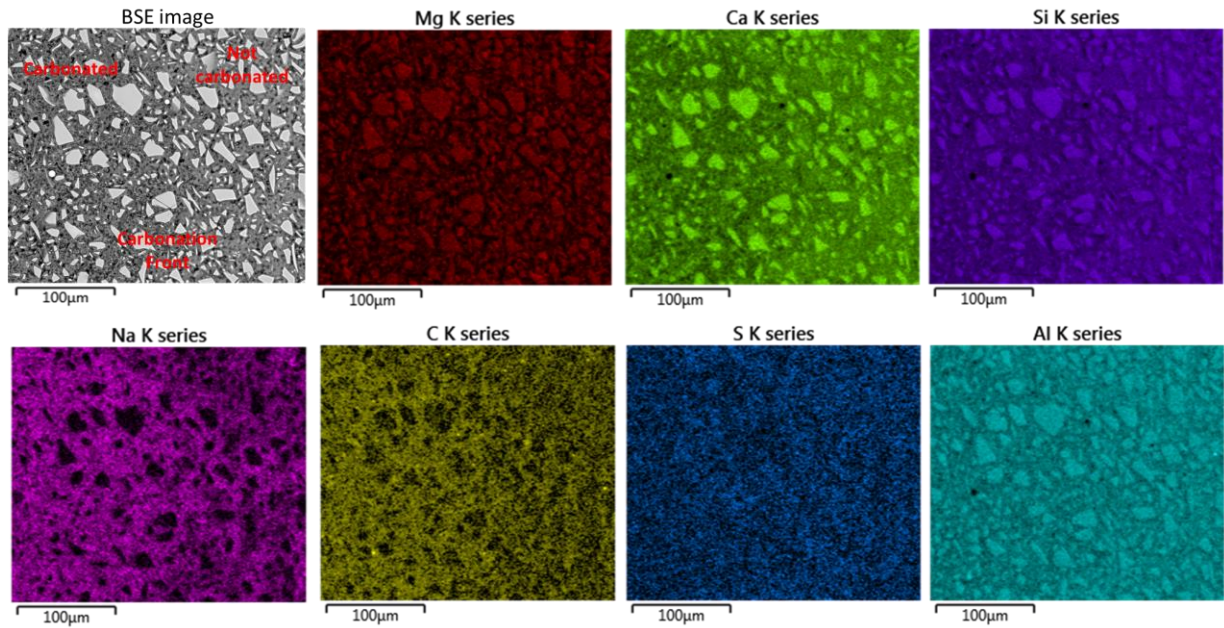
Figure 6.16: Elemental maps and backscattered electron image of the carbonation front of the sample kept inside in the chamber for 12 months.

The BSE images in Figure 6.12 show that the carbonation fronts look different depending on the samples. The carbonation front for the sample sheltered outside is only a few micrometres in width. The one outside exposed to the rain is wider; between the non-carbonated part and the carbonated part there is an intermediate region of around 50 μm. The carbonation fronts of the samples kept inside are also distinct. Both samples kept inside have some small patches of carbonated sample in the non-carbonated part, and vice versa. Nedeljković showed in her PhD thesis [84], that the carbonation front for slag based AAM in a laboratory environment is wide, around 50 μm. Indeed, she explained that the partially carbonated zone, zone between the pore solution carbonation and the hydrate products decalcification, is wide and comprised between the non-carbonated and carbonated parts. The conditions outside seem to favour a small partially carbonated zone, and the efflorescence reduce consequently this zone. The pH of the pore solution and the content of alkali ions, are reduced by the efflorescence process [77]. Consequently, when the CO_2 dissolves in the pore solution, it might not react with the alkali, but instead will react directly and progressively with the C-A-S-H gel.

156

In Figure 6.12, a change of porosity can be observed in all the samples. Larger pores appear in the carbonated area, as well as microcracks, to a different extent depending on the samples. The carbonation has been shown to induce the formation of mesopores while reducing the amount of micropores, as the calcium carbonates precipitate in the interlayers and gel pores, but leads to the decalcification of the gel which leads to the formation of mesopores [198]. The decalcification of C-A-S-H gel leads to the formation of microcracks [196]. In Figure 6.14, the sample exposed to both efflorescence and carbonation shows a large amount of microcracking compared to the other samples. This sample also has larger cracks that follow the carbonation front. The combination of efflorescence, which leads to a lower amount of calcium in the sample, and carbonation increases the decalcification of the gel, as the NMR results from Chapter 5 show, and thus further reduces the Ca/Si ratio of the gel as the atomic ratio in section 6.3.3.5 shows [77]. Consequently, as the study of Chen *et al.* highlighted [200], the precipitation followed by the polymerisation of the aluminosilicate gel will cause significant shrinkage which leads to cracks. The subflorescence, which is the precipitation of the salts in the pore of the materials, also leads to a higher amount of cracks in the sample [152].

The carbonated areas of the BSE images reveal the formation of lighter grey phases in between the unreacted slag particles. These phases are calcium carbonate, and as calcium has a higher atomic number than silicon and aluminium, it appears lighter than the aluminosilicate gel which appears darker [176,252,253]. Calcium carbonates were formed progressively after the dissolution fronts.

As the elemental maps Figure 6.13, Figure 6.14, Figure 6.15 and Figure 6.16 show, the calcium distribution changes after the carbonation front. The distribution of this element is homogeneously spread within the hydrated phases of the non-carbonated parts, while it is spread unevenly in between the unreacted slag particles in the carbonated parts. This change of distribution is due to the decalcification of the C-A-S-H and the formation of calcium carbonates during carbonation [168]. Similarly, the distribution of aluminium and silicon is affected by the carbonation, and is more sporadic due to the formation of calcium carbonates.

Sodium is migrating towards the carbonated parts in all of the elemental maps above. Similar results have been observed in several studies [84,254,255]. The dissolution of CO_2 leads to the precipitation of sodium from the pore solution as sodium carbonates [113]. According to

Zhang *et al.,* the gradient of humidity between the part of the sample that matches the relative humidity outside and the part inside leads to the migration of the sodium, with capillary water, towards the outside part of the sample [254]. The sodium carbonate needs a dry environment to stay stable, which is not the case within the sample, so it dissolves in the pore solution to be integrated in the aluminosilicate gel. The sodium will be incorporated in the aluminosilicate gel as a charge balancing ions for the silicon sites $Q^4(3Al)$ and $Q^4(4Al)$. Figure 6.14 shows that in the sample exposed to efflorescence and carbonation outside, the sodium is even more concentrated in the dissolution front. This is due to the intermittent formation of a layer of water on top of the sample, that will increase the gradient of RH between the outside and inside of the sample [254]. In this front, the content of calcium is low when the sodium content is high. According to Zhang et al., calcium content tends to be lower in the region where the sodium content is higher, due to their complementary effects [254].

The sulphur also shows a change in content depending on the carbonation front. In Figure 6.14 and Figure 6.15, the content of sulphur is higher in the non-carbonated area than in the carbonated area. These samples also show a "front" between these two areas where the content of sulphur is slightly higher. This sulphur front is just before the "sodium front" which corresponds to the dissolution front. This observation is in agreement with previous studies [84,255]. Figure 6.14 shows also a higher content of sulphur in the non-carbonated area compared to the carbonated area for the sample protected from the rain outside. Finally, for the sample exposed to carbonation inside in the chamber, Figure 6.15 shows no observable change of sulphur content within the region used for this EDS analysis. The sulphur evolution during carbonation will be further analysed in the following paragraphs.

Carbon is usually hard to detect by EDS as it has a low atomic number [177]. However, in Figure 6.15 and Figure 6.16, a higher content of carbon can be observed in the carbonated parts. The carbonation inherently raises the content of carbon by bringing carbon dioxide into the sample.

6.3.3.4 Images of carbonated regions

Backscattered electron (BSE) images and elemental maps obtained by EDS analysis of the carbonated parts of the samples were taken. The BSE images at two different magnifications,

one high and one low, are presented in Figure 6.17. The EDS maps of the samples outside, exposed to and protected from the rain, are respectively presented in Figure 6.18 and Figure 6.19. The carbonation fronts of the samples kept inside in the laboratory and in the chamber are presented respectively in Figure 6.20 and Figure 6.21.
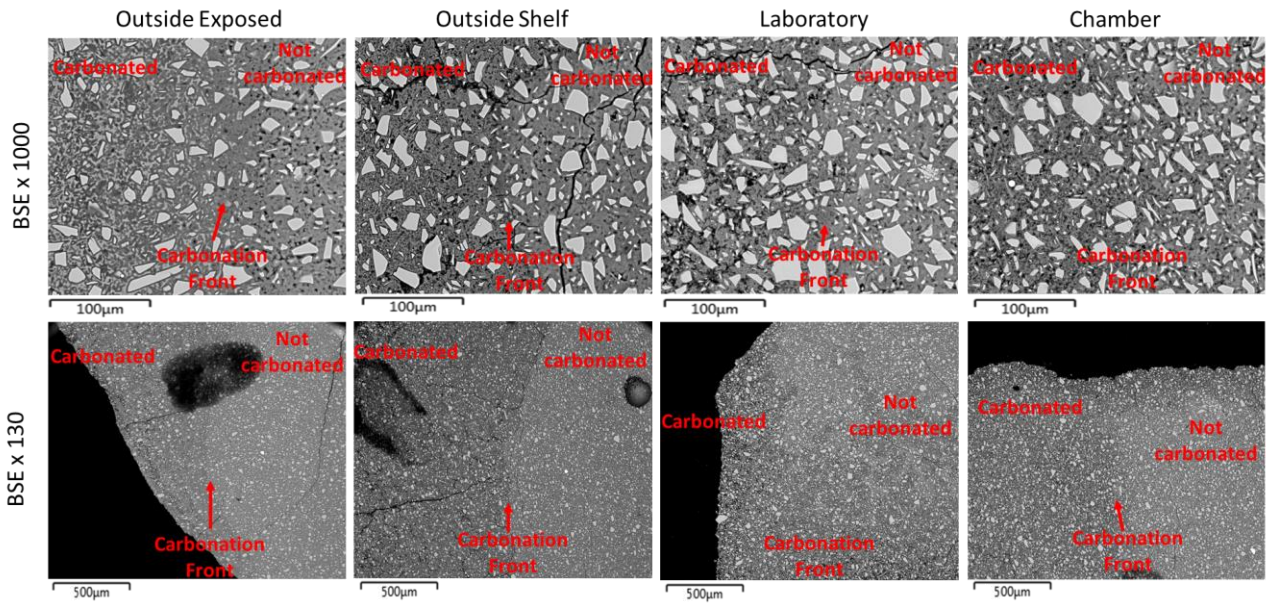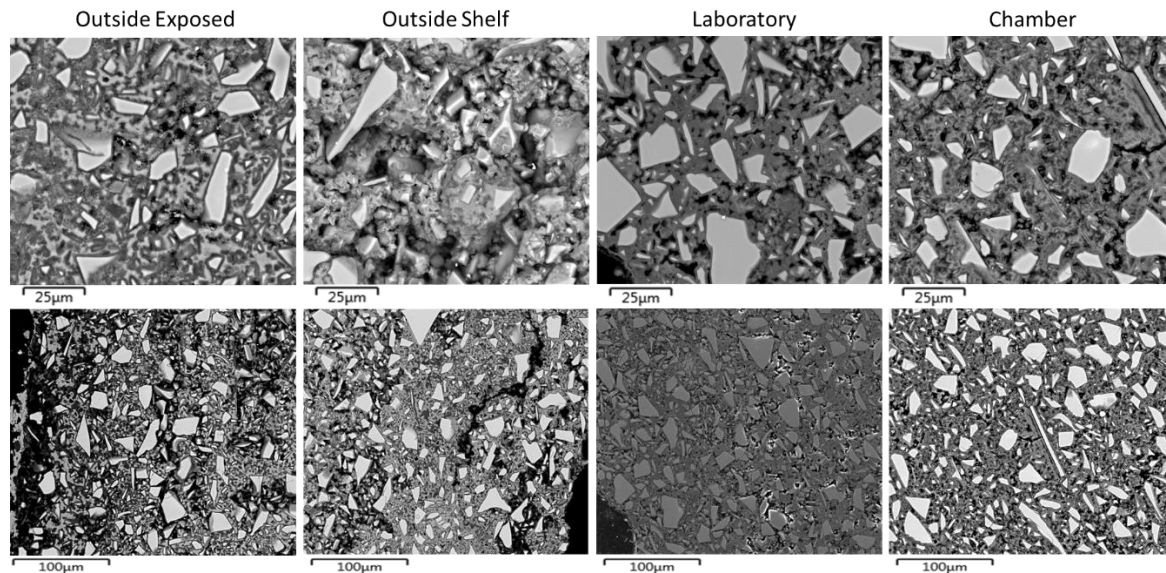

Figure 6.17: Backscattered electron images of carbonated parts of the samples exposed to different environments for a year. The images on the top row correspond to the images analysed by EDS. The images in the lower row are from a different carbonated part of the sample. The lower image for the Laboratory sample is a Secondary Electron rather than a BSE image, because the BSE image at corresponding magnification was not available.

The bottom images in Figure 6.17 show the carbonated parts of the samples. The left side of each images corresponds the closest to the exterior areas of the sample. The black parts are more accessible pores or the exterior of the sample (at the extreme left as shown). For the two samples outside, a large amount of cracking is present. Some parts of the samples even show only the unreacted particles and nothing visible in between. However, it is not representative of the sample, because if they were only unreacted slag particles and no binders in between, it would be powder. However, the sample was solid while cut as Figure 6.2 shows. So the cracks and pores appear during the sample preparation. The polishing removed some of the phases, probably some of the calcium carbonates, even though calcium carbonates are still apparent in these images. The product of the C-A-S-H decalcification, the aluminosilicate gel, is probably also removed from some zones of the sample during the polishing, which might show that their binding capacity is low. The samples kept inside have

not been affected by this deterioration as much, probably because they have a lesser extent of carbonation of C-A-S-H carbonated as the previous chapters explained. So the remaining C-A-S-H has probably still acted as binding phases, and helps to avoid this deterioration.

The bottom images in Figure 6.17 show different parts of the carbonated area of the samples. If the image of the sample in the laboratory corresponds to the border of the sample, it was not possible to take a similar image for both samples exposed outside, as a lot of the products at the border have been removed by the sample preparation as explained previously. All of the samples present products identified in the previous paragraphs: in light grey, unreacted slag particles, in lesser light medium grey, calcium carbonate, in darker grey a remnant of C-A-S-H, especially around the slag particles (so it is mainly the inner C-A-S-H), and in even darker grey, aluminosilicate gel. The inner C-A-S-H situated around the unreacted slag particles seems to carbonate after the outer C-A-S-H, as it is present in all the images contrary to the outer C-A-S-H, even though not all the slag particles are surrounded by this inner C-A-S-H in the sample outside protected from the rain. The inner gel has less calcium than the outer gel. [251] Consequently, the outer C-A-S-H is carbonated first as it has the higher Ca/Si ratio, then the inner C-A-S-H is carbonated [111].
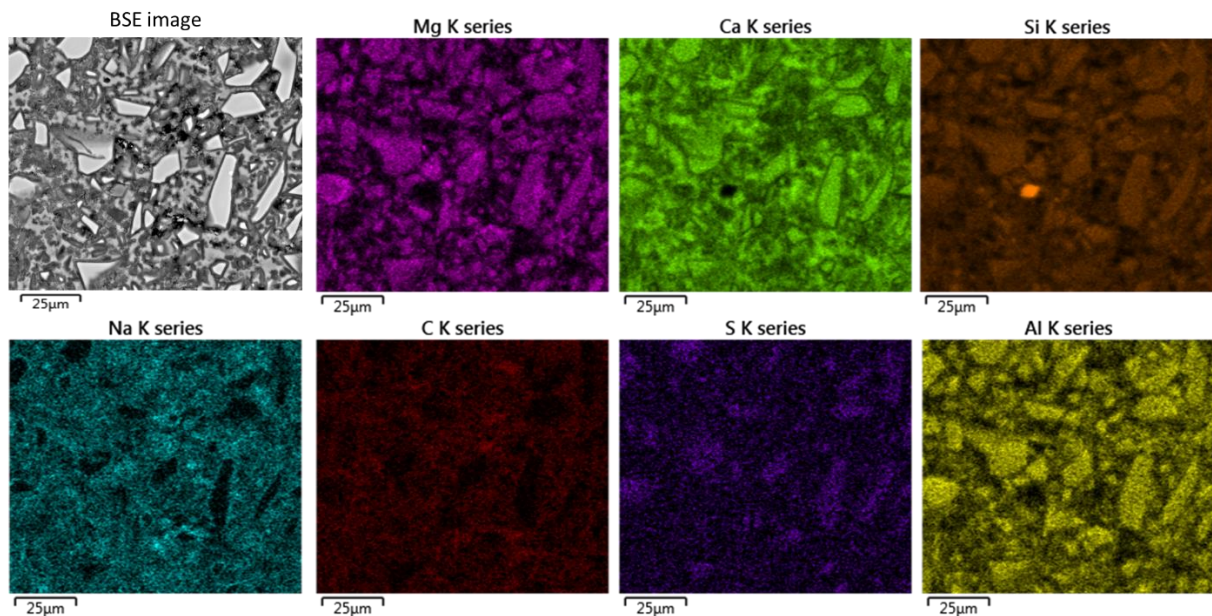
Figure 6.18: Elemental maps and backscattered electron image of the carbonated parts of the sample outside exposed to the rain for 12 months.
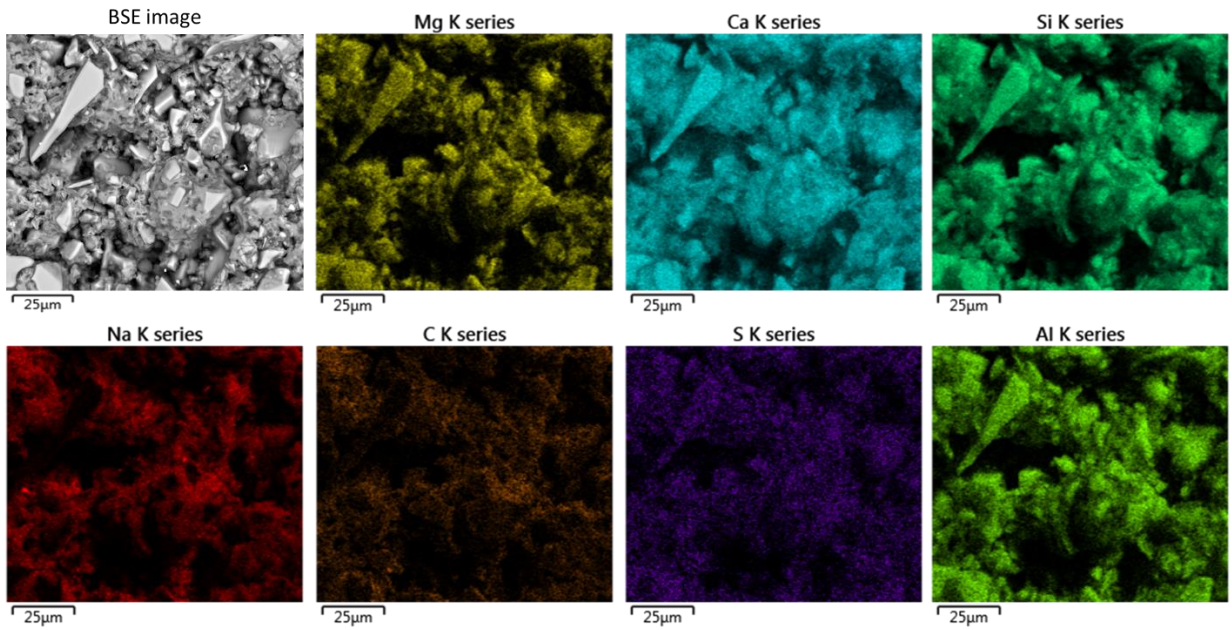
Figure 6.19: Elemental maps and backscattered electron image of the carbonated parts of the sample outside protected from the rain for 12 months.
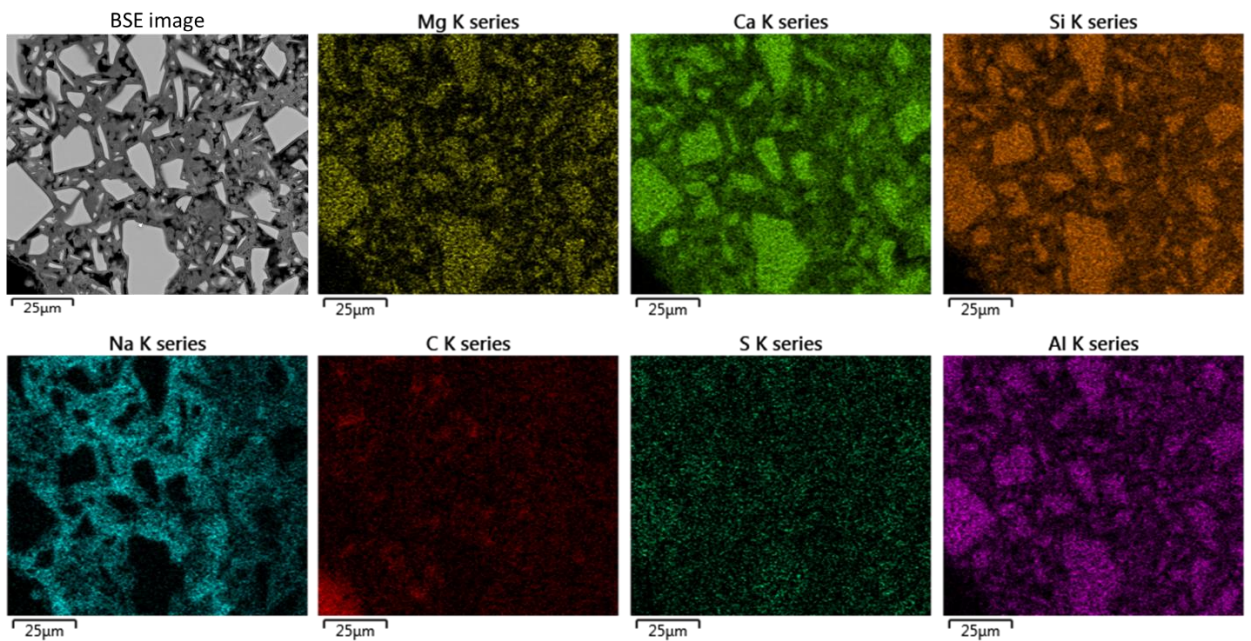
Figure 6.20: Elemental maps and backscattered electron image of the carbonated parts of the sample kept inside in the laboratory for 12 months.
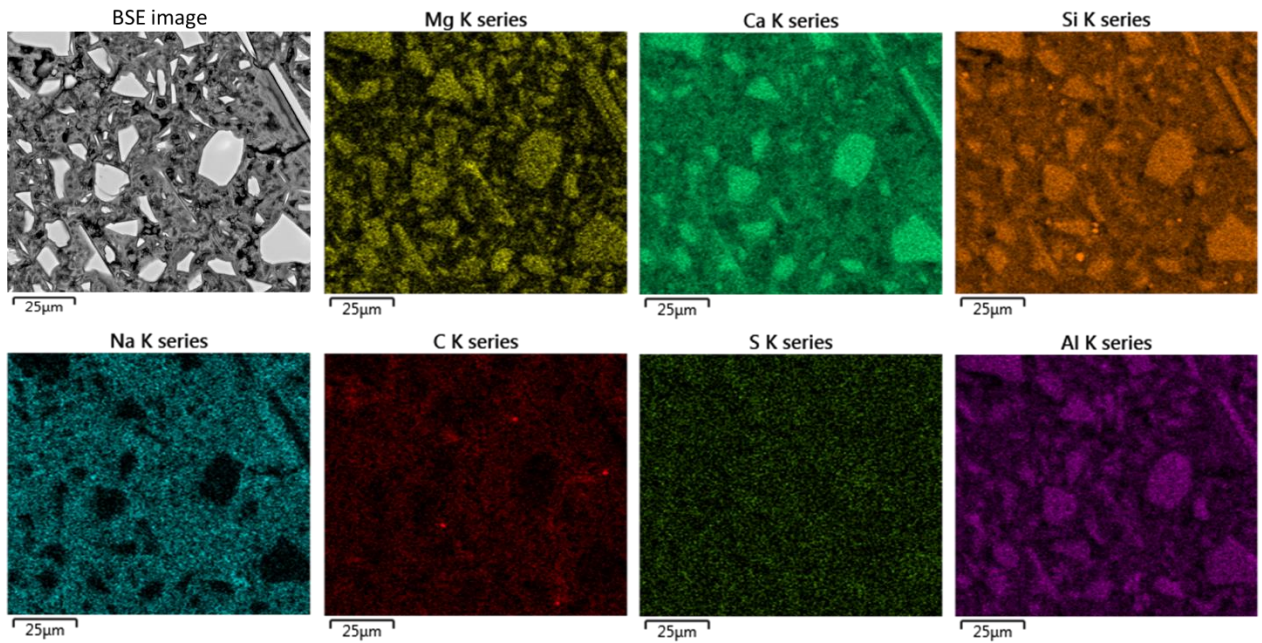
Figure 6.21: Elemental maps and backscattered electron image of the carbonated parts of the sample kept inside in the chamber for 12 months.

The calcium elemental map of Figure 6.18 highlights the presence of calcium carbonate as light grey phases. Some of these phases do not have a defined morphology, so they could be the transient amorphous calcium carbonates that have been identified via thermogravimetry in the previous chapter, and in the literature as transient products in the carbonation of C-(A)-S-H [109,256]. The calcium carbonate structure in Figure 6.21 is similar to the one in Figure 6.18. Conversely, some calcium carbonates phases look crystalline in Figure 6.19. The image has been taken further from the carbonation front, and closer to the exposed part, than Figure 6.18. Consequently, these calcium carbonates appear to be the calcite and vaterite identified in the previous chapter.

The samples kept in the chamber, and the ones outside exposed and protected from the rain, all present a high concentration of sodium in the pores, probably due to the sodium carbonates. In Figure 6.18, the sodium elemental map confirmed that the crystalline phases in needle shapes in the pore region are sodium carbonate. The sodium and calcium elemental maps of Figure 6.21 show that the content of sodium is high in the middle where the calcium content in the hydrated product is low. This observation is similar to what has been observed for the front region in Figure 6.14.

6.3.3.5 Atomic ratios

The Ca/Si and Al/Si atomic ratio of each sample, with the carbonated parts in blue and non-carbonated in red, are presented in Figure 6.22. The EDS atomic ratio is not precisely defined as being only for the surface material, as it evaluates the atomic compositions of the sample 1-2 μm below the surface for the BSE points chosen [176]. So it is likely that, despite choosing a point in the middle of a hydrated product or carbonated product, the EDS gives the composition of some hydrated products and some unreacted slag particles that were situated below, or potentially another product. This ratio shows that almost all the non-carbonated hydrated products have Ca/Si ratios of 1.6 ± 0.2 except for the sample outside exposed to the rain, where the Ca/Si is in the range between 1.6 to 5. Similarly, the samples have an Al/Si ratio of 0.3 ± 0.1 except for the sample exposed to the rain, which has a ratio between 0.2 to 1.1. These results highlight that the soft water leaching is leading to the formation of $CaCO_3$ and a more heterogeneous aluminosilicate gel.

The carbonation process is increasing the measured Ca/Si ratio for all the samples, due to the decalcification of the C-A-S-H gel to form regions that are very enriched in calcium carbonate. The Ca/Si reaches as high as 7 for some points in the sample outside, confirming the higher level of decalcification and $CaCO_3$ formation observed in the previous chapter. This high Ca/Si corresponds to the measurements of calcium carbonates [253]. Some points with lower Ca/Si can be observed for the sample in the laboratory and in the sample outside protected from the rain; these points correspond to the aluminosilicate resulting from the decalcification of the C-A-S-H [103,168,257]. The Al/Si ratio after carbonation is less scattered than before, except for the sample that have been exposed to the rain, and it is almost all in the interval between 0.2 and 0.3. This is due to the carbonation of the hydrotalcite that leads to a reduction of the Al/Si in these phases [113,168]. This observation is coherent with the ^{27}Al NMR results.
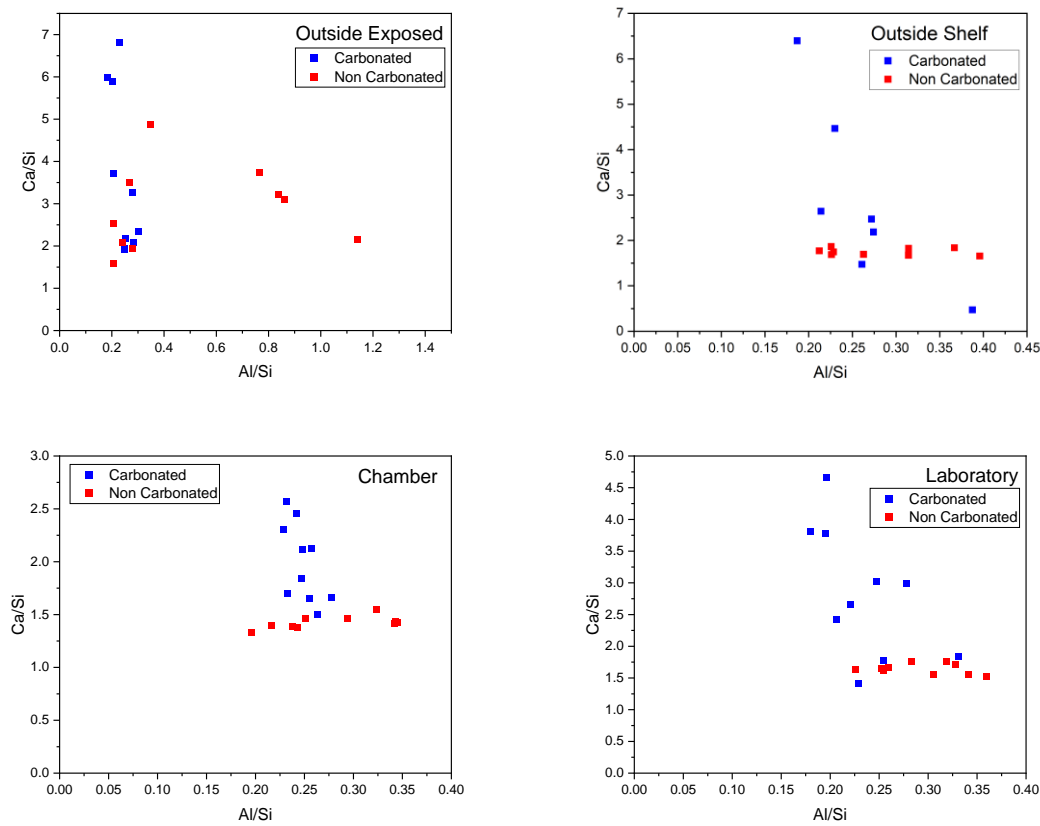
Figure 6.22: Atomic ratios Al/Si versus Cal/Si for the uncarbonated and carbonated parts of the sample in different exposure conditions.

6.3.4 X-ray fluorescence analysis

The silicon, sulphur, aluminium, magnesium and sodium distributions for the sample outside exposed to the rain, outside protected from the rain, and inside in the chamber are presented respectively in Figure 6.23, Figure 6.24 and Figure 6.25. Photographs of the samples analysed are also in these Figures at the top right. The three shades of colours can be observed in the photographs of Figure 6.23 and Figure 6.24: grey-white on top for the carbonated part, light yellow-white in the middle for the oxidised part, and blue on the bottom for the non-oxidised part. The sample in the chamber only shows the carbonated and oxidised parts.
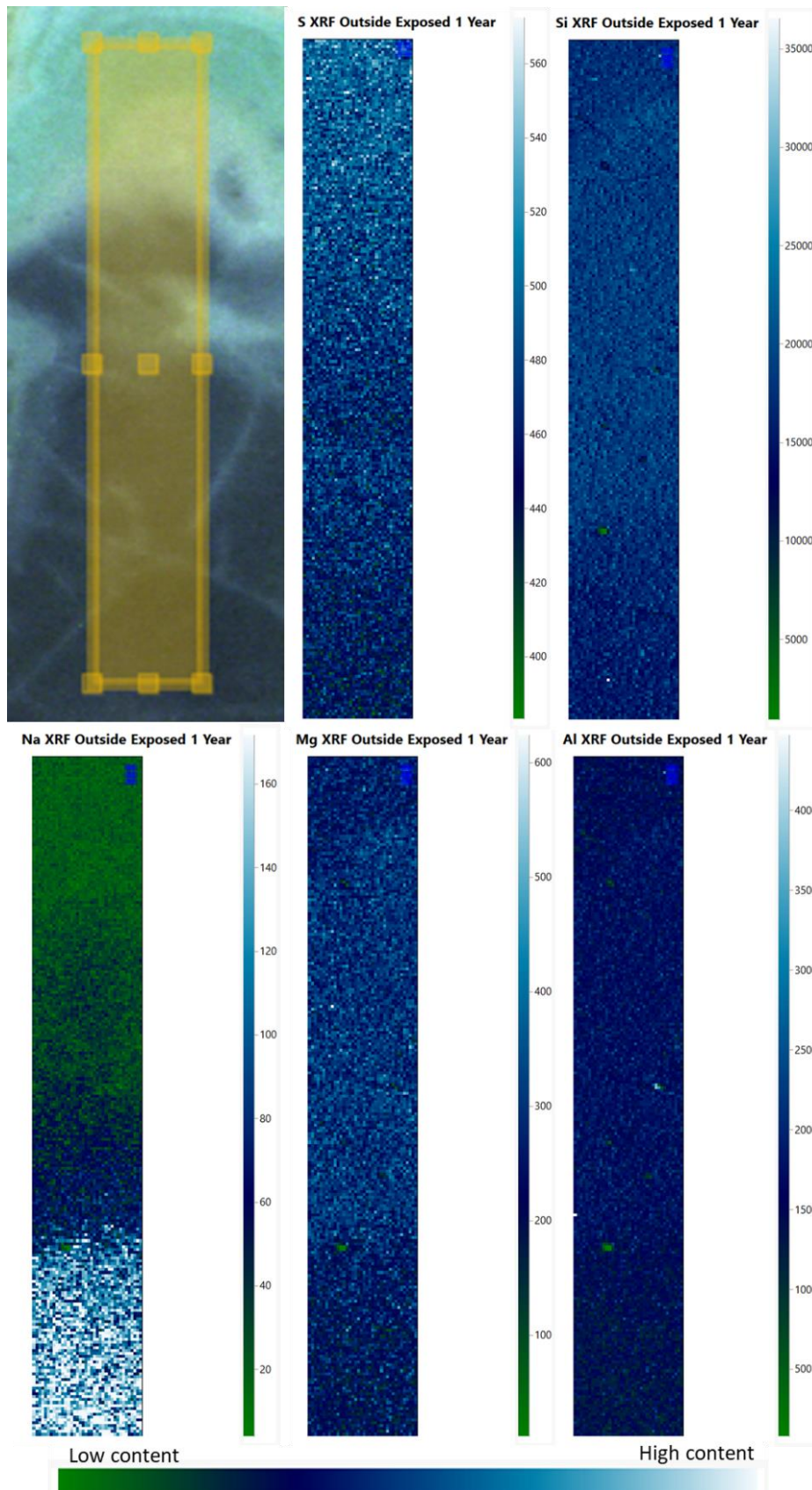
Figure 6.23: Elemental distribution for the sample outside exposed to the rain obtained by μ-XRF with an incident beam of 2600 eV, map size 0.75 mm x 4.68 mm with step of 0.02 mm.
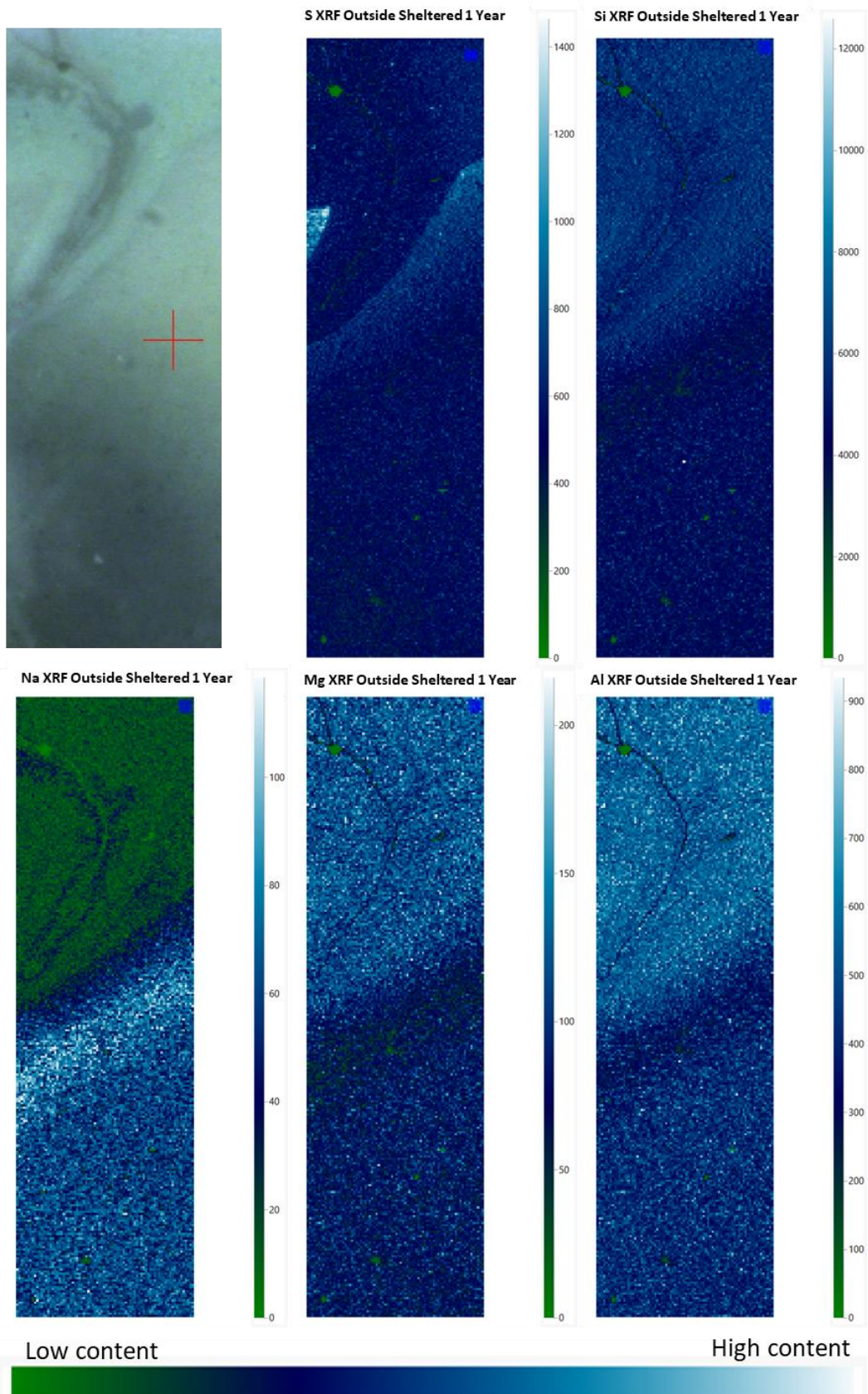
Figure 6.24: elemental distribution for the sample outside protected from the rain obtained by μ-XRF with an incident beam of 2600 eV, map size 1.58 mm x 5.58 mm with step of 0.02 mm.
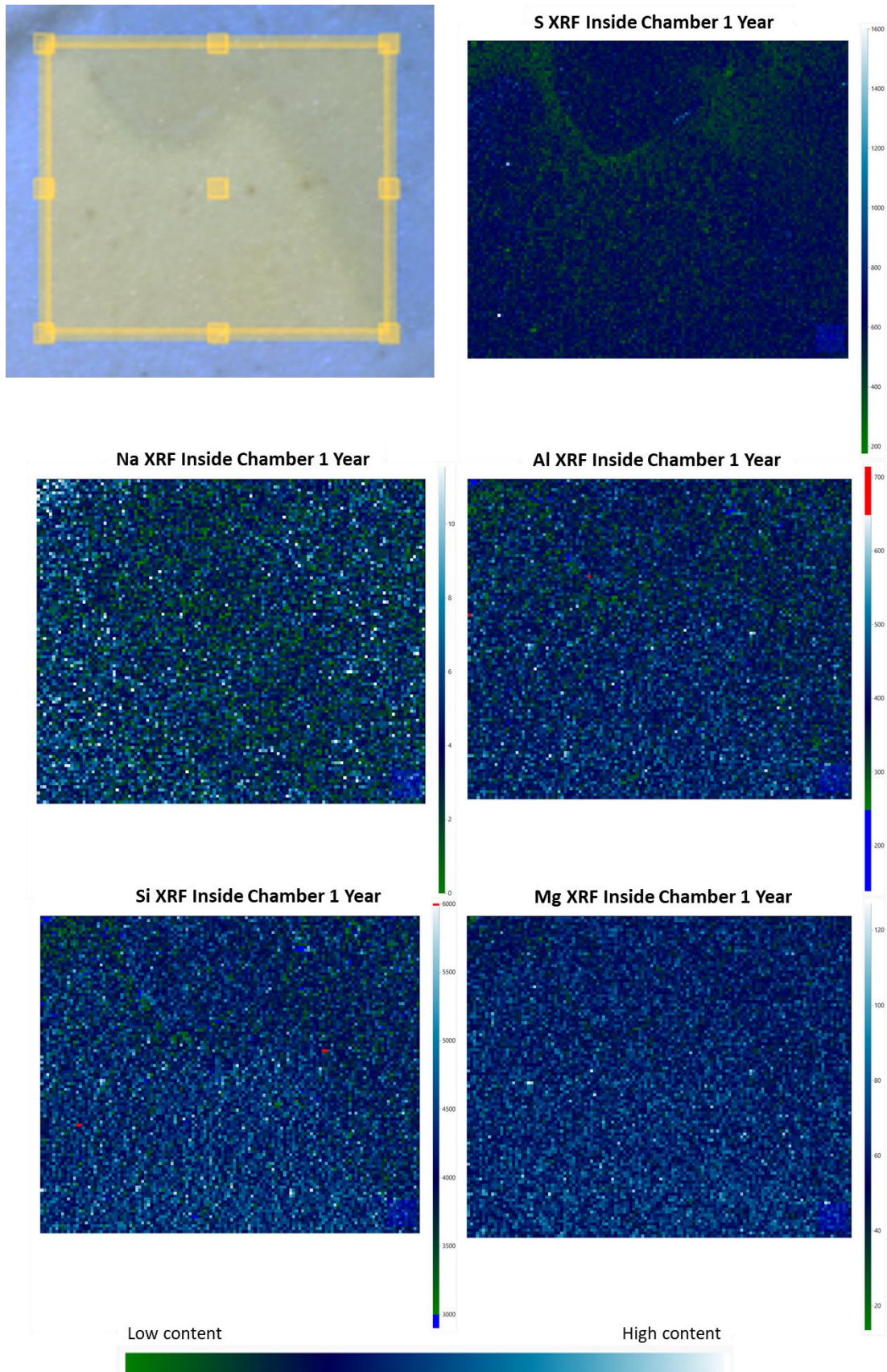
Figure 6.25: Elemental distribution for the sample exposed to carbonation in the chamber, obtained by μ-XRF with an incident beam of 2600 eV, map size 2.12 mm x 2.54 mm with step of 0.02 mm.

The aluminium maps of Figure 6.23 and Figure 6.25 both show no noticeable change in the aluminium distribution, apart from at the carbonation front where the content of aluminium is slightly less high than in the rest of the sample. Conversely, in Figure 6.24, the aluminium content changes at the partially carbonated zone. The content of aluminium decreases at the dissolution front, and then increases in the carbonated area compare to the non-carbonated area. The same observation can be made for the magnesium and the silicon. Both of these elements show no apparent change between the carbonated and non-carbonated areas in their distributions in Figure 6.23 and Figure 6.25, whereas a change of distribution can be observed in their elemental maps in Figure 6.24. These elemental contents decrease slightly around the dissolution front and then increase in the carbonated part. Consequently, as the carbonation is not affecting the aluminium content (Figure 6.25), the efflorescence must be responsible for this change of composition. The SEM-EDS results in Figure 6.13, Figure 6.15 and Figure 6.16 showed a change of distribution in these elements at a smaller scale, and the corresponding µ-XRF maps of these elements confirm that this difference of distribution is not affecting the overall content of these elements, when the sample is exposed to carbonation alone or combined with soft water leaching. In Figure 6.14, a change in the repartition of silicon and aluminium, after the carbonation combined to efflorescence, was observed by SEM-EDS. However, the same observation is not made in the other conditions. This change in composition might be due to densification effect or to a repartition more scattered of the phases. The first one is due to the water content decreasing with the change of gel composition, which leads to a denser content of silicon, magnesium and aluminium [200]. The second one is due to a repartition more scattered of the phases due to the decalcification of the gel and the formation of calcium carbonates.

The sodium elemental map in Figure 6.25 shows no significant change when the carbonation is the only reaction. However, the EDS sodium elemental maps in Figure 6.15 and Figure 6.16 showed an increase of the sodium at the carbonation front. The point sizes of both technique are on a different order of magnitude, the point size for EDS is smaller than for µXRF, so the difference in results might come from the different spatial resolution of each technique. The sodium content changes at a smaller scale but not at a larger scale, as the µ-XRF results show. Conversely, both Figure 6.23 and Figure 6.24 highlight a decrease of the sodium content after the carbonation front when the carbonation is coupled with efflorescence from soft water

leaching. The combined actions of efflorescence and carbonation cause an abrupt decrease in the sodium content at the partially carbonated zone, then, after this front, the sodium decrease gradually. The high content of sodium at the partially carbonated zone has been observed by SEM-EDS in Figure 6.14. The efflorescence is leaching out the sodium to form sodium carbonates at the surface, so the content of sodium in the sample decreases closer to the surface [18,77,151]. The combined action of the soft water leaching leads to an increase of the sodium content at the partially carbonated zone, followed by a sharp decrease at the carbonation front, which corresponds to the "decalcification front"; another sharp decrease is then observed, leading to an almost null concentration of sodium. The sodium is leached out due to the rainfall that leads to soft water leaching [160]. This result also shows that the soft water leads to the leaching out of the sodium only from the carbonated area, as the content of sodium is constant in the non-carbonated area.

When the carbonation is not combined with other forms of durability attack, the sulphur content is higher at the carbonation front, as Figure 6.25 shows. The carbonation front also corresponds to the change between the yellow-white and grey-white regions. The EDS sulphur elemental map of Figure 6.15 shows a slight decrease of the sulphur content at the carbonation front, while the sulphur elemental map of Figure 6.16 shows no change in the sulphur content. As explained in the paragraph above, the difference in results between the two methods might come from the difference of sensitivity between the two methods. As Figure 6.23 shows, the combined action of the carbonation with the soft water leaching leads to a gradual increase of the sodium content in the carbonated part. In Figure 6.24, when the carbonation is combined with efflorescence, the sulphur content increases just before the colour front, and then the content of sulphur is similar between the carbonated and non-carbonated area. The sulphur evolution will be studied more in detail in the next paragraphs.

6.3.5 Sulphur X-ray absorption near edge spectroscopy

6.3.5.1 Standards

Figure 6.26 shows the maximum derivative energy of the edge, called edge energy, of each of the mineral standards that have been tested during the beamline experiment. The red curve

is the linear fit of these points. The equation of this curve gave us the edge energy for each oxidation number for the following paragraph.
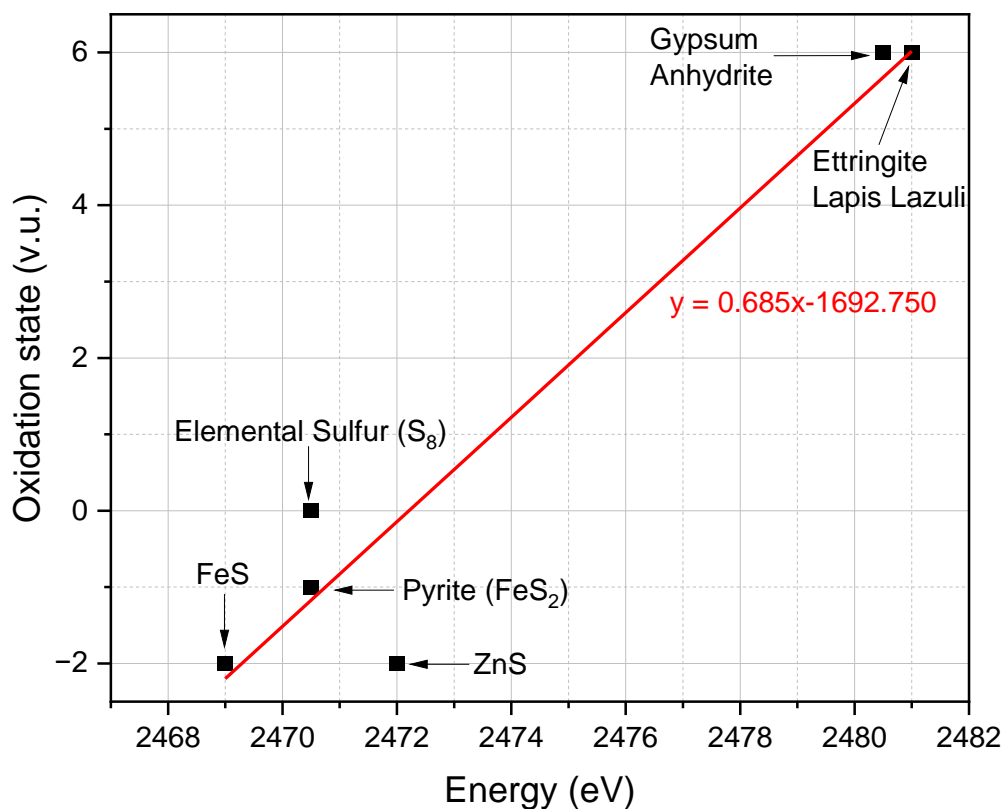
Figure 6.26: Edge energies of XANES for the standard materials as a function of sulphur oxidation state

The shifted edge energy at 2472 eV for ZnS compared to other sulphides, has been observed in several studies [258,259]. This shifted is due to the hybridisation between the orbital 3p of the sulphur and the orbital 3d of the metal, Zn in this case [259,260]. Native sulphur is supposed to be at 2472 eV instead of 2470.5 eV according to previous studies [259,261]. This shift can be due to the quality of the native sulphur that is used. The shift between the edge energies of the different elements depends on the elements surrounding the sulphur and has been criticized by several studies, that suggest to show the overall XANES spectra of the standards instead, as its shape and main shoulder energies are more representative of each phase than the edge energy alone [260,262]. Table 6.2 shows the edge energies and the XAS main shoulders of the standards tested.

Table 6.2: Edge energy and main XAS features of the standards.

Compound	Formula	Pre-edge energy (eV)	Sulphur oxidation state	XAS main shoulders (eV)
Zinc Sulphide	ZnS	2472	S^{2-}	2481; 2485; 2499; 2506; 2524
		2477		
Iron(II) sulphide	FeS	2469	S^{2-}	2488; 2508
		2477		
Pyrite	FeS_2	2470.5	S^{1-}	2479; 2485; 2490; 2518
Native sulphur	S_8	2470.5	S^0	2478; 2486
Gypsum	$CaSO_4 \cdot 2H_2O$	2480.5	S^{6+}	2484, 2491; 2498
		2477		
		2470.5		
Anhydrite	$CaSO_4$	2480.5	S^{6+}	2484; 2493; 2499
		2477		
		2470.5		
Ettringite	$Ca_3Al_2O_6 \cdot 3CaSO_4 \cdot 32H_2O$	2481	S^{6+}	2497
		2477		
		2470.5		
Lapis Lazuli	$(NaCa)_8[Al_6Si_6O_{24}](SO_4,S,Cl)_2$	2481	S^{6+}	2492; 2498
		2470.5		
		2477		
		2468		

The edge energies of 2477 eV and 2470.5 eV in italics in Table 6.2 correspond to small edge features present in most of the standards. These energies are most likely attributed to cross contamination as they are present in most of the samples and show small peaks. Further analysis should have been performed on the samples during the beamline experiments to draw definitive conclusions on the origin of these peaks, but this was not possible because of limited beamtime allocation. The standards and the samples to test have not been prepared similarly: the standards were pellet pressed and the samples were cut, cast in epoxy resin and polished. Consequently, there is not a chance of cross contamination that could affect the sample spectra. Both anhydrite and gypsum present some large XAS shoulders that are characteristics of the crystalline sulphate in these compounds [258,259,263]. Ettringite presents only a large hump at 2497 eV as the sulphate is not bound directly to a cation [262,263]. Lapis lazuli presents a characteristic peak at 2468 eV that corresponds to the disulphur S_2^- and trisulphur S_3^- radical species that are contained in a aluminosilicate cage [20,239,260,264]. These radicals are responsible for the blue colour of the lapis lazuli. The edges at 2470.5 eV and 2477 eV are larger than the other similar edges for the other standards. These edges correspond to the envelope formed around the radical species [264]. Finally, the sulphate peak of this standard is situated at 2481 eV like the sulphate peak of ettringite.

6.3.5.2 Sulphur K-edge XANES scans

The XANES spectra of representative areas of the sample exposed to carbonation outside exposed to the rain are presented in Figure 6.27. The XANES spectra of representative areas of the sample exposed to carbonation outside protected from the rain are presented in Figure 6.28. The yellow white corresponding to the non-carbonated part and the grey white area corresponding to the carbonated area of the sample in the chamber have been analysed, and the XANES spectra are presented in Figure 6.29.
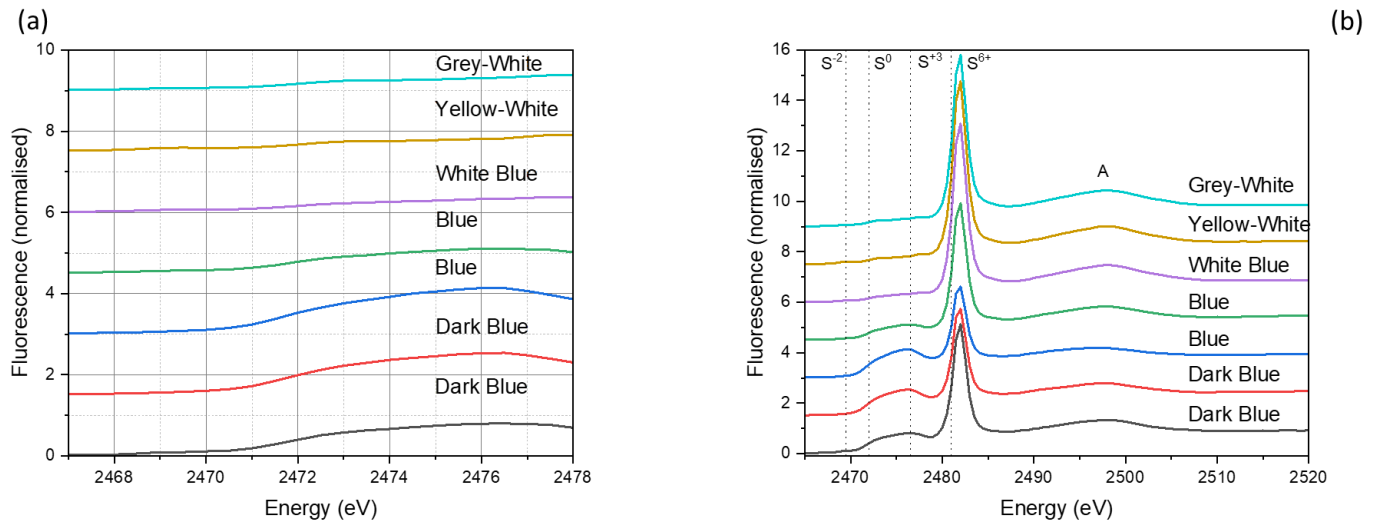
Figure 6.27: Normalised sulphur K-edge XANES spectra of different areas of the sample outside exposed to the rain. The figure (a) is a focus on the lower energy range of figure (b).
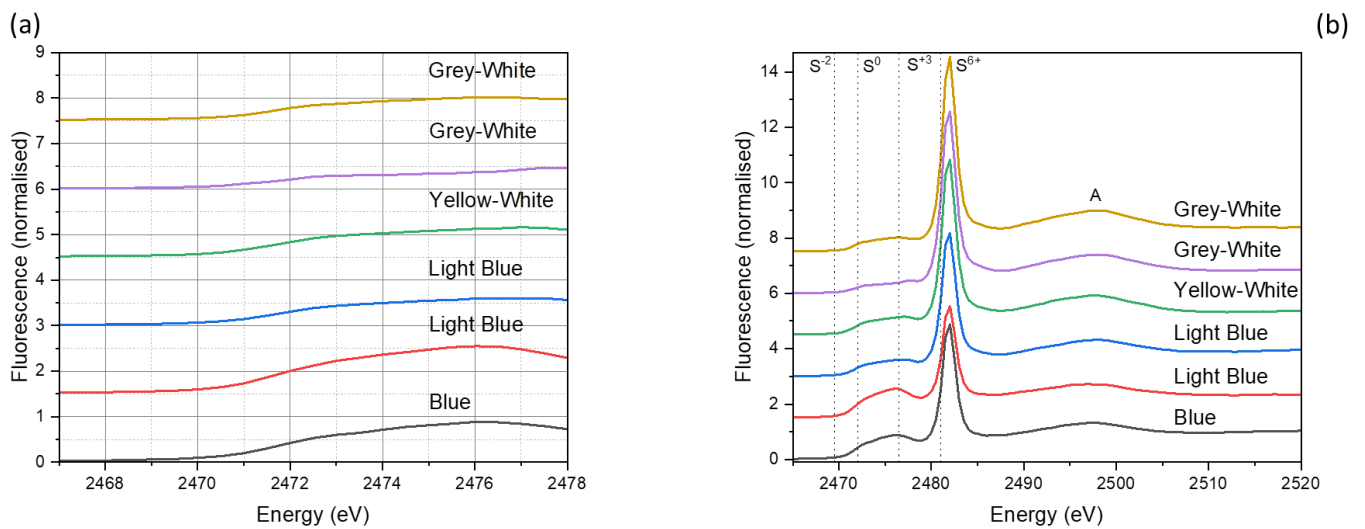
Figure 6.28: Normalised sulphur K-edge XANES spectra of different areas of the sample outside protected from the rain. Figure (a) is a focus on the lower energy range of figure (b).
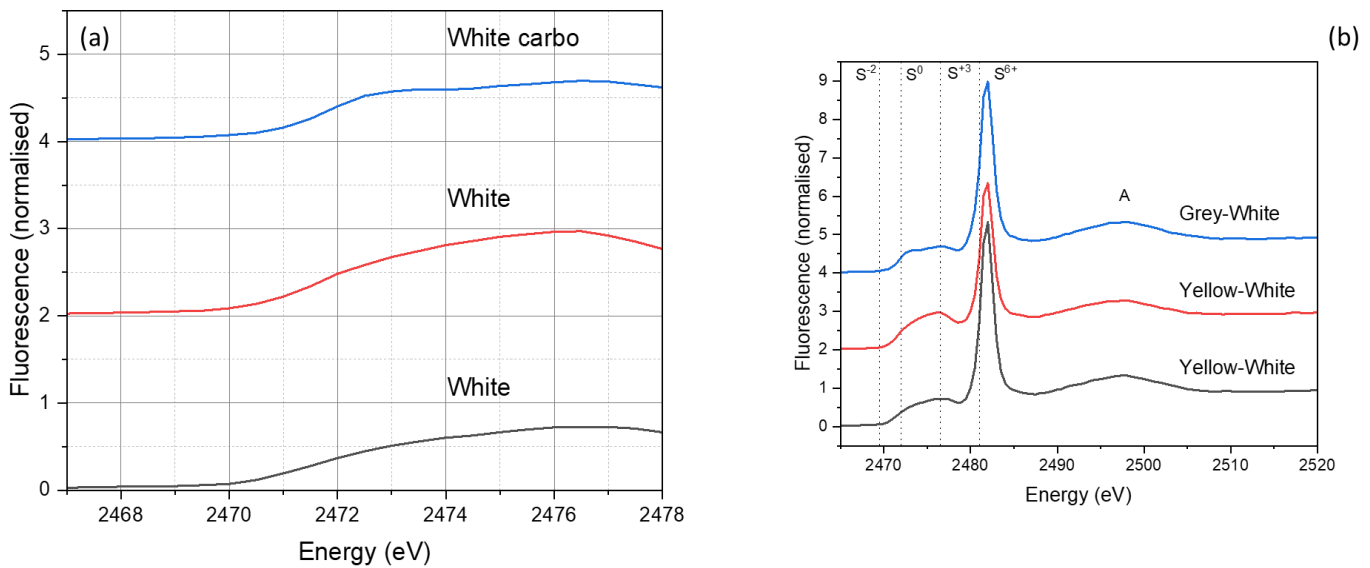
Figure 6.29: Normalised sulphur K-edge XANES spectra of different areas of the sample kept inside in the chamber for a year. Figure (a) is a focus on the lower energy range of figure (b).

The XAS shoulder, named A, has its maximum at 2498 eV. This broad feature is similar to the ettringite XAS shoulder, and it is at the same position as the second XAS feature of the lapis lazuli. This wide peak is likely due to sulphur not linked to a cation like the sulphur in ettringite, or in an amorphous state [258,262,263]. A similar XAS featured is observed in the XANES spectra of ground granulated blast furnace slag or cement paste mixes containing GGBS [20,263]. Figure 6.27 and Figure 6.28 show that this feature increases when the sharp peak associated with S^{6+} at 2481 eV increases. This feature is similar for every scan in *Figure 6.29,* and similarly the S^{6+} is similar for every graph.

The right hand graph of Figure 6.29 shows that the carbonation in this sample does not seem to affect the sulphur in the S^{6+} state, as the main peak associated to the 2481 eV edge energy is similar for every spectrum. Conversely, the S^{6+} peak increases with carbonation and oxidation in Figure 6.27 and Figure 6.28. The peak increases when it passes from blue to white, and then increases more when the sample is more carbonated, for the spectra of the samples carbonated outside, either exposed or protected from the rain. These results show that the content of sulphate increases with oxidation and then with carbonation.

The spectra of the sample stored in the chamber, in Figure 6.29, presents a small rise at 2468 eV, which corresponds to S^{2-} sulphur according to Figure 6.26. These spectra also display a

174

peak with an edge energy at 2471 eV: this peak, which corresponds to S^- sulphur according to Figure 6.26, is higher for the carbonated sample than the non-carbonated. Fleet et al. observed a small peak between 2470 eV and 2471 eV in basaltic glass that is attributed to sulphide that is dissolved in the glasses. This S^{2-} peak is slightly shifted due to the presence of calcium cations in close proximity to this sulphide [265]. Consequently, the peak at 2470.5 eV might not be S^- species but rather S^{2-} species close to calcium cations. In the following paragraphs, it will be assumed that the peak 2470.5 eV corresponds to S^{2-} species with calcium cations in their close environment. Finally, both samples present a peak with an edge energy of 2475 eV; this peak that corresponds to S^{2+} sulphur is similar for all the spectra. A small peak at 2477 eV, which corresponds to S^{4+} sulphur, is visible for the carbonated spectrum.

The spectra of the sample exposed to the rain, in Figure 6.27, and the spectra of the sample protected from the rain, in Figure 6.28, are similar so in the following paragraphs, they will be described together. All the non-carbonated spectra presents a small rise at 2468 eV, whereas the carbonated sample presents almost no rise. The blue and dark blue present two peaks that blend into each other, one smaller with an edge energy at 2471.5 eV, and a taller one with an edge energy at 2475 eV. The exact edge energy of the second one is imprecise as the two peaks blend together. Consequently, the blue parts present a higher content of S^{2-} than S^{2+}. The white parts, carbonated and not carbonated, also present these two peaks, but there are smaller and the same size as each other. The spectra associated to the white parts present a small peak at 2477 eV, which corresponds to S^{4+}: this peak is also slightly visible in the interface parts, named white blue or light blue. The reduction of the 2468 eV peak for the white sample show a decrease and then an oxidation of the radical species. Similar results have been observed in the study of Chaouche *et al.* [20].

This decrease is also associated to a decrease of the peak at 2470.5 eV and an increase of the sulphate peak at 2481 eV, which confirm that the sulphur is being oxidised. The XANES peak also contains the peak associated with the sulphur in the unreacted slag particles. According to Roy, the sulphur in GGBS is present as sulphate, sulphur and sulphide [263]. The decrease of this peak is linked to the oxidation of these species, present in the hydrated phases of the sample. This oxidation leads then to the increase of S^{6+} species [266]. The sulphide peak at 2470.5 eV does not disappear completely as the sulphur species present in the slag are not affected by the oxidation [20].

The results highlight that the main difference between the blue parts and the white parts is the sulphur oxidation state. The blue parts contain more sulphur in lower oxidation states, while the white parts contain more sulphur in higher oxidation states, with the increase of S^{6+} content and the appearance of S^{4+} sulphur. According to Chaouche *et al.* the blue/green colour of the slag based cementitious material is due to the S_3^- and S_2^- radical trapped in an "aluminosilicate cage", in this study, the "cage" is either a structural feature of the C-A-S-H, or the N-A-S-H that forms as an ancillary phase in alkali-activated slags[20,237]. Slavík *et al.* highlighted the presence of sodalite cages in the low calcium content AAM, so N-A-S-H gel is more likely to contains sulphur radicals trapped [267]. The presence of these radicals trapped in an "aluminosilicate cage" is responsible for the blue colour of the lapis lazuli as well [264]. Consequently, the blue spectra of the alkali activated sample should be similar to the lapis lazuli tested. The blue samples present a similar XAS feature at 2498 eV to the lapis lazuli tested. However, the XAS features at 2492 eV of the lapis lazuli is not observable in the blue sample as the 2498 eV feature is broad, and it might be too small to be visible. The peak at 2471 eV is only shifted by 0.5 eV compared to the lapis lazuli peak at 2470.5 eV. This shift can be due to a slight difference between both chemical environments of the sulphur [259,260]. The carbonation, efflorescence and soft water leaching affect the C-A-S-H, as has been shown in the previous chapter. Consequently, the sulphur present in the C-A-S-H is released and oxidised during these chemical attacks.

The presence of S^{4+} sulphur can be due to X-ray beam damage, that causes the photo-reduction of the S^{6+} state into S^{4+}, according to Wilke *et al.* [268]. However, in this study, the systematic observation of the peak associated with S^{4+} in the white parts of the samples and not in the blue parts, even though all the measurements have been done at the same time with the same conditions, proves that the presence of this species is not due to the beam damage, but to the oxidation of the sulphur. Sulphite, (SO_3^{2-}), with the sulphur in a S^{4+} oxidation state, is presented as an intermediate state during the oxidation of S^{2-} into S^{6+} [261,269]. Consequently, in this study, the sulphite species are intermediate sulphur oxidation products. The carbonated spectrum in Figure 6.27 shows a small amount of S^{4+} which is likely due to the oxidation of S^{2-} species. Consequently, the carbonation affects the sulphur by promoting the formation of sulphite according to these results.

6.4 Conclusion

The phenolphthalein experiments presented in this chapter highlighted several observations. Firstly, the carbonation in these materials leads to a reduction of pH, but the pH does not drop below 9 as it does in Portland cement systems [100,104]. Conversely, the low relative humidity leads to a higher advancement of the carbonation front in AAM cement paste, as it promotes the formation of cracks via drying shrinkage [270]. Finally, the soft water leaching combined with carbonation leads to a significant decrease of the pH as the soft water leaching promotes the leaching of the alkali ions present in the pore solution.

The SEM and μ-XRF studies revealed the impact of the combined chemical attacks on the alkali activated materials. As Hay *et al.* highlighted in their work, the outer C-A-S-H gel is carbonated before the inner C-A-S-H gel during the carbonation [111]. The SEM results clearly show that the samples kept inside present a smaller amount of calcium carbonate phases in their carbonated parts compared to their counterparts outside. This is due to the lower RH inside than outside, that limits the formation of calcium carbonates. The combined attacks of efflorescence with carbonation seem to particularly damage the structure of the carbonated parts, as the Ca/Si and Al/Si ratios of the hydrated phases are more heterogeneous than the ratios when the samples are carbonated alone or combined with soft water leaching. The efflorescence also reduces the size of the CO_2 dissolution front compared with the other samples placed in different conditions. The μ-XRF data also revealed that the content of aluminum, silicon and magnesium is reduced by the carbonation and efflorescence. Finally, carbonation combined with efflorescence or soft water leaching significantly reduce the content of sodium.

The change of colours in slag-based AAM over time is due to the oxidation of the sulphur from the slag, as Chaouche *et al.* demonstrated [20]. The XRD results show no change in the crystalline phases during the oxidation of the sulphur. The SEM-EDS did not show major changes at the oxidation front, but as the oxygen characteristic X-ray energy is low, in this method it might be too low to be detected accurately by EDS [177]. The S^{2-} species are oxidised and form sulphite first as a transient species, to then form later sulphate [261,269]. The disulphur and trisulphur radicals, that are responsible for these blue/green colours, are in aluminosilicate cages, which is either in the C-A-S-H or N-A-S-H. Consequently, the

carbonation combined with efflorescence or with soft water leaching can promote sulphur oxidation by affecting the C-(N)-A-S-H. The higher the relative humidity is, the shorter the oxidation front is, as the oxygen is diffusing less fast in the capillary pores.

Chapter 7 : Conclusions and Future work

7.1 Conclusions

The purpose of this study was to understand the impact of carbonation on slag based AAM, in different environments that were close to on-site exposure. In this thesis, the carbonation mechanism has been evaluated for slag based AAM, with innovative test methods that aim to give the parameters necessary to the carbonation prediction. This study also aims to evaluate the impacts of carbonation alone, but also coupled with efflorescence or soft water leaching on slag based AAM. To achieve this, the impact of different environments and in particular of the relative humidity on the material carbonation is compared.

The findings of this thesis have added to the knowledge of high calcium content AAM carbonation, and particularly to the combined effects of carbonation and efflorescence, or carbonation and soft water leaching, on these materials. This thesis also highlights the importance of using alternative test methods to evaluate the carbonation extent of cementitious materials containing a high GGBS content.

7.1.1 GGBS based AAM carbonation evaluation

Chapter 4 highlighted the possibility to use alternative test methods to evaluate the carbonation extent on these materials. Two complementary methods have been used, the first one to evaluate the effective gas diffusion coefficient and the second one to evaluate the CO_2 binding capacity. These methods developed for PC systems gave coherent results for carbonated samples. However, the samples that were not carbonated and not oxidised, tested with the effective gas diffusion coefficient method did not give coherent results. As this method relies on the oxygen passing through the sample, the results obtained were altered by the uptake of oxygen by the sulphur. Consequently, it is necessary to test materials containing sulphur radicals, such as high GGBS content cementitious materials, using another inert gas to prevent misevaluation of this parameter.

Chapter 4 also leads to the prediction of the carbonation extent, with the two parameters obtained implemented in the Papadakis model. These cost effective test methods enable the evaluation of the necessary parameters to predict carbonation in different environments, which is not the case of the current standardized carbonation tests. The predictions obtained

were coherent with the experimental data for the accelerated carbonation when the CO_2 effective diffusion coefficient of the carbonated samples was combined with the degree of carbonation obtained with the innovative test method. However, the prediction leads to an overestimation of the carbonation rate for samples tested under natural carbonation. It is concluded that this overestimation is due to the diffusion parameters. Indeed, these parameters were obtained with samples carbonated under accelerated carbonation. To accurately predict the carbonation rate of AAM under natural carbonation, the diffusion coefficient should be evaluated on samples carbonated under natural carbonation, and not accelerated.

Finally, this PhD study highlights that AAM carbonation mechanisms differ from PC and the relationship between accelerated and natural carbonation that apply to PC, does not apply to AAM. Even though accelerated carbonation can still be used to compare one GGBS based AAM against another GGBS based AAM, PC based materials should not be compared against AAM under accelerated carbonation as it will lead to a misjudgement regarding the AAM in situ carbonation rate. This should be considered while designing performance-based standards for concrete specifications, especially if these standards are targeting AAM.

7.1.2 Durability impacts of carbonation, efflorescence and soft water leaching

The two methods in Chapter 4 have been performed at several RH values to evaluate the effect of the RH on these parameters. As it is the case for PC based materials, the RH has an inverse impact on both parameters; even though a higher RH encourages the carbonation of the carbonatable compounds, a higher RH leads to a decrease of the diffusivity of the CO_2 in these materials. However, above 60%, the RH has a similar impact on the carbonation of the carbonatable compounds.

Chapter 5 evaluated the impact of the carbonation alone on the high calcium content AAM microstructure. Several new findings added to the previous knowledge of the impact of these reactions on high calcium AAMs. The third aluminate hydrate, which has been identified as a bridging site in the interlayer of C-A-S-H, disappears following the reaction of the calcium cations with the bi/carbonate ions. These cations were charge balancing the TAH, so the decrease of their content leads to the decrease of this site. This chapter also reveals that

under natural carbonation, the decalcification of the C-A-S-H leads to the formation of a transient product, the amorphous calcium carbonates, that are later followed by the formation of crystalline calcium carbonate. C-A-S-H is also a product of PC blends containing a high content of GGBS, so this transient phase could also be present in these mixes. The impact of this transient phase on carbonation shrinkage should be evaluated in the future, to assess if its presence could be detrimental to the durability of cementitious materials containing a high level of GGBS.

Chapter 5 also evaluated the impact of the carbonation combined with efflorescence on the high calcium content AAM microstructure. Despite having similar effects to the carbonation alone, on the carbonated regions of these materials, these combined attacks tend to promote the decalcification of the C-A-S-H gel in the non-carbonated regions, and the formation of a small amount of aluminosilicate gel in these regions. Carbonation combined with efflorescence also leads to a higher amount of microcracks. The combined impact of efflorescence and carbonation should be evaluated for AAM before designing a structural concrete element. Indeed, if AAM is designed using performance based standards; these standards should incorporate risks posed by combined attacks of efflorescence and carbonation in the testing program.

Finally, Chapter 5 studied the combined impact of the soft water leaching with carbonation on these materials. As observed when the carbonation occurs alone, the non-carbonated regions remain unaffected by these durability attacks. Conversely, in the carbonated regions, C-A-S-H presents a higher degree of cross-linking than in the samples only exposed to carbonation, and the calcium carbonate that forms is vaterite. The combined impact of soft water leaching and carbonation should be considered while designing AAM structures, especially in regions with a high rate of rainfall, such as the UK.

When AAM are integrated in the specification standards for concrete, such as BS 8500 in the UK, these standards should evolve to include carbonation as a risk for unreinforced concrete if the formation of aluminosilicate gel is revealed to be detrimental for the mechanical properties. Indeed, carbonation is only considered to pose a threat to the corrosion of rebar in reinforced concrete. Consequently, carbonation is not taken into account in the specification of unreinforced concrete.

7.1.3 Carbonation and oxidation mechanisms of GGBS based AAM

Chapter 6 studied the nature of the colour change front in the samples exposed to carbonation, or to carbonation combined with efflorescence or soft water leaching. The change of colours observed in the slag based AAM is due to the oxidation of the disulphur and trisulphur radicals. These radicals are trapped in aluminosilicate cages present in the N-A-S-H, and maybe also C-A-S-H, gel. The oxidation of the sulphur happens in two steps: first the S^{2-} species are oxidised and form sulphite as a transient species, to then form later sulphate. The carbonation combined with efflorescence or with soft water leaching can promote sulphur oxidation by affecting the C-(N)-A-S-H.

Chapter 6 also studied the impact on the carbonation fronts of the carbonation alone, or combined with efflorescence or with soft water leaching. This chapter reveals that combined attacks of efflorescence with carbonation seem to particularly damage the structure of the carbonated regions which presents a large amount of microcracks compared to the carbonated regions of the samples that are carbonated alone or combined with soft water leaching. The efflorescence also reduces the depth of the CO_2 dissolution front compared with the other samples placed in different conditions.

Finally, carbonation combined with efflorescence or soft water leaching significantly reduced the content of sodium. A lower amount of sodium could lead to a lower pH, and consequently the corrosion of the rebar in reinforced concrete if the pH is low enough to depassivate the steel rebar. Consequently, the design of AAM reinforced concretes should be taken into consideration when carbonation is associated to efflorescence or soft water leaching, as it could cause a threat to the integrity of the structure.

7.2 Directions for future work

Additional research works can be required to confirm the results found in this study regarding the impact of carbonation, efflorescence and soft water leaching on the microstructure of high calcium content AAM. Specifically, the following works could be performed:

- Evaluation of the CO_2 effective diffusion coefficient of slag based AAM, that is not carbonated, with an alternative gas such as nitrogen;

- Evaluation of the CO_2 effective diffusion coefficient of slag based AAM under natural conditions;

- Alternative investigation of the formation and presence of the carbonation transient phase, amorphous calcium carbonates, with techniques such as ^{13}C MAS NMR or Raman spectroscopy;

- Evaluation of the impact of the alumiosilicate gel formation on the mechanical properties of AAM, whether it is due to carbonation alone, or combined with soft water leaching or efflorescence. If the formation of this gel is detrimental to the mechanical properties of AAM, the standards for AAM concrete specification should be revised to integrate this parameter.

- Evaluation of the carbonation shrinkage and the impact on the mechanical properties of high calcium content AAM.

- Iron K-edge XANES to fully confirm that the oxidation of the sulphur is the only process responsible for the colour change.

Finally, another piece of work that could be interesting would be to reproduce the relevant studies done in this thesis on low calcium content AAM, or AAMs containing alternative precursors that are more promising on environmental aspects.

References

[1]   F. Krausmann, C. Lauk, W. Haas, D. Wiedenhofer, From resource extraction to outflows of wastes and emissions : The socioeconomic metabolism of the global economy , 1900 – 2015, Glob. Environ. Chang. 52 (2018) 131–140. https://doi.org/10.1016/j.gloenvcha.2018.07.003.

[2]   S.A. Miller, V.M. John, S.A. Pacca, A. Horvath, Carbon dioxide reduction potential in the global cement industry by 2050, Cem. Concr. Res. 114 (2018) 115–124. https://doi.org/10.1016/j.cemconres.2017.08.026.

[3]   B. Bajželj, J.M. Allwood, J.M. Cullen, Designing climate change mitigation plans that add up, Environ. Sci. Technol. 47 (2013) 8062–8069.

[4]   G. Habert, S.A. Miller, V.M. John, J.L. Provis, A. Favier, A. Horvath, K.L. Scrivener, Environmental impacts and decarbonization strategies in the cement and concrete industries, Nat. Rev. Earth Environ. 2020. (2020) 1–15. https://doi.org/10.1038/s43017-020-0093-3.

[5]   J.L. Provis, S.A. Bernal, Geopolymers and related alkali-activated materials, Annu. Rev. Mater. Res. 44 (2014) 299–327. https://doi.org/10.1146/annurev-matsci-070813-113515.

[6]   J. Whiting, Manufacture of cement, U.S. Patent 544,706, 1895.

[7]   V.D. Glukhovsky, Gruntosilikaty (Soil silicates). Kiev,, 1959.

[8]   A.O. Purdon, The action of alkalis on blast furnace slag, J. Soc. Chem. Ind. 59 (1940) 191-202.

[9]   D.W. Hobbs, Concrete deterioration: Causes, diagnosis, and minimising risk, Int. Mater. Rev. 46 (2001) 117–144. https://doi.org/10.1179/095066001101528420.

[10]   M. Fernández Bertos, S.J.R. Simons, C.D. Hills, P.J. Carey, A review of accelerated carbonation technology in the treatment of cement-based materials and sequestration of CO_2, J. Hazard. Mater. 112 (2004) 193–205. https://doi.org/10.1016/j.jhazmat.2004.04.019.

[11]   V.G. Papadakis, C.G. Vayenas, M.N. Fardis, Fundamental modeling and experimental

investigation of concrete carbonation, ACI Mater. J. 88 (1991) 363–373. https://doi.org/10.14359/1863.

[12] M. Palacios, F. Puertas, Effect of carbonation on alkali-activated slag paste, J. Am. Ceram. Soc. 89 (2006) 3211–3221. https://doi.org/10.1111/j.1551-2916.2006.01214.x.

[13] S.A. Bernal, X. Ke, M. Criado, S. Mundra, J.L. Provis, Factors controlling carbonation resistance of alkali-activated materials, ACI Special Publication 320 (2017) 36.1-36.10.

[14] C. Shi, P. V Krivenko, D. Roy, Alkali-Activated Cements and Concretes. CRC Press, Boca Raton, 2006. https://doi.org/10.4324/9780203390672.

[15] I. Galan, C. Andrade, M. Castellote, Natural and accelerated CO_2 binding kinetics in cement paste at different relative humidities, Cem. Concr. Res. 49 (2013) 21–28. https://doi.org/10.1016/j.cemconres.2013.03.009.

[16] S.A. Bernal, J.L. Provis, R. Mejía de Gutiérrez, J.S.J. van Deventer, Accelerated carbonation testing of alkali-activated slag/metakaolin blended concretes: effect of exposure conditions, Mater. Struct. 48 (2014) 653–669. https://doi.org/10.1617/s11527-014-0289-4.

[17] X. Yao, T. Yang, Z. Zhang, Compressive strength development and shrinkage of alkali-activated fly ash–slag blends associated with efflorescence, Mater. Struct. 49 (2016) 2907–2918. https://doi.org/10.1617/s11527-015-0694-3.

[18] F. Škvára, V. Šmilauer, P. Hlaváček, L. Kopecký, Z. Cílová, A weak alkali bond in (N, K)-A-S-H gels: Evidence from leaching and modeling, Ceram. - Silikaty. 56 (2012) 374–382.

[19] L. Srinivasamurthy, V.S. Chevali, Z. Zhang, H. Wang, Phase changes under efflorescence in alkali activated materials with mixed activators, Constr. Build. Mater. 283 (2021) 122678. https://doi.org/10.1016/j.conbuildmat.2021.122678.

[20] M. Chaouche, X.X. Gao, M. Cyr, M. Cotte, L. Frouin, On the origin of the blue/green color of blast-furnace slag-based materials: Sulfur K-edge XANES investigation, J. Am. Ceram. Soc. 100 (2017) 1707–1716. https://doi.org/10.1111/jace.14670.

[21] L.G. Mallinson, I.L. Davies, Nuclear Science and technology - A historical examination of concrete, Comission of the European Cummunities, 1987.

[22] C.R. Gagg, Cement and concrete as an engineering material: An historic appraisal and

case study analysis, Eng. Fail. Anal. 40 (2014) 114–140. https://doi.org/10.1016/j.engfailanal.2014.02.004.

[23] P.C. Hewlett (ed.), Lea's Chemistry of Cement and Concrete - Fourth Edition, Elsevier, 1998.

[24] J.S. Damtoft, J. Lukasik, D. Herfort, D. Sorrentino, E.M. Gartner, Sustainable development and climate change initiatives, Cem. Concr. Res. 38 (2008) 115–127. https://doi.org/10.1016/j.cemconres.2007.09.008.

[25] Emissions Gap Report 2022: The closing window - Climate crisis calls for rapid transformation of societies, Nairobi, 2022. https://www.unep.org/resources/emissions-gap-report-2022.

[26] Emissions Gap Report 2020, (2020). https://www.unep.org/resources/emissions-gap-report-2020.

[27] J. Lehne, F. Preston, Making concrete change innovation in low-carbon cement and concrete, London, 2018. https://www.chathamhouse.org/2018/06/making-concrete-change-innovation-low-carbon-cement-and-concrete.

[28] B. Tempest, O. Sanusi, J. Gergely, V. Ogunro, D. Weggel, Compressive strength and embodied energy optimization of fly ash based geopolymer concrete, 3rd World Coal Ash, WOCA Conf. - Proc. (2009) 1–17.

[29] E. von Weizsäcker, K. Hargroves, M.H. Smith, C. Desha, P. Stasinopoulos, Transforming the Global Economy through 80% Improvements in Resource Productivity, Earthscan (2009).

[30] R. Caron, R.A. Patel, G.D. Miron, C. Le Galliard, B. Lothenbach, F. Dehn, Microstructure development of slag activated with sodium silicate solution: experimental characterization and thermodynamic modeling, J. Build. Eng. (2023) 106398. https://doi.org/10.1016/j.jobe.2023.106398.

[31] C. Chen, G. Habert, Y. Bouzidi, A. Jullien, A. Ventura, LCA allocation procedure used as an incitative method for waste recycling: An application to mineral additions in concrete, Resour. Conserv. Recycl. 54 (2010) 1231–1240. https://doi.org/10.1016/j.resconrec.2010.04.001.

[32] A. Komkova, G. Habert, Environmental impact assessment of alkali-activated materials: Examining impacts of variability in constituent production processes and transportation, Constr. Build. Mater. 363 (2023) 129032. https://doi.org/10.1016/j.conbuildmat.2022.129032.

[33] V. Shobeiri, B. Bennett, T. Xie, P. Visintin, A comprehensive assessment of the global warming potential of geopolymer concrete, J. Clean. Prod. 297 (2021) 126669. https://doi.org/10.1016/j.jclepro.2021.126669.

[34] IPCC, Global warming of 1.5°C, IPCC Spec. Rep. (2018). https://doi.org/10.1038/291285a0.

[35] M. Abdulkareem, A. Komkova, J. Havukainen, G. Habert, M. Horttanainen, Identifying optimal precursors for geopolymer composite mix design for different regional settings: A multi-objective optimization study, Recycling. 8 (2023) 32. https://doi.org/10.3390/recycling8020032.

[36] B.H. Andersen, A. Komkova, Circular economic modelling: Barriers and opportunities in turning circular within the construction sector, E3S Web Conf. 349 (2022). https://doi.org/10.1051/e3sconf/202234901009.

[37] A. Komkova, G. Habert, Optimal supply chain networks for waste materials used in alkali-activated concrete fostering circular economy, Resour. Conserv. Recycl. 193 (2023) 106949. https://doi.org/10.1016/j.resconrec.2023.106949.

[38] J.L. Provis, Activating solution chemistry for geopolymers, in: Geopolymers: Structures, Processing, Properties, and Industrial Applications, J.L. Provis & J.S.J. van Deventer, eds. Woodhead, Abingdon, 2009, pp. 50-71. https://doi.org/10.1533/9781845696382.1.50.

[39] F. Pacheco-Torgal, J.A. Labrincha, C. Leonelli, A. Palomo, P. Chindaprasirt (eds.), Handbook of Alkali-Activated Cements, Mortars and Concretes, 2014. https://doi.org/10.1016/C2013-0-16511-7.

[40] J.L. Provis, J.S.J. Van Deventer, Alkali Activated Materials: State-of-the-Art Report, RILEM TC 224-AAM, Springer Science & Business Media, Dordrecht, 2014.

[41] O.N. Petropavlovsky, Slag alkaline binding systems and concretes based on steelmaking slag, Thesis, Kiev Civil Engineering Institute (1987).

[42]   D. Li, X. Wu, Improvement of early strength of steel slag cement, Jiangsu Build. Mater. 4 (1992) 24–27.

[43]   C. Shi, X. Wu, M. Tang, Research on alkali-activated cementitious systems in China: a review, Adv. Cem. Res. 5 (1993) 1–7. https://doi.org/10.1680/adcr.1993.5.17.1.

[44]   J. Małolepszy, J. Deja, W. Brylicki, Industrial application of slag alkaline concretes, in: Proc. First Int. Conf. Alkaline Cem. Concr. Kiev, Ukr., 1994: pp. 989–1001.

[45]   C. Jian-Xiong, C. Han-bin, X. Pei, Z. Lan-Fang, A study on complex alkali-slag environmental concrete, Sustain. Dev. Concr. Technol. (2004) 299.

[46]   X. Bin, X. Yuan, Research of Alkali--Activated Nickel Slag Cement, in: Proc. Second Int. Conf. Alkaline Cem. Concr., Kiev, Ukraine, 1999.

[47]   Z. Huanhai, W. Xuequan, X. Zhongzi, T. Mingshu, Kinetic study on hydration of alkali-activated slag, Cem. Concr. Res. 23 (1993) 1253–1258. https://doi.org/10.1016/0008-8846(93)90062-E.

[48]   R.J. Myers, B. Lothenbach, S.A. Bernal, J.L. Provis, Thermodynamic modelling of alkali-activated slag cements, Appl. Geochem. 61 (2015) 233–247. https://doi.org/10.1016/j.apgeochem.2015.06.006.

[49]   J.I. Escalante-García, A.F. Fuentes, A. Gorokhovsky, P.E. Fraire-Luna, G. Mendoza-Suarez, Hydration products and reactivity of blast-furnace slag activated by various alkalis, J. Am. Ceram. Soc. 86 (2003) 2148–2153. https://doi.org/10.1111/j.1151-2916.2003.tb03623.x.

[50]   A.R. Brough, A. Atkinson, Sodium silicate-based, alkali-activated slag mortars - Part I. Strength, hydration and microstructure, Cem. Concr. Res. 32 (2002) 865–879. https://doi.org/10.1016/S0008-8846(02)00717-2.

[51]   B. Lothenbach, A. Gruskovnjak, Hydration of alkali-activated slag: Thermodynamic modelling, Adv. Cem. Res. 19 (2007) 81–92. https://doi.org/10.1680/adcr.2007.19.2.81.

[52]   S.A. Bernal, R. Mejía de Gutiérrez, J.L. Provis, V. Rose, Effect of silicate modulus and metakaolin incorporation on the carbonation of alkali silicate-activated slags, Cem. Concr. Res. 40 (2010) 898–907. https://doi.org/10.1016/j.cemconres.2010.02.003.

[53]   M. Ben Haha, B. Lothenbach, G. Le Saout, F. Winnefeld, Influence of slag chemistry on the hydration of alkali-activated blast-furnace slag - Part I: Effect of MgO, Cem. Concr. Res. 41 (2011) 955–963. https://doi.org/10.1016/j.cemconres.2011.05.002.

[54]   L. Black, 17 - Low clinker cement as a sustainable construction material, in: J.M. Khatib (Ed.), Sustainability of Construction Materials, 2nd Ed., Woodhead Publishing, 2016: pp. 415–457. https://doi.org/10.1016/B978-0-08-100370-1.00017-2.

[55]   A. Palomo, M.W. Grutzeck, M.T. Blanco, Alkali-activated fly ashes: A cement for the future, Cem. Concr. Res. 29 (1999) 1323–1329. https://doi.org/https://doi.org/10.1016/S0008-8846(98)00243-9.

[56]   A. Fernández-Jiménez, A. Palomo, I. Sobrados, J. Sanz, The role played by the reactive alumina content in the alkaline activation of fly ashes, Microporous Mesoporous Mater. 91 (2006) 111–119. https://doi.org/https://doi.org/10.1016/j.micromeso.2005.11.015.

[57]   A. Fernández-Jiménez, A. Palomo, M. Criado, Microstructure development of alkali-activated fly ash cement: a descriptive model, Cem. Concr. Res. 35 (2005) 1204–1209. https://doi.org/https://doi.org/10.1016/j.cemconres.2004.08.021.

[58]   P. Duxson, J.L. Provis, Designing precursors for geopolymer cements, J. Am. Ceram. Soc. 91 (2008) 3864–3869. https://doi.org/10.1111/j.1551-2916.2008.02787.x.

[59]   T. Bakharev, Geopolymeric materials prepared using Class F fly ash and elevated temperature curing, Cem. Concr. Res. 35 (2005) 1224–1232. https://doi.org/https://doi.org/10.1016/j.cemconres.2004.06.031.

[60]   M. Criado, A. Palomo, A. Fernández-Jiménez, Alkali activation of fly ashes. Part 1: Effect of curing conditions on the carbonation of the reaction products, Fuel. 84 (2005) 2048–2054. https://doi.org/https://doi.org/10.1016/j.fuel.2005.03.030.

[61]   American Concrete Institute, Durability of Concrete, (n.d.). https://www.concrete.org/topicsinconcrete/topicdetail/durability of concrete?search=durability of concrete.

[62]   M. Morgese, F. Ansari, M. Domaneschi, G.P. Cimellaro, Post-collapse analysis of Morandi's Polcevera viaduct in Genoa Italy, J. Civ. Struct. Heal. Monit. 10 (2020) 69–

85. https://doi.org/10.1007/s13349-019-00370-7.

[63] S.A. Bernal, J.L. Provis, Durability of alkali-activated materials: Progress and perspectives, J. Am. Ceram. Soc. 97 (2014) 997–1008. https://doi.org/10.1111/jace.12831.

[64] L. Rossi, L. Miranda de Lima, Y. Sun, F. Dehn, J.L. Provis, G. Ye, G. De Schutter, View of Future perspectives for alkali-activated materials from existing standards to structural applications, RILEM Tech. Lett. (2022) 159–177.

[65] H. Ye, A. Radlińska, Shrinkage mechanisms of alkali-activated slag, Cem. Concr. Res. 88 (2016) 126–135. https://doi.org/10.1016/j.cemconres.2016.07.001.

[66] H. Ye, C. Cartwright, F. Rajabipour, A. Radlińska, Understanding the drying shrinkage performance of alkali-activated slag mortars, Cem. Concr. Compos. 76 (2017) 13–24. https://doi.org/10.1016/j.cemconcomp.2016.11.010.

[67] E.E. Holt, Early age autogenous shrinkage of concrete, VTT Publ. (2001) 2–184.

[68] M. Palacios, F. Puertas, Effect of shrinkage-reducing admixtures on the properties of alkali-activated slag mortars and pastes, Cem. Concr. Res. 37 (2007) 691–702. https://doi.org/10.1016/j.cemconres.2006.11.021.

[69] J.D. Wallat, D. Hardjito, 10 - Assessing the shrinkage and creep of alkali-activated concrete binders, in: Handb. Alkali-Activated Cem. Mortars Concr., 2015: pp. 264–290.

[70] K. Sagoe-Crentsil, T. Brown, A. Taylor, Drying shrinkage and creep performance of geopolymer concrete, J. Sustain. Cem. Mater. 2 (2013) 35–42. https://doi.org/10.1080/21650373.2013.764963.

[71] V. Bilek, O. Sucharda, D. Bujdos, Frost resistance of alkali-activated concrete—an important pillar of their sustainability, Sustain. 13 (2021) 1–13. https://doi.org/10.3390/su13020473.

[72] M. Cyr, R. Pouhet, 11 - The frost resistance of alkali-activated cement-based binders, in: Handb. Alkali-Activated Cem. Mortars Concr., 2015: pp. 293–318.

[73] A. Arce, C. Le Galliard, A. Komkova, C.G. Papanicolaou, T.C. Triantafillou, Optimal design of ferronickel slag alkali-activated mortar for repair exposed to high thermal load, Mater. Struct. 56 (2023) #34. https://doi.org/10.1617/s11527-023-02117-9.

[74]   D.L.Y. Kong, J.G. Sanjayan, Effect of elevated temperatures on geopolymer paste, mortar and concrete, Cem. Concr. Res. 40 (2010) 334–339. https://doi.org/10.1016/j.cemconres.2009.10.017.

[75]   D. Panias, E. Balomenos, K. Sakkas, 16 - The fire resistance of alkali-activated cement-based concrete binders, in: Handb. Alkali-Activated Cem. Mortars Concr., 2015: pp. 423–462.

[76]   F. Škvára, L. Kopecký, V. Šmilauer, Z. Bittnar, Material and structural characterization of alkali activated low-calcium brown coal fly ash, J. Hazard. Mater. 168 (2009) 711–720. https://doi.org/10.1016/j.jhazmat.2009.02.089.

[77]   M.A. Longhi, Z. Zhang, E.D. Rodríguez, A.P. Kirchheim, H. Wang, Efflorescence of alkali-activated cements (geopolymers) and the impacts on material structures: A critical analysis, Front. Mater. 6 (2019) #89. https://doi.org/10.3389/fmats.2019.00089.

[78]   M. Cyr, R. Pouhet, 15 - Resistance to alkali-aggregate reaction (AAR) of alkaliactivated cement-based binders, in: Handb. Alkali-Activated Cem. Mortars Concr., 2015: pp. 397–422.

[79]   A. Runci, M. Serdar, J. Provis, Chloride-induced corrosion of steel embedded in alkali-activated materials: state of the art, 5th Symposium on Doctoral Studies in Civil Engineering (2019) 175–185. https://doi.org/10.5592/co/phdsym.2019.15.

[80]   S.A. Bernal, 12 - The resistance of alkali-activated cement-based binders to carbonation, in: F. Pacheco-Torgal, J.A. Labrincha, C. Leonelli, A. Palomo, P. Chindaprasirt (Eds.), Handb. Alkali-Activated Cem. Mortars Concr., Woodhead Publishing, Oxford, 2015: pp. 319–332. https://doi.org/https://doi.org/10.1533/9781782422884.3.319.

[81]   G.J.G. Gluth, X. Ke, A. Vollpracht, L. Weiler, S.A. Bernal, M. Cyr, D.A. Geddes, C. Grengg, C. Le, G. Marija, J.L. Provis, L. Valentini, B. Walkley, A. Basheer, S.A. Bernal, H.D. Beushausen, A. Camo, G.P. Cordoba, M. Cyr, P. Dangla, N. De, Y. Dhandapani, K. Dombrowski-daube, Y. Elakneswaran, J. Elsen, J. Manuel, G. Geng, B. Ghiassi, G. Gluth, E. Gruyaert, R.D. Hooton, B. Huet, K. Imamoto, S. Joseph, J. Li, N. Li, T. Ling, Q. Liu, B. Lothenbach, I. Martins, Carbonation rate of alkali-activated concretes and high- volume SCM concretes : a literature data analysis by RILEM TC 281-CCC, Mater. Struct. 55

(2022) #225. https://doi.org/10.1617/s11527-022-02041-4.

[82] A. Fabbri, J. Corvisier, A. Schubnel, F. Brunet, B. Goffé, G. Rimmele, V. Barlet-Gouédard, Effect of carbonation on the hydro-mechanical properties of Portland cements, Cem. Concr. Res. 39 (2009) 1156–1163. https://doi.org/10.1016/j.cemconres.2009.07.028.

[83] B. Bary, A. Sellier, Coupled moisture - Carbon dioxide-calcium transfer model for carbonation of concrete, Cem. Concr. Res. 34 (2004) 1859–1872. https://doi.org/10.1016/j.cemconres.2004.01.025.

[84] M. Nedeljković, Carbonation mechanism of alkali-activated fly ash and slag materials in view of long-term performance predictions, 2019.

[85] S. Goñi, M.T. Gaztañaga, A. Guerrero, Role of cement type on carbonation attack, J. Mater. Res. 17 (2002) 1834–1842. https://doi.org/10.1557/JMR.2002.0271.

[86] Y.F. Houst, F.H. Wittmann, Influence of porosity and water content on the diffusivity of CO_2 and O_2 through hydrated cement paste, Cem. Concr. Res. 24 (1994) 1165–1176. https://doi.org/10.1016/0008-8846(94)90040-X.

[87] F. Puertas, M. Palacios, Carbonation process of alkali-activated slag mortars, J. Am. Ceram. Soc. 41 (2006) 3071–3082. https://doi.org/10.1007/s10853-005-1821-2.

[88] A. Buchwald, M. Vanooteghem, E. Gruyaert, H. Hilbig, N. De Belie, Purdocement: application of alkali-activated slag cement in Belgium in the 1950s, Mater. Struct. 48 (2015) 501–511. https://doi.org/10.1617/s11527-013-0200-8.

[89] K. Pasupathy, M. Berndt, A. Castel, J. Sanjayan, R. Pathmanathan, Carbonation of a blended slag-fly ash geopolymer concrete in field conditions after 8 years, Constr. Build. Mater. 125 (2016) 661–669. https://doi.org/10.1016/j.conbuildmat.2016.08.078.

[90] I. Ismail, S.A. Bernal, J.L. Provis, S. Hamdan, J.S.J. Van Deventer, Drying-induced changes in the structure of alkali-activated pastes, J. Mater. Sci. 48 (2013) 3566–3577. https://doi.org/10.1007/s10853-013-7152-9.

[91] A.A. Melo Neto, M.A. Cincotto, W. Repette, Drying and autogenous shrinkage of pastes and mortars with activated slag cement, Cem. Concr. Res. 38 (2008) 565–574. https://doi.org/10.1016/j.cemconres.2007.11.002.

[92] F. Collins, J.G. Sanjayan, Cracking tendency of alkali-activated slag concrete subjected to restrained shrinkage, Cem. Concr. Res. 30 (2000) 791–798. https://doi.org/10.1016/S0008-8846(00)00243-X.

[93] D.E. Cadore, C. Angulski, M.H.F. De Medeiros, An investigation of the carbonation of alkaline activated cement made from blast furnace slag generated by charcoal, Constr. Build. Mater. 226 (2019) 117–125. https://doi.org/10.1016/j.conbuildmat.2019.07.209.

[94] O. Levenspiel, Chemical Reaction Engineering, Third Ed, John Wiley & Sons, 1999.

[95] S.W. Webb, K. Pruess, The use of Fick's law for modeling trace gas diffusion in porous media, Transp. Porous Media. 51 (2003) 327–341. https://doi.org/10.1023/A:1022379016613.

[96] M. Boumaaza, B. Huet, G. Pham, P. Turcry, A. Aït-Mokhtar, C. Gehlen, A new test method to determine the gaseous oxygen diffusion coefficient of cement pastes as a function of hydration duration, microstructure, and relative humidity, Mater. Struct. 51 (2018) #51. https://doi.org/10.1617/s11527-018-1178-z.

[97] M. Boumaaza, Experimental investigation of gas diffusivity and CO_2-binding capacity of cementitious materials, PhD thesis, Université de La Rochelle - Technische Universität München, 2020.

[98] M. Boumaaza, P. Turcry, B. Huet, A. Aït-Mokhtar, Influence of carbonation on the microstructure and the gas diffusivity of hardened cement pastes, Constr. Build. Mater. 253 (2020) 119227. https://doi.org/10.1016/j.conbuildmat.2020.119227.

[99] T. Graham, On the law of the diffusion of gases, London Edinburgh Dublin Philos. Mag. J. Sci. 2 (1833) 175–190, 269–276, 351–358.

[100] S.A. Bernal, J.L. Provis, D.G. Brice, A. Kilcullen, P. Duxson, J.S.J. Van Deventer, Accelerated carbonation testing of alkali-activated binders significantly underestimates service life: The role of pore solution chemistry, Cem. Concr. Res. 42 (2012) 1317–1326. https://doi.org/10.1016/j.cemconres.2012.07.002.

[101] M. Nedeljković, Y. Zuo, K. Arbi, G. Ye, Carbonation resistance of alkali-activated slag under natural and accelerated conditions, J. Sustain. Metall. 4 (2018) 33–49.

https://doi.org/10.1007/s40831-018-0166-4.

[102] M. Nedeljković, B. Ghiassi, S. Melzer, C. Kooij, S. van der Laan, G. Ye, CO_2 binding capacity of alkali-activated fly ash and slag pastes, Ceram. Int. 44 (2018) 19646–19660. https://doi.org/10.1016/j.ceramint.2018.07.216.

[103] M. Nedeljković, B. Šavija, Y. Zuo, M. Luković, G. Ye, Effect of natural carbonation on the pore structure and elastic modulus of the alkali-activated fly ash and slag pastes, Constr. Build. Mater. 161 (2018) 687–704. https://doi.org/10.1016/j.conbuildmat.2017.12.005.

[104] M. Cyr, R. Pouhet, Carbonation in the pore solution of metakaolin-based geopolymer, Cem. Concr. Res. 88 (2016) 227–235. https://doi.org/10.1016/j.cemconres.2016.05.008.

[105] R.R. Lloyd, J.L. Provis, J.S.J. Van Deventer, Pore solution composition and alkali diffusion in inorganic polymer cement, Cem. Concr. Res. 40 (2010) 1386–1392. https://doi.org/10.1016/j.cemconres.2010.04.008.

[106] I.P. Eugster, Sodium carbonate-bicarbonate, J. Geophys. Res. 71 (1966) 3369–3377.

[107] T.N. Nguyen, Q.T. Phung, Z. Yu, L. Frederickx, D. Jacques, Alteration in molecular structure of alkali activated slag with various water to binder ratios under accelerated carbonation, Sci. Rep. 12 (2022) #5524. https://doi.org/10.1038/s41598-022-09491-4.

[108] S.A. Bernal, Effect of the activator dose on the compressive strength and accelerated carbonation resistance of alkali silicate-activated slag/metakaolin blended materials, Constr. Build. Mater. 98 (2015) 217–226. https://doi.org/10.1016/j.conbuildmat.2015.08.013.

[109] T.F. Sevelsted, J. Skibsted, Carbonation of C-S-H and C-A-S-H samples studied by ^{13}C, ^{27}Al and ^{29}Si MAS NMR spectroscopy, Cem. Concr. Res. 71 (2015) 56–65. https://doi.org/10.1016/j.cemconres.2015.01.019.

[110] S. Ortaboy, J. Li, G. Geng, R.J. Myers, P.J.M. Monteiro, R. Maboudian, C. Carraro, Effects of CO_2 and temperature on the structure and chemistry of C-(A-)S-H investigated by Raman spectroscopy, RSC Adv. 7 (2017) 48925–48933. https://doi.org/10.1039/c7ra07266j.

[111] R. Hay, J. Li, K. Celik, Phase evolution, micromechanical properties, and morphology of calcium (alumino)silicate hydrates C-(A-)S-H under carbonation, Cem. Concr. Res. 152 (2022) 106683. https://doi.org/10.1016/j.cemconres.2021.106683.

[112] Z. Shi, C. Shi, S. Wan, N. Li, Z. Zhang, Effect of alkali dosage and silicate modulus on carbonation of alkali-activated slag mortars, Cem. Concr. Res. 113 (2018) 55–64. https://doi.org/10.1016/j.cemconres.2018.07.005.

[113] S.A. Bernal, J.L. Provis, B. Walkley, R. San, J.D. Gehman, D.G. Brice, A.R. Kilcullen, P. Duxson, J.S.J. Van Deventer, Gel nanostructure in alkali-activated binders based on slag and fly ash, and effects of accelerated carbonation, Cem. Concr. Res. 53 (2013) 127–144. https://doi.org/10.1016/j.cemconres.2013.06.007.

[114] J. Zhang, C. Shi, Z. Zhang, Carbonation induced phase evolution in alkali-activated slag / fly ash cements : The effect of silicate modulus of activators, Constr. Build. Mater. 223 (2019) 566–582. https://doi.org/10.1016/j.conbuildmat.2019.07.024.

[115] S. Badar, K. Kupwade-Patil, S.A. Bernal, J.L. Provis, E.N. Allouche, Corrosion of steel bars induced by accelerated carbonation in low and high calcium fly ash geopolymer concretes, Constr. Build. Mater. 61 (2014) 79–89. https://doi.org/10.1016/j.conbuildmat.2014.03.015.

[116] A. Sarkar, S. Mahapatra, Synthesis of all crystalline phases of anhydrous calcium carbonate, Cryst. Growth Des. 10 (2010) 2129–2135. https://doi.org/10.1021/cg9012813.

[117] A.E. Morandeau, C.E. White, In situ X-ray pair distribution function analysis of accelerated carbonation of a synthetic calcium–silicate–hydrate gel, J. Mater. Chem. A. 3 (2015) 8597-8605.

[118] X. Ke, M. Criado, J.L. Provis, S.A. Bernal, Slag-based cements that resist damage induced by carbon dioxide, ACS Sustain. Chem. Eng. (2018) 5067–5075. https://doi.org/10.1021/acssuschemeng.7b04730.

[119] A.E. Morandeau, C.E. White, Role of magnesium-stabilized amorphous calcium carbonate in mitigating the extent of carbonation in alkali-activated slag, Chem. Mater. 27 (2015) 6625–6634. https://doi.org/10.1021/acs.chemmater.5b02382.

[120] S.Y. Wang, E. Mccaslin, C.E. White, Effects of magnesium content and carbonation on the multiscale pore structure of alkali-activated slags, Cem. Concr. Res. 130 (2020) 105979. https://doi.org/10.1016/j.cemconres.2020.105979.

[121] S.A. Bernal, R. San Nicolas, R.J. Myers, R. Mejía De Gutiérrez, F. Puertas, J.S.J. Van Deventer, J.L. Provis, MgO content of slag controls phase evolution and structural changes induced by accelerated carbonation in alkali-activated binders, Cem. Concr. Res. 57 (2014) 33–43. https://doi.org/10.1016/j.cemconres.2013.12.003.

[122] N.T. Dung, T.J.N. Hooper, C. Unluer, Improving the carbonation resistance of Na2CO3-activated slag mixes via the use of reactive MgO and nucleation seeding, Cem. Concr. Compos. 115 (2021) 103832. https://doi.org/10.1016/j.cemconcomp.2020.103832.

[123] E.R. McCaslin, C.E. White, A parametric study of accelerated carbonation in alkali-activated slag, Cem. Concr. Res. 145 (2021) 106454. https://doi.org/10.1016/j.cemconres.2021.106454.

[124] E. Konigsberger, L. Konigsberger, H. Gamsjager, Low temperature thermodynamic model for the system Na_2CO_3-$MgCO_3$-$CaCO_3$-H_2O, Geochim. Cosmochim. Acta. 63 (1999) 3105–3119. https://doi.org/http://dx.doi.org/10.1016/S0016-7037(99)00238-0.

[125] Products and Systems for the Protection and Repair of Concrete Structures - Test Methods - Determination of resistance to carbonation (EN 13295:2004), (2004).

[126] Durabilité des Bétons: Methodes recommandées pour la mesure des grandeurs associées à la durabilité. Compte-rendu des journees techniques AFPC-AFREM., Laboratoire Matériaux et Durabilité des Constructions INSA-UPS, 1997. https://books.google.co.uk/books?id=jwIeywEACAAJ.

[127] Laboratório Nacional de Engenharia Civil: Betões. Determinação da resistência à carbonatação. Estacionário (LNEC E391), (1993).

[128] NORDTEST: Concrete, Repairing Materialsand Protective Coating: Carbonation resistance (NT Build 357), (1989).

[129] British Standards Institution, B BS EN 12390-12:2020, (2019) 18.

[130] British Standards Institution., BS EN 12390-10-2018: Determination of the carbonation

resistance of concrete at atmospheric levels of carbon dioxide (2018).

[131] L. Basso, A. Crotwell, H. Dolman, L. Gatti, C. Gerbig, D. Griffith, B. Hall, A. Jordan, P. Krummel, M. Leuenberger, Z. Loh, S. Mikaloff-Fletcher, Y. Sawa, M. Schibig, O. Tarasova, J. Turnbull, A. Vermeulen, WMO Greenhouse Gas Bulletin (GHG Bulletin) - No.17: The State of Greenhouse Gases in the Atmosphere Based on Global Observations through 2020, (2021) 1–10.

[132] G.J.G. Gluth, K. Arbi, S.A. Bernal, D. Bondar, K.D. Ashish, D. Vilma, D. Karl, P. Pipilikaki, S.L.A. Valcke, G. Ye, Y. Zuo, J.L. Provis, RILEM TC 247-DTA round robin test : carbonation and chloride penetration testing of alkali-activated concretes, Mater. Struct. 53 (2020) #21. https://doi.org/10.1617/s11527-020-1449-3.

[133] S. Chinchón-Payá, C. Andrade, S. Chinchón, Indicator of carbonation front in concrete as substitute to phenolphthalein, Cem. Concr. Res. 82 (2016) 87–91. https://doi.org/10.1016/j.cemconres.2015.12.010.

[134] C. Grengg, B. Müller, C. Staudinger, F. Mittermayr, J. Breininger, B. Ungerböck, S.M. Borisov, T. Mayr, M. Dietzel, High-resolution optical pH imaging of concrete exposed to chemically corrosive environments, Cem. Concr. Res. 116 (2019) 231–237. https://doi.org/10.1016/j.cemconres.2018.10.027.

[135] E. Liu, M. Ghandehari, C. Brückner, G. Khalil, J. Worlinsky, W. Jin, A. Sidelev, M.A. Hyland, Mapping high pH levels in hydrated calcium silicates, Cem. Concr. Res. 95 (2017) 232–239. https://doi.org/10.1016/j.cemconres.2017.02.001.

[136] P.R. Vassie, Measurement Techniques For The Diagnosis Detection And Rate Estimation Of Corrosion In Concrete Structures, in: Control. Concr. Degrad., n.d.: pp. 215–229. https://doi.org/10.1680/ccd.28197.0020.

[137] R.E. Melchers, C.Q. Li, M.A. Davison, Observations and analysis of a 63-year-old reinforced concrete promenade railing exposed to the North Sea, Mag. Concr. Res. 61 (2009) 233–243. https://doi.org/10.1680/macr.2007.00093.

[138] British Standards Institution, BS EN 12390-16:2019: Determination of the Shrinkage of the concrete, (2019).

[139] V.L. Ta, S. Bonnet, T. Senga Kiesse, A. Ventura, A new meta-model to calculate

carbonation front depth within concrete structures, Constr. Build. Mater. 129 (2016) 172–181. https://doi.org/10.1016/j.conbuildmat.2016.10.103.

[140] B. Bary, C. Mügler, Simplified modelling and numerical simulations of concrete carbonation in unsaturated conditions, Rev. Eur. Génie Civ. 10 (2006) 1049–1072. https://doi.org/10.3166/regc.10.1049-1072.

[141] K.H. Yang, E.A. Seo, S.H. Tae, Carbonation and CO_2 uptake of concrete, Environ. Impact Assess. Rev. 46 (2014) 43–52. https://doi.org/10.1016/j.eiar.2014.01.004.

[142] K.Y. Ann, S.W. Pack, J.P. Hwang, H.W. Song, S.H. Kim, Service life prediction of a concrete bridge structure subjected to carbonation, Constr. Build. Mater. 24 (2010) 1494–1501. https://doi.org/10.1016/j.conbuildmat.2010.01.023.

[143] O.B. Isgor, A.G. Razaqpur, Finite element modeling of coupled heat transfer, moisture transport and carbonation processes in concrete structures, Cem. Concr. Compos. 26 (2004) 57–73. https://doi.org/10.1016/S0958-9465(02)00125-7.

[144] M.R. Jones, R.K. Dhir, M.D. Newlands, A.M.O. Abbas, Study of the CEN test method for measurement of the carbonation depth of hardened concrete, Mater. Struct. Constr. 33 (2000) 135–142. https://doi.org/10.1007/bf02484168.

[145] N. Seigneur, E. Kangni-Foli, V. Lagneau, A. Dauzères, S. Poyet, P. Le Bescop, E. L'Hôpital, J.B. d'Espinose de Lacaillerie, Predicting the atmospheric carbonation of cementitious materials using fully coupled two-phase reactive transport modelling, Cem. Concr. Res. 130 (2020) 105966. https://doi.org/10.1016/j.cemconres.2019.105966.

[146] S. Gordon, B.J. McBride, Computer Program for Calculation of Complex Chemical Equilibrium Compositions and Applications I. Analysis, (1994) 58. https://doi.org/NASA RP-1311.

[147] X. Ke, S.A. Bernal, J.L. Provis, B. Lothenbach, Thermodynamic modelling of phase evolution in alkali-activated slag cements exposed to carbon dioxide, Cem. Concr. Res. 136 (2020) 106158. https://doi.org/10.1016/j.cemconres.2020.106158.

[148] T. Wagner, D.A. Kulik, F.F. Hingerl, S. V. Dmytrievava, GEM-Selektor geochemical modeling package: TSolMod library and data interface for multicomponent phase models, Can. Mineral. 50 (2012) 1173–1195.

https://doi.org/10.3749/canmin.50.5.1173.

[149] B. Lothenbach, D.A. Kulik, T. Matschei, M. Balonis, L. Baquerizo, B. Dilnesa, G.D. Miron, R.J. Myers, Cemdata18: A chemical thermodynamic database for hydrated Portland cements and alkali-activated materials, Cem. Concr. Res. 115 (2019) 472–506. https://doi.org/10.1016/j.cemconres.2018.04.018.

[150] S. Park, B. Lothenbach, J.G. Jang, H. Kim, N. Lee, Thermodynamic modeling and experimental study of carbonation of alkali-activated slag cements, ACS Sustain. Chem. Eng. 11 (2023) 4049–4063. https://doi.org/10.1021/acssuschemeng.2c05789.

[151] C. Dow, F.P. Glasser, Calcium carbonate efflorescence on Portland cement and building materials, Cem. Concr. Res. 33 (2003) 147–154. https://doi.org/10.1016/S0008-8846(02)00937-7.

[152] Z. Zhang, J.L. Provis, X. Ma, A. Reid, X. Wang, Efflorescence and subflorescence induced microstructural and mechanical evolution in fly ash-based geopolymers, Cem. Concr. Compos. 92 (2018) 165–177.

[153] J. Cowie, F.P. Glasser, The reaction between cement and natural waters containing dissolved carbon dioxide, Adv. Cem. Res. 4 (1992) 119–134. https://doi.org/10.1680/adcr.1992.4.15.119.

[154] R.J. Charlson, H. Rodhe, Factors controlling the acidity of natural rainwater, Nature. 295 (1982) 683–685. https://doi.org/10.1038/295683a0.

[155] E. Najafi Kani, A. Allahverdi, J.L. Provis, Efflorescence control in geopolymer binders based on natural pozzolan, Cem. Concr. Compos. 34 (2012) 25–33. https://doi.org/10.1016/j.cemconcomp.2011.07.007.

[156] R.R. Lloyd, J.L. Provis, J.S.J. Van Deventer, Pore solution composition and alkali diffusion in inorganic polymer cement, Cem. Concr. Res. 40 (2010) 1386–1392. https://doi.org/10.1016/j.cemconres.2010.04.008.

[157] Z. Zhang, J.L. Provis, A. Reid, H. Wang, Fly ash-based geopolymers : The relationship between composition , pore structure and ef fl orescence, Cem. Concr. Res. 64 (2014) 30–41. https://doi.org/10.1016/j.cemconres.2014.06.004.

[158] A. Saludung, T. Azeyanagi, Y. Ogawa, K. Kawai, Effect of silica fume on efflorescence

formation and alkali leaching of alkali-activated slag, J. Clean. Prod. 315 (2021) 128210. https://doi.org/10.1016/j.jclepro.2021.128210.

[159] M.A. Longhi, E.D. Rodríguez, B. Walkley, D. Eckhard, Z. Zhang, J.L. Provis, A.P. Kirchheim, Metakaolin-based geopolymers: Efflorescence and its effect on microstructure and mechanical properties, Ceram. Int. 48 (2022) 2212–2229. https://doi.org/10.1016/j.ceramint.2021.09.313.

[160] N. Schiopu, L. Tiruta-Barna, E. Jayr, J. Méhu, P. Moszkowicz, Modelling and simulation of concrete leaching under outdoor exposure conditions, Sci. Total Environ. 407 (2009) 1613–1630. https://doi.org/10.1016/j.scitotenv.2008.11.027.

[161] C. Conolly, K. Vincent, A. Sanocka, S. Richie, D. Knight, B. Donovan, T. Jackson, E. Osbourne, M. Twigg, C. Braban, UK Eutrophying and Acidifying Atmospheric Polluants (UKEAP) 2021 annual report, 2021.

[162] P.E. Grattan-Bellew, Microstructural investigation of deteriorated Portland cement concretes, Constr. Build. Mater. 10 (1996) 3–16. https://doi.org/10.1016/0950-0618(95)00066-6.

[163] E. Rozière, A. Loukili, Performance-based assessment of concrete resistance to leaching, Cem. Concr. Compos. 33 (2011) 451–456. https://doi.org/10.1016/j.cemconcomp.2011.02.002.

[164] T. Milović, O. Rudić, S.O. Furgan, M. Radeka, M. Malešev, V. Radonjanin, S. Baloš, M. Laban, Effects of soft water attack on Portland and natural zeolite blended cements, Chem. Ind. Chem. Eng. Q. 27 (2021) 403–415. https://doi.org/10.2298/CICEQ201120009M.

[165] K. Kannapiran, T. Sujatha, S. Nagan, Resistance of reinforced geopolymer concrete beams to acid and chloride migration, Asian J. Civ. Eng. 14 (2013) 225–238.

[166] S.H. Sanni, R.B. Khadiranaikar, Performance of geopolymer concrete under severe environmental conditions, Int. J. Civ. Struct. Eng. 3 (2012) 396–407.

[167] Greenpeace, Climate change and extreme weather, (n.d.). https://www.greenpeace.org.uk/challenges/climate-change/climate-change-extreme-weather/.

[168] S.A. Bernal, R. San Nicolas, J.L. Provis, R. Majía de Gutiérrez, J.S.J. Van Deventer, Natural carbonation of aged alkali-activated slag concretes, Mater. Struct. 47 (2014) 693–707. https://doi.org/10.1617/s11527-013-0089-2.

[169] A. Saludung, T. Azeyanagi, Y. Ogawa, K. Kawai, Effect of silica fume on efflorescence formation and alkali leaching of alkali-activated slag, J. Clean. Prod. 315 (2021) 128210. https://doi.org/10.1016/j.jclepro.2021.128210.

[170] K. Liang, K. Cui, M.M.S. Sabri, J. Huang, Influence factors in the wide application of alkali-activated materials: A critical review about efflorescence, Materials (Basel). 15 (2022) 6436. https://doi.org/10.3390/ma15186436.

[171] L. Stefanini, Design of alkali-activated cements with maximised recycled content, PhD thesis, University of Sheffield, 2023.

[172] J. Zhang, G.W. Scherer, Comparison of methods for arresting hydration of cement, Cem. Concr. Res. 41 (2011) 1024–1036. https://doi.org/10.1016/j.cemconres.2011.06.003.

[173] K.L. Scrivener, R. Snellings, B. Lothenbach, eds., A Practical Guide to Microstructural Analysis of Cementitious Materials, CRC Press, Boca Raton, 2016. https://doi.org/10.1201/b19074.

[174] B. Dickens, W.E. Brown, Crystal structures of CaNa$_2$(CO$_3$)2.5H$_2$O, synthetic gaylussite, and CaNa$_2$(CO$_3$)$_2$.2H$_2$O, synthetic pirssonite, Inorg. Chem. 8 (1969) 2093–2103. https://doi.org/10.1021/ic50080a012.

[175] C.S. Choi, A.D. Mighell, Neutron diffraction study of sodium sesquicarbonate dihydrate, Acta Crystallogr. Sect. B. 38 (1982) 2874–2876. https://doi.org/10.1107/S0567740882010164.

[176] K.L. Scrivener, Backscattered electron imaging of cementitious microstructures: Understanding and quantification, Cem. Concr. Compos. 26 (2004) 935–945. https://doi.org/10.1016/j.cemconcomp.2004.02.029.

[177] K.L. Scrivener, A. Bazzoni, B. Mota, J.E. Rossen, Electron Microscopy, in: Scrivener, K. L., Snellings, R., Lothenbach, B. (Eds), A Practical Guide to Microstructural Analysis of Cementitious Materials, (2016) 353–416. http://link.springer.com/10.1007/978-1-

62703-776-1.

[178]   R.J. Myers, S.A. Bernal, R. San Nicolas, J.L. Provis, Generalized structural description of calcium-sodium aluminosilicate hydrate gels: The cross-linked substituted tobermorite model, Langmuir. 29 (2013) 5294–5306. https://doi.org/10.1021/la4000473.

[179]   Q. Zeng, K. Li, T. Fen-Chong, P. Dangla, Analysis of pore structure, contact angle and pore entrapment of blended cement pastes from mercury porosimetry data, Cem. Concr. Compos. 34 (2012) 1053–1060. https://doi.org/10.1016/j.cemconcomp.2012.06.005.

[180]   M. Boumaaza, B. Huet, C. Le Galliard, P. Turcry, A. Aït-Mokhtar, C. Gehlen, Experimental determination of carbonation related durability indicators : gas diffusivity and CO_2 binding capacity, 15th Int. Congr. Chem. Cem., Prague (2019).

[181]   M. Boumaaza, B. Huet, P. Turcry, A. Aït-Mokhtar, The CO_2-binding capacity of synthetic anhydrous and hydrates: Validation of a test method based on the instantaneous reaction rate, Cem. Concr. Res. 135 (2020) 106113. https://doi.org/10.1016/j.cemconres.2020.106113.

[182]   Storage ring - Diamond Light Source, (n.d.). https://www.diamond.ac.uk/Science/Machine/Components/storagering.html.

[183]   J. Garrevoet, B. Vekemans, S. Bauters, A. Demey, L. Vincze, Development and applications of a laboratory micro X-ray fluorescence (μXRF) spectrometer using monochromatic excitation for quantitative elemental analysis, Anal. Chem. 87 (2015) 6544–6552. https://doi.org/10.1021/acs.analchem.5b00770.

[184]   L.R. Blackburn, Understanding the Effectiveness of Plutonium Surrogates for Waste and Stockpile Immobilisation, PhD thesis, University of Sheffield, 2021.

[185]   B. Bary, A. Sellier, Coupled moisture—carbon dioxide–calcium transfer model for carbonation of concrete, Cem. Concr. Res. 34 (2004) 1859–1872. https://doi.org/10.1016/j.cemconres.2004.01.025.

[186]   G. Lewis, Humidity fixed points of binary saturated aqueous solutions, J. Res. Natl. Bur. Stand. - A. Phys. Chem. 81 A (1977) 89–96.

[187]   A. Hidalgo, C. Domingo, C. Garcia, S. Petit, C. Andrade, C. Alonso, Microstructural

changes induced in Portland cement-based materials due to natural and supercritical carbonation, J. Mater. Sci. 43 (2008) 3101–3111. https://doi.org/10.1007/s10853-008-2521-5.

[188] M. Ben Haha, G. Le Saout, F. Winnefeld, B. Lothenbach, Influence of activator type on hydration kinetics, hydrate assemblage and microstructural development of alkali activated blast-furnace slags, Cem. Concr. Res. 41 (2011) 301–310. https://doi.org/10.1016/j.cemconres.2010.11.016.

[189] Y. Zuo, M. Nedeljković, G. Ye, Coupled thermodynamic modelling and experimental study of sodium hydroxide activated slag, Constr. Build. Mater. 188 (2018) 262–279. https://doi.org/10.1016/j.conbuildmat.2018.08.087.

[190] X. Ke, S.A. Bernal, J.L. Provis, Uptake of chloride and carbonate by Mg-Al and Ca-Al layered double hydroxides in simulated pore solutions of alkali-activated slag cement, Cem. Concr. Res. 100 (2017) 1–13. https://doi.org/10.1016/j.cemconres.2017.05.015.

[191] S.A. Bernal, Microstructural changes induced by CO_2 exposure in alkali-activated slag / metakaolin pastes, Front. Mater. 3 (2016) #43. https://doi.org/10.3389/fmats.2016.00043.

[192] N.C. Collier, Transition and decomposition temperatures of cement phases – a collection of thermal analysis data, Ceram.-Silikáty. 60 (2016) 338–343. https://doi.org/10.13168/cs.2016.0050.

[193] J. Bu, Z. Tian, S. Zheng, Z. Tang, Effect of sand content on strength and pore structure of cement mortar, J. Wuhan Univ. Technol. Mater. Sci. Ed. 32 (2017) 382–390. https://doi.org/10.1007/s11595-017-1607-9.

[194] V.T. Ngala, C.L. Page, Effects of carbonation on pore structure and diffusional properties of hydrated cement pastes, Cem. Concr. Res. 27 (1997) 995–1007.

[195] V. Shah, K. Scrivener, B. Bhattacharjee, S. Bishnoi, Changes in microstructure characteristics of cement paste on carbonation, Cem. Concr. Res. 109 (2018) 184–197. https://doi.org/10.1016/j.cemconres.2018.04.016.

[196] S. Ghahramani, Y. Guan, A. Radlińska, P. Shokouhi, Monitoring the carbonation-induced microcracking in alkali-activated slag (AAS) by nonlinear resonant acoustic

spectroscopy (NRAS), Adv. Civ. Eng. Mater. 7 (2018) 20170133. https://doi.org/10.1520/acem20170133.

[197] Y. Zhang, B. Yang, Y. Zhengxian, G. Ye, Ink-bottle effect and pore size distribution of cementitious materials identified by pressurization – depressurization cycling mercury, Materials (Basel). 12 (2019). https://doi.org/10.3390/ma12091454.

[198] N. Li, N. Farzadnia, C. Shi, Microstructural changes in alkali-activated slag mortars induced by accelerated carbonation, Cem. Concr. Res. 100 (2017) 214–226. https://doi.org/10.1016/j.cemconres.2017.07.008.

[199] S. Diamond, Mercury porosimetry: An inappropriate method for the measurement of pore size distributions in cement-based materials, Cem. Concr. Res. 30 (2000) 1517–1525.

[200] J.J. Chen, J.J. Thomas, H.M. Jennings, Decalcification shrinkage of cement paste, Cem. Concr. Res. 36 (2006) 801–809. https://doi.org/10.1016/j.cemconres.2005.11.003.

[201] K. Pasupathy, D. Singh Cheema, J. Sanjayan, Durability performance of fly ash-based geopolymer concrete buried in saline environment for 10 years, Constr. Build. Mater. 281 (2021) 122596. https://doi.org/10.1016/j.conbuildmat.2021.122596.

[202] M. Auroy, S. Poyet, P. Le Bescop, J.M. Torrenti, T. Charpentier, M. Moskura, X. Bourbon, Comparison between natural and accelerated carbonation (3% CO_2): Impact on mineralogy, microstructure, water retention and cracking, Cem. Concr. Res. 109 (2018) 64–80. https://doi.org/10.1016/j.cemconres.2018.04.012.

[203] H.S. Wong, M. Zobel, N.R. Buenfeld, R.W. Zimmerman, Influence of the interfacial transition zone and microcracking on the diffusivity , permeability and sorptivity of cement-based materials after drying, Mag. Concr. Res. 61 (2009) 571–589. https://doi.org/10.1680/macr.2008.61.8.571.

[204] H.S. Wong, N.R. Buenfeld, J. Hill, A.W. Harris, Mass transport properties of mature wasteform grouts, Adv. Cem. Res. 19 (2007) 35–46.

[205] T.C. Powers and T.L. Brownyard, Studies of the physical properties of hardened Portland cement paste, ACI J. Proc. 43 (1946). https://doi.org/10.14359/15302.

[206] K. Sisomphon, L. Franke, Carbonation rates of concretes containing high volume of

pozzolanic materials, Cem. Concr. Compos. 37 (2007) 1647–1653. https://doi.org/10.1016/j.cemconres.2007.08.014.

[207] R. Kondo, S. Ohsawa, Studies on a method to determine the amount of granulated Blast furnace slag and the rate of hydration of slag in cements, in: Proc. 5th Int. Congr. Chem. Cem., Tokyo, 1968: Vol. IV p255-262.

[208] S. Peng, Q. Hu, S. Hamamoto, Diffusivity of rocks : Gas diffusion measurements and correlation to porosity and pore size distribution, Water Resources Res. 48 (2012). https://doi.org/10.1029/2011WR011098.

[209] Y. Sakai, Relationship between air diffusivity and permeability coefficients of cementitious materials, RILEM Tech. Lett. 5 (2020) 26–32.

[210] J.L. Provis, R.J. Myers, C.E. White, V. Rose, J.S.J. Van Deventer, X-ray microtomography shows pore structure and tortuosity in alkali-activated binders, Cem. Concr. Res. 42 (2012) 855–864. https://doi.org/10.1016/j.cemconres.2012.03.004.

[211] F. Collins, J.G. Sanjayan, Effect of pore size distribution on drying shrinkage of alkali-activated slag concrete, Cem. Concr. Res. 30 (2000) 1401–1406.

[212] S.Y. Wang, E. Mccaslin, C.E. White, Effects of magnesium content and carbonation on the multiscale pore structure of alkali-activated slags, Cem. Concr. Res. 130 (2020) 105979. https://doi.org/10.1016/j.cemconres.2020.105979.

[213] V.G. Papadakis, C.G. Vayenas, M.N. Fardis, A reaction engineering approach to the problem of concrete carbonation, AIChE J. 35 (1989) 1639–1650. https://doi.org/10.1002/aic.690351008.

[214] Sheffield Weather, (n.d.). https://www.sheffieldweather.net/index.htm.

[215] S.P. Kang, S.J. Kwon, Effects of red mud and Alkali-Activated Slag Cement on efflorescence in cement mortar, Constr. Build. Mater. 133 (2017) 459–467. https://doi.org/10.1016/j.conbuildmat.2016.12.123.

[216] X. Yao, T. Yang, Z. Zhang, Fly ash-based geopolymers : Effect of slag addition on efflorescence, J. Wuhan Univ. Technol. - Mater. Sci. Ed. 31 (2016) 689–694. https://doi.org/10.1007/s11595-016-1430-8.

[217] S. Grangeon, F. Claret, Y. Linard, C. Chiaberge, X-ray diffraction: A powerful tool to

probe and understand the structure of nanocrystalline calcium silicate hydrates, Acta Cryst. B. Struct. Sci. Cryst. Eng. Mater. 69 (2013) 465–473. https://doi.org/10.1107/S2052519213021155.

[218] I. Narasimha Murthy, J. Babu Rao, Investigations on physical and chemical properties of high silica sand, Fe-Cr slag and blast furnace slag for foundry applications, Procedia Environ. Sci. 35 (2016) 583–596. https://doi.org/10.1016/j.proenv.2016.07.045.

[219] A.E.S. Van Driessche, M. Kellermeier, L.G. Benning, D. Gebauer, New Perspectives on Mineral Nucleation and Growth, Springer Nature, 2017. https://doi.org/ 10.1007/978-3-319-45669-0.

[220] A. V Radha, T.Z. Forbes, C.E. Killian, P.U.P.A. Gilbert, A. Navrotsky, Transformation and crystallization energetics of synthetic and biogenic amorphous calcium carbonate, Proc. Natl. Acad. Sci. 107 (2010) 16438–16443. https://doi.org/doi.org/10.1073/pnas.1009959107.

[221] L. Brečević, D. Kralj, On calcium carbonates : from fundamental research to application, Croat. Chem. Acta. 39 (2007) 467-484.

[222] P. López-arce, L.S. Gómez-villalba, S. Martínez-ramírez, M.Á. De Buergo, R. Fort, Influence of relative humidity on the carbonation of calcium hydroxide nanoparticles and the formation of calcium carbonate polymorphs, Powder Technol. 205 (2011) 263–269. https://doi.org/10.1016/j.powtec.2010.09.026.

[223] E. Bernard, W.J. Zucha, B. Lothenbach, U. Mäder, Stability of hydrotalcite (Mg-Al layered double hydroxide) in presence of different anions, Cem. Concr. Res. 152 (2022) 106674. https://doi.org/10.1016/j.cemconres.2021.106674.

[224] X. Xu, J.T. Han, D.H. Kim, K. Cho, Two modes of transformation of amorphous calcium carbonate films in air, J. Phys. Chem. B. 110 (2006) 2764–2770.

[225] P.J. Sideris, Z. Gan, C.P. Grey, Identification of cation clustering in Mg–Al layered double hydroxides using multinuclear solid state nuclear magnetic resonance spectroscopy, Chem. Mater. 24 (2012) 2449–2461.

[226] M.D. Andersen, H.J. Jakobsen, J. Skibsted, Incorporation of aluminum in the calcium silicate hydrate (C-S-H) of hydrated Portland cements: A high-field ^{27}Al and ^{29}Si MAS

NMR investigation, Inorg. Chem. 42 (2003) 2280–2287. https://doi.org/10.1021/ic020607b.

[227] B. Walkley, R. San Nicolas, M. Sani, G.J. Rees, J. V Hanna, J.S.J. Van Deventer, J.L. Provis, Phase evolution of C-(N)-A-S-H / N-A-S-H gel blends investigated via alkali-activation of synthetic calcium aluminosilicate precursors, Cem. Concr. Res. 89 (2016) 120–135. https://doi.org/10.1016/j.cemconres.2016.08.010.

[228] A. Vyalikh, D. Massiot, U. Scheler, Structural characterisation of aluminium layered double hydroxides by ^{27}Al solid-state NMR, Solid State Nucl. Magn. Reson. 36 (2009) 19–23. https://doi.org/10.1016/j.ssnmr.2009.04.002.

[229] B. Walkley, S.J. Page, G.J. Rees, J.L. Provis, J. V. Hanna, Nanostructure of CaO-(Na$_2$O)-Al$_2$O$_3$-SiO$_2$-H$_2$O Gels revealed by multinuclear solid-state magic angle spinning and multiple quantum magic angle spinning nuclear magnetic resonance spectroscopy, J. Phys. Chem. C. 124 (2020) 1681–1694. https://doi.org/10.1021/acs.jpcc.9b10133.

[230] G. Renaudin, J. Russias, F. Leroux, C. Cau-Dit-Coumes, F. Frizon, Structural characterization of C-S-H and C-A-S-H samples — Part II : Local environment investigated by spectroscopic analyses, J. Solid State Chem. 182 (2009) 3320–3329. https://doi.org/10.1016/j.jssc.2009.09.024.

[231] A. Kunhi Mohamed, P. Moutzouri, P. Berruyer, B.J. Walder, J. Siramanont, M. Harris, M. Negroni, S.C. Galmarini, S.C. Parker, K.L. Scrivener, L. Emsley, P. Bowen, The atomic-level structure of cementitious calcium aluminate silicate hydrate, J. Am. Chem. Soc. 142 (2020) 11060–11071. https://doi.org/10.1021/jacs.0c02988.

[232] B. Walkley, X. Ke, J.L. Provis, S.A. Bernal, Activator anion influences the nanostructure of alkali-activated slag cements, J. Phys. Chem. C. 125 (2021) 20727–20739. https://doi.org/10.1021/acs.jpcc.1c07328.

[233] B. Walkley, J.L. Provis, Solid-state nuclear magnetic resonance spectroscopy of cements, Mater. Today Adv. 1 (2019) 100007. https://doi.org/10.1016/j.mtadv.2019.100007.

[234] R.J. Myers, Thermodynamic modelling of CaO-Al$_2$O$_3$-SiO$_2$-H$_2$O based cements, PhD thesis, The University of Sheffield, 2015.

[235] X. Ke, Improved durability and sustainability of alkali-activated slag cements, PhD Thesis, The University of Sheffield, (2017).

[236] X. Gao, Q.L. Yu, H.J.H. Brouwers, Apply ^{29}Si, ^{27}Al MAS NMR and selective dissolution in identifying the reaction degree of alkali activated slag-fly ash composites, Ceram. Int. 43 (2017) 12408–12419. https://doi.org/10.1016/j.ceramint.2017.06.108.

[237] R.J. Myers, S.A. Bernal, J.D. Gehman, J.S.J. Van Deventer, J.L. Provis, The role of Al in cross-linking of alkali-activated slag cements, J. Am. Ceram. Soc. 98 (2015) 996–1004. https://doi.org/10.1111/jace.13360.

[238] A. Favier, G. Habert, N. Roussel, J.B. D'Espinose de Lacaillerie, A multinuclear static NMR study of geopolymerisation, Cem. Concr. Res. 75 (2015) 104–109. https://doi.org/10.1016/j.cemconres.2015.03.003.

[239] D. Le Cornec, Q. Wang, L. Galoisy, G. Renaudin, L. Izoret, G. Calas, Greening effect in slag cement materials, Cem. Concr. Compos. 84 (2017) 93–98. https://doi.org/10.1016/j.cemconcomp.2017.08.017.

[240] B. Sioulas, J.G. Sanjayan, The coloration phenomenon associated with slag blended cements, Cem. Concr. Res. 31 (2001) 313–320. https://doi.org/10.1016/S0008-8846(00)00371-9.

[241] N.K. Lee, J.G. Jang, H.K. Lee, Shrinkage characteristics of alkali-activated fly ash/slag paste and mortar at early ages, Cem. Concr. Compos. 53 (2014) 239–248. https://doi.org/10.1016/j.cemconcomp.2014.07.007.

[242] H. Ye, C. Cartwright, F. Rajabipour, A. Radlińska, Effect of drying rate on shrinkage of alkali-activated slag cements, Proc. 4th Int. Conf. Durab. Concr. Struct. ICDCS 2014. (2014) 254–261.

[243] J. Yang, Q. Wang, Y. Zhou, Influence of curing time on the drying shrinkage of concretes with different binders and water-to-binder ratios, Adv. Mater. Sci. Eng. 2017 (2017). https://doi.org/10.1155/2017/2695435.

[244] S.A. Bernal, V. Rose, J.L. Provis, The fate of iron in blast furnace slag particles during alkali-activation, Mater. Chem. Phys. 146 (2014) 1–5. https://doi.org/10.1016/j.matchemphys.2014.03.017.

[245] A. Mancini, B. Lothenbach, G. Geng, D. Grolimund, D.F. Sanchez, S.C. Fakra, R. Dähn, B. Wehrli, E. Wieland, Iron speciation in blast furnace slag cements, Cem. Concr. Res. 140 (2021) 106287. https://doi.org/10.1016/j.cemconres.2020.106287.

[246] Y. Lo, H.M. Lee, Curing effects on carbonation of concrete using a phenolphthalein indicator and Fourier-transform infrared spectroscopy, Build. Environ. 37 (2002) 507–514. https://doi.org/10.1016/S0360-1323(01)00052-X.

[247] G. Wittke, Reactions of phenolphthalein at various pH values, J. Chem. Educ. 60 (1983) 239–240. https://doi.org/10.1021/ed060p239.

[248] J.W. McBain, LXXXV.—The use of phenolphthalein as an indicator. The slow rate of neutralisation of carbonic acid, J. Chem. Soc. Trans. (1912) 814–820.

[249] M. Ben Haha, B. Lothenbach, G. Le Saout, F. Winnefeld, Influence of slag chemistry on the hydration of alkali-activated blast-furnace slag - Part II: Effect of Al_2O_3, Cem. Concr. Res. 42 (2012) 74–83. https://doi.org/10.1016/j.cemconres.2011.08.005.

[250] M. Ben Haha, G. Le Saout, F. Winnefeld, B. Lothenbach, Influence of activator type on hydration kinetics, hydrate assemblage and microstructural development of alkali activated blast-furnace slags, Cem. Concr. Res. 41 (2011) 301–310. https://doi.org/10.1016/j.cemconres.2010.11.016.

[251] H. Ye, A. Radlińska, Quantitative analysis of phase assemblage and chemical shrinkage of alkali-activated slag, J. Adv. Concr. Technol. 14 (2016) 245–260. https://doi.org/10.3151/jact.14.245.

[252] V.N.E. Robinson, Imaging with backscattered electrons in a scanning electron microscope, Scanning. 3 (1980) 15–26. https://doi.org/10.1002/sca.4950030103.

[253] S. Miyahara, E. Owaki, M. Ogino, E. Sakai, Carbonation of a concrete using a large amount of blast furnace slag powder, J. Ceram. Soc. Japan. 125 (2017) 533–538. https://doi.org/10.2109/jcersj2.16269.

[254] P. Zhang, J.B. Lewis, O. Klein-BenDavid, A.C. Garrabrants, R. Delapp, H.A. van der Sloot, D.S. Kosson, The role of environmental conditions on the carbonation of an alkali-activated cementitious waste form, Cem. Concr. Res. 151 (2022) 106645. https://doi.org/10.1016/j.cemconres.2021.106645.

[255] N.C. Collier, D.W. Heyes, E.J. Butcher, J. Borwick, A.E. Milodowski, L.P. Field, S.J. Kemp, I. Mounteney, S.A. Bernal, C.L. Corkhill, N.C. Hyatt, J.L. Provis, L. Black, Gaseous carbonation of cementitious backfill for geological disposal of radioactive waste: Nirex Reference Vault Backfill, Appl. Geochemistry. 106 (2019) 120–133. https://doi.org/10.1016/j.apgeochem.2019.04.020.

[256] L. Black, C. Breen, J. Yarwood, Structural features of C–S–H(I) and its carbonation in Air—A Raman spectroscopic study. Part II: Carbonated phases, J. Am. Ceram. S (2007) 908–917. https://doi.org/10.1111/j.1551-2916.2006.01429.x.

[257] K. De Weerdt, G. Plusquellec, A. Belda Revert, M.R. Geiker, B. Lothenbach, Effect of carbonation on the pore solution of mortar, Cem. Concr. Res. 118 (2019) 38–56. https://doi.org/10.1016/j.cemconres.2019.02.004.

[258] B. Debret, M. Andreani, A. Delacour, S. Rouméjon, N. Trcera, EIMF (Edinburgh Ion Microprobe Facility), H. Williams, Assessing sulfur redox state and distribution in abyssal serpentinites using XANES spectroscopy, Earth Planet. Sci. Lett. 466 (2017) 1–11. https://doi.org/10.1016/j.epsl.2017.02.029.

[259] R. Alonso Mori, E. Paris, G. Giuli, S.G. Eeckhout, M. Kavčič, M. Žitnik, K. Bučar, L.G.M. Pettersson, P. Glatzel, Electronic structure of sulfur studied by X-ray absorption and emission spectroscopy, Anal. Chem. 81 (2009) 6516–6525. https://doi.org/10.1039/b819257j.(33).

[260] M.E. Fleet, XANES spectroscopy of sulfur in earth materials, Can. Mineral. 43 (2005) 1811–1838.

[261] P.A. Bingham, A.J. Connelly, R.J. Hand, N.C. Hyatt, P.A. Northrup, R.A. Mori, P. Glatzel, M. Kavčič, M. Žitnik, K. Bučar, R. Edge, A multi-spectroscopic investigation of sulphur speciation in silicate glasses and slags, Glas. Technol. Eur. J. Glas. Sci. Technol. Part A. 51 (2010) 63–80.

[262] S.C.B. Myneni, X-ray and vibrational spectroscopy of sulfate in earth materials, Sulfate Miner. Crystallogr. Geochemistry, Environ. Significance. 40 (2019) 113–172. https://doi.org/10.2138/rmg.2000.40.2.

[263] A. Roy, Sulfur speciation in granulated blast furnace slag: An X-ray absorption

spectroscopic investigation, Cem. Concr. Res. 39 (2009) 659–663. https://doi.org/10.1016/j.cemconres.2009.05.007.

[264] A.A. Gambardella, M. Cotte, W. De Nolf, K. Schnetz, R. Erdmann, R. Van Elsas, V. Gonzalez, A. Wallert, P.D. Iedema, M. Eveno, K. Keune, Sulfur K-edge micro- and full-field XANES identify marker for preparation method of ultramarine pigment from lapis lazuli in historical paints, Sci. Adv. 6 (2020).

[265] M.E. Fleet, X. Liu, S.L. Harmer, P.L. King, Sulfur K-edge XANES spectroscopy : Chemical state and content of sulfur in silicate glasses, Can. Mineral. 43 (2005) 1727–1740. https://doi.org/10.2113/gscanmin.43.5.1605.

[266] M. Criado, S.A. Bernal, P. Garcia-Triñanes, J.L. Provis, Influence of slag composition on the stability of steel in alkali-activated cementitious materials, J. Mater. Sci. 53 (2018) 5016–5035. https://doi.org/10.1007/s10853-017-1919-3.

[267] R. Slavík, V. Bednařík, M. Vondruška, O. Skoba, T. Hanzlíček, Proof of the sodalite structures in geopolymers, Chem. Listy (2005) 471–472.

[268] M. Wilke, P.J. Jugo, K. Kevin, J. Susini, R. Botcharnikov, S.C. Kohn, M. Janousch, The origin of S^{4+} detected in silicate glasses by XANES, Am. Mineral. 93 (2008) 235–240. https://doi.org/10.2138/am.2008.2765.

[269] A. Izaguirre, J. Lanas, J.I. Álvarez, Ageing of lime mortars with admixtures : Durability and strength assessment, Cem. Concr. Res. 40 (2010) 1081–1095. https://doi.org/10.1016/j.cemconres.2010.02.013.

[270] S.A. Bernal, J. Bisschop, J.S.J. Van Deventer, J.L. Provis, Drying shrinkage microcracking of alkali-activated slag materials, in Proceedings of the 34th Cement and Concrete Science Conference (2014).

Appendix one: Microstructure development of slag activated with sodium silicate solution: Experimental characterization and thermodynamic modeling

Full length article

Microstructure development of slag activated with sodium silicate solution: Experimental characterization and thermodynamic modeling

Richard Caron [a,b], Ravi A. Patel [a,b,*], George D. Miron [c], Cassandre Le Galliard [d], Barbara Lothenbach [e], Frank Dehn [a,b]

[a] Karlsruhe Institute of Technology (KIT), Institute of Building Materials and Concrete Structures (IMB), DE-76131 Karlsruhe, Germany
[b] Materials Testing and Research Institute Karlsruhe (MPA), Karlsruhe Institute of Technology (KIT), DE-76131 Karlsruhe, Germany
[c] Laboratory for Waste Management (LES), Paul Scherrer Institute (PSI), Forschungsstr. 111, Villigen PSI, 5232, Switzerland
[d] Department of Materials Science and Engineering, The University of Sheffield, Sir Robert Hadfield Building, Sheffield, S1 3JD, United Kingdom
[e] Empa, Concrete & Asphalt Laboratory, Überlandstrasse 129, Dübendorf, 8600, Switzerland

ARTICLE INFO

ABSTRACT

Slag is a by-product of the steel industry that can be used as a binder with alkali solutions. In this study, the microstructural development is discussed for two alkali-activated slag mixes with promising properties for structural applications. The reaction products for both mixes were characterized by X-ray diffraction, thermogravimetry, Fourier-transform infrared spectroscopy and nuclear magnetic resonance. The Ca/Si ratio of C-A-S-H gel and the secondary products such as hydrotalcite, M-S-H and zeolites depend on the activator solution. The dissolution kinetics is followed by isothermal calorimetry and scanning electron microscopy. Calorimetry data can be adjusted with the maximum heat release obtained from thermodynamic modeling to predict the degree of dissolution. Thermodynamic modeling using the Pitzer ion activity model was applied for alkali-activated slag. This model is relevant for the first two days of reaction. For later age, the extended Debye–Hückel ion activity model and the Pitzer ion activity model give identical results. Phase assemblage predicted using thermodynamic modeling with the correct CASH model and consistent M-S-H and zeolite datasets agreed well with experiments.

Appendix two: Optimal design of ferronickel slag alkali-activated mortar for repair exposed to high thermal load

ORIGINAL ARTICLE

Optimal design of ferronickel slag alkali-activated mortar for repair exposed to high thermal load

Andres Arce · Cassandre Le Galliard · Anastasija Komkova ·
Catherine G. Papanicolaou · Thanasis C. Triantafillou

Abstract In this work, the optimal design of a mortar based on alkali-activated material technology is presented. Ferronickel slag, a byproduct of the ferronickel alloy industry, was used both as a binder component (in a finely ground form) and as fine aggregate in alignment with a circular economy approach. The proportions of binder, fine aggregate, and water were optimized using Design of Experiment Design of Mixtures. The performance indicators evaluated were flow, flexural and compressive strength both before and after high-temperature exposure, mass loss, and thermal shrinkage. Life cycle assessment was used to calculate the relative environmental cost of the studied mixes in comparison to a counterpart traditional Ordinary Portland Cement mortar. The optimal mix design exhibited high flexural strength (8.5 and 10.5 MPa, before and after high-temperature exposure, respectively), an unheated compressive strength equal to 69.5 MPa, and a post-heating residual one of 33.9 MPa, 7.7% mass loss and 3.4% thermal shrinkage. Mercury Intrusion Porosimetry along with Scanning Electron Microscopy with Energy Dispersive X-Ray Analysis were also performed on optimal mortar samples in order to link micro-structural heat-induced changes to residual (post-heating) macro-mechanical performances. Finally, when compared to OPC-based products, the optimized mortar mix resulted in 70% lower CO_2 emissions indicating great potential for the construction sector where concern about environmental impact keeps growing.

Keywords Alkali-activated cement · Mortar · Refractory cement · Waste management · Modeling